ISSN (p) 1857-1727
ISSN (e) 2345-1688

Volume 11 No. 1, 2016

CHEMISTRY
JOURNAL OF MOLDOVA

General, Industrial and Ecological Chemistry

Editor-in-Chief: Gheorghe DUCA

NCAA national scientific journals ranking: Category A

Academy of Sciences of Moldova
Institute of Chemistry
Moldova State University

© Chemistry Journal of Moldova
Institute of Chemistry A.S.M. (publisher)

CHEMISTRY JOURNAL OF MOLDOVA
General, Industrial and Ecological Chemistry

is included/abstracted/indexed in:

Web of Science (Thomson Reuters-Emerging Source Citation Index)
CAS (Chemical Abstracts Service/ SciFinder)
SCOPUS (accepted, May 2016)
VINITI (Russian Scientific and Technical Information Institute)
DOAJ (Directory Open Access Journals)
ROAD (Directory of Open Access Scholarly Resources)
SHERPA/ROMEO
OAJI (Open Academic Journals Index)
HINARI, Research in Health Programme, WHO
EVISA (European Virtual Institute for Speciation Analysis)
EIFL-OA Moldova (On-line Journals of Moldova)
BASE (Bielefeld Academic Search Engine)
Cite Factor (Directory Indexing of International Research Journals)
PubsHub Journals & Congresses
Academic Keys
Scholar Steer
Library of Moldova State University
Electronic Journals Library Database
Electronic Catalog of Academy of Sciences of Belarus
V. I. Vernadsky National Library of Ukraine
ZDB (Berlin State Library)
German National Library of Science and Technology University Library Hannover (Germany)
Temple University Libraries (USA)
The Royal Library Copenhagen/Copenhagen University Library (Denmark)
Digital library of "Dunarea de Jos" University (Romania)
Digital library of Ghent University (Belgium)
Digital library of Wroclaw University (Poland)
Digital library of Helsinki University (Finland)
Digital library of KTH Royal Institute of Technology (Sweden)
Digital library of Manchester University (UK)
Digital library of Cambridge University (UK)
Digital library of Sheffield University (UK)
Digital library of University of Texas at Austin (SUA)
Digital library of Indiana University (SUA)
Digital library of Simon Fraser University (Canada)
Digital library of University of Saskatchewan (Canada)
Digital library of Laval University (Canada)
Digital library of Auckland University (New Zealand)
Digital library of Queensland University of Technology (Australia)
Digital library of Victoria University (Australia)

Editorial production and secretariat:
Dr. Larisa Postolachi
Lilia Anghel
Dr. Elena Gorincioi

Editorial office address:
Institute of Chemistry of Academy of Sciences of Moldova, 3, Academiei Str., Chisinau, MD-2028, Republic of Moldova
Tel: + 373 22 725490; Fax: +373 22 739954; e-mail: chemjm@asm.md, chemjm@gmail.com, chemjm_correspondence@yahoo.com
Web: www.cjm.asm.md

Academy of Sciences of Moldova, Institute of Chemistry
Moldova State University, Faculty of Chemistry and Chemical Technology

CHEMISTRY JOURNAL OF MOLDOVA

General, Industrial and Ecological Chemistry

Editor-in-Chief: **Academician Gheorghe DUCA**, Academy of Sciences of Moldova
Editors: **Corr. member Tudor LUPASCU**, Academy of Sciences of Moldova
Dr. Viorica GLADCHI, Moldova State University

Local Editorial Board:
Dr. Hab. A. ARICU
Academy of Sciences of Moldova

Dr. Hab. I. BULHAC
Academy of Sciences of Moldova

Dr. G. DRAGALINA
Moldova State University

Corr. member I. GERU
Academy of Sciences of Moldova

Dr. Hab. M. GONTA
Moldova State University

Acad. A. GULEA
Moldova State University

Dr. V. KULCITKI
Academy of Sciences of Moldova

Dr. Hab. F. MACAEV
Academy of Sciences of Moldova

Dr. R. NASTAS, scientific secretary
of the editorial board,
Academy of Sciences of Moldova

Dr. Hab. I. POVAR
Academy of Sciences of Moldova

Dr. Hab. V. RUSU
Academy of Sciences of Moldova

Dr. Hab. R. STURZA
Technical University of Moldova

Dr. Hab. V. SARAGOV
A. Russo State University of Balti

Dr. Hab. N. UNGUR
Academy of Sciences of Moldova

Acad. P. VLAD
Academy of Sciences of Moldova

International Editorial Board:
Acad. S. ALDOSHIN
Russian Academy of Sciences

Acad. S. ANDRONATI
National Academy of Sciences of Ukraine

Acad. M. ANDRUH
University of Bucharest, Bucharest, Romania

Prof. V. ARION
University of Vienna, Austria

Prof. M. BAHADIR
Technical University of Braunschweig, Germany

Prof. A. BENNISTON
Newcastle University, UK

Acad. I. BERSUKER
University of Texas at Austin, USA

Prof. J. de BOER
Vrije University Amsterdam, The Netherlands

Prof. L. CHIBOTARU
Katholieke Universiteit Leuven, Belgium

Prof. A. GARABADZHIU
St-Petersburg State Institute of Technology, Russia

Acad. N. KARTEL
National Academy of Sciences of Ukraine

Acad. J. LIPKOWSKI
Polish Academy of Sciences

Prof. I. SANDU
A.I. Cuza University, Iasi, Romania

Acad. B. SIMIONESCU
Romanian Academy, Iasi, Romania

Corr. member B. TSUKERBLAT
Ben-Gurion University of the Negev, Israel

Journal Quality Factor (for the year 2016 is 1.20)
Infobase Index (IBI Factor for the year 2015 is 3.2)
Cosmos Impact Factor (for the year 2015 is 5.224)
Universal Impact Factor (for the year 2014 is 0.135)

ISSUE CONTENTS LIST WITH GRAPHICAL ABSTRACTS

SPECIAL ISSUE DEDICATED TO THE 70TH ANNIVERSARY FROM THE FOUNDATION OF THE FIRST ACADEMIC INSTITUTIONS AND TO THE 55TH FROM THE FOUNDATION OF THE ACADEMY OF SCIENCES OF MOLDOVA

SPECIAL ISSUE DEDICATED TO THE 70TH ANNIVERSARY FROM THE FOUNDATION OF THE FIRST ACADEMIC INSTITUTIONS AND TO THE 55TH FROM THE FOUNDATION OF THE ACADEMY OF SCIENCES OF MOLDOVA

Foundation of the Academy of Sciences of Moldova

On the basis of the decision of the Government of the USSR of March 11, 1946 to organize in Chisinau the Base of scientific researches of the Academy of Sciences of USSR, the Council of Ministries of MSSR and the Bureau of CC of the CP(b) of Moldova adopted on June 12, 1946 the Decision No. 583 "On the creation of the Moldovan Base of scientific researches of the Academy of Sciences of USSR in Chisinau. On June 29 the Presidium of the Academy of Sciences of the USSR approved the structure of the Base, its main directions of research and the governing bodies. Subsequently, in 1949, the Base was transformed in the Moldovan Branch of the Academy of Sciences of USSR. The inaugural act of constitution and opening of the Academy of Sciences of the Moldovan SSR took place on August 2, 1961.

The first President of the Academy of Sciences of Moldova was Prof. Iachim Grosul, Corresponding Member of the Academy of Sciences of USSR, Academician of the ASM, Doctor Habilitate of Historical Sciences (1961-1976), followed by Prof. Alexandru Jucenco, Corresponding Member of the Academy of Sciences of USSR, Academician of the ASM, Doctor Habilitate of Biological Sciences (1977-1989), by Prof. Andrei Andries, Academician of the ASM, Doctor Habilitate of Physical and Mathematical Sciences (1989-2004) and Prof. Gheorghe Duca, Academician of the ASM, Doctor Habilitate of Chemical Sciences (beginning with 2004).

The Institute of Chemistry of the Academy of Sciences of Moldova

The Institute of Chemistry of the ASM was founded in 1959 on the basis of the departments of organic chemistry, of inorganic chemistry and the laboratory of analytical chemistry of the Moldovan Branch of the Academy of Sciences of the USSR.

The cornerstones of scientific directions of the Institute of Chemistry were laid down by famous researchers, members of the Academy of Sciences, founders of scientific schools in Moldova: A.V. Ablov (1905-1978) – School of Coordination Compounds Chemistry; G.V. Lazurievski (1906-1987) – School of Organic and Bioorganic Chemistry, Yu.S. Lealicov (1909-1976), organizer and leader of research related to physical-chemical methods of analysis – School of Polarography.

Later, new scientific schools were created: School of Quantum Chemistry – headed by academician I. Bersuker; School of Organic, Bioorganic Chemistry, Chemistry of Natural and Physiologically Active Compounds – headed by academician P. Vlad; School of Coordination Chemistry, Macrocyclic and Supramolecular Compounds – headed by academician N. Garbalau; School of Ecological Chemistry – headed by academician Gh. Duca, School of Bioinorganic Chemistry – headed by academician C. Turta and Scientific School in the field of Chemistry of Adsorbents – headed by the corresponding member T. Lupascu.

In 2006, the Institute of Chemistry launched the publication (in English) of the peer-reviewed scientific journal ***Chemistry Journal of Moldova. General, Industrial and Ecological Chemistry*** (ChemJMold). Recently, ChemJMold has been included in *Thomson Reuters-Emerging Source Citation Index* (ESCI) based on relevance to a scholarly community, interest to opinion leaders, coverage of emerging fields, and feedback given by Web of Science customers.

Main results

The research direction of the Institute of Chemistry of the ASM is *SYNTHESIS, STRUCTURE AND PROPERTIES OF NEW POLYFUNCTIONAL SUBSTANCES; PROCESSES AND TECHNOLOGIES FOR ENVIRONMENTAL TREATMENT.*

Investigations of the influence of the electronic structure on the nuclei configuration and dynamics were crowned with the discovery entitled „The effect of tunnel cleavage of energetic levels of polyatomic systems in the state of electronic degeneration".

Importantly, there were also developed in the theory and practice of the template synthesis of coordination compounds of transition metals with organic ligands of chelating and macrocyclic type, amongst which compounds of practical utility were marked out.

Original methods were also developed related to the synthesis of new coordination compounds of biometals with polyfunctional ligands, including compounds with significant antitumor antiviral, anti-chlorosis activity, as well as compounds with psychotropic properties.

The scientific school in the chemistry of natural compounds, founded at the institute, is the world leader known in the study of superacidic cyclization of terpenes. The laws of this reaction were established for various classes of terpene compounds (alcohols, their acetates, acids, esters, phenyl sulphones, etc.).

Technologies of the production of activated carbon from vegetable by-products were elaborated to be used for the detoxification of human body, for treatment of waste waters, of surface and ground waters.

Most valuable findings:

✓ Coordination compounds with various useful properties: polynuclear compounds of Cr(III) as molecular magnets, catalysts of technological and biotechnological processes, macrocyclic colorants for plastics and synthetic fibres; new compounds for obtaining extra-pure metals, compounds for ion selective electrodes; agents for anticorrosive coating and protection of metals.

✓ Coordination combinations with anticancer, antiviral, antibacterial, anticoccidial, antidote properties; growth regulators for plants and algae.

✓ Odorant products, aromatizers and biologically active products based on natural terpenes, used in tobacco processing, perfumery, medicine.

✓ Methods of obtaining: organic substances with psycho-stimulating, anticonvulsant, sedative, tranquilizing, antimycotic effects; regulators of cardiac activity; compounds with significant tuberculostatic activity.

✓ Procedures of obtaining and regenerating activated carbons from vegetable waste; medicinal preparations based on activated carbons, catalysts and adsorbents for the purification of ground and surface waters.

✓ New functionalized ionic liquids as renewable catalysts for chemoselective redox processes.

✓ New preparations from grape seeds for medicine, veterinary and agriculture (ENOXIL-M and ENOXIL-A, and a dermatological cream based on Enoxil). In 2010, for the first time in its history, the Institute of Chemistry registered a trademark at the National Register of Trademarks and received a certificate for preparations based on the biologically active substance “ENOXIL”, thus obtaining protection on the territory of the Republic of Moldova for a period of 10 years.

✓ Technologies for removing hydrogen sulphide from ground waters and processing of underground waters from divalent iron and manganese ions.

✓ Green technology for recycling plastic waste so as to make new products.

✓ New compositions to be used as plaster for the interior surface coatings of buildings.

✓ Efficient methods of dosing heavy metals (Pb, Cu, Cd, Fe, Ni, Zn, and Mo) in foodstuffs and environmental objects.

✓ Development and application of optimal compositions of biofuel blends, using physico-chemical modelling.

Corresponding Member, Doctor Habilitate, Professor Tudor LUPASCU,
Director of the Institute of Chemistry of the Academy of Sciences of Moldova

The 6th International Conference
ECOLOGICAL & ENVIRONMENTAL CHEMISTRY 2017

March 2-3, 2017, Chisinau, Republic of Moldova

The 6th International Conference **ECOLOGICAL & ENVIRONMENTAL CHEMISTRY 2017** (EEC-2017) will be held on 2-3 March, 2017 in Chisinau, Republic of Moldova.

Topics:

A. Ecological Chemistry
- Physico-chemical and chemico-biological processes which determine composition, structure and chemical properties of the environment
- Chemical risk assessment of human health and ecological system

B. Environmental Chemistry and Engineering
- Chemical processes of water, air and waste treatment
- Preventing of soil degradation

C. Green Chemistry
- Preventing and reducing the negative impact of chemistry to the environment
- Design of ecological friendly technologies and chemical products that minimize the use and generation of hazardous substances

D. Ecological & Environmental Aspects in Chemical Research and Education
- Ecological & environmental methodological aspects in chemical research and innovation activities
- Ecological & environmental methodological aspects in chemical education

Registration of the EEC-2017 Conference participants, submission of abstracts for publication and other conference-related issues will be performed on-line via the website: **http://eec-2017.mrda.md/.** Deadline for the **Abstracts submission** is October 1st, 2016.

Abstracts Book

All accepted abstracts will be published in Abstracts Book of the Conference EEC-2017, which will be available at the time of registration.

Proceedings

EEC-2017 full papers can be submitted for publication in a special issue of the ***Chemistry Journal of Moldova*** (**http://www.cjm.asm.md/**). Chemistry Journal of Moldova is a fully open access journal. Submitted manuscripts will follow the standard peer-review.

Conference Chairman
Academician Gheorghe DUCA
President of the Academy of Sciences of Moldova
1 Stefan cel Mare Blvd.
MD 2001, Chisinau, Republic of Moldova
Tel: +373-22-271478
Fax: +373-22-276014
e-mail: duca@asm.md

Conference Secretariat
Dr. Lidia ROMANCIUC
Lilia ANGHEL
e-mail: EEC-2017@mrda.md
web page: www.EEC-2017.mrda.md

THE NATURE OF THE Co-C BOND CLEAVAGE PROCESSES IN METHYLCOB(II)ALAMIN AND ADENOSYLCOB(III)ALAMIN

Tudor Spataru[a*], Francisco Fernandez[b]

[a]*Department of Chemistry, Columbia University, New York, New York 10027, United States*
[b]*Natural Sciences Department, Hostos Community College, 500 Grand Concourse, Bronx, New York 10451, United States*
[*]*email: ts2407@columbia.edu; phone: (1) -212-854-1080; fax: (1)-212-932-1289*

In Memory of the Academician Constantin Turta

Abstract. Unfortunately, there are still significant disagreements between experimental and theoretical data of rate constants, energy barriers for Co-C bond cleavage process and coordination numbers of vitamin B_{12} coenzyme species in spite of the remarkable efforts done by research community. Therefore, no grounded mechanisms for Co-C vitamin B_{12} coenzyme bond breaking process and subsequent reactions have been found up to now. The influence of the mixing orbitals e.g. Pseudo-Jahn-Teller and similar effects on the reactions paths of bond-cleavage mechanisms of vitamin B_{12} co-factors must be taken into account by utilizing multi-reference methods, in particular multi-configurational self-consistent field (MCSCF) method. Then, the change in total energy along the normal coordinate *Q* for the stretching mode including Co-C and Co-N bonds in vitamin B_{12} cofactors is expected due to a "vibronic" coupling term, which couples an excited state and ground state by a second order derivative potential-energy operator. The strong state mixing effect is expected to lead to low energy barriers and to Co-C and Co-N axial bond cleavage events in agreement with experimental data. Afterward, the updated mechanisms of vitamin B_{12} bio-processes can be determined.

Keywords: vitamin B_{12}, mechanism, bio-catalysis, Pseudo-Jahn-Teller effect, DFT, MCSCF.

Received: December 2015/ Revised final: February 2016/ Accepted: February 2016

Introduction

Vitamin B_{12} cofactor is one of eight B vitamins and is involved in mammalian cellular metabolism, influencing amino acid and DNA synthesis [1] and hematopoiesis. The best known human physiological function of vitamin B_{12} is its role in promoting normal health in the brain and nervous system. Vitamin B_{12} anemia can cause such neurologic dysfunction as weakness, fatigue, light-headedness, rapid heartbeat, rapid breathing, pale skin color, bruising, and bleeding (including bleeding gums). The more severe vitamin B_{12} anemia dysfunctions are characterized by tingling or numbness of the fingers and toes, difficulty walking, mood changes, depression, memory loss, disorientation and, in most severe cases, dementia [2]. Vitamin B_{12} deficiency has even been considered in playing a role in the development of Alzheimer's disease [3-7].

The vitamin B_{12} cofactor contains a cobalt atom surrounded by an equatorial corrin ring. Covalently linked to the central atom is a dimethylbenzimidazole that occupies one of the axial coordination positions. The opposite coordinate is available for several ligands in bio-medium or in solution; however, known biologically active structures containing adenosyl- or methyl have been considered most often (Figure 1).

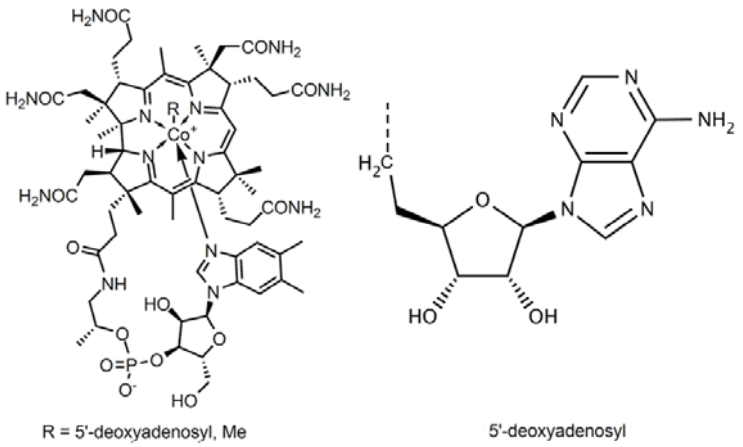

Figure 1. The structure of vitamin B_{12} cofactor (left side) and of 5-deoxyadenosyl ligand (right side) with coordinating dash bond [8-10].

Vitamin B_{12} is known to participate in at least two types of enzyme-catalyzed reactions [8-10] in the human body: a) isomerase rearrangements with participation of the adenosylcobalamin form of vitamin B_{12}; b) methyltransferases with participation of the methylcobalamin form of vitamin B_{12}. To date, human consumption of the various vitamin B_{12} varieties and their mechanisms of action in the human body are still under study. The best form of vitamin B_{12} to be recommended to patients is still not fully established in the medical community [6-10]. Moreover, the recommended dosage of vitamin B_{12} varies from one author to another [3-7]. One of the more controversial areas of research regarding the vitamin B_{12} mechanism is its activation that starts with Co-C bond cleavage under influence of electron transfer and/or substrate influence. There is little agreement between experimental and theoretical data in spite of a significant amount of research on this problem. The mechanism of vitamin B_{12} must be updated with correct theoretical and experimental data that is in agreement with each other.

This review is dedicated to a better understanding of the chemistry involved with B_{12} bio-catalysis in searching of a firmer foundation upon which we can treat the various forms of anemia and neurologic dysfunction diseases associated with vitamin B_{12}.

The mechanisms of methylcobalamin and adenosylcobalamin activation

Vitamin B_{12} and its derivatives have received considerable attention for their use in organic chemistry [11-19]. The cobalamin cofactor plays an integral role in methyl transfer by donating methyl groups to homocysteine and accepting them from CH_3 –H_4 folate [20-22]. The biological reactions catalyzed by cobalamin-dependent methionine synthase generally include as a primary turnover the enzyme-bound cobalamin prosthetic group cycling between methylcob(III)alamin and cob(I)alamin forms. All corrinoid-dependent methyl transferases bind the corriniod cofactor with displacement of the dimethylbenzimidazole ligand: in most cases the side chain of histidine residue (Figure 2) from the enzyme is a new ligand [11,23-28].

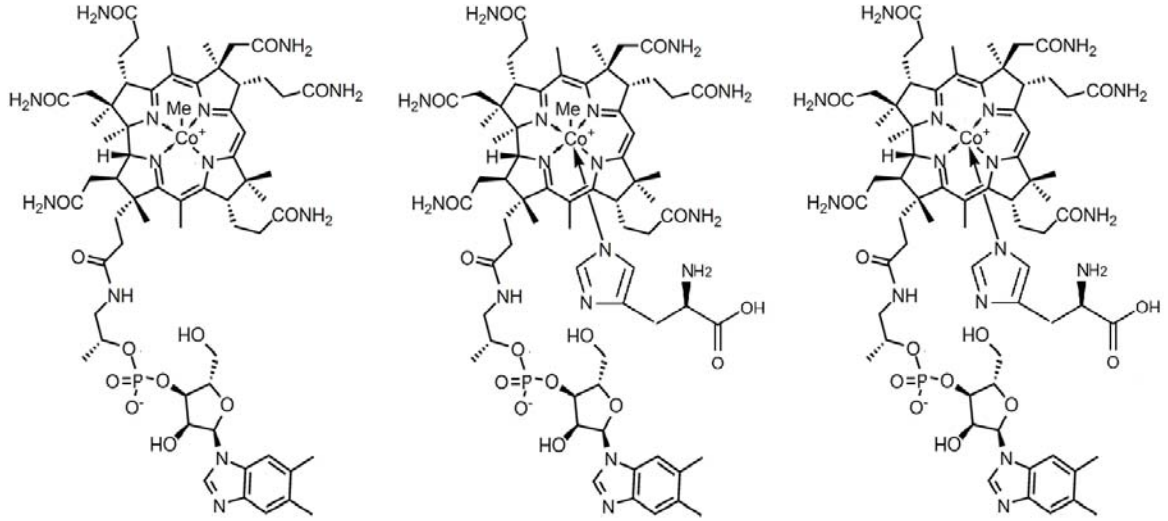

Figure 2. The schemes of the methylcobalamin coenzyme common structures found by X-ray diffractions [11,23-28].

Adenosylcobalamin is the cofactor of several enzymatic processes [29-37], such as melanoma cell adhesion molecule (MCAM), glutamate mutase, methyleneglutaratemutase, class II ribonucleoside triphosphate reductase, ethanolamine ammonia lysase, and diol- glycerol dehydratase. A common feature of these enzymes is that the Co-C bond of adenosylcobalamin is cleaved homolytically to initiate the reaction, giving rise to a five-coordinate cob(II)alamin and an adenosyl radical. Measurements of the rate constant for cob(II)alamin formation demonstrate that the enzyme increases the rate of homolysis of the Co-C bond by 10^{12}-fold both for B_{12} – dependent methylmalonyl-Co-A mutase and adenosylcobalamin-dependent glutamate mutases [33,34]. Finally, we should point out the differences between the initial stages in methyl- and adenosyl-dependent mutases considering the Co-C cleavage process. As it is depicted in Figure 3: (a) the methylcobalamin-dependent methionine synthase generally includes as a primary turnover the cycling between Co(III) methylcobalamin and cob(I)alamin, which allows the heterolytic Co-C cleavage process, while in the adenosyl-cobalamin-dependent mutases the Co-C bond of adenosylcobalamin is cleaved homolytically, giving rise to a five-coordinate cob(II)alamin and an adenosyl radical; (b) the association of the substrate and adenosyl-ligand during the Co-C cleavage process in adenosylcobalamin dependent mutases has been proved by various experimental data including X-ray diffraction results [35-37], while such effect is totally absent in studies regarding methylcobalamin-dependent mutases.

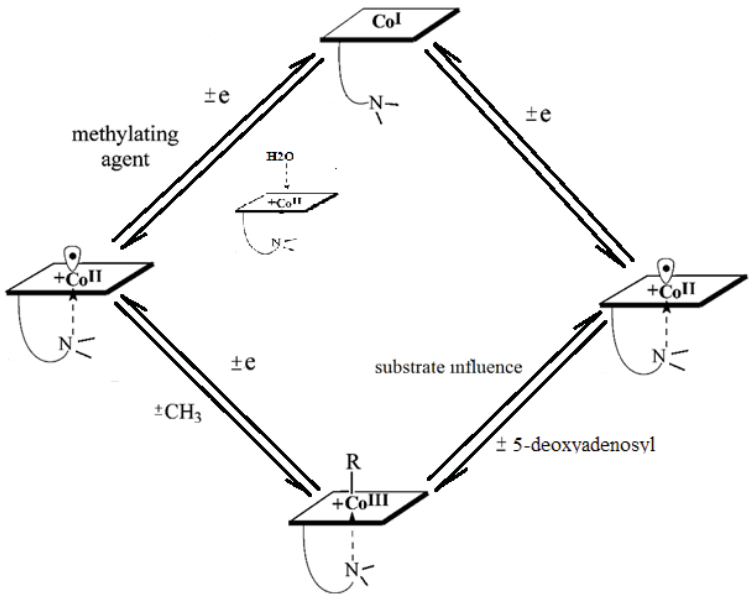

Figure 3. The generalized scheme of the methylcobalamin and adenosylcobalamin coenzyme turnovers [38-67].

The Co-C cleavage and electron transfer processes have been studied by different methods such as electrochemistry [38-40], thermo- [41] or photochemistry [42-46] of methylcobalamin Co(III) by a significant number of researchers. As a result, many triggering factors of Co-C bond breaking have been considered and various mechanistic mechanisms of the Co-C cleavage process have been proposed. Many researchers have considered axial ligand trans-influence, steric effects, structural strain, protein influence, in addition to others [47-58] as determinant factors in the Co-C cleavage process. The hydrogen transfer from the substrate to 5-deoxysdenosyl ligand has also been considered as a triggering factor of the Co-C bond breaking [59-67]. These suggestions have been largely unconfirmed by subsequent data. Only substrate influence on the Co-C cleavage process in the case of the adenosylcobalamin vitamin B_{12} species has been confirmed [35-37]. New approaches and new strategies are needed for the analysis of this challenging biological phenomenon.

The reductive activation mechanism of methylcobalamin has been studied by D. Lexa and J.M. Savèant using cyclic voltammetry of two similar compounds, methylcobalamine (base-on species) and methylcobalamide (base-off species) in DMF-1-propanol [38]. The methylcobalamide compound shows a single irreversible cathodic wave at low sweep rates corresponding to the reductive cleavage of the cobalt-carbon bond. At the slow scan rate of 0.3 V/s the cyclic voltammetry (CV) of methylcobalamin showed no return wave; however, as the scan rate increased to 10 V/s and above at −20 °C, a return wave appeared which allowed Lexa and Savéant [38] to propose the multistep electrochemical mechanism (Figure 4). Upon raising the sweep rate the cathodic wave becomes progressively reversible, clearly showing the existence of a one-electron intermediate before cleavage of the cobalt-carbon bond.

$$\text{R-Cbl} + e^- \rightleftharpoons [\text{R-Cbl}]^-_{\text{base-on}} \rightarrow \text{R}\cdot + \text{B12s}^-$$
$$\downarrow\uparrow$$
$$[\text{R-Cbl}]^-_{\text{base-off}} \rightarrow \text{R}\cdot + \text{B12s}^-$$

Figure 4. The scheme of the methylcobalamin reductive electrochemical mechanism [38,39]. Here, R is a methyl group.
We [39,40] and Martin & Finke [41] have determined similar methylcobalamine reductive mechanisms.

Unfortunately, the above mechanism is not fully supported by theory when considering DFT calculation data [39,40]. Additionally, the generally accepted methylcobalamin reductive mechanism (Figures 2 and 3), based on various experimental methods including X-ray diffraction, does not fit exactly with the electrochemistry based methylcobalamin reductive mechanism (Figure 4). It is obvious that experimental and theoretical data do not combine to provide a clear understanding of vitamin B_{12} activation in the human body. Deeper and more detailed studies using adequate and modern methods should be performed to ensure a sound basis of the mechanism of activation of vitamin B_{12}.

Density Functional Theory (DFT) and Quantum Mechanics/ Molecular Mechanics (QM/MM) calculations on vitamin B_{12} cofactors

We [39,40] and others have performed DFT calculations of vitamin B_{12} models [68-100]. Consequently, various properties have been studied, including electron densities and reduction potentials determination [69,76,88,91,96], the comparison of DFT and CASSCF electronic structure data of truncated models of methylcobalamin species [70,71,74,81,85], the influence of various factors on the Co-C bond forming and cleavage in methyl- and 5-adenosylcobalamin models [68,72-76,79,80,83,84,89,90,92,94,97,99,100], and excited states, spectroscopy and photo-dissociation analysis of vitamin B_{12} species [78,82,86,87,93,95,98]. We used DFT calculations on Me-Cbl models to calculate total energy as a function of Co-C bond distance as the bond is stretched [39]. The generally used base-on model of R-Cbl(III)(R=CH_3) includes the full corrin ring with all side-chain groups replaced by hydrogen atoms and with the dimethylbenzimidazole base ligand replaced by benzimidazole (or imidazole), as it is shown in Figure 5.

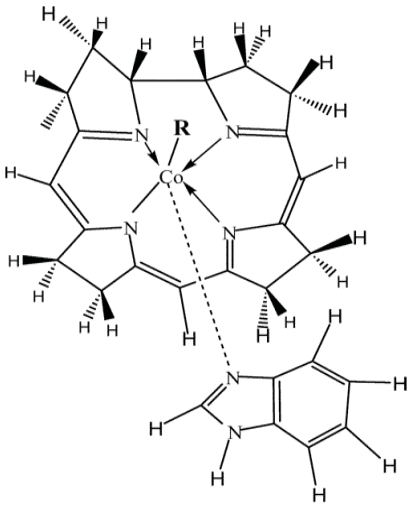

Figure 5. The methylcobalamin model used in DFT calculations [39, 106].

This approach was taken for construction of base-on and base-off models of positively charged CH3-Co(III)$^+$ and likewise for the neutral reduced CH3-Co(II) [41]. The optimized DFT geometry for all four species at B3LYP/LANL2DZ theory level showed nearly the same equilibrium C-Co bond distance of around 2.00Å. The dissociation total energy barrier heights from single-point calculations for both the base-on and base-off CH3-Co(III)$^+$ models were almost the same, ca. 2.8 eV (Figure 6); however, for the base-on CH3-Co(II) model, this dissociation energy was much lower, ca. 1.6 eV, and for the base-off species, even lower, ca. 1.1 eV.

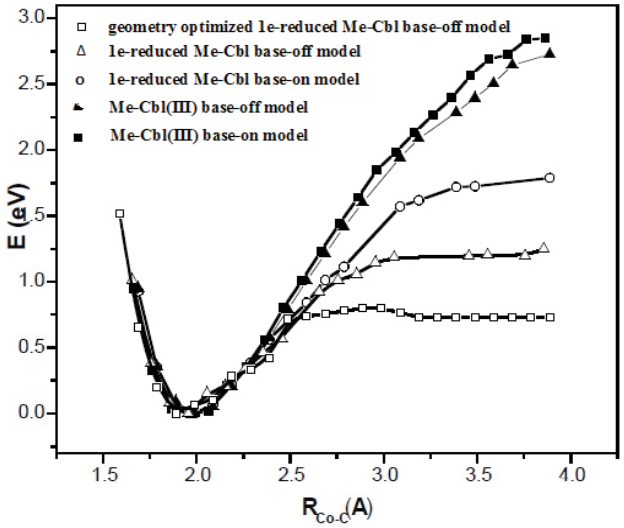

Figure 6. Total B3LYP/LANL2DZ energy (eV) as a function of Co-C bond distance (Å) for methylcobalamin model compounds for different redox species and axial base conditions.
The energy of all curves has been aligned at the minimum [39,106].

Despite the progress made by the research community on the theoretical explanation of vitamin B_{12} cofactor reaction, there are still significant disagreements of theoretical results with experimental data. Thus, our calculation of the total energy with geometry optimization at each constrained C-Co bond length for the base-off CH3-Co(II) model gives the lowest energy barrier for C-Co bond breaking (value of 0.7 eV, Figure 6) [39,106]. However, even with this barrier, a kinetic calculation shows that fast bond cleavage is improbable. Furthermore, the energy barrier of the Co-C bond breaking is much higher for base-on compared to the base-off species [39,68,106]. Our estimations show that the energy barrier of the geometry optimized 1e-reduced base-on specie is higher by about 0.5 eV compared to the energy barrier of the geometry optimized 1e-reduced base-off specie (see Figure 7 for single points calculations). Therefore, according to DFT calculations the rate constant of Co-C bond cleavage has a much lower value for base-on species compared to the rate constant of similar reactions for base-off species. This enters a flagrant contradiction with the experimental data, which demonstrates that the reaction rate constant of Co-C bond breaking is much higher in base-on species compared with the same reaction rate constant for base-off species [38]. Moreover, base-off methylcob(II)alamin compound cannot be considered in Co-C bond cleavage reaction of bio-reactions since is predicting a four coordinate vitamin B_{12} specie immediately after a Co-C bond cleavage of methylcobalamin compound [39,68,106]. Instead, several experimental results show that methylco(II)calamine cofactor is five coordinate [23-28,101,102] immediately after Co-C bond cleavage.

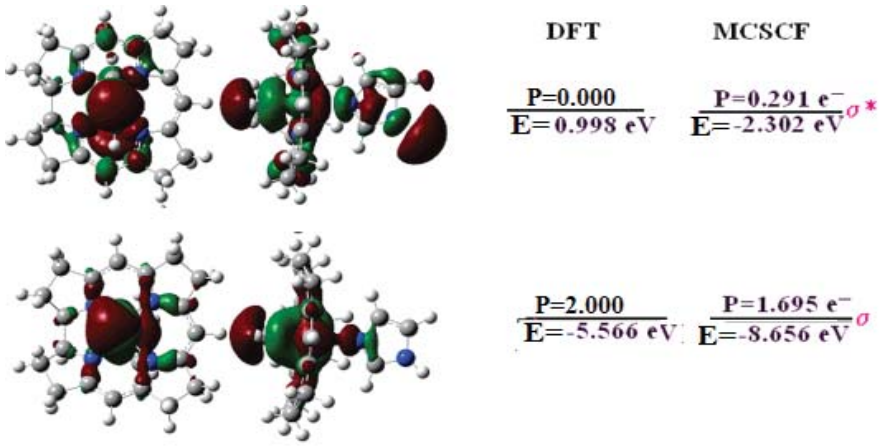

Figure 7. The methylco(II)balamin DFT-B3LYP/LANDL2DZ and MCSCF (9,7) (CASSCF) surfaces, energies and populations of σ and σ* MO [39,106].

Another unfortunate discrepancy is that theoretical results support the existence of a six-coordinate methylcobal(II)aminecofactor with dimethybenzimidazol ligand bonded to cobalt ion. Such a six-coordinate specie, which has not been mentioned by any experiment up to now, has a clear minimum (Figure 6) of total energy in the DFT method [39,106], testifying in favor of its stability. Finally, no theoretical model gave the expected Co-C bond cleavage energy barrier for the methylcob(II)alamin models. The closest to the desired results up to now have been obtained byusing QM/MM and DFT methods, which, unfortunately, still give greater than expected barriers for either, base-on or base-off species, equal to 8.3 kcal/mol, 10.5 kcal/mol, and 7.3 kcal/mol, respectively [72,73,80] (in *vivo* Co-C cleavage process is supposed to run without barrier). Finally, we conclude that there is an evident requirement to improve the models used in theoretical calculations and the use of more advanced theoretical treatments for the study of vitamin B_{12} activation.

The multi-configuration effects in methylcob(II)alamin and its Co-C bond cleavage

Although, the study of the *in-situ* electron transfer in reduced cobalamin compounds is quite a challenging problem, the real catalytic process and electronic transfer in cobalamin-dependent enzymes are even more complicated. For instance, the electron transfer problem includes also the role of mixed valence feredoxin compounds, which participate in electron transfer [103-105] to a series of biosystems and participate into turn-over of cobalamin-dependent enzyme processes. The mixed valence feredoxin compounds are a common example of vibronic (Jahn-Teller) systems in chemistry, due to their symmetry. On the other hand, our recent electron structure studies show that the HOMO-LUMO and Co-C σ-σ^* MO gaps are significantly smaller in the Co(II) methylcobalamin system compared with Co(III) methylcobalamin, proving that the orbital mixing is effective [106]. Therefore, the activation of Co-C bond cleavage in cobalamin bio-chemistry must be treated as an orbital mixing process and the Co(II) methylcobalamin system cannot be treated correctly by DFT methods [107], as it is a Pseudo-Jahn-Teller system [108]. Such orbital mixing leads to

a fractional population of the σ and σ* orbitals, including also several bonding occupied and antibonding unoccupied orbitals [106]. The σ* orbital, which is situated significantly above π* SOMO, is coupled strongly with formal σ. As a result, the energy of these two σ and σ* molecular orbitals change significantly during the geometry optimization (Figure 7). The population of the σ* antibonding orbital increase and the population of the σ bonding orbital decrease, thus "weakening" the force constants along the Co-C and Co-N bonds. This strong state mixing (similar to the pseudo-Jahn-Teller effect) leads to an increase in the Co-C bond and Co-N_{ax} bond lengths with about 0.2 Å for base-off Co(II) methylcobalamin model compounds and base-on Co(II) methylcobalamin model compounds (Figure 8). This coupling explains also the much lower Co-C bond dissociation enthalpy and much faster bond cleavage rate for the one-electron reduced methylcobalamin radical anion compared to the methylcobalamin neutral system. Such calculations like MCSCF with strong orbital coupling are extremely sensitive to any perturbation. We have obtained a similar result for Co-C bond cleavage in the case of the Co(III) adenosylcobalamin system under the perturbation (slight interaction influence) of the enzyme substrate. Therefore, it is reasonable to consider the influence of the substrate as a perturbation factor of the electronic structure influencing the Co-C and Co-N bond breaking for vitamin B_{12} cofactors species. We believe that this concept can be generalized for electron transfer or for substrate influence and subsequent bond cleavage in important biological systems.

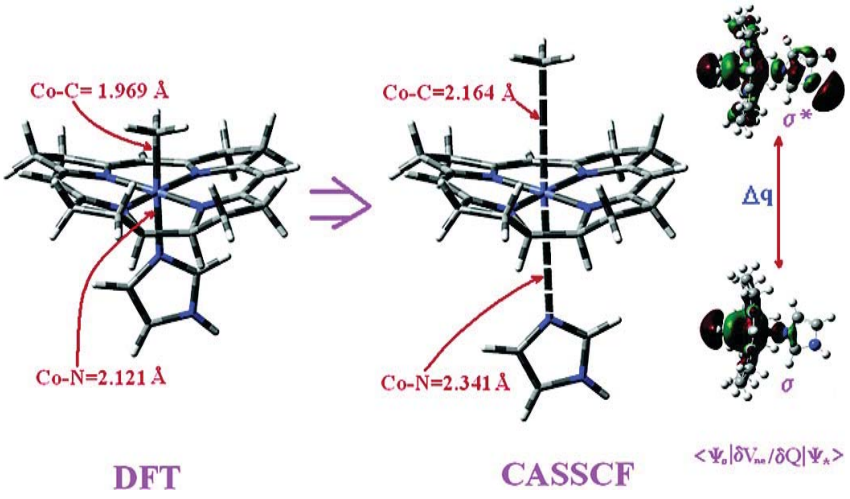

Figure 8. The cartoon of σ and σ* MO coupling influence on axial Co-C and Co-N bonds of one electron reduced methylcobalamin [39,106].

Generally speaking, the MCSCF method, which takes into account multi-configuration interactions, is among the most accurate methods of electronic structure calculations. Unfortunately, the number of electrons and orbitals taken into consideration in our previous calculation [106] are not in harmony with the needs for totally accurate calculation results of the MCSCF method with a complete active space that can be compared with experimental data and that can serve as the basis to develop a precise and reliable mechanism of activation for vitamin B_{12}. In the computing process it is necessary to take into account more orbitals (including a complete MCSCF active space) and a larger truer-to-size model of vitamin B_{12} should be used in the calculation according to the needs of today's knowledge of the mechanism of activation.

Conclusions

There are several possible mechanisms for the intramolecular electron transfer step, including distortion and coupling of orbitals of different symmetries, the possibility of a conical intersection, and a vibronic coupling mechanism-all of which are not mutually exclusive. The bond dissociation energy (BDE) for the cobalamin base-off species gives a value of 0.7 eV or ~16 kcal/mol based on a π* ground state potential energy dissociation curve calculated at the B3LYP/LANL2DZ level and optimized at each Co-C distance; however, this result is considered inaccurate because it is still too large to explain the experimental electrochemical kinetics.

The mechanism describing the bond-breaking of the base-off species in the solvent cage cannot explain the large difference in cleavage rates between reduced MeCbl and $MeCbi^+$, and DFT calculations therefore give inaccurate energy barriers in this situation. The alternative methodologies such as open-shell multi-configurational methods in theoretical calculations and perturbation factors along with the bond length estimations and mechanism fitting must be used for studying these processes.

Acknowledgements

This research was supported, in part, under National Science Foundation Grants CNS-0958379 and CNS-0855217 and the City University of New York High Performance Computing Center at the College of Staten Island and by the National Science Foundation through TeraGrid resources provided by the TeraGrid Science Gateways program under grants CHE090082 and CHE0000036.

References

1. Sigel, A.; Sigel, H.; Sigel, R.K.O. Eds. Interrelations between Essential Metal Ions and Human Diseases. Metal Ions in Life Sciences 13. Springer, 2013, pp.295–320.
2. Wald, I.; Członkowska, A.; Dowżenko A. Clinical Neurology, Warsaw: National Institute of Medical Publications, 1987, 451 p. (in Polish).
3. Morris, M.C.; Evans, D.A.; Schneider, J.A.; Tangney, C.C.; Bienias, J.L.; Aggarwal, N.T. Dietary folate and vitamins B-12 and B-6 not associated with incident Alzheimer's disease Journal of Alzheimer's Disease, 2006, 9, pp. 435–443.
4. Siuda, J.; Gorzkowska, A.; Patalong-Ogiewa, M.; Krzystanek, E.; Czech, E.; Wiechuła, B.; Garczorz, W.; Danch, A.; Jasińska-Myga, B.; Opala, G. From mild cognitive impairment to Alzheimer's disease - influence of homocysteine, vitamin B12 and folate on cognition over time: results from one-year follow-up. Polish Journal of Neurology and Neurosurgery, 2009, 43(4), pp. 321–329. (in Polish).
5. Kivipelto, M.; Annerbo, S.; Hultdin, J.; Bäckman, L.; Viitanen, M.; Fratiglioni, L.; Lökk, J. Homocysteine and holo-transcobalamin and the risk of dementia and Alzheimers disease: a prospective study. European Journal of Neurology, 2009, 16, pp. 808–813.
6. Kageyama, M.; Hiraoka, M.; Kagawa, Y. Relationship between genetic polymorphism, serum folate and homocysteine in Alzheimer's disease. Asia-Pacific Journal of Public Health. 2008, 20, Supplement, pp. 111–117.
7. Prodan, C.I.; Cowan, L.D.; Stoner, J.A.; Ross, E.D. Cumulative incidence of vitamin B12 deficiency in patients with Alzheimer disease. Journal of the Neurological Sciences, 2009, 284, pp. 144–148.
8. Li, Y.N.; Gulati, S.; Baker, P.J.; Brody, L.C.; Banerjee, R.; Kruger, W.D. Cloning, Mapping and RNA Analysis of the Human Methionine Synthase Gene. Human Molecular Genetics, 1996, 5, pp. 1851–1858.
9. Voet, J.G.; Voet, D. Biochemistry. J. Wiley & Sons: New York, 1995, 675 p.
10. Banerjee, R; Ragsdale, S.W. The Many Faces of Vitamin B12: Catalysis by Cobalamin-Dependent Enzymes1. Annual Review of Biochemistry, 2003, 72, pp. 209–247.
11. Scheffold, R.; Abrecht, S.; Ruf, H.-R.; Stamouli, P.; Tinembart, O.; Walder, L.; Weymuth, C. Vitamin B12-mediated electrochemical reactions in the synthesis of natural products Pure and Applied Chemistry, 1987, 59, pp. 363−372.
12. Ogoshi, H.; Kikuchi, Y.; Yamaguchi, T.; Toi, H.; Aoyama, Y. Asymmetric induction in the nucleophilic cyclopropane ring cleavage reaction with vitamin B12s. Organometallics, 1987, 6, pp. 2175−2178.
13. Pattenden, G. Simonsen Lecture. Cobalt-mediated radical reactions in organic synthesis. Chemical Society Reviews, 1988, 17, pp. 361−382.
14. Baldwin, D.A.; Betterton, E.A.; Chemaly, S.M.; Pratt, J.M.J. The chemistry of vitamin B12. Part 25. Mechanism of the β-elimination of olefins from alkylcorrinoids; evidence for an initial homolytic fission of the Co–C bond Journal of the Chemical Society, Dalton Transactions, 1985, pp. 1613−1618.
15. Baldwin, J.E.; Adlington, R.M.; Kang, T.W. Direct Ring Expansion of Penicillins to 3-Exomethylene Cephalosporins. Tetrahedron Letters, 1991, 48, pp. 7093−7096.
16. Paquette, L. Ed. Encyclopedia of Reagents for Organic Synthesis. Wiley: New York, 1995, pp 5511−5514.
17. Lee, E. R.; Lakomy, I.; Bigler, P.; Scheffold, R. Reductive Radical Cyclisations of Bromo Acetals and (Bromomethyl) silyl Ethers of Terpenoid Alcohols. Helvetica Chimica Acta, 1991, 74, pp. 146-162.
18. Shey, J.; McGinley, C.M.; McCauley, K.M.; Dearth, A.S.; Young, B.T.; van der Donk, W.A. Mechanistic Investigation of a Novel Vitamin B12-Catalyzed Carbon−Carbon Bond Forming Reaction, the Reductive Dimerization of Arylalkenes. Journal of Organic Chemistry, 2002, 67, pp. 837–846.
19. McGinley, C.M.; Relyea, H.A.; van der Donk, W.A. Vitamin B12 Catalyzed Radical Cyclizations of Arylalkenes. Synlett, 2006, pp. 211–214.
20. Banerjee, R. Ed. Chemistry and Biochemistry of B_{12}. John Wiley &Sons: New York, 1999, pp. 73-112.
21. Matthews, R.G. Cobalamin-Dependent Methyltransferases. Accounts of Chemical Research, 2001, 34, pp. 681-689.
22. Banerjee, R. Ed. Chemistry and Biochemistry of B_{12}. John Wiley &Sons: New York, 1999, pp. 681-706.
23. Drennan, C.L.; Huang, S.; Drummond, J.T.; Methews, R.G.; Ludwig, M.L. How a protein binds B12: A 3.0 A X-ray structure of B12-binding domains of methionine synthase. Science, 1994, 266, pp. 1669-1674.
24. Mancia, F.;Keep, N.M.; Nakagawa, A.; Leadlay, P.F.; McSweeney, S.; Rasmussen, B.; Bosecke, P.; Diat, O.; Evans, P.F. How coenzyme B12 radicals are generated: the crystal structure of methylmalonyl-coenzyme A mutase at 2 Å resolution. Structure, 1996,4, pp. 339-350.

25. Mera, P.E.; Escalante-Semerena, J.C. Multiple roles of ATP: cob(I)alamin adenosyltransferases in the conversion of B_{12} to coenzyme B_{12}. Applied Microbiology and Biotechnology, 2010, 88, pp. 41–48.
26. Matthews, R.G.; Koutmos, M.; Datta, S. Cobalamin-dependent and cobamide-dependent methyltransferases. Current Opinion in Structural Biology, 2008, 18, pp. 658–666.
27. Koutmos, M.; Datta, S.; Pattridge, K.A.; Smith, J.L.; Matthews, R.G. Insights into the reactivation of cobalamin-dependent methionine synthase. Proceedings of the National Academy of Sciences, USA, 2009, 106(44), pp. 18527–18532.
28. Hagemeier, C.H.; Kruer, M.; Thauer, R.K.; Warkentin, E.; Ermler, U. Insight into the mechanism of biological methanol activation based on the crystal structure of the methanol-cobalamin methyltransferase complex. Proceedings of the National Academy of Sciences, USA, 2006, 103(50), pp. 18917–18922.
29. Marsh, E.N.G. Review Article Coenzyme-B12-Dependent Glutamate Mutase. Bioorganic Chemistry, 2000, 28, pp. 176-189.
30. Kräutler, B.; Arigoni, D.; Golding, B.T. Eds. Vitamin B_{12} and the B_{12} proteins. Wiley-VCH: Weinheim, 1998, Chapter 12, pp. 491-504.
31. Babior, B.M.; Carty, T.J.; Abeles, R.H. The mechanism of action of ethanolamine ammonia-lyase, a B12-dependent enzyme. The reversible formation of 5'-deoxyadenosine from adenosylcobalamin during the catalytic process. The Journal of Biological Chemistry, 1974, 249, pp. 1689-1695.
32. Toraya, T. Radical catalysis of B-12 enzymes: structure, mechanism, inactivation, andreactivation of diol and glycerol dehydratases. Cellular and Molecular Life Science, 2000, 57, pp. 106-127.
33. Marsh, E.N.G.; Ballou D.P. Coupling of Cobalt−Carbon bond homolysis and hydrogen atom abstraction in adenosylcobalamin-dependent glutamate mutase. Biochemistry, 1998, 37, pp. 11864-11872.
34. Chowdhury, S.; Banerjee, R. Thermodynamic and kinetic characterization of Co−C bond homolysis catalyzed by coenzyme b12-dependent methylmalonyl-CoA mutase. Biochemistry, 2000, 39, pp. 7998-8006.
35. Gruber, K.; Reitzer, R.; Kratky, C. Radical shuttling in a protein: ribose pseudorotation controls alkyl-radical transfer in the coenzyme B12 dependent enzyme glutamate mutase. Angewandte Chemie International Edition, 2001, 40, pp. 3377-3380.
36. Reitzer, R.; Gruber, K.; Jogl, G.; Wagner, U.G.; Bothe, H.; Buckel, W.; Kratky, C. Glutamate mutase from Clostridium cochlearium: the structure of a coenzyme B12-dependent enzyme provides new mechanistic insights. Structure, 1999, 7, pp. 891-902.
37. Kräutler, B.; Arigoni, D.; Golding, B.T. Eds. Vitamin B_{12} and the B_{12} proteins. Wiley-VCH: Weinheim, 1998, Chapter 16, pp. 189-197.
38. Lexa, D.; Savéant, J.-M. Electrochemistry of vitamin B_{12}. 3. One-electron intermediates in the reduction of methylcobalamin and methylcobinamide. Journal of the American Chemical Society, 1978, 100, pp. 3220-3222.
39. Birke, R.L.; Qingdong, H.; Spataru, T.; Gosser, D. K. Jr. Electroreduction of a Series of Alkylcobalamins: Mechanism of Stepwise Reductive Cleavage of the Co−C Bond. Journal of the American Chemical Society, 2006, 128, pp. 1922-1936.
40. Spataru, T.; Birke, R.L. The effect of solvent on the electrode process of methylcobalamine as studied by cyclic voltammetry. Electroanalitical Chemistry, 2006, 593, pp. 74-86.
41. Martin, B.D.; Finke, R.G. Methylcobalamin's Full- vs. Half-Strength Cobalt-Carbon sigma Bonds and Bond Dissociation Enthalpies: A>10^15 Co-CH_3 Homolysis Rate Enhancement following One-Antibonding-Electron Reduction of Methlycobalamin. Journal of the American Chemical Society, 1992, 114, pp. 585-592.
42. Kunkely, H.; Vogler, A. Photolysis of methylcobalamin. Nature of the reactive excited state. Journal of Organometallic Chemisctry, 1993, 453, pp. 269-272.
43. Walker, L.A.; II; Jarrett, J.T.; Anderson, N.A.; Pullen, S.H.; Mattews, R.G.; Sension, R.J. Time-Resolved Spectroscopic Studies of B12 Coenzymes: The Identification of a Metastable Cob(III)alamin Photoproduct in the Photolysis of Methylcobalamin. Journal of the American Chemical Society, 1998, 120, pp. 3597-3603.
44. Luo, L.B.; Chen, H.L.; Fu, S.W.; Zhang, S.Y. Laser-induced photoacoustic calorimetric determination of enthalpy and volume changes in photolysis of 5′-deoxyadenosylcobalamin and methylcobalamin. Journal of the Chemical Society, Dalton Transactions, 1998, pp. 2103-2107.
45. Shiang, J.J.; Walker, L.A.; Anderson, N.A.; Cole, A.G.; Sension, R.J. The Time-Resolved Spectroscopic Studies of B12 Coenzymes: The Photolysis of Methylcobalamin Is Wavelength Dependent. Journal of Physical Chemistry B, 1999, 103, pp. 10532-10539.
46. Cole, A.G.; Yoder, L.M.; Shiang, J.J.; Andeson, N.A.; Walker, L.A.; Banaszak Holl, M.M.; Sension, R.J. Time-Resolved Spectroscopic Studies of B12 Coenzymes: A Comparison of the Primary Photolysis Mechanism in Methyl-, Ethyl-, n-Propyl-, and 5'-Deoxyadenosylcobalamin. Journal of the American Chemical Society, 2002, 124, pp. 434-438.
47. Hayward, G.C.; Hill, H.A.O.; Pratt, J.M.; Vanston, N.J.; Williams R.J.P. The chemistry of vitamin B12. Part IV. The thermodynamic trans-effect. The Journal of the Chemical Society, 1965, pp. 6485-6493.

48. Grate, J.H.; Schrauzer, G.N. Chemistry of cobalamins and related compounds. 48. Sterically induced, spontaneous dealkylation of secondary alkylcobalamins due to axial base coordination and conformational changes of the corrin ligand. Journal of the American Chemical Society, 1979, 101, pp. 4601-4611.
49. Halpern, J. Mechanisms of coenzyme B12-dependent rearrangements. Science, 1985, 227, pp. 869-875.
50. Marsh, E.N.G.; Drennan, C.L. Adenosylcobalamin-dependent isomerases: new insights into structure and mechanism. Current Opinion in Chemical Biology, 2001, 5, pp. 499-505.
51. Brown, K.L.; Zou, X.J. Thermolysis of coenzymes B12 at physiological temperatures: activation parameters for cobalt-carbon bond homolysis and a quantitative analysis of the perturbation of the homolysis equilibrium by the ribonucleoside triphosphate reductase from Lactobacillus leichmannii. Inorganic Biochemistry, 1999, 77, pp. 185-195.
52. Dong, S.L.; Padmakumar, R.; Banerjee, R.; Spiro, T.G. Co−C Bond Activation in B12-Dependent Enzymes: Cryogenic Resonance Raman Studies of Methylmalonyl-Coenzyme A Mutase. Journal of the American Chemical Society, 1999, 121, pp. 7063-7070.
53. Bresciana-Pahor, N.; Forcolin, M.; Marzilli, L.G.; Randaccio, L.; Summers, M.F.; Toscano, P.J. Organocobalt B_{12} models: axial ligand effects on the structural and coordination chemistry of cobaloximes. Coordination Chemistry Reviews, 1985, 63, pp. 1-125.
54. Mancia, F.; Evans, P.R. Conformational changes on substrate binding to methylmalonyl CoA mutase and new insights into the free radical mechanism. Structure, 1998, 6, pp. 711-720.
55. Vlasie, M.D.; Banerjee, R. Tyrosine 89 Accelerates Co−Carbon Bond Homolysis in Methylmalonyl-CoA Mutase. Journal of the American Chemical Society, 2003, 125, pp. 5431-5435.
56. Thomä, N.H.; Meier, T.W.; Evans, P.R.; Leadlay, P.F. Stabilization of Radical Intermediates by an Active-Site Tyrosine Residue in Methylmalonyl-CoA Mutase. Biochemistry, 1998, 37, pp. 14386-14393.
57. Toraya, T.; Ishida, A. Acceleration of cleavage of the carbon-cobalt bond of sterically hindered alkylcobalamins by binding to apoprotein of diol dehydrase. Biochemistry, 1988, 27, pp. 7677-7682.
58. Zhu, L.; Kostic, N.M. Molecular orbital study of coenzyme B12. Activation of the cobalt-carbon bond by angular distortions. Inorganic Chemistry, 1987, 26, pp. 4194-4197.
59. Padmakumar, R.; Padmakumar, R.; Banerjee, R. Evidence that Cobalt−Carbon Bond Homolysis is Coupled to Hydrogen Atom Abstraction from Substrate in Methylmalonyl-CoA Mutase. Biochemistry, 1997, 36, pp. 3713-3718.
60. Marsh, E.N.G.; Ballou D.P. Coupling of Cobalt−Carbon Bond Homolysis and Hydrogen Atom Abstraction in Adenosylcobalamin-Dependent Glutamate Mutase. Biochemistry, 1998, 37, pp. 11864-11872.
61. Babior, B.M.; Moss, T.H.; Orme-Johnson, W.H.; Beinert, H. The Mechanism of Action of Ethanolamine Ammonia-Lyase, a “B,, -dependent Enzyme. The Journal of Biological Chemistry, 1974, 249, pp. 4537-4544.
62. Licht, S.S.; Booker, S.; Stubbe, J. Studies on the Catalysis of Carbon−Cobalt Bond Homolysis by Ribonucleoside Triphosphate Reductase: Evidence for Concerted Carbon−Cobalt Bond Homolysis and Thiyl Radical Formation. Biochemistry, 1999, 38, pp. 1221-1233.
63. Meier, T.W.; Thomä, N.H.; Evans, P.R.; Leadlay, P.F. Tritium Isotope Effects in Adenosylcobalamin-Dependent Methylmalonyl-CoA Mutase. Biochemistry, 1996, 35, pp. 11791-11796.
64. Chih, H. –W.; Marsh, E.N.G. Pre-Steady-State Kinetic Investigation of Intermediates in the Reaction Catalyzed by Adenosylcobalamin-Dependent Glutamate Mutase. Biochemistry, 1999, 38, pp. 13684-13691.
65. Bandarian, V.; Reed, G.H. Isotope Effects in the Transient Phases of the Reaction Catalyzed by Ethanolamine Ammonia-Lyase: Determination of the Number of Exchangeable Hydrogens in the Enzyme−Cofactor Complex. Biochemistry, 2000, 39, pp. 12069-12075.
66. Kräutler, B.; Arigoni, D.; Golding, B.T. Eds. Vitamin B_{12} and the B_{12} proteins. Wiley-VCH: Weinheim, 1998, Chapter 25, pp. 383-402.
67. Barnerjee, R. The Yin-Yang of cobalamin biochemistry. Chemistry & Biology, 1997, 4, pp. 175-186.
68. Kozlowsky, P.M.; Kuta, J.; Galezowski, W. Reductive Cleavage Mechanism of Methylcobalamin: Elementary Steps of Co−C Bond Breaking. The Journal of Physical Chemistry, B, 2007, 111, pp. 7638-7645.
69. Chmielowska, A.; Lodowski, P.; Jaworska, M. Redox Potentials and Protonation of the A-Cluster from Acetyl-CoA Synthase. A Density Functional Theory Study. The Journal of Physical Chemistry A, 2013, 117, 47, pp. 12484-12496.
70. Kumar, N.; Kuta, J.; Galezowski, W.; Kozlowski, P.M. Electronic Structure of One-Electron-Oxidized Form of the Methylcobalamin Cofactor: Spin Density Distribution and Pseudo-Jahn–Teller Effect. Inorganic Chemistry, 2013, 52, 4, pp. 1762-1771.
71. Kumar, N.; Jaworska, M.; Lodowski, P.; Kumar, M.; Kozlowski, P.M. Electronic Structure of Cofactor−Substrate Reactant Complex Involved in the Methyl Transfer Reaction Catalyzed by Cobalamin-Dependent Methionine Synthase. The Journal of Physical Chemistry B, 2011, 115, pp. 6722-6731.
72. Alfonso-Prieto, M.; Biarnés, X.; Kumar, M.; Rovira, C.; Kozlowski, P.M. Reductive Cleavage Mechanism of

Co−C Bond in Cobalamin-Dependent Methionine Synthase. The Journal of Physical Chemistry B, 2010, 114, pp. 12965-12971.
73. Jensen, K.P.; Ryde, U. Conversion of Homocysteine to Methionine by Methionine Synthase: A Density Functional Study. Journal of the American Chemical Society, 2003, 125(46), pp. 13970-13971.
74. Kozlowski, P.M.; Kamachi, T.; Kumar, M.; Nakayama, T.; Yoshizawa, K. Theoretical Analysis of the Diradical Nature of Adenosylcobalamin Cofactor−Tyrosine Complex in B12-Dependent Mutases: Inspiring PCET-Driven Enzymatic Catalysis. The Journal of Physical Chemistry B, 2010, 114, pp. 5928-5939.
75. Kumar, M.; Kozlowski, P.M. Role of Tyrosine Residue in the Activation of Co−C Bond in Coenzyme B12-Dependent Enzymes: Another Case of Proton-Coupled Electron Transfer? The Journal of Physical Chemistry B, 2009, 113, pp. 9050-9054.
76. Mebs, S.; Henn, J.; Dittrich, B.; Paulmann, C.; Luger, P. Electron Densities of Three B12 Vitamins. The Journal of Physical Chemistry A, 2009, 113, pp. 8366-8378.
77. Chen, S.L.; Blomberg, M.R.; Siegbahn, P.E. How Is a Co-Methyl Intermediate Formed in the Reaction of Cobalamin-Dependent Methionine Synthase? Theoretical Evidence for a Two-Step Methyl Cation Transfer Mechanism. The Journal of Physical Chemistry B, 2011, 115, pp. 4066-4077.
78. Liptak, M.D.; Fleischhacker, A.S.; Matthews, R.G.; Telser, J.; Brunold, T.C. Spectroscopic and Computational Characterization of the Base-off Forms of Cob(II)alamin. The Journal of Physical Chemistry B, 2009, 113, pp. 5245-5254.
79. Kumar, N.; Kozlowski, P.M. Mechanistic Insights for Formation of an Organometallic Co–C Bond in the Methyl Transfer Reaction Catalyzed by Methionine Synthase. The Journal of Physical Chemistry B, 2013, 117, pp. 16044-16057.
80. Kozlowski, P.M.; Kamachi, T.; Kumar, M.; Yoshizawa, K. Reductive elimination pathway for homocysteine to methionine conversion in cobalamin-dependent methionine synthase. Journal of Biological Inorganic Chemistry, 2012, 17, pp. 611-619.
81. Kumar, N.; Alfonso-Prieto, M.; Rovira, C.; Lodowski, P.; Jaworska, M.; Kozlowski, P.M. Role of the Axial Base in the Modulation of the Cob(I)alamin Electronic Properties: Insight from QM/MM, DFT, and CASSCF Calculations. Journal of the Chemical Theory and Computation, 2011, 7, pp. 1541-1551.
82. Reig, A.J.; Conrad, K.S.; Brunold, T.C. Combined Spectroscopic/Computational Studies of Vitamin B12 Precursors: Geometric and Electronic Structures of Cobinamides. Inorganic Chemistry, 2012, 51, pp. 2867-2879.
83. Kobylianskii, I.J.; Widner, F.J.; Kräutler, B.; Chen, P. Co–C Bond Energies in Adenosylcobinamide and Methylcobinamide in the Gas Phase and in Silico. Journal of the American Chemical Society, 2013, 135, pp. 13648-13651.
84. Kepp, K.P. Co–C Dissociation of Adenosylcobalamin (Coenzyme B12): Role of Dispersion, Induction Effects, Solvent Polarity, and Relativistic and Thermal Corrections. The Journal of Physical Chemistry A, 2014, 118, pp. 7104-7117.
85. Kozlowski, P.M.; Kumar, M.; Piecuch, P.; Wei Li, Bauman, N.P.; Hansen, J.A.; Lodowski, P.; Jaworska, M. The cobalt–methyl bond dissociation in methylcobalamin: new benchmark analysis based on density functional theory and completely renormalized coupled-cluster calculations. Journal of the Chemical Theory and Computation, 2012, 8, pp. 1870-1894.
86. Kornobis, K.; Kumar, N.; Wong, B. M.; Lodowski, P.; Jaworska, M.; Andruniow, T.; Ruud, K.; Kozlowski, P. M. Electronically Excited States of Vitamin B12: Benchmark Calculations Including Time-Dependent Density Functional Theory and Correlated ab Initio Methods. The Journal of Physical Chemistry A, 2011, 115, pp. 1280-1292.
87. Lodowski, P.; Jaworska, M.; Kornobis, K.; Andruniow, T.; Kozlowski, P.M. Electronic and Structural Properties of Low-lying Excited States of Vitamin B12. The Journal of Physical Chemistry B, 2011, 115, pp. 13304-13319.
88. Kumar, N.; Liu, S.B.; Kozlowski, P.M. Charge Separation Propensity of the Coenzyme B12–Tyrosine Complex in Adenosylcobalamin-Dependent Methylmalonyl–CoA Mutase Enzyme. The Journal of Physical Chemistry Letters, 2012, 3, pp. 1035-1038.
89. Govender, P.P.; Navizet, I.; Perry, C.B.; Marques, H.M. DFT Studies of Trans and Cis Influences in the Homolysis of the Co–C Bond in Models of the Alkylcobalamins. The Journal of Physical Chemistry A, 2013, 117, pp. 3057-3068.
90. Kozlowski, P.M.; Kamachi, T.; Kumar, M.; Yoshizawa, K. Initial step of B12-dependent enzymatic catalysis: energetic implications regarding involvement of the one-electron-reduced form of adenosylcobalamin cofactor. Journal of Biological Inorganic Chemistry, 2012, 17, pp. 293-300.
91. Kumar, M.; Hirao, H.; Kozlowski, P.M. Co+–H interaction inspired alternate coordination geometries of biologically important cob (I) alamin: possible structural and mechanistic consequences for methyltransferases. Journal of Biological Inorganic Chemistry, 2012, 17, pp. 1107-1121.
92. Jensen, K.P.; Ryde, U. How the Co−C Bond Is Cleaved in Coenzyme B12 Enzymes: A Theoretical Study. Journal of the American Chemical Society, 2005, 127, pp. 9117-9128.

93. Brunold, T.C.; Conrad, K.S.; Liptak, M.D.; Park, K. Spectroscopically validated density functional theory studies of the B12 cofactors and their interactions with enzyme active sites. Coordination Chemistry Reviews, 2009, 253, pp. 779-794.
94. Li, X.; Chung, L.W.; Paneth, P.; Morokuma, K. DFT and ONIOM(DFT:MM) Studies on Co−C Bond Cleavage and Hydrogen Transfer in B12-Dependent Methylmalonyl-CoA Mutase. Stepwise or Concerted Mechanism? Journal of the American Chemical Society, 2009, 131, pp. 5115-5125.
95. Solheim, H.; Kornobis, K.; Ruud, K.; Kozlowski, P.M. Electronically Excited States of Vitamin B12 and Methylcobalamin: Theoretical Analysis of Absorption, CD, and MCD Data. The Journal of Physical Chemistry B, 2011, 115, pp. 737-748.
96. Kumar, M.; Galezowski, W.; Kozlowski, P.M. Computational modeling of standard reduction potentials of B12 cofactors. International Journal of Quantum Chemistry, 2013, 113, pp. 479-488.
97. Hirao, H. Which DFT Functional Performs Well in the Calculation of Methylcobalamin? Comparison of the B3LYP and BP86 Functionals and Evaluation of the Impact of Empirical Dispersion Correction. The Journal of Physical Chemistry B, 2011, 115, pp. 9308-9313.
98. Park, K.; Brunold, T.C. Combined Spectroscopic and Computational Analysis of the Vibrational Properties of Vitamin B12 in its Co3+, Co2+, and Co1+ Oxidation States. The Journal of Physical Chemistry B, 2013, 117, pp. 5397-5410.
99. Kwiecien, R.A.; Khavrutskii, I.V.; Musaev, D.G.; Morokuma, K.; Banerjee, R.; Paneth, P. Computational Insights into the Mechanism of Radical Generation in B12-Dependent Methylmalonyl-CoA Mutase. Journal of the American Chemical Society, 2006, 128(4), pp. 1287–1292.
100. Banerjee, R.; Dybala-Defratyka, A.; Paneth, P. Quantum catalysis in B12-dependent methylmalonyl-CoA mutase: experimental and computational insights. Philosophical Transactions of the Royal Society of London B, Biological Sciences, 2006, 361(1472), pp. 1333–1339.
101. Kraeutler, B.; Keller, W.; Kratky, C. Coenzyme B12 chemistry: the crystal and molecular structure of cob(II) alamin. Journal of the American Chemical Society, 1989, 111, pp. 8936–8938.
102. Liptak, M.D.; Datta, S.; Matthews, R.G; Brunold, T.C. Spectroscopic Study of the Cobalamin-Dependent Methionine Synthase in the Activation Conformation: Effects of the Y1139 Residue and S-Adenosylmethionine on the B12 Cofactor. Journal of the American Chemical Society, 2008, 130, pp. 16374-16381.
103. Berkovitch, F.; Nicolet, Y.; Wan, J.T.; Jarrett, J.T.; Drennan, C.L. Crystal structure of biotin synthase, an S-adenosylmethionine-dependent radical enzyme. Science, (Washington, DC, United States), 2004, 303, 5654, pp. 76-80.
104. Broach, R.B.; Jarrett, J.T. Role of the [2Fe-2S]2+ Cluster in Biotin Synthase: Mutagenesis of the Atypical Metal Ligand Arginine 260. Biochemistry, 2006, 45, pp. 14166-14174.
105. Jarrett, J.T. The novel structure and chemistry of iron–sulfur clusters in the adenosylmethionine-dependent radical enzyme biotin synthase. Archives of Biochemistry and Biophysics, 2005, 433, pp. 312-321.
106. Spataru, T.; Birke, R.L. Carbon−Cobalt Bond Distance and Bond Cleavage in One-Electron Reduced Methylcobalamin: A Failure of the Conventional DFT Method. The Journal of Physical Chemistry A, 2006, 110, pp. 8599-8604.
107. Bersuker, I.B. Limitations of density functional theory in application to degenerate states. Journal of Computational Chemistry, 1997, 2, pp. 260-267.
108. Bearpark, M.J.; Blancafort, L.; Robb, M.A. Molecular Physics: The pseudo-Jahn–Teller effect: a CASSCF diagnostic. An International Journal at the Interface Between Chemistry and Physics, 2002, 100, pp. 1735-1739.

ECOLOGICAL POTENTIAL OF SURFACE WATERS IN NATURAL SCIENTIFIC RESERVE "LOWER PRUT"

Maria Sandu[a*], Anatol Tarita[a], Raisa Lozan[a], Natalia Zgircu[b], Elena Mosanu[a], Tatiana Goreacioc[a], Alexandru Zlotea[a], Anna Comarnitchi[b], Iulia Sidoren[a], Sergiu Turcan[a], Adrian Tarita[a]

[a]*Institute of Ecology and Geography of Academy of Sciences of Moldova, 1 Academiei str., Chisinau MD-2028, Republic of Moldova*
[b]*State Hydrometeorological Service, 134 Grenoble str., Chisinau MD-2072, Republic of Moldova*
[*]*e-mail: sandu_mr@yahoo.com; phone: (+373 22) 72 55 42*

Abstract. According to the Regulation on monitoring and systematic evidence of the surface and groundwater status, the Beleu Lake is included in the network of surface waters state monitoring in the Republic of Moldova. The research results have marked a low value of the self-purification capacity for Beleu Lake water, between 0.12 and 0.19, which is of 1.2-2 times lower than those from Prut River (0.25), correlating positively with the values of BOD_5, COD-Cr and the time of biochemical oxidation of ammonium ions. The oxidation of ammonium into nitrite (NH_4^+(NH_3) → NO_2^-) in the nitrification process in lake water (collected in November 2014) takes place about 25 days and the process NO_2^- → NO_3^- being more than 35 days. The period of nitrification is about 2 times higher than in lake water collected in 2015 and 2.8-3.0 times higher than those of the model with water from Prut River.

Keywords: Lake Beleu, self-purification capacity, nitrification process, BOD_5, COD-Cr.

Received: October 2015/ Revised final: November 2015/ Accepted: December 2015

Introduction

The Republic of Moldova has three Wetlands of International Importance with total area of 94705 ha and became a member of the Ramsar Convention in June 2000, when the "Lower Prut Lakes" (19152.5 ha) was included in the List of Wetlands of international importance.

Scientific reservation "Lower Prut" is located at the South of republic between Prut River and village Slobozia Mare, South of Cahul city. It covers 1691 ha, including 312 ha of forest and Beleu Lake (10 km^2). In that zone there were registered 39 species of mammals, 5 being included in the Red Book of Moldova (RBM), 203 bird species (27 included RBM), 5 species of reptiles (2 included RBM), 9 amphibians (one included RBM) and 41 species of fish (6 included RBM) [1].

Beleu Lake and Manta water body (Rotunda, Dracele and Badelnic Lakes) represent some unique ecosystems. Both water bodies can be considered natural, or at least close to natural as floods characteristic [2].

Medium area of Beleu Lake is of 9.5 km^2, being one of the largest natural lakes in the Republic of Moldova with water volume of 8.39 million m^3. The length of the lake is of 5 km, width - 2 km, the depth average – 0.5-1.5 m and maximum - of 2.5 m. About 1/3 of the scientific reservation surface constitutes waters of Beleu Lake. Water reaches in the Beleu Lake by two arms that come together in one. The water level in the lake overflows and floods depends on spring and summer of the Danube and Prut Rivers.

A problem in the reservation is that oil extraction is done from the wells that are close to the strictly protected area of the reservation, about 200 m from aquatic bird nesting. Oil is extracted on a platform with an area of 40 m^2 completely surrounded by water [3].

Article 26 of the Law on State Protected Natural Areas, no. 1538 of 25.02.1998 [4] provides that in the scientific reserve prohibited activities that could lead to disruption of the natural evolution of natural processes, in particular: b) exploration and extraction of natural resources, except those of national importance (oil, natural gas), provided the special environmental protection set by the central authority with natural resource management and environmental protection.

Since oil extraction in Moldova takes place from wells, located near the protected area of the reserve "Lower Prut" [4], it is necessary to study the state of its environmental compounds according to Decision of Republic of Moldova Government No. 932 of 20.11.2013 [5] and EU Water Framework Directive (WFD, 2000/60/EC [6]).

So, Beleu Lake, in conformity with the Republic of Moldova Regulation on monitoring and systematic record of the status of surface and groundwater monitoring network is included in no. 52: Beleu natural Lake, Slobozia Mare, Cahul, 45° 35' 12.88" North, 28° 09' 09.65" East, Alt. 5. Monitoring and systematic evidence of surface waters state in the Republic of Moldova lies by the State Hydrometeorological Service in Activity Program which provides 4 times on year the evaluating the physical and chemical parameters of water quality in Beleu Lake [5].

Status of surface water quality in Beleu and Manta Lakes is present in reports of State Hydrometeorological Service, being analyzed the content of macro compounds, dissolved O_2, BOD, COD, petroleum products, anionic surfactants, nitrogen and phosphorus compounds, some heavy metals, etc. In accordance with these reports, during of 2009-2013 years the water quality of Beleu Lake can be attributed to class II of quality (clean) in 2009 and class III (moderately polluted)

in 2012-2013 [2]. However the analyses do not include the investigation of lakes water self-purification and nitrification process of ammonium ions, as similar previously studies for surface and small rivers water [7-9].

This study includes the common estimating with State Hydrometeorological Service of the chemical status of lake water based on measured concentrations of monitored parameters, for the first time determining the capacity of water self-purification and nitrification.

Experimental part

Water sampling was done according to the Guidelines for taking water from natural and artificial lakes [10]. The analyses were performed in three replicates to yield average values. The concentrations of anions and cations were determined using national standards [11]. The amounts of nitrogen compounds, phosphorus, sulphate ions, iron, were determined photometrically. Titrimetrically there were estimated alkalinity, chloride content, the amount of calcium and magnesium. The pH of the water was determined by potentiometric method [12]. The value of BOD_5 and COD-Cr provide information about oxygen content required for oxidation the content of organic matter from water [13,14]. Using gas chromatography it was determined the content of oil in lake water [15].

In order to establish the environmental status, the classification of water quality in the lake was done according to Governmental Decision no. 890 of 12.11.2013, Annex 1 [16]. Self-purification capacity was calculated by the ratio BOD_5: COD-Cr [15, 17]. The study of ammonium ions biochemical transformation in natural water of Beleu Lake was performed using laboratory modelling [18]. Water solutions obtained after adding ammonium ions were exposed to light (which excluded direct sunlight). Daily there were determined the concentration of NH_4^+, NO_2^-, NO_3^- ions and value of pH, the modelling tests being done at 20-22°C.

The correlation between nitrification time and indices that characterize the level of organic pollution (CCO-Cr, BOD_5, days-nitrification) from natural surface waters was performed using double correlative analysis method that enables recording and evaluation of concentration dependence of 2 chemical components of water. Lower $K_{0.05}$ of calculated values was considered statistically unsignificant [19].

In this study there was evaluated the physical-chemical composition of water collected from various points of Beleu Lake on 14.11.2014, 28.05.2015 and 20.08.2015.

Results and discussion

The results of physicochemical analyses performed during of 2009-2013 years show that the water quality of Beleu Lake, village Slobozia Mare, according to Water Pollution Index (WPI) is attributed to class II of quality (WPI = 0.78 - pure) in 2009 and class III (WPI = 1.21 - moderately polluted) in 2012. During of 2013 year the mineralization (about 500 mg/dm^3 of dissolved solids, attributed to class I of quality) did not exceed maximum allowable concentration (MAC) values. The content of dissolved oxygen has been ranged from 9.44 to 10.17 mg/dm^3 (class I of quality). Nitrite concentration was between 0.022 and 0.11 mg/dm^3 (1.7 MAC, class I-II of quality), oil products content was between 0.23 mg/dm^3 in 2013 and 0.24 mg/dm^3 in 2012 (4.6-4.8 MAC, class II-III of quality) [2, 20].

In water samples from the lake, assessed in this study (2014-2015 years), the concentration of chlorine ions was ranged between 26-36 mg/dm^3, ammonium ions in the range of 0 - 0.14 mg/dm^3, nitrates from 0 to 0.77 mg/dm^3, anionic surface active substances - 0.01 mg/dm^3, BOD_5 value from 2.29 to 2.62 mg/dm^{3}O and mineralization in the range of 195-490 mg/dm^3 that correspond to I class of surface water quality (Table 1).

Table 1

Physical-chemical composition and quality class of Beleu Lake water.

No.	*Parameter*		*2012*	*14.11.2014*		*27.05.2015*			*Quality class*
				Brooks					
			Village Slobozia Mare	*Rotaru -Manolescu*	*Popovca -Rotaru*	*Popovca -Rotaru*	*Rotaru -Manolescu*	*Mano-lescu*	
1	pH		8.33-8.68	8.47	8.48	8.8	8.18	8.3	II
2	Hardness, me/dm^3		3.2-8.9	4.6	4.8	2.9	4.1	3.7	I-II
3	BOD_5, mg/dm^3 O		2.34-3.63	2.52	2.62	2.4	2.29	2.45	I
4	COD-Cr, mg/dm^3 O		-	20.2	17.0	12.7	13.3	15.3	II-V
5	Suspensions		50-303	50	105	57	63	267	V->V
6	SO_4^{2-}		71.8-132	146	153	32.8	85.2	89.8	I-II
7	Cl^-		31.9-111	35.4	35.4	36.1	26.9	26.2	I
8	Mineralization		377-842	460	475	195	309	326	I
9	NH_4^+	mg/dm^3	0.07-0.83	0.14	0.06	0	0	0	I-III
10	NO_2^-		0-0.061	0.007	0.007	0.005	0.018	0.009	I-II
11	NO_3^-		0-4	0.65	0.77	0	0.77	0.72	I
12	P_{tot}		0.104-0.26	0.098	0.108	0.048	0.094	0.096	I-II
13	Petroleum products		0.05-0.24	0.09	0.07	0.09	0.1	0.3	I-III
14	Surface active substances		0-0.02	0.01	<0.01	0.01	0.01	0.01	I

According to pH values (8.18 to 8.8), hardness (2.9 to 4.8 me/dm^3), content of sulphates (32.8 to 153 mg/dm^3), concentration of nitrite (0.005 to 0.018 mg/dm^3) and of total phosphorus (0.048 to 0.108 mg/dm^3) in all sections, the lake water is attributed to class I-II of quality. The research results are indicated that the content of particles in suspension is varied from 50 mg/dm^3 (brook Rotaru-Manolescu) to 267 mg/dm^3 (brook Manolescu) which differ significantly between the majority of lake brooks and the Beleu Lake (brook Manolescu), where class of quality is V->V. According to the petroleum products concentration, the lake water in the brook Manolescu is attributed to class III, while in the other sampling points it is attributed to class of quality I-II.

The content of ammonium ions in lake water (section village Slobozia Mare) varied significantly in 2012 (from 0.07 to 0.83 mg/dm^3) with seasonal character, lower values being reported during April-September when nitrification process occurs intensively. In May of 2015 the concentration of nitrates and ammonium ions did not exceed MAC. According to concentrations of pollutants, the Beleu Lake water is attributed to class III-V of quality.

Analyzing chemical parameters of Beleu and Rotunda Lakes water (village Manta, May of 2015) it was found that the concentration of organic substances (COD-Cr) ranged from 10.6 (Rotunda Lake) to 28.4 mg/dm^{3}O, BOD_5 has been maximum – 3.17 mg/dm^{3}O (Beleu Lake). Water collected in different seasons, according to values of BOD_5 and COD-Cr, falling within class I-II of quality except Beleu Lake sample taken in spring, around oil drilling activity (class I-III of quality). Self-purification capacity of water, which is depending on the season, is also different in studied waters. Self-purification capacity of Prut River water is medium (0.26), being 1.2 to 4 times more than for Beleu Lake, which is worth between 0.04 (practically absence) and 0.24 (Table 2 and Figure 1).

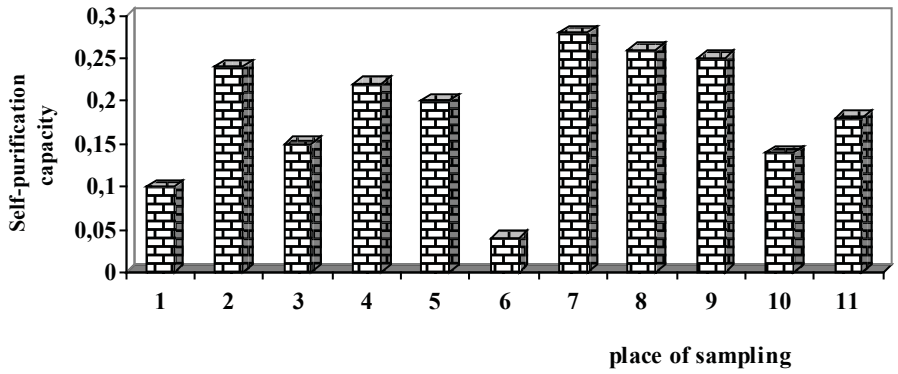

Figure 1. Self-purification capacity of water from Beleu and Rotunda Lakes compared to the Prut River (winter, spring, summer, 2015).
***Beleu Lake*: brooks Rotaru and Manolescu, near oil extraction taken in winter (1), spring (2), summer (3); brooks Popovca and Rotaru taken in winter (4), spring (5); brook Manolescu taken in spring (6), summer (7); village Slobozia Mare (8); Rounda Lake, village Manta (9).**
***Prut River*: village Valeni taken in spring (10), summer (11).**

Table 2

The concentration of organic matter and water quality class according to chemical and biochemical oxygen demand, 2015.

Water samples		*Season*	*COD-Cr*	*BOD_5*	*Quality class*
			mg/dm^3 O		
Beleu Lake	brooks Rotaru and Manolescu, near oil extraction	winter	17.26	1.77	I-II
		spring	28.4	1.31	I-III
		summer	22.0	3.01	I-II
	brooks Popovca and Rotaru	winter	12.2	3.02	I-II
		spring	16.08	2.44	I-II
	brook Manolescu	spring	13.8	3.02	I-II
		summer	14.9	2.66	I-II
	village Slobozia Mare	spring	15.7	3.17	I-II
Rotunda Lake	village Manta	spring	10.6	3.01	I-II
Prut River	village Valeni	spring	12.06	3.08	I-II
		summer	8.65	2.15	I

Nitrification of NH_4^+ ions in Beleu Lake water

Ions of nitrite (NO_2^-) and ammonium (NH_4^+) are present in the case of pollution of aquatic medium and are toxic to living organisms. For this reason in the laboratory conditions was modelled the biochemical oxidation of NH_4^+ ions in Beleu Lake water during the cold and warm period of years (2014 and 2015).

Inorganic compounds with nitrogen (NH_4^+, NH_3, NO_2^-, NO_3^-) are present actually in all natural waters. Their amount varies depending on the degree of pollution [7]. Ammonia and ammonium ions in natural waters are oxidized biochemically by 2 steps:

$$NH_4^+ (NH_3) + 3O_2 \rightarrow 2NO_2^- + 4H^+ + 2H_2O + 54.9 \text{ kcal } (\textit{Nitrosomonas}) \quad (1)$$

$$NO_2^- + O_2 \rightarrow 2\,NO_3^- + 18 \text{ kcal } (\textit{Nitrobacter}) \quad (2)$$

A lot of chemicals present in the water hinder biochemical processes in the environment. Previously, it was studied the influence of phenol, copper ions and of some pesticides and surfactants on the oxidation of ammonium ions in surface waters [8, 9].

The oxidation of ammonium into nitrite ($NH_4^+(NH_3) \rightarrow NO_2^-$) in Beleu Lake water (collected in November of 2014) takes place in 25 days (Figure 2a) and in 2015 – in 9-15 days (Figure 3a). The transformation of nitrite into nitrate (process $NO_2^- \rightarrow NO_3^-$) takes place more than 35 days (Figure 2b), being by 2 times higher than the period in lake water sampled in 2015 and by 2.8-3.0 times higher than those for model with water from the Prut River (Figure 3b).

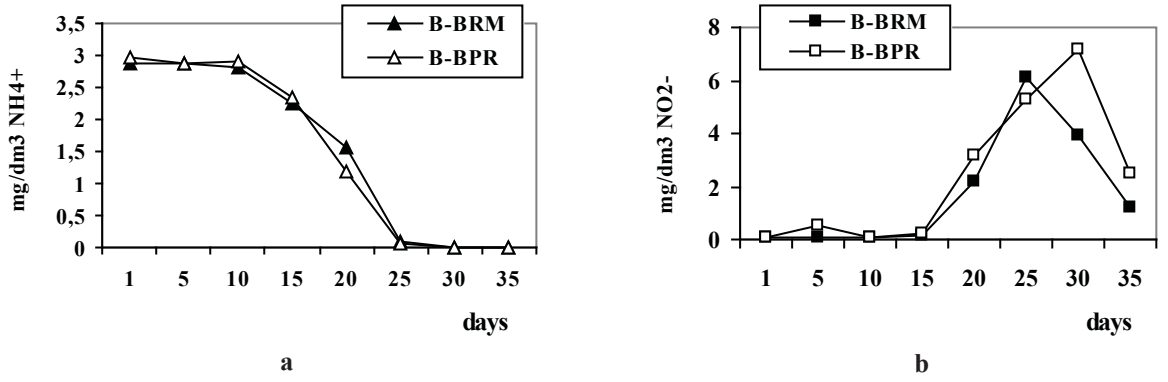

Figure 2. Dynamics of NH_4^+ ions concentration in the oxidation $NH_4^+ \rightarrow NO_2^-$ process (a) and of NO_2^- ions content in the oxidation step $NO_2^- \rightarrow NO_3^-$(b) in water samples taken from the Beleu Lake in autumn of 2014. B-BPR: brooks Popovca – Rotaru; B-BRM: brooks Rotaru – Manolescu.

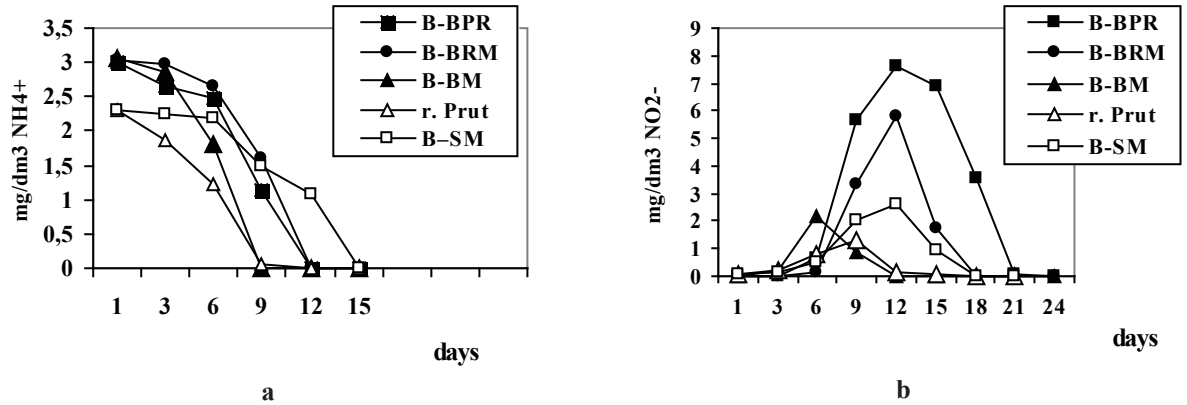

Figure 3. Dynamics of NH_4^+ ions concentration in the oxidation $NH_4^+ \rightarrow NO_2^-$ process (a) and of NO_2^- ions content in the oxidation step $NO_2^- \rightarrow NO_3^-$(b) in water samples taken from the Beleu Lake and Prut River (village Valeni) in summer of 2015.
***Beleu Lake*: B-BPR: brooks Popovca - Rotaru; B-BRM: brooks Rotaru - Manolescu; B-BM: brook Manolescu; B-SM: village Slobozia Mare.**

It is known that many chemicals affect the biochemical processes in natural waters [8,9,18]. Taking into account that oil extraction is done from the wells that are close to the protected area which include Beleu Lake, in laboratory conditions there was carried out the influence of petroleum products (PP) on nitrification of ammonium ions in water of Beleu Lake and Prut River (for comparison), samples collected in 20.08.2015. The amount of PP added was of 2.5 mg/dm^3, the permissible content discharged into natural water bodies [21].

The results of study show that in the water samples taken from Prut River and Beleu Lake, brook Manolescu (water entering from Prut into the lake) the oxidation of ammonium into nitrite ($NH_4^+ \rightarrow NO_2^-$) takes place 8 days. With 2 days longer it take place the process in the water out of the lake (brook Rotaru), including in the presence of the normative content of petroleum products (Figure 4a). Step II of nitrification ($NO_2^- \rightarrow NO_3^-$) in the samples from Prut River and Beleu Lake, brook Manolescu, including in the presence of PP, takes place 13 days. More obvious it is the influence of water composition (not PP) of Beleu Lake, brook Rotaru - out of the lake, on the process $NO_2^- \rightarrow NO_3^-$, which in 13 days only about 10% of NO_2^- have oxidized (Figure 4b). So, in the water out of Beleu Lake there are substances which determine a low self-purification capacity and diminish the nitrification process in water (Table 3).

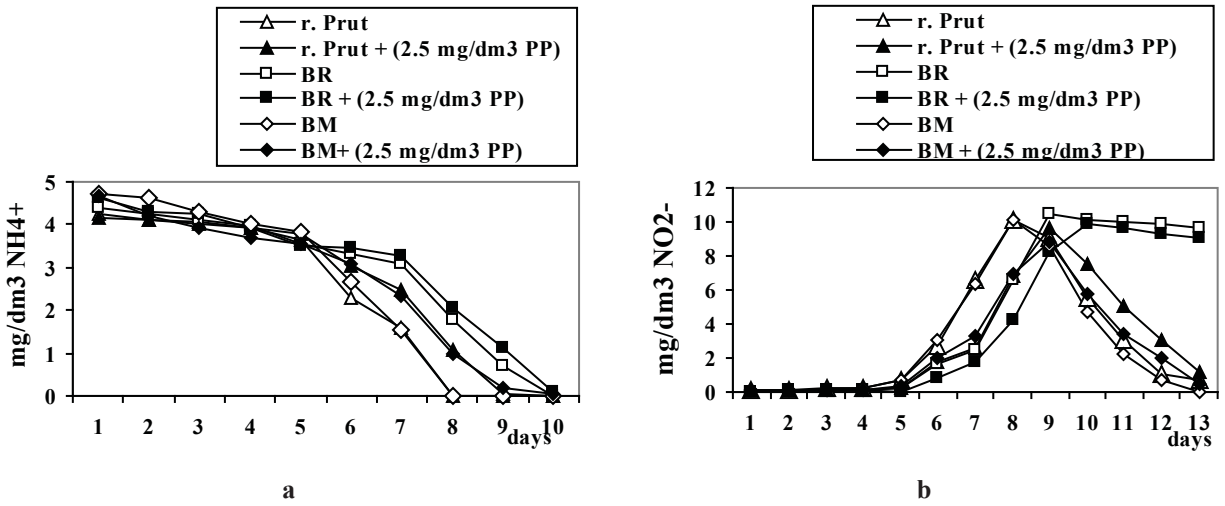

a **b**

Figure 4. Dynamics of NH_4^+ ions concentration in $NH_4^+ \rightarrow NO_2^-$ step (a) and NO_2^- ions content in $NO_2^- \rightarrow NO_3^-$ step (b) in ammonium ions oxidation process in water samples taken from Prut River (village Valeni) and Beleu Lake in August of 2015.
***Beleu Lake*: BM - brook Manolescu; BR - brook Rotaru, out of the lake.**

Self-purification capacity has positive correlation trends for following values: BOD_5 ($y = 0.085x + 2.2833$, $r^2 = 0.2653$), COD-Cr ($y = 0.85x + 15.8$, $r^2 = 0.1167$) and period of NH_4^+ ion nitrification: $NH_4^+ \rightarrow NO_2^-$ step ($y = 1.5x + 8$, $r^2 = 0.75$) and $NO_2^- \rightarrow NO_3^-$ ($y = 4.5x + 8$, $r^2 = 0.9643$) (Figure 5).

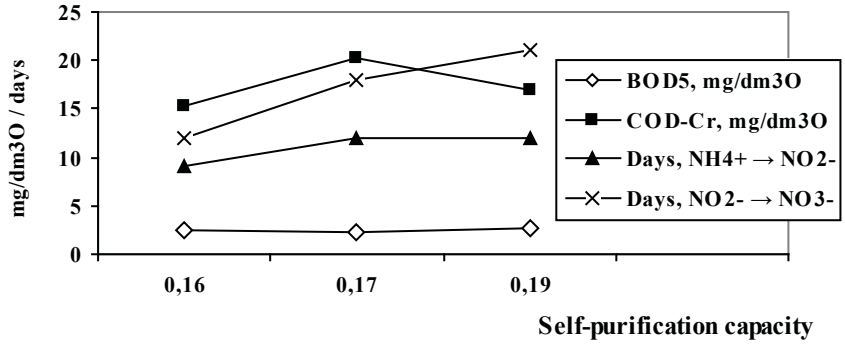

Figure 5. Correlation of self-purification capacity values to BOD_5 ($r^2 = 0.2653$), COD-Cr ($r^2 = 0.1167$) and period of NH_4^+ ion nitrification: $NH_4^+ \rightarrow NO_2^-$ stage ($r^2 = 0.75$) and $NO_2^- \rightarrow NO_3^-$ ($r^2 = 0.9643$).

So, it is outlines the influence of persistent organic pollutants and those degrading biochemical on the self-purification and nitrification of ammonium ions process in the water of Beleu Lake.

Based on information regarding the water quality of Beleu Lake, it is concluded that is necessary to create conditions to increase the self-purification capacity, given the multitude of biotic and abiotic factors, which determine the effectiveness of polluted natural waters improvements.

Conclusions

Values of self-purification capacity of the lake water are between 0.12 and 0.19 for Beleu Lake, which are by 1.2-2 times lower than the one for Prut River (0.25).

The values of BOD_5, COD-Cr and the time for biochemical oxidation of ammonium ions are positively correlated with self-purification capacity of water from Beleu Lake, confirming the existence of organic matter pollution.

Study shows that in water from Prut River and Beleu Lake, brook Manolescu (water entering from Prut River into the lake) the nitrification of ammonium ions, inclusive in the presence of petroleum products, took place 13 days, while in water sampled out of lake (brook Rotaru), in the absence and presence of PP, about 90% of NO_2^- were still unoxidized.

References

1. Eremia, A. Hydronyms of Prut basin. Left tributaries of the river. Academos, 2014, 4(35), pp. 147-152. (in Romanian).
2. Status of surface water quality according hydro indices in the Republic of Moldova. http://www.meteo.md/monitor/anuare/2013/anuarapei_2013.pdf. (in Romanian).
3. Republic of Moldova State of the environment report 2004 (National Report). National Institute of Ecology: Chisinau, 2005, pp. 33-34.
4. Law No. 1538 on State Protected Natural Areas of 25.02.1998. Official Monitor of Republic of Moldova, no. 66-68, art. no. 442. Last update: LP200 din 12.07.2013, MO191-197/06.09.13 art.617. (in Romanian).
5. Decision of Republic of Moldova Government No. 932 of 20.11.2013, Annex. 1: Monitoring and systematic record of the status of surface water. Physical-chemical parameters, procedures and technical measures necessary for their monitoring. (in Romanian).
6. EC Directive, Directive 2000/60/EC of the European Parliament and of the Council of 23 October 2000, establishing a framework for Community action in the field of water policy. Official Journal of the European Communities, L 327, 22.12.2000, Brussels.
7. Water resources of Moldova. www.apelemoldovei.gov.md/public/files/anexe_ro_draft.docx (in Romanian).
8. Mosanu, E.; Spataru, P.; Lupascu, T.; Sandu, M.; Goreacioc, T.; Tarita, A. The evolution of biochemical oxidation of ammonia ions in small rivers water. Chemistry Journal of Moldova, 2010, 5(1), pp. 78-83.
9. Sandu, M.; Lozan, R.; Ropot, V.; Munteanu, V.; Rusu V. The role of phenol in self-purification processes of surface waters. Symposium "Environmental protection - restructuring of the Romanian economy", Bucharest, 1995, p. 68. (in Romanian).
10. SM SR ISO 5667-4:2007. Water quality. Sampling. Part 4: Guidance on sampling from natural and artificial lakes (in Romanian).
11. Catalogue of Republic of Moldova's national standards. National Institute of Standardisation: Chisinau, 2014, vol. 1, 920 p. (in Romanian).
12. SM SR ISO 10523:2011. Water quality. Determination of pH (in Romanian).
13. SM SR EN ISO 1899-2:2007. Water quality. Determination of biochemical oxygen demand after n days (BOD_n). (in Romanian).
14. SM SR ISO 6060: 2006. Water quality. Determination of chemical oxygen demand (in Romanian).
15. Leite, V. Determination of organic contaminants in drinking, natural and waste waters. Himija: Moscow, 1975, 200 p. (in Russian).
16. Decision of Republic of Moldova Government No. 890 of 12.11.2013 for approving the Regulation on environmental quality requirements for surface water. Official Monitor no. 262-267 in 22.11.2013, art. no. 1006. (in Romanian).
17. Matveeva, N.P.; Klimenko, O.A.; Pyatnitsyna, R.S. Laboratory simulation of natural waters self-purification processes, contaminated with organic substances. Hydrochemical materials. Hydrometeoizdat: Leningrad, 1989, vol. 106, pp. 114-124. (in Russian).
18. Aizatulin, T.A.; Leonov, A.A. The kinetics of nitrogen compounds transformation in natural water. Formation of chemical composition of surface water and the methods of analysis. Hydrochemical materials, Hydrometeoizdat: Leningrad, 1975, vol. 64, pp. 177-183. (in Russian).
19. Tyutyunova, F.I. Geochemistry technogenesis. Nauka: Moscow, 1987, 325 p. (in Russian).
20. Sandu, M. Toxicity of pesticides in the presence of heavy metals on biochemical oxidation of ammonia ions. 8th International HCH and Pesticides Forum for Central European and EECCA, Sofia, 2005, pp. 179-181.
21. Decision of Republic of Moldova Government No. 950 of 25.11.2013 for approving the Regulation on requirements gathering, treatment and discharge of wastewater into the sewage system and/or in water bodies for urban and rural areas. Official Monitor no. 284-289 of 06.12.2013, art. no. 1061. (in Romanian).

EFFECT OF ALUMINIUM SULPHATE *AGING* ON COAGULATION PROCESS FOR THE PRUT RIVER WATER TREATMENT

Larisa Postolachi*, Vasile Rusu, Tudor Lupascu

Institute of Chemistry of Academy of Sciences of Moldova, 3 Academiei str., Chisinau MD-2028, Republic of Moldova
**e-mail: larisa.postolachi@gmail.com; phone: (373 22) 73 97 31; fax: (373 22) 73 99 54*

Abstract. Aluminium sulphate is one of the most widely used coagulants for water treatment and has been proven to be an effective coagulant for the removal of certain contaminants, turbidity and colour. Aluminium sulphate used during the coagulation process is hydrolyzed in the water, forming polynuclear complexes. *Aged* aluminium solutions show different coagulation behaviour than that of freshly prepared solutions. The aim of presented research was to highlight the influence of the *aging* of aluminium sulphate solution on the turbidity removal from water. Obtained results reveal that using of optimal *aging* solution of coagulant improves the coagulation process.

Keywords: coagulation, *Jar-test*, aluminium sulphate, *aging*.

Received: January 2016/ Revised final: February 2016/ Accepted: March 2016

Introduction

The quality of river or reservoir water is commonly characterized by the content of suspended solids, colloidal particles, natural organic matter and other soluble, mostly inorganic compounds, present in different concentrations. Therefore, when the river or reservoir water is intended for human consumption, an appropriate treatment process is usually considered as necessary to meet the respective drinking water standards. One of the most important steps during the conventional treatment process is coagulation/flocculation [1].

Coagulation is a common process in water treatment for destabilizing dissolved and colloid impurities and for transforming small particles into larger aggregates (flocs) which can be removed from the water in subsequent clarification/filtration processes [2-4].

The coagulation process consists of three sequential steps: coagulant formation, colloid/particle destabilisation, and particle aggregation. Coagulant formation and colloid/particle destabilisation are promoted in a rapid-mixing stage where treatment chemicals are added and dispersed throughout the water to be treated. Particle aggregation (floc formation) is then promoted in a flocculation stage where inter-particles collisions create large floc particles amenable to separation from the treated water [3].

Aluminium sulphate is one of the most widely used coagulants for water treatment and has been proven to be an effective coagulant for the removal of certain contaminants, turbidity and colour [5-7]. When dosed into water the aluminium ions hydrolyse rapidly and in an uncontrolled manner, to form a range of metal hydrolysis species [3].

Hydrolysis products may be monomeric or polymeric hydroxyl complexes [8]. Most of them, such as $Al(OH)^{2+}$, $Al(OH)_2^{+}$, $Al_2(OH)_2^{4+}$, $Al_3(OH)_2^{5+}$ and $Al_{13}O_4(OH)_{24}^{7+}$ (or "Al_{13}"), are positively charged and can interact strongly with the negative colloids, resulting in destabilization and coagulation [1].

The aluminium species distribution in coagulant solutions can be influenced by many parameters [5]. A range of factors such as the nature of the water, the coagulation pH and the dose of coagulant together influence the range of species formed and subsequently, the treatment performance [3]. The pH value of the medium is of the primary importance in the establishing the mean charge of the hydrolysis products and, consequently, is of significance for the rate of coagulation (Scheme 1). The pH of aluminium solutions decreases during *aging* and in the speciality literature there are shown that *aged* aluminium solutions give entirely different coagulation values than *unaged* aluminium solutions [9].

$$\underset{<4}{Al^{3+}} \rightarrow \underset{4.5}{Al(OH)^{2+}} \rightarrow \underset{5.5}{Al(OH)_2^{+}} \rightarrow \underset{6.5}{Al(OH)_3} \rightarrow \underset{>8}{Al(OH)_4^{-}}$$

$$\underbrace{\qquad\qquad\qquad\qquad\qquad\qquad\qquad\qquad}_{pH}$$

Scheme 1. Hydrolysis products of aluminium in relation to pH value [1].

The main water supply sources of the Republic of Moldova are the Dniester River, which covers about 54% of the total water quantity, the Prut River – 16%, other sources of surface water – 7% and groundwater sources – 23% [10]. The water quality from water supply sources often does not correspond to the drinking water criteria, because of the high turbidity, the high content bacteria or dangerous dissolved substances. Therefore, before to be consumed the natural water would be processed.

The main stages, at the Water Treatment Plant, Municipal Company "Apa-Canal", the town Ungheni (Republic of Moldova), applied in the potabilization technologies include also the coagulation of particulate materials from the Prut River water. In previous study [11], in order to optimize the process of coagulation there were studied the several factors, namely the influence of mixing speed and of concentration of coagulant added in the process of coagulation. The aim of presented research was to highlight the influence of the *aging* of aluminium sulphate solution on the turbidity removal from water.

Experimental

Laboratory coagulation tests were performed on two different types of raw water:

1. Model solution. In order to simulate the presence of suspended solids (turbidity) in tap water there were dispersed the bottom sediments. The initial turbidity of model solution using during coagulation tests was ranged in the limits 32 and 39 NTU (nephelometric turbidity units).

2. River (raw) water samples were taken from the Prut River at the Water Treatment Plant, Municipal Company "Apa-Canal", the town Ungheni (Republic of Moldova). The coagulation process was studied on raw water with turbidity between 33 and 63 NTU.

In Table 1 there are presented the characteristics of initial samples used during coagulation process.

Table 1

Characteristics of the water samples, used for coagulation experiments.

Water type	*pH*	*Temperature, °C*	*Turbidity, NTU*
Model solution	7.87 ÷ 8.05	15.6 ÷ 18.5	32 ÷ 39
Prut River	7.82 ÷ 7.93	20.5 ÷ 24.7	33 ÷ 63

Coagulant

The aluminium sulphate ($Al_2(SO_4)_3 \cdot 18H_2O$, purchased from Sigma-Aldrich) was used as coagulant, the working solutions being of 10 and 25%. The coagulant doses used were as following: 3.7, 4.9 and 9.8 mg/L.

Aging process

All coagulant solutions were *aged* at room temperature and kept in the dark before coagulation experiments. During the entire *aging* period, samples were clear to the naked eye.

Jar-test procedures

Coagulation experiments were carried out using a *Jar-test* apparatus [12, 13]. The scheme of *Jar-tester* used for coagulation experiments is presented in Figure 1. The sample (800 mL of water) was dosed with the appropriate amount of coagulant. The suspensions were stirred rapidly at 500 rpm for 2 minutes during coagulant addition, followed by slow stirring at 120 rpm for 20 min. After mixing the samples have been left for settling of flocs. At the end of the settling period (20, 40 and 60 minutes), the supernatant is withdrawn for analyses.

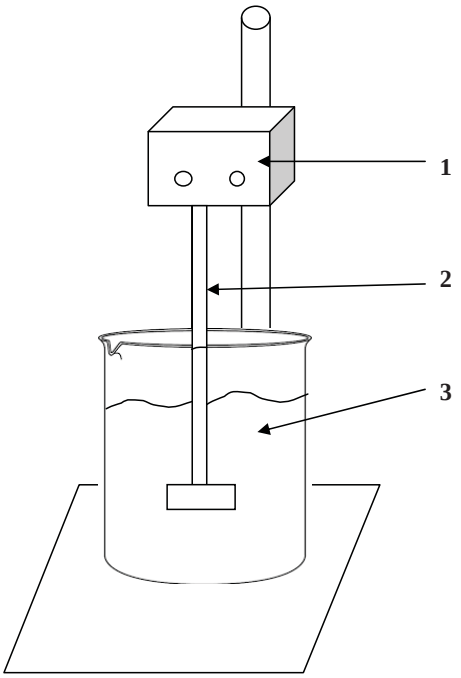

Figure 1. Scheme of *Jar-tester*, used for coagulation experiments.
1 – battery and control box, 2 – stirrer, 3 – jar.

Turbidity measurement

The turbidity of water samples has been determined according to World Health Organisation recommendations [14], using the UV/Vis spectrophotometer, Jenway model 6505.

The turbidity removal (R_T, %), which expresses the efficiency of the process, was calculated by Eq.(1) [15]:

$$R_T = \frac{T_i - T_r}{T_i} \cdot 100\% , \quad (1)$$

where: T_i – initial turbidity, NTU;

T_r – residual turbidity, NTU (the turbidity of supernatant after coagulation and settlement).

Results and discussion

The influence of coagulant aging time on coagulation process performed on model solution

The *aged* aluminium solutions show different coagulation behaviour than that of freshly prepared solutions [9]. The influence of *aging* time of the coagulant (coagulant concentrations of 10% and 25%) on the degree of turbidity removal (R_T, %) was carried out at different settling time (Figures 2 and 3). The *Jar-tests* were performed using different doses of coagulant, namely 3.7, 4.9 and 9.8 mg/L. The coagulation process was studied on model solution with turbidity between 32 and 39 NTU. The coagulant solutions were *aged* for 1-10 days (coagulant concentration of 10%) and 1-6 days (coagulant concentration of 25%).

The use of *aged* coagulant exhibits a better coagulation performance in comparison with *unaged* coagulant. It was established that for the coagulant solution of 10% the coagulation process in model solution pass off more efficiently in case of *aged* coagulant for 4-5 days, registering higher values of the degree of turbidity removal (Figure 2).

For coagulant solution of 25% the coagulation process in model solution pass off more efficiently at the addition of *aged* coagulant for period of 3-4 days (Figure 3), since the processes of *aging* are faster in the solutions with higher concentrations of hydroxyl ions [9].

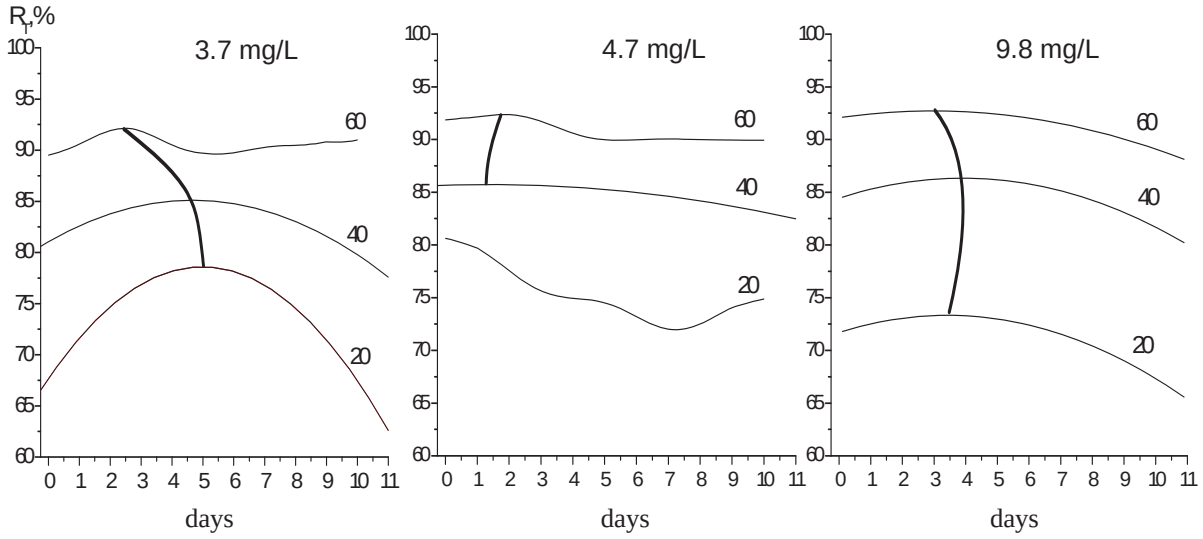

Figure 2. The influence of *aging* time of the coagulant solution (10%) on the degree of turbidity removal (R_T, %) of model solution. Coagulant doses: 3.7, 4.9 and 9.8 mg/L. Settling time: 20, 40 and 60 minutes.

The influence of coagulant aging time on coagulation process performed on natural water

During the coagulation process, there are two types of colloids: (i) those present in the water to be treated, and (ii) those formed by added coagulants [9].

The influence of coagulant *aging* time (coagulant concentrations of 10% and 25%) on turbidity removal was shown in Figures 4 and 5. The *Jar-tests* were performed on natural water (Prut River) with turbidity ranged in limits 33-63 UNT. The coagulant solutions were *aged* for 1-7 days (coagulant concentration of 10%) and 1-3 days (coagulant concentration of 25%).

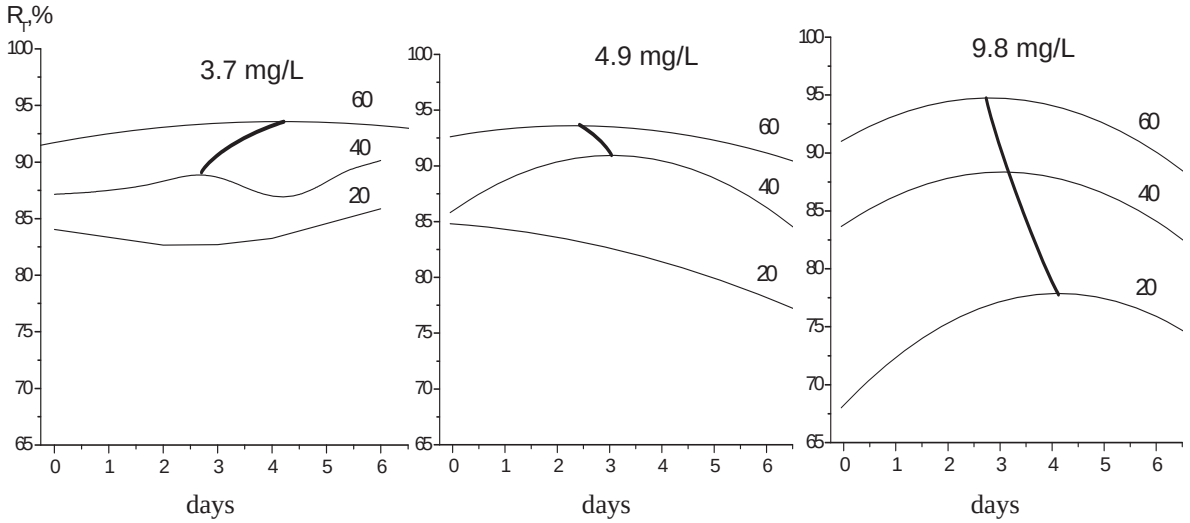

**Figure 3. The influence of *aging* time of the coagulant solution (25%) on the degree of turbidity removal (R_T, %) of model solution.
Coagulant doses: 3.7, 4.9 and 9.8 mg/L.
Settling time: 20, 40 and 60 minutes.**

The coagulation efficiency, for aluminium sulphate solution (10%), increased along with the increasing *aging* time, especially when the *aging* time exceeded 4 days. Thus, during *Jar-testing*, it was established that for coagulant concentration of 10% the coagulation process pass off more efficiently using the *aged* coagulant for 4-5 days, being recorded the values of turbidity removal in the range 90-98% (Figure 4).

The *aging* reactions are more rapid in solutions having higher hydroxide aluminium concentration, or at elevated temperatures [9]. On the basis of the results for coagulant concentration of 25%, it can be seen that the *aged* coagulant for 2 days is more effective for turbidity removal, registering the values of turbidity removal in the range 95-99% (Figure 5).

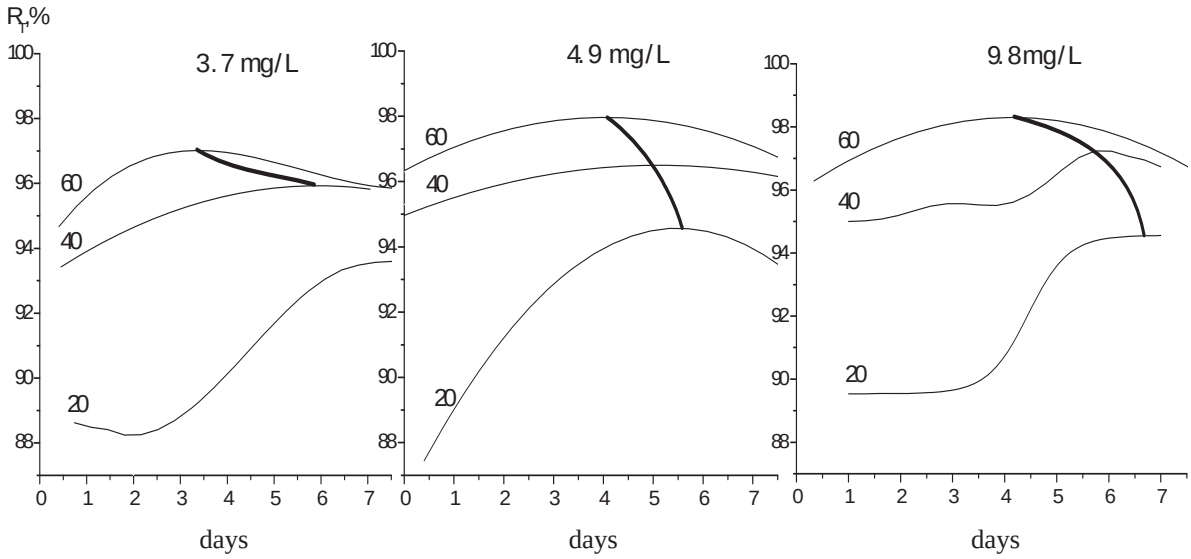

**Figure 4. The influence of *aging* time of the coagulant solution (10%) on the degree of turbidity removal (R_T, %) of the Prut River water.
Coagulant doses: 3.7, 4.9 and 9.8 mg/L.
Settling time: 20, 40 and 60 minutes.**

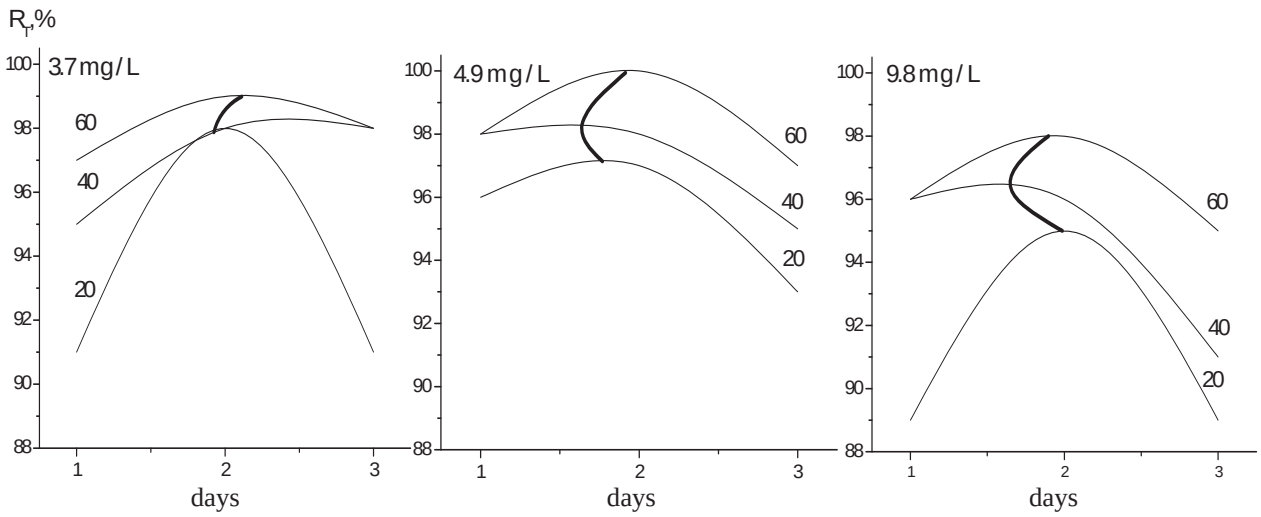

Figure 5. The influence of *aging* time of the coagulant solution (25%) on the degree of turbidity removal (R_T, %) of the Prut River water. Coagulant doses: 3.7, 4.9 and 9.8 mg/L. Settling time: 20, 40 and 60 minutes.

The variation of residual turbidity in the Prut River water during coagulation in function of settling time is presented in Table 1. The lowest value of residual turbidity in raw water is recorded after 60 minutes of settling, being in limits 0.4 – 1.7 UNT in case of aluminium sulphate solution of 10% and 0.3 – 1.6 UNT in case of aluminium sulphate solution of 25%. The recorded values of residual turbidity are less than 5 NTU, which framing in limits of the existing criteria for drinking water [16].

Table 2

Dynamics of residual turbidity (T_r) in the Prut River water during coagulation in function of settling time. Coagulant dose: 4.9 mg/L.

Aging time	*Initial turbidity, NTU*	*T_r after 20 minutes of settling, NTU*	*T_r after 40 minutes of settling, NTU*	*T_r after 60 minutes of settling, NTU*
Aluminium sulphate solution of 10%				
1 day *aged*	63	6.8	3.2	1.7
2 days *aged*	51	4.1	2.0	0.8
3 days *aged*	54	5.1	2.0	1.6
4 days *aged*	44	2.0	1.2	0.4
5 days *aged*	33	1.6	1.2	1.0
7 days *aged*	50	3.1	2.1	1.3
Aluminium sulphate solution of 25%				
1 day *aged*	63	2.5	1.3	1.3
2 days *aged*	51	1.6	0.8	0
3 days *aged*	54	4.0	2.4	1.6

Conclusions

The results presented in this study suggest that the using of optimal *aging* solution of coagulant improves the coagulation process. The coagulation process, performed on the Prut River, pass off more efficiently using the *aged* coagulant for 4-5 days in case of aluminium sulphate of 10% and the *aged* coagulant for 2 days in case of aluminium sulphate of 25%. The lowest value of residual turbidity in raw water is recorded after 60 minutes of settling. The recorded values of residual turbidity are less than 5 NTU, which framing in limits of the existing criteria for drinking water.

Acknowledgments

Thanks to deputy-director Ms. Natalia Bors for permission to perform this study at the Municipal Water Treatment Company “Apa-Canal” of the town Ungheni.

References

1. Zouboulis, A.; Traskas, G. Comparable evaluation of various commercially available aluminium-based coagulants for the treatment of surface water and for the post-treatment of urban wastewater. Journal of Chemical Technology and Biotechnology, 2005, 80, pp.1136–1147.
2. Gao, B.; Hahn, H.; Hoffmann, E. Evaluation of aluminum-silicate polymer composite as a coagulant for water treatment. Water Research, 2002, 36, pp. 3573–3581.
3. Jiang, J.-Q.; Graham, N. Pre-polymerised inorganic coagulants and phosphorus removal by coagulation - A review. Water SA, 1998, 24(3), pp. 237–244.
4. Zeng, Y.; Park, J. Characterization and coagulation performance of a novel inorganic polymer coagulant–Poly-zinc-silicate-sulfate. Colloids and Surfaces A: Physicochemical and Engineering Aspects, 2009, 334, pp. 147–154.
5. Zhang, P.; Hahn, H.; Hoffmann, E.; Zeng, G. Influence of some additives to aluminium species distribution in aluminium coagulants. Chemosphere, 2004, 57, pp. 1489–1494.
6. Shen, Y.-H.; Dempsey, B. Synthesis and speciation of polyaluminum chloride for water treatment. Environment International, 1998, 24(8), pp. 899–910.
7. Dolejs, P. Treatment of low alkalinity humic waters with partially neutralized aluminium sulphate. Environmental Technology Letters, 1989, 10, pp. 41–48.
8. Wu. Z.; Zhang, P.; Zeng, G.; Zhang, M.; Jiang, J. Humic acid removal from water with polyaluminum coagulants: effect of sulfate on aluminum polymerization. Journal of Environmental Engineering, 2012, 138(3), pp. 293–298.
9. Stumm, W.; Morgan, J. Chemical aspects of coagulation. Journal of the American Water Works Association, 1962, 54, pp. 971–992.
10. Children's health and environment in the Republic of Moldova, Chisinau, 2010. http://www.mediu.gov.md/images/documente/starea_mediului/rapoarte/nationale/p5_raport_parma_en.pdf.
11. Postolachi, L.; Rusu, V.; Lupascu, T.; Maftuleac A. Improvement of coagulation process for the Prut River water treatment using aluminum sulphate. Chemistry Journal of Moldova, 2015, 10(1), pp. 25–32.
12. Satterfield, Z. Jar Testing. Technical Brief, 2005, 5(1), pp. 1–4.
13. Pask, D. Jar Testing: Getting started on a low budget. On Tap, 1993, 2(2), pp. 4–6.
14. Madera, V.; Allen, H. E.; Minear, R. A., Eds. Examination of Water for Pollution Control, World Health Organization. Pergamon Press: Copenhagen, Denmark, 1982, 1st Ed., vol. 2, pp. 37–42.
15. Stefan, D.; Costache, C.; Ruxandu, V.; Balas, M.; Stefan, M. Comparative study on surface water treatment using aluminum sulphate and polyaluminum chlorides as coagulant reagents. Environmental Engineering and Management Journal, 2009, 8(4), pp. 859–863.
16. Governmental Decision no. 934 of 15 August 2007 regarding the establishment of automated information system "State Register of natural mineral and drinking waters and soft bottled drinks". Official Journal of the Republic of Moldova, 24.08.2007, no. 131-135 (970). (in Romanian). http://lex.justice.md/viewdoc.php?action=view&view=doc&id=326557&lang=1.

THE FORMATION MECHANISM OF ASSEMBLED COMPLEXES BRIDGED BY 1,3–BIS(4–PYRIDYL)PROPANE

Haruka Dote[a], Hiroki Yasuhara[a], Satoru Nakashima[a,b*]

[a]*Department of Chemistry, Graduate School of Science, Hiroshima University*
1-3-1 Kagamiyama, Higashi-Hiroshima, Hiroshima 739-8526, Japan
[b]*Natural Science Center for Basic Research and Development (N-BARD), Hiroshima University*
1-4-2 Kagamiyama, Higashi-Hiroshima, Hiroshima 739-8526, Japan
[*]*e-mail: snaka@hiroshima-u.ac.jp*

Abstract. Several types of differently coloured crystals (light blue, blue and red) were obtained in the synthesis of assembled complex of mixed crystals with three metals by using solvent diffusion method. The mechanism of obtaining the assembled complexes is discussed based on the structure and colour change. The red crystal has 2D interpenetrated structure. The light-blue samples were $[H_2(bpp)][M(NCS)_4]$ and they were built up spirally. The blue samples were $M(NCS)_2(bpp)$ and they formed 1D chain. $[H_2(bpp)][M(NCS)_4]$ changed to 1D chain polymer ($M(NCS)_2(bpp)$) by releasing HNCS from the cation and anion in a reaction vessel. Inductively Coupled Plasma Atomic Emission Spectroscopy, Electrospray Ionization Mass Spectrometry and X-Ray diffraction were used for characterization of the obtained complexes.

Keywords: mixed crystal, assembled complex, 1,3-bis(4-pyridyl)propane, crystal formation.

Received: December 2015/ Revised final: February 2016/ Accepted: February 2016

Introduction

Self-assembled coordination polymers containing transition metal ions and organic bridging ligands have attracted intensive interest in virtue of their potential abilities for selective inclusion and transformation of ions and molecules [1]. Up to now various assembled structures have been reported [2-8]. We have studied iron complexes bridged by 1,3–bis(4–pyridyl)propane (bpp), containing three methylene groups, by using single crystal X–ray diffraction analysis, Mössbauer spectroscopy and Superconducting Quantum Interference Device (SQUID) measurements. $Fe(NCX)_2(bpp)_2$ (X = S, Se and BH_3) had a 2D interpenetrated structure and the $NCBH_3$ complex showed a spin–crossover phenomenon [9]. When the benzene is enclathrated, the structure becomes 1D chain [10]. Recently, we discussed the spin state of the mixed crystals of iron with zinc or cobalt ion in the 2D interpenetrated structure for the assembled complexes bridged by bpp, and we revealed that NCSe complex had a lowered spin state, in comparison with pure Fe complex, because iron atom is forced to reduce its radius in the zinc or cobalt complexes having smaller unit cell [11].

Herein we report on the synthesis of mixed crystals including zinc, cobalt, and iron atoms. Several types of crystals appeared and the colour changed in the reaction medium. The mechanism of obtaining the assembled complexes is put into discussion on the basis of structure and colour modification.

Experimental

Synthesis

Mixed crystals including three metals were obtained by solvent diffusion method. Solvent diffusion method- 1) bottom layer: metal salts (($FeSO_4 \cdot 7H_2O$ (0.33 mmol) + $ZnSO_4 \cdot 6H_2O$ (0.33 mmol) + $CoSO_4 \cdot 7H_2O$ (0.33 mmol)), NaNCS (2 mmol) and *L*-ascorbic acid to avoid oxidation in H_2O (20 mL); 2) middle layer: H_2O (20 mL) and cyclohexane (20 mL); 3) top layer: bpp (2 mmol) in EtOH (1 mL) and cyclohexane (19 mL). Light-blue crystals appeared about 4 hours after the setting and they decreased time to time because of dissolution. Precipitates were mixtures of light-blue crystals, blue crystals, and red crystals. Light-blue crystals were dissolved in acetone and they could be isolated. Anal. found (calc.)%: for $\{[H_2(bpp)][M(NCS)_4]\}_n$, C, 41.67 (41.08); H, 3.21 (3.24); N 16.74 (16.91); S, 24.76 (25.81)($M = Fe_{0.06}Zn_{0.87}Co_{0.07}$). Single crystals of blue crystals were picked up from the reaction vessel. Anal. found (calc.)%: for $\{M(NCS)_2(bpp)\}_n$ (blue crystal), C, 47.79 (47.43); H, 3.64 (3.72); N 14.80 (14.75); S, 16.89 (16.89)($M = Fe_{0.01}Zn_{0.95}Co_{0.04}$). Anal. found (calc.)%: for red crystal, C, 58.65 (58.47); H, 4.67 (4.91); N 14.72 (14.62); S, 11.20 (11.15) ($M = Fe_{0.20}Zn_{0.63}Co_{0.17}$).

Light-blue crystals were selectively obtained when the diluted HNO_3 (0.16 M, 20 mL) was added to the water phase. Single crystals appeared in the bottom.

Zn complex was obtained by solvent diffusion method. Solvent diffusion method: bottom layer; $ZnSO_4 \cdot 6H_2O$ (0.2 mmol), NaNCS (or KNCS) (0.4 mmol) in H_2O (20 mL), middle layer; H_2O (20 mL) and EtOH (20 mL), top layer; bpp (0.2 mmol) in EtOH (20 mL). Crystals appeared about 1 week after the setting.

ICP-AES analyses

The metal fraction, Fe:Zn:Co was determined by Inductively Coupled Plasma Atomic Emission Spectroscopy

(ICP-AES) at SPS3510 spectrometer (*SII NanoTechnology Inc*.). Calibration curves were drawn by measuring intensity of 1, 0.5, 0.1, and 0.01 ppm for iron and zinc standard solution and 0.994, 0.497, 0.099, and 0.050 ppm for cobalt standard solution and ultrapure water. Scan range of iron, zinc, and cobalt was around 238.204, 202.548, and 228.616 nm, respectively.

ESI-MS measurements

Electrospray Ionization Mass Spectrometry (ESI-MS) was performed using LTQ Orbitrap XL spectrometer (Thermo Fisher Scientific).

X-ray diffraction measurements

The powder X-ray diffraction patterns were measured on a Rigaku RAD-X system using Cu-Kα radiation and employing a scan rate of 5.0 °/min, step of 0.02°, and region from 5.0 to 60.0°. All measurements were performed under air at room temperature (RT).

Zn complex and light-blue crystals were obtained as a single crystal, and the structures were determined by single crystal X–ray structural analysis. The crystal data can be obtained free of charge from the Cambridge Crystallographic Data Centre *via* www.ccdc.cam.ac.uk/data_request/cif. (CCDC:1433079 and 1455350).

Results and discussion

Figure 1 shows powder X-ray diffraction patterns of pure iron complex and mixed metal complexes. They revealed that the red crystals has 2D interpenetrated structure, which is similar to the structure of $Fe(NCS)_2(bpp)_2$. The light-blue and blue crystals showed new structure and structural change in the reaction vessel.

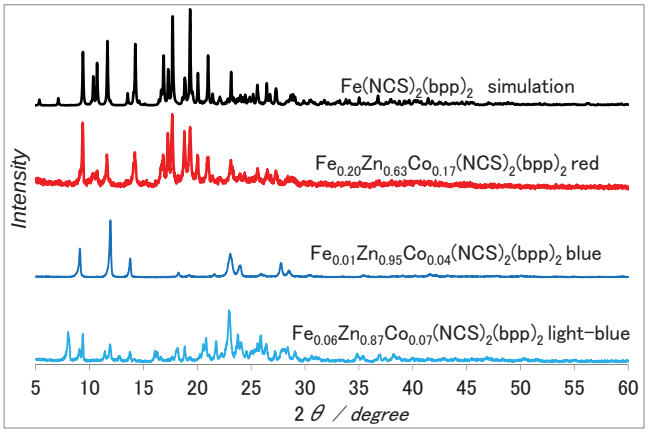

Figure 1. Powder X-ray diffraction patterns of $Fe(NCS)_2(bpp)_2$, red, blue and light-blue mixed crystals.

Figure 2 shows ESI mass spectra of the light-blue crystals measured in the positive and negative ion modes (measurements and simulations). These results along with elemental analysis data prove the composition $[H_2(bpp)][M(NCS)_4]$. Figure 3 shows Oak Ridge Thermal-Ellipsoid Plot Program (ORTEP) drawing and packing view of light-blue crystal. Crystal data are shown in Table 1. Selected bond lengths and angles are shown in Table 2.

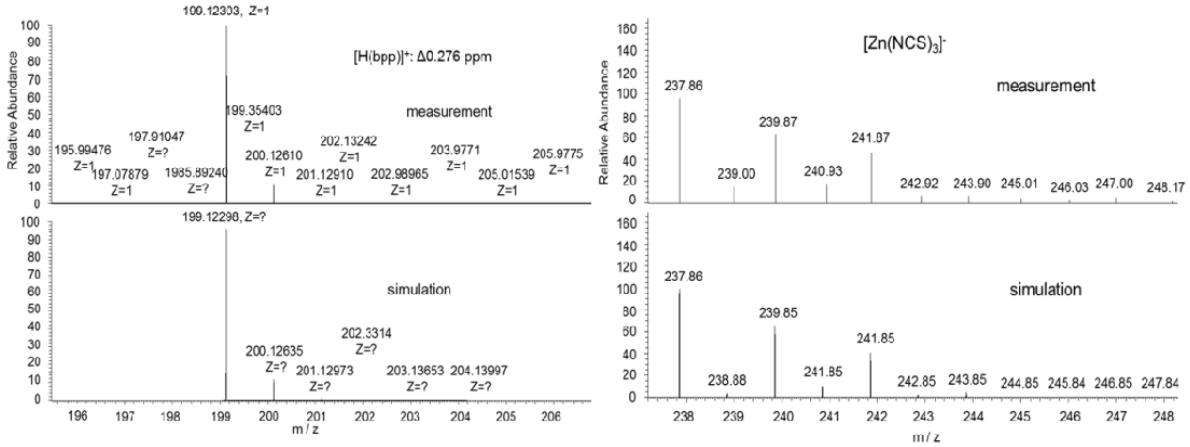

Figure 2. ESI mass spectra of the light-blue crystal measured in the positive and negative ion modes (measurements and simulations).

Table 1

Crystal data of light-blue crystal ($[H_2(bpp)][Fe_{0.06}Zn_{0.87}Co_{0.07}(NCS)_4]$).

Parameter	*Value*
Formula	$C_{13}\,H_{16}\,N_2 + C_4\,N_4\,S_4\,Zn$
Temperature	RT
Crystal system	Orthorhombic
Space Group	$P2_12_12$
Z	4
a / Å	21.7042 (7)
b / Å	22.002 (3)
c / Å	4.639 (3)
Volume/Å^3	2215.3 (16)
R	0.0316
wR	0.0749
Goodness of Fit	1.042

Table 2

Selected bond lengths and angles of light-blue crystal ($[H_2(bpp)][Fe_{0.06}Zn_{0.87}Co_{0.07}(NCS)_4]$).

$[H_2(bpp)][Zn(NCS)_4]$	*Bond lengths or angles*
Zn-N1(NCS) /Å	1.951 (4)
Zn-N2(NCS) /Å	1.954 (4)
Zn-N3(NCS) /Å	1.960 (4)
Zn-N4(NCS) /Å	1.971 (3)
S1-S3' /Å	3.4550 (16)
S2-S4' /Å	3.5058 (14)
S2'-N5(bpp) /Å	3.407 (4)
S4-N5'(bpp) /Å	3.403 (4)
S3'-N6(bpp) /Å	3.405 (4)
S1-N6(bpp) /Å	3.423 (4)
N1-Zn-N2 /°	107.72(14)
N1-Zn-N3 /°	115.57(18)
N1-Zn-N4 /°	104.93(14)
N2-Zn-N3 /°	107.91(15)
N2-Zn-N4 /°	115.56(17)
N3-Zn-N4 /°	105.42(14)

Metals are tetrahedrally coordinated by four NCS anions to become $[M(NCS)_4]^{2-}$ and bpp is doubly protonated-$[H_2(bpp)]^{2+}$. Thus, the whole composition becomes $[H_2(bpp)][M(NCS)_4]$, and this is a mononuclear complex. This structure organisation explains the better dissolution of this sample in the solvent, as compared with blue and red crystals, respectively. The packing view in one plane is shown in Figure 3(b). $[H_2(bpp)]^{2+}$ is surrounded by four $[M(NCS)_4]^{2-}$, $[M(NCS)_4]^{2-}$ in turn, being also surrounded by four $[H_2(bpp)]^{2+}$ in the same plane. The fragments $[H_2(bpp)]$ are placed almost perpendicular to each other. This plane is stacked to each other to form crystal (Figure 3(c)), the structure being similar to [4,4'-bipyH_2][$Zn(NCS)_4$][13]. Each sulphur atom of the $[Zn(NCS)_4]^{2-}$ anion has a weak S…S contact with a sulphur atom from an adjacent $[Zn(NCS)_4]^{2-}$ anion. The distances of these contacts being 3.4550(16) or 3.5058(14) Å, they are slightly shorter than that in [4,4'-bipyH_2][$Zn(NCS)_4$][13](3.63 Å), and also slightly shorter than the sum of the *van der Waals* radii of two sulphur atoms, indicating weak interaction [14]. The frame constructed by weak S…S contact was built spirally. The sulphur atoms also form hydrogen bonds with the $[H_2(bpp)]^{2+}$ cations. The distances are 2.6591(14), 2.7601(13), 2.7224(13), or 2.6913(12) Å, which are slightly longer than that in [4,4'-bipyH_2][$Zn(NCS)_4$] [13] (2.404(3) Å). This is due to the difference that $[H_2(bpp)]^{2+}$ is placed in centre between anion, while [4,4'-bipyH_2]$^{2+}$ approaches the one side of anion.

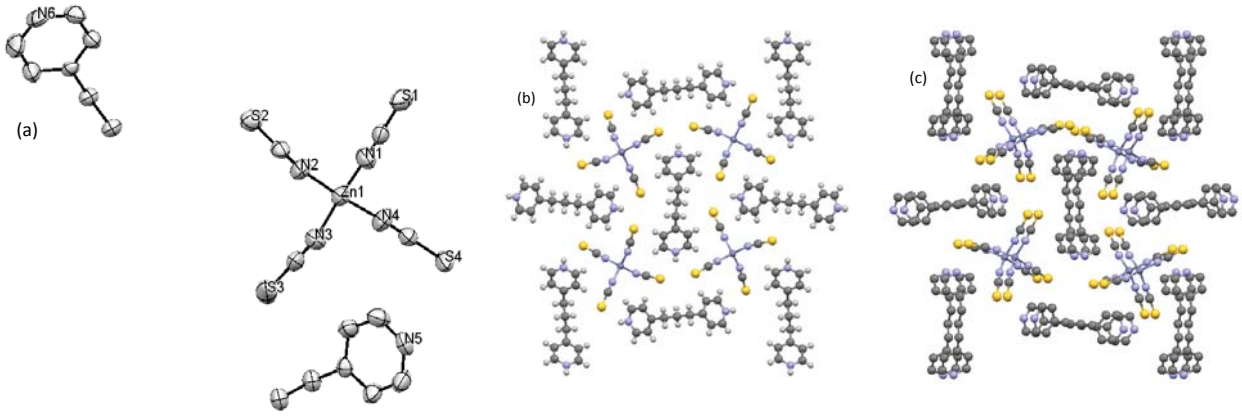

Figure 3. Crystal structure of light-blue crystal ([H_2(bpp)][$Fe_{0.06}Zn_{0.87}Co_{0.07}(NCS)_4$]). (a)- ORTEP drawing, (b)- packing view in one plane, and (c)- packing view.

Blue sample could not be isolated as a single crystal, but as an aggregation of very small crystals. By comparing the powder X-ray diffraction patterns (Figure 4) and on the basis of elemental analysis data, it was confirmed, that blue crystals and pure zinc complex ($Zn(NCS)_2$(bpp)) have identical structures. It can be considered that the structures are controlled by the Zn metal. The structure of $Zn(NCS)_2$(bpp) was determined by single X-ray structural analysis. Crystal data are shown in Table 3. Selected bond lengths and angles are shown in Table 4. Figure 5(a) shows ORTEP drawing of pure zinc complex. Zn is tetrahedrally coordinated by one bpp and two NCS to form 1D chain. The 1D chain is shown in Figure 5 (b). This is not an ionic complex, but neutral 1D chain polymer.

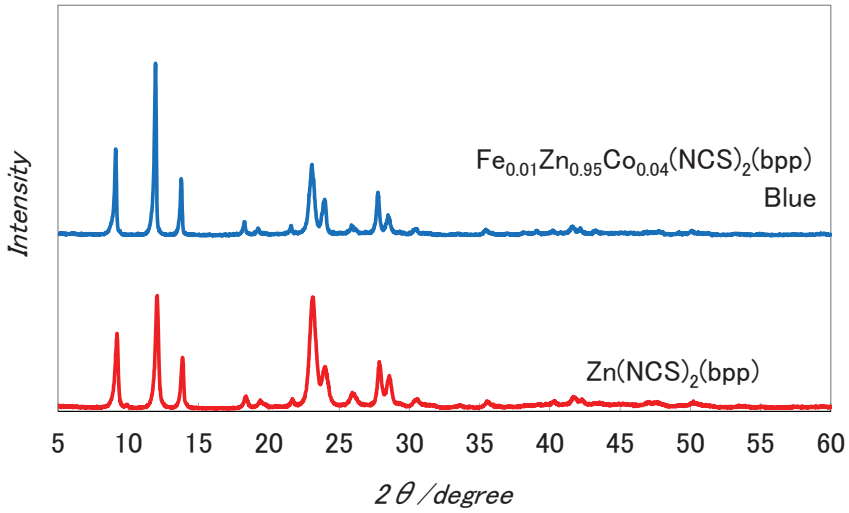

Figure 4. Comparison of powder X-ray diffraction patterns of $Fe_{0.01}Zn_{0.95}Co_{0.04}$ $(NCS)_2$(bpp) and $Zn(NCS)_2$(bpp).

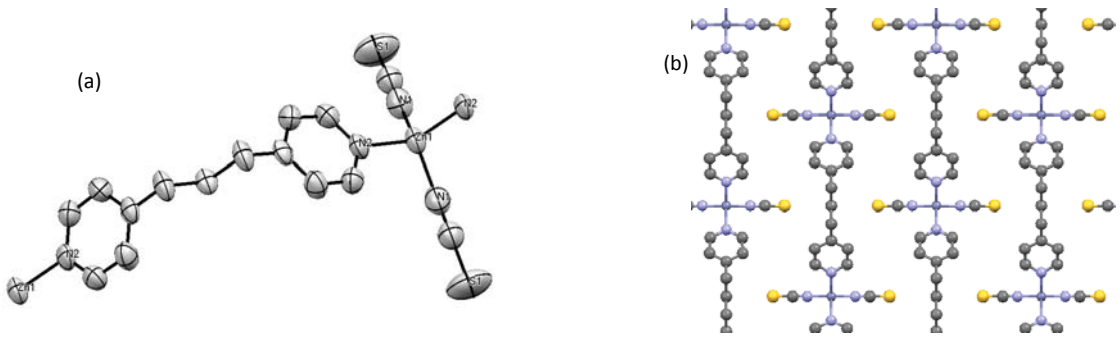

Figure 5. Crystal structure of $Zn(NCS)_2$(bpp). (a)- ORTEP drawing and (b)- packing view.

Table 3

Crystal data of $Zn(NCS)_2(bpp)$.

Parameter	*Value*
Formula	$C_{15}H_{14}N_4S_2Zn$
Temperature	RT
Crystal system	Orthorhombic
Space Group	Imm2
Z	2
a / Å	12.859 (6)
b / Å	14.891 (7)
c / Å	4.779 (2)
Volume/Å^3	915.1 (7)
R	0.0533
wR	0.1300
Goodness of Fit	1.139

The light-blue crystals are easily dissolved in acetone. The light-blue crystals changed to blue in the reaction vessel in acetone solution. Usually, metals and ligands gather to each other to form a stable assembled structure in the synthetic process of assembling complexes. In the present study, it was shown that at the first stage the ionic crystals are obtained and subsequently, the crystal changed to more stable assembled structure. It is considered that initially $[H_2(bpp)]^{2+}$ and $[M(NCS)_4]^{2-}$ are formed in water or EtOH, which then precipitate as $[H_2(bpp)][M(NCS)_4]$. This is not the most stable structure in the reaction vessel. It undergoes modifications, to form 1D polymer chain structure by releasing HNCS from the cation and anion.

Table 4

Selected bond lengths and angles of $Zn(NCS)_2(bpp)$.

$Zn(NCS)_2(bpp)$	*Bond lengths or angles*
Zn-N1(NCS) /Å	1.929 (11)
Zn-N2(bpp) /Å	2.022 (9)
N1-Zn-N1' /°	123.6 (7)
N1-Zn-N2 /°	104.9 (2)
N2-Zn-N2' /°	114.1 (5)
Zn-N1(NCS) /Å	1.929 (11)
Zn-N2(bpp) /Å	2.022 (9)
N1-Zn-N1' /°	123.6 (7)
N1-Zn-N2 /°	104.9 (2)

Conclusions

In conclusion, several types of crystals having different colour (light blue, blue and red) were obtained in the synthesis of assembled complex of mixed crystals with three metals by solvent diffusion method. The formation mechanism of the assembled complexes bridged by 1,3–bis(4–pyridyl)propane is proposed on the basis of structure and colour modification. The red crystals have 2D interpenetrated structure. The samples of light-blue ionic crystals were $[H_2(bpp)][M(NCS)_4]$ and they were built up spirally. The blue samples were $M(NCS)_2(bpp)$ and they formed neutral 1D chain. $[H_2(bpp)][M(NCS)_4]$ changed to 1D chain polymer ($M(NCS)_2(bpp)$) by releasing HNCS from the cation and anion in the reaction medium. The obtained complexes were characterized by ICP-AES, ESI-MS and X-Ray-diffraction methods.

References

1. Moulton, B.; Zaworotko, M.J. From molecules to crystal engineering: supramolecular isomerism and polymorphism in network solids. Chemical Reviews, 2001, 101, pp. 1629-1658.
2. Carlucci, L.; Ciani, G.; Proserpio, D.M.; Sironi, A. Interpenetrating diamondoid frameworks of silver(I) cations linked by N,N'-bidentatemolecular rods. Journal of the Chemical Society, Chemical Communications, 1994, pp. 2755-2756.
3. Gardner, G.B.; Venkataraman, D.; Moore, J.S.; Lee, S. Spontaneous assembly of a hinged coordination network. Nature (London), 1994, 374, pp. 792-795.

4. Biradha, K.; Seward, C.; Zaworotko, M.J. Helical coordination polymers with large chiral cavities. Angewandte Chemie International Edition, 1999, 38, pp. 492-495.
5. Zheng, L.-M.; Fang X.; Lii, K.-H.; Song, H.-H.; Xin, X.-Q.; Fun, H.-K.; Chinnakali, K.; Razak, I.A. Syntheses, crystal structures and magnetic properties of two novel layered compounds: $[Fe_3(C_2O_4)_3(4,4'\text{-bpy})_4]$ and $[Co(C_2O_4)(4,4'\text{-bpy})]$ (4,4'-bpy = 4,4'-bipyridine). Journal of the Chemical Society, Dalton Transactions, 1999, pp. 2311-2316.
6. Carlucci, L.; Ciani, G.; Proserpio, D.M. A new type of supramolecular entanglement in the silver(I) coordination polymer $[Ag_2(bpethy)_5](BF_4)_2$ [bpethy = 1,2-bis(4-pyridyl)ethyne]. Chemical Communications, 1999, pp. 449-450.
7. Gudbjartson, H.; Biradha, K.; Poirier, K.M.; Zaworotko, M.K. Novel nanoporous coordination polymer sustained by self-assembly of T-shaped moieties. Journal of the American Chemical Society, 1999, 121, pp. 2599-2600.
8. Subramanian, S.; Zaworotko, M.J. Porous solids by design: $[Zn(4,4'\text{-bpy})_2(SiF_6)]_n \cdot x$DMF, a single framework octahedral coordination polymer with large square channels. Angewandte Chemie, International Edition in English, 1995, 34, pp. 2127-2129.
9. Atsuchi, M.; Higashikawa, H.; Yoshida, Y.; Nakashima, S.; K. Inoue, K. Novel 2D interpenetrated structure and occurrence of the spin-crossover phenomena od assembled complexes, $Fe(NCX)_2(bpp)_2$ (X = S, Se, BH_3; bpp = 1,3-bis(4-pyridyl)propane. Chemistry Letters, 2007, 36, pp. 1064-1065.
10. Atsuchi, M.; Inoue, K.; Nakashima, S. Reversible structural change of host framework triggered by desorption and adsorption of guest molecules in $Fe(NCS)_2(bpp)_2 \cdot 2$(benzene) (bpp = 1,3-bis(4-pyridyl)propane). Inorganica Chimica Acta, 2011, 370, pp. 82-88.
11. Nakashima, S.; Dote, H.; Atsuchi, M.; Inoue, I. Spin state of mixed crystals of iron with zinc or cobalt for the assembled complexes bridged by 1,3-bis(4-pyridyl)propanes. Journal of Physics: Conference Series. 2010, 217, 01035.
12. Dote, H.; Nakashima, S. Crystal structure and spin state of mixed-crystals of iron with zinc and cobalt for the assembled complexes bridged by 1,3-bis(4-pyridyl)propanes. Hyperfine Interactions, 2012, 205, pp. 27–30.
13. Chen, H.-J.; Zhang, L.-Z.; Cai, Z.-G.; Yang, G.; Chen, X.-M. Organic-inorganic hybrid materials assembled through weak intermolecular interactions. Syntheses, structures and non-linear optical properties of $[4,4'\text{-bipyH}_2][M(NCS)_4]$ ($M = Mn^{2+}$, Co^{2+}, or Zn^{2+}; 4,4'-bipy = 4,4'-bipyridine). Journal of the Chemical Society, Dalton Transactions, 2000, pp. 2463-2466.
14. Zhong, J.C.; Misaki, Y.; Munakata, M.; Kuroda-Sowa, T.; Maekawa, M.; Suenaga, Y.; Konaka, H. Silver(I) coordination polymer of 2,5-bis(4',5'-bis(methylthio)-1',3'-dithiol-2'-ylidene)-1,3,4,6-tetrathiapentalene (TTM-TTP) and its highly conductive iodine derivative. Inorganic Chemistry, 2001, 40, pp. 7096-7098.

STRUCTURE AND SOME BIOLOGICAL PROPERTIES OF Fe(III) COMPLEXES WITH NITROGEN-CONTAINING LIGANDS

Ion Bulhac[a*], Alexandra Deseatnic-Ciloci[b], Paulina Bourosh[c], Janetta Tiurina[b], Olga Bologa[a], Cezara Bivol[b], Steliana Clapco[b], Ana Verejan[a], Svetlana Labliuc[b], Olga Danilescu[a]

[a]*Institute of Chemistry of Academy of Sciences of Moldova, 3, Academiei str., Chisinau MD-2028, Republic of Moldova*
[b]*Institute of Microbiology and Biotechnology of Academy of Sciences of Moldova, 1, Academiei str., Chisinau MD-2028, Republic of Moldova*
[c]*Institute of Applied Physics of Academy of Sciences of Moldova, 5, Academiei str., Chisinau MD-2028, Republic of Moldova*
[*]*e-mail: ionbulhac@yahoo.com*

Abstract. Four coordination compounds of iron(III) with ligands based on hydrazine and sulfadiazine: $[Fe(dig)]Cl_3 \cdot 2H_2O$ (**I**) (dig-semicarbazide diacetic acid dihydrazide), $[Fe(HL)SO_4]$ (**II**) (HL - sulfadiazine), $[Fe(H_2L^1)(H_2O)_2](NO_3)_3 \cdot 5H_2O$ (**III**) (H_2L^1-2,6-diacetylpyridine bis(nicotinoylhydrazone) and $[Fe(H_2L^2)(H_2O)_2](NO_3)_3 \cdot 1.5H_2O$ (**IV**) (H_2L^2 - 2,6-diacetylpyridine bis(isonicotinoylhydrazone) were synthesized. The spectroscopic and structure characterisation, as well as their biological properties, are presented. All tested coordination compounds, caused an inhibitory effect on the biosynthesis of hydrolases of the producer *Aspergillus niger* CNMN FD-10. The effect increased with the raise of the concentration from 5 mg/L to 15 mg/L. The complexes largely inhibited cellobiohydrolase and less- *β*-glucosidase. The inhibitory effect of the coordination compounds was quite similar in the case of endoglucanase and xylanase. Compound **I**, containing both chloride ions and dig, demonstrated a stronger inhibitory effect, while compound **III**, containing NO_3^- ions, showed the weakest inhibitory action.

Keywords: iron complexes, nitrogen-containing ligands, structure, biological properties.

Received: October 2015/ Revised final: January 2016/ Accepted: February 2016

Introduction

In the modern microbiology, investigation of the effects of external factors on the physiology of microorganisms remains an actual issue. Such studies allow solving the practical problems and implementation of the new technologies in biology and medicine.

The literature, in the last decades, denotes high physiological activity of the coordination compounds of transition metals on biological objects, including microorganisms [1-13]. Some authors note a significant role of these compounds in the directed synthesis of biologically active substances from microalgae and cyanobacteria, filamentous fungi and yeast [1-10,12].

Studies of the effects of coordination compounds on biosynthesis of extracellular hydrolases in filamentous fungi have been previously carried out [3-7,14]. It was established that these effects depend both on the properties of compounds (chemical composition, molecular structure, nature of the ligand and coordinated metal atom) and genus and species of the micromycetes strains, and specificity of the synthesized enzymes [3-7,14]. Some coordination compounds exhibit a selective action on the components of the synthesized enzyme complex. Thus, by adding the molybdenum complex with valine - $MoO_2(acac)_2Val$ (acac=acetylacetone, Val=valine) into the nutrient medium, the biosynthesis of *β*-glucosidase in micromycete *Penicillium expansum* CNMN FD 5C – producer of cellulases was enhanced by 69.4%, while the level of endoglucanase and cellobiohydrolase was not modified. Study of the influence of $(NH_4)_2VO_2Gly$ (Gly=glycine) on biosynthesis of cellulases of the same strain showed that the dioxovanadium complex increased the activity of all components of cellulase complex by 17.6-40.3% [14].

The targeted application of the coordination compounds of 3*d*-elements as regulators of the microbial synthesis of bioactive substances requires accumulation of factual material on the nature of their influence on all phases of the development of microorganisms and also identification of optimal conditions for their use. All of this information will ensure the resolution of some theoretical issues, such as elucidation of the mechanism of action of coordination compounds, establishing the relationship between the composition, structure and enzyme activity of the microorganisms, as well as the development of methods for their practical use. These objectives can be achieved by expanding both, the diversity of microorganisms and the involved in researches complexes.

Iron is one of the essential microelements for microorganisms. It is involved in the respiration in microorganisms, being also necessary for the protein, carbohydrate and lipid metabolism, including protein synthesis. Iron is crucial structure component of the cytochromes, which catalyze the process of electron transfer in the mitochondria. In living organisms redox system Fe^{3+}/Fe^{2+} plays an unique role [15,16].

This study was aimed at investigation of the effect of iron(III) complexes with various organic ligands derived from hydrazine and sulfadiazine on the biosynthesis of cellulases and xylanases at *Aspergillus niger* CNMN FD 10 micromycete.

Materials and methods

Chemistry

[Fe(dig)]$Cl_3 \cdot 2H_2O$ (**I**) was obtained by mixing the ethanolic solutions of $FeCl_3 \cdot 6H_2O$ (1.0g, 3.7 mmol in 50 mL ethanol) and digsemi (0.8 g, 3.7 mmol in 40 mL ethanol). The formed dark brown residue was separated by filtration, washed with ethanol and diethyl ether. The complex is soluble in water, less soluble in alcohol and diethyl ether. Yield- 75% [17,18].

[Fe(HL)SO_4] (**II**) was obtained by refluxing $FeSO_4 \cdot 7H_2O$ (2.0 g, 0.72 mmol) and sulfadiazine (0.22 g, 0.88 mmol) in methanol (20 mL) for 2 hours in a water bath. The brown precipitate was separated from the mother liquor by filtration, washed with methanol and diethyl ether. The complex is well soluble in methanol and DMF, less soluble in water and diethyl ether. Yield- 80% [13].

Methods for the synthesis of coordination compounds of iron with semicarbazide diacetic acid dihydrazide, sulfadiazine, 2,6-diacetylpyridine *bis*(nicotinoylhydrazone) and 2,6-diacetylpyridine bis(isonicotinoylhydrazone) have been developed. The complexes of iron(III) with Schiff bases on the basis of 2,6-diacetylpyridine were obtained in two ways: by condensation reactions of 2,6-diacetylpyridine with hydrazides of nicotinic and isonicotinic acid on the matrix of iron ions and by direct interaction of iron salt with the corresponding Schiff bases.

For determining the composition, spectral characteristics, molecular and crystal structures of the complexes elemental analysis, IR and Mössbauer spectroscopy and single crystal X-ray diffraction were applied. The composition and structure of the complexes **III** and **IV** were established by IR spectroscopy and X-ray diffraction and can be described by the following formulas: $[Fe(H_2L^1)(H_2O)_2](NO_3)_3 \cdot 5H_2O$ (**III**) and $[Fe(H_2L^2)(H_2O)_2](NO_3)_3 \cdot 1.5H_2O$ (**IV**).

IR spectroscopy

The IR spectra of the ligands and complexes were recorded on spectrophotometer FT-IR Perkin-Elmer "Spectrum 100" in the vaseline oil in the region 4000-400 cm^{-1} and ATR in the region 4000-650 cm^{-1}, and the absorption bands has been attributed according to the reference literature [23-26], (s. - strong, v.s. - very strong, m. – middle, w. – weak, sh. – shoulder, br. - broad).

Mössbauer spectroscopy

The ^{57}Fe-Mössbauer spectra were recorded with a common spectrometer in the constant-acceleration mode (MS4, Edina, USA) equipped with a ^{57}Co source in a rhodium matrix.

X-ray Crystallography

The unit cell parameters and the sets of reflections intensity were measured at 293 K on a Xcalibur E CCD diffractometer for crystals **III** and **IV** (MoK_α radiation, graphite monochromator). The structures of compounds **III** and **IV** were solved by the direct methods and refined by least squares in the anisotropic full matrix approximation for non-hydrogen atoms (SHELX-97) [19]. The C, N, and O-bound H atoms were placed in calculated positions and were treated using a riding model approximation with $U_{iso}(H) = 1.2U_{eq}(C)$ or $U_{iso}(H) = 1.5U_{eq}(O, C(CH_3)$. The crystallographic data and X-ray experiment details for structures **III** and **IV** are presented in Table 1, the selected interatomic distances are listed in Table 2 and the geometric parameters of hydrogen bonds are given in Table 3. Crystallographic data for **III** and **IV** have been deposited with the Cambridge Crystallographic Data Center, CCDC 1429807, 1429808. Copies of this information may be obtained from The Director, CCDC, 12 Union Road, Cambridge, CB2 1EZ, UK (fax: +44-1233-336033; e-mail: deposit@ccdc.cam.ac.uk or www: http://www.ccdc.cam.ac.uk).

Table 1

Crystal data and structure refinement data for III and IV.

Parameter	*Compound* ***III***	*Compound* ***IV***
Formula	$C_{21}H_{33}FeN_{10}O_{18}$	$C_{21}H_{25}FeN_{10}O_{14.50}$
M	769.42	705.36
Crystal system	monoclinic	monoclinic
Space group	$P2_1/n$	$P2_1/c$
a, Å	13.0459(5)	13.4325(6)
b, Å	16.6677(4)	15.0766(5)
c, Å	15.2842(5)	15.3908(8)
β, °	100.730(3)°	107.895(5)
V, Å^3	3265.38(17)	2966.1(2)
Z	4	4
ρ_{calc}, g/cm^3	1.565	1.580
μ, mm^{-1}	0.555	0.595
F(000)	1596	1452
Crystal size, mm	0.35x0.2x0.1	0.2x0.15x0.15
θ range for data collection, °	2.91 – 25.50	3.04 – 25.50
Index ranges	$-11 \le h \le 15$	$-12 \le h \le 16$
	$-19 \le k \le 11$	$-16 \le k \le 18$
	$-18 \le l \le 11$	$-18 \le l \le 18$

Continuation of Table 1

Parameter	*Compound* ***III***	*Compound* ***IV***
Reflections collected/ Independent reflections	10714/6047 [R(int) = 0.0294]	10286/5472 [R(int) = 0.0476]
Reflections with $I>2\sigma(I)$	6047	5472
Parameters	451	424
GOOF	0.998	1.003
Final *R* indices ($I>2\sigma(I)$)	R_1 = 0.0544 wR_2 = 0.1221	R_1=0.0631, wR_2 = 0.1415
R indices (all data)	R_1 = 0.1117 wR_2 = 0.1453	R_1 = 0.1083, wR_2 = 0.1628
$\Delta\rho_{max}$, $\Delta\rho_{min}$, $e\times$Å^{-3}	0.553, –0.328	0.558, –0.370

Table 2

Bond lengths (Å) in coordination polihedra of III and IV.

Bond	*Compound* ***III***	*Compound* ***IV***
Fe(1)−O(1)	2.033(2)	2.087(3)
Fe(1)−O(2)	2.029(2)	2.043(3)
Fe(1)−O(1W)	2.036(2)	2.035(3)
Fe(1)−O(2W)	2.035(2)	2.028(3)
Fe(1)−N(3)	2.194(3)	2.176(3)
Fe(1)−N(4)	2.188(3)	2.203(3)
Fe(1)−N(5)	2.194(3)	2.187(3)

Table 3

Geometric parameters of hydrogen bonds for III and IV (Å and °).

D−*H*···*A*	*d, Å*			∠*DHA*, °	*Symmetry transformations used to generate equivalent atoms*
	D–*H*	*H*···*A*	*D*···*A*		
			Compound ***III***		
O(1W)−H(1W1)···O(6A)	0.80	1.91	2.701(4)	173	*x, y, z*
O(1W)−H(2W1)···O(3W)	0.83	1.85	2.679(3)	179	*−x*+1/2, *y−1/2, −z*+3/2
O(2W)−H(1W2)···O(7W)	0.82	1.77	2.580(4)	169	*−x*+3/2, *y*+1/2, *−z*+3/2
O(2W)−H(2W2)···O(9A)	0.80	1.91	2.699(4)	170	*x, y, z*
N(1)−H(1A)···O(6W)	0.86	1.87	2.715(4)	170	*x, y, z*
N(7)−H(7A)···O(1A)	0.86	1.85	2.713(4)	177	*x, y, z*
N(7)−H(7A)···O(2A)	0.86	2.60	3.200(5)	128	*x, y, z*
O(3W)−H(1W3)···O(4A)	0.84	1.93	2.769(4)	173	*x, y, z*
O(3W)−H(2W3)···O(5W)	0.84	1.91	2.726(4)	162	*x, y, z*
O(4W)−H(1W4)···O(3W)	0.86	2.55	2.959(4)	110	*−x*+1,*−y*+1,*−z*+1
O(4W)−H(2W4)···O(9A)	0.84	2.04	2.855(4)	163	*x, y, z*
O(5W)−H(1W5)···O(8A)	0.84	2.25	2.962(4)	143	*−x*+1,*−y*+1,*−z*+1
O(5W)−H(1W5)···O(9A)	0.84	2.31	3.102(5)	158	*−x*+1,*−y*+1,*−z*+1
O(5W)−H(2W5)···O(1A)	0.85	1.93	2.777(4)	174	*x, y*+1, *z*
O(6W)−H(1W6)···O(3A)	0.83	2.24	2.968(5)	147	*x, y, z*
O(6W)−H(1W6)···O(2A)	0.83	2.26	3.033(5)	156	*x, y, z*
O(6W)−H(2W6)···O(4W)	0.80	2.03	2.737(4)	147	*−x*+3/2, *y*−1/2, *−z*+3/2
O(7W)−H(1W7)···O(6W)	0.80	2.26	3.054(5)	168	*x, y, z*
O(7W)−H(2W7)···O(8A)	0.85	2.20	3.013(5)	160	*x, y, z*
O(7W)−H(2W7)···O(7A)	0.85	2.27	2.952(5)	138	*x, y, z*
			Compound ***IV***		
O(1W)−H(1W1)···O(3W)	1.02	1.68	2.568(9)	143	*x, y, z*
O(1W)−H(1W1)···O(4W)	1.02	1.73	2.649(11)	148	*x, y, z*
O(1W)−H(2W1)···O(1A)	0.93	1.76	2.683(4)	172	*x, y, z*

Continuation of Table 3

D−H···A	*d, Å*			*∠DHA, °*	*Symmetry transformations used to generate equivalent atoms*
	D–H	*H···A*	*D···A*		
			Compound ***IV***		
O(2W)−H(1W2)···O(3A)	0.89	1.82	2.669(4)	159	*x,−y*+1/2, *z*+1/2
O(2W)−H(1W2)···O(2A)	0.89	2.63	3.338(5)	138	*x,−y*+1/2, *z*+1/2
O(2W)−H(2W2)···O(1)	0.94	1.84	2.769(4)	171	*−x,−y,−z*+2
N(1)−H(1A)···O(5A)	0.86	1.91	2.759(5)	171	*x, y, z*
N(7)−H(7A)···O(9A)	0.86	1.97	2.805(6)	162	*x, y, z*
N(7)−H(7A)···O(8A)	0.86	2.27	2.994(7)	142	*x, y, z*

Microbiology

The effects of the synthesized coordination compounds on the biosynthesis of cellulases (cellobiohydrolase, endoglucanase, *β*-glucosidase) and xylanases at *Aspergillus niger* CNMN FD 10 micromycete have been investigated [20]. The method of submerged cultivation was applied. The producer was cultivated on the nutrient medium with the chosen composition (g/L): beet pulp - 20.0, KH_2PO_4 – 1.0, $CaCl_2 \cdot 2H_2O$ – 0.1, KCl – 0.1, $MgSO_4 \cdot 7H_2O$ – 0.3, $NaNO_3$ – 2.5, $FeCl_3$ – 0.01, H_2O – 1.0, pH 5.5-6.0, at 28-30ºC under constant stirring on shaker at 180-220 rpm. The duration of the cultivation was 6-9 days; during this period a maximum of biosynthesis of the aforementioned enzymes is observed. The complexes were added to nutrient medium in the concentrations of 5, 10 and 15 mg/L. The samples without the coordination compounds served as control.

Results and discussion

Chemistry

In compound **I** dig behaves like tridentate tripodal ligand. In the IR spectrum the complex absorption bands corresponding to stretching vibrations of NH and NH_2 groups are found in the region 3050-3500 cm^{-1}. However, the band of stretching vibrations of the bonds of amino group NH in the complex spectrum is shifted to longer wavelength region with ≈ 100 cm^{-1}, as compared with its position in the spectrum of the free dihydrazide, indicating on the presence of Me←NH_2 bond [21]. For dig, three bands are in the range of 1600-1700 cm^{-1} (1695, 1670 and 1635 cm^{-1}). Due to complexation, these bands are displaced by 30-50 cm^{-1} in the low frequency region, forming two strips (one wider), which suggests that the oxygen atoms of the carboxyl group are coordinated to the central atom [22].

The recorded at 300 and 80K Mössbauer spectra of $[Fe(dig)]Cl_3 \cdot 2H_2O$ (**I**) have been studied. They show a symmetrical doublet with the following parameters: at 300K IS = 0.69 mm/s and QS = 1.37 mm/s; at 80K IS = 0.79 mm/s and QS = 1.39 mm/s. The experimental value of the effective magnetic moment is equal to 6.04 MB (the pure spin value μ_{eff} for 5 unpaired electron is equal to 5.92 MB). The values of Mössbauer spectrum and μ_{eff} correspond to the metal oxidation state +3, *i.e.* iron is in the high-spin state. According to the value of the isomer shift and quadrupole splitting, the coordination environment of the central ion is nearly spherical, being completed by the donors of the organic ligand (O, NH, N) and two water molecules. The molar conductivity of the aqueous solution of the complex is 391.8 $ohm^{-1} \cdot cm^2 \cdot mol^{-1}$, which corresponds to four ions [17,18].

The IR spectrum of $[Fe(HL)SO_4]$ (**II**) contains typical bands for the sulfadiazine: 3400-3200 (NH and NH_2 groups), 1600-1500 cm^{-1} (aromatic ring), 1320-1160 cm^{-1} (SO_2 group) [13].

$[Fe(H_2L^1)(H_2O)_2](NO_3)_3 \cdot 5H_2O$ (**III**), IR, ν(**(**cm^{-1}): 3381 m., br., 3193 m., br., 3124 sh., 3085 m., 3063 m., 2988 m., br., 2750 m., br., 2650 m.,br., 2420 w., br., 2350 w.,br., 2106 w., 2006 w., 1752 w., 1737 w., 1630 m., 1617 sh., 1598w., 1566 m., 1533 s., 1507 m., 1395 v.s., 1380 v.s., 1357 v.s., 1313 v.s., 1272 sh., 1212 sh., 1165 s., 1148 m., 1108 m., 1075 w., 1056 s., 1039 s., 1020 m., 997 m., 978 sh., 958 w., 920 m., 885 w., 874 w., 820 s., 773 w., 752 w., 731 s., 702 m., 689 w., 689 m., 664 w., 621 m., 565 m., 554 sh., 533 s., 495 w., 445 s.

The IR spectrum of complex **III** at 3600-1900 cm^{-1} is almost identical with the spectrum of compound **IV**. The high-intensity band corresponding to ν(C=O), which in the spectrum of the non-coordinated ligand H_2L^1 appears at 1663 cm^{-1}, shifts to 1637 cm^{-1} in the spectrum of complex **III**, which proves that this group participates in the coordination to the metal atom. The absorption band at 1617 cm^{-1} can be assigned to the ν(CN) heterocycle, the bands at 1598, 1533 and 752 cm^{-1} - to the pyridine ring vibrations, and the band at 1566 cm^{-1} - to δ(NH) hydrazide fragment. The absorption bands associated with the NO_3^- anions vibrations, with different functions, could be observed at 1507, 1313 (the most intense band in the spectrum), 1300, 1039 and 997 cm^{-1}. The fact that the main bands (1313 and 1300 cm^{-1}), associated with fluctuations of NO_3^- anions vibrations of the complex, shift to shorter wavelengths, as compared to those for free NO_3^- anions (1380-1350 cm^{-1}), demonstrated that these anions are involved in the formation of various hydrogen bonds in the complex, which correspond by value of this frequencies to the monocoordinated and chelate-bidentate NO_3^- ions [23,26]. The band corresponding to ν(N-N) appears at 1165 cm^{-1}. The deformation vibrations δ(C-H) of the aromatic rings were found: planar vibrations at 1148, 1108 and 1020 cm^{-1}; non-planar vibrations at

752 cm^{-1} (three adjacent hydrogen atoms) and 820 cm^{-1} (isolated hydrogen atom) [23-25]. The stretching vibrations Fe-N are located at 688 and 678 cm^{-1}, and Fe-O - at 495 and 445 cm^{-1}.

$[Fe(H_2L^2)(H_2O)_2](NO_3)_3 \cdot 1.5H_2O$ (**IV**), IR, ν(cm^{-1}): 3522 m., br., 3151 w., 3117 w., 3080 m., 2990 m., br., 2894 m., br., 2793 m., br., 2762 m., br., 2652 m., br., 2581 m., br., 2452 m., br., 2342 sh., 1744 w., 1637 s., 1612 m., 1584 w., 1567 m., 1548 m., 1535 sh., 1498 m., 1409 s., 1379 sh., 1365 s., 1345 s., 1306 v.s., 1291 v.s., 1273 s., 1207 m., 1186 m., 1170 m., 1161 s., 1094 m., 1080 m., 1059 m., 1050 m., 1043 m., 1034 m., 1019 w., 1004 sh., 996 m., 913 m., 843 s., 827 s., 754 s., 722 w., 713 w., 691 m., 684 s., 651 w., 569 w., 556 w., 534 w., 500 w., 487 w., 442 m.

The IR spectrum is characterized by broad absorption in the range of 3500-1900 cm^{-1}, the absorption bands of 3151 and 3117 cm^{-1} being distinguished on its background. These bands can be attributed to the stretching vibrations associated to OH and NH-groups, respectively. The intense band at 1637 cm^{-1} can be referred to a coordinated C=O group. The band of medium intensity at 1612 cm^{-1} can be assigned to the ν(CN) of the pyridine heterocycle and absorption bands at 1584, 1534 and 754 cm^{-1} – to the heterocycle vibrations itself. The deformation vibrations δ(NH) were found at 1567 cm^{-1}. The intense absorption band at 1409 cm^{-1} can be regarded as the result of interaction of ν(C=N) and ν(C=C) vibrations [23-25].

The most intense absorption bands of the spectrum are associated with the vibrations of NO_3^- anion, which exerts various functions in the crystal lattice of the complex: 1498, 1306, 1291, 1043 and 996 cm^{-1}. Shift of the most intense absorption band of NO_3^- (1291 cm^{-1}) to higher frequencies, in comparison with that of the free NO_3^- anions (1380-1350 cm^{-1}), proves that these anions are involved in the formation of various hydrogen bonds in the complex and by the value is close to the frequency of mono coordinated and chelate-bidentate NO_3^- anions [23-26]. The intense band at 1161 cm^{-1} refers to ν(N-N). The planar C-H deformation vibrations appear through the 1207, 1050 cm^{-1} (1,4-substituted aromatic ring) and 1171, 1080 and 1034 cm^{-1} (1,2,3-substituted aromatic ring) absorption bands. Non-planar C-H deformation vibrations of the aromatic rings appear at 827 cm^{-1} (for two adjacent hydrogen atoms) and 754 cm^{-1} (for three adjacent hydrogen atoms) [24,25]. The ν(Fe-N) oscillations are identified by bands at 692 and 685 cm^{-1} and ν(Fe-O)– by bands at 487 and 442 cm^{-1}, correspondingly.

The crystal and molecular structures of compounds **III** and **IV** were obtained by X-ray diffraction. It was established, that their crystals consists of complex mononuclear cations $[Fe(H_2L^1)(H_2O)_2]^{3+}$ and $[Fe(H_2L^2)(H_2O)_2]^{3+}$, NO_3^- anions and solvated water molecules. The polyhedral coordination of Fe(III) consists of pentagonal bipyramids formed by N_3O_2 donor atoms set of pentadentate neutral ligands H_2L^1/H_2L^2 and two oxygen atoms of the coordinated H_2O molecules (Figures 1 and 2).

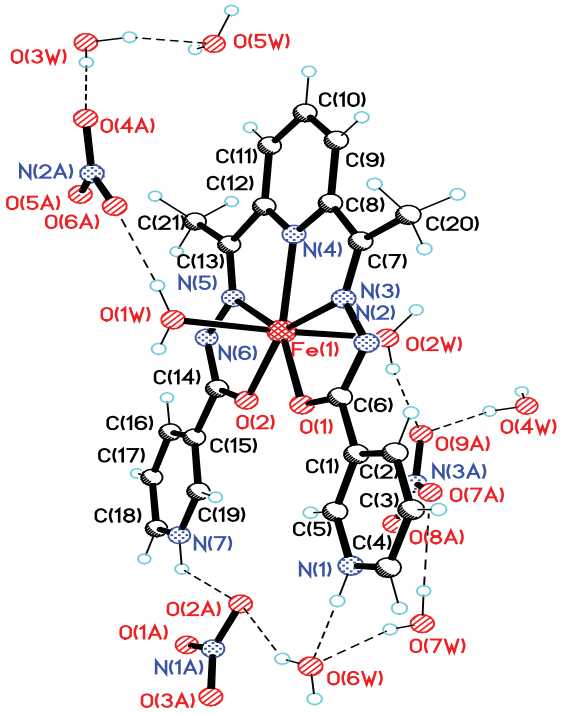

Figure 1. View of formula unit of III with numbering scheme.

The interatomic distances metal-ligand (H_2L^1/H_2L^2) in the equatorial plane are: Fe(1)−O(1) 2.033(2)/2.087(3) Å, Fe(1)−O(2) 2.029(2)/2.043(3) Å, Fe(1)−N(3) 2.194(3)/2.176(3) Å, Fe(1)−N(4) 2.188(3)/2.203(3) Å, Fe(1)−N(5) 2.194(3)/2.187(3) Å, while metal - apical atoms distances are – Fe(1)−O(1W) 2.036(2)/2.035(3) Å, Fe(1)−O(2W)

2.035(2)/ 2.028(3) Å (Table 2). The obtained values of the interatomic distances do not differ from those found in the complex diaqua-(2',2'''-(2,6-pyridinediyldiethylidyne)dioxamohydrazide)-iron(III) perchlorate hydrate [27,28]. In the Cambridge Structural Database 47 hits on structures of compounds of transition metals with ligands of this class are reported [29], mainly manganese or cobalt compounds, only 6 of them being iron compounds [27-33].

The analysis of the geometry of the ligands H_2L^1/H_2L^2 in **III** and **IV** shows that they are flat and four articulated pentametallocycles are formed as a result of their coordination to the metal in the equatorial plane. Two of the metallocycles are formed by the atoms OCNNFe, and two- by NCCNFe. Herewith, the values of dihedral angles between the formed metallocycles are in the range 1.1 – 5.7° in **III** and 0.4 – 2.2° in **IV**. In the same interval are the values of the dihedral angles between the coordinated atoms N_3O_2 of the ligand H_2L and the planes of the terminal pyridine rings, and between the terminal pyridine rings (2.9, 2.0, 5.3, 3.4° in **III** and 2.6, 3.0, 13.0, 13.5° in **IV**).

The analysis of positioning the hydrogen atoms from the ligands H_2L^1/H_2L^2 demonstrated the proton transfer from the N(2) and N(6) atom position to the N(1) and N(7) atoms. These conclusions are based both on the analysis of Fourier synthesis and geometrical considerations (distances N···O).

In the crystal of compound **III** the complex cation $[Fe(H_2L^1)(H_2O)_2]^{3+}$ is bound to anions (NO_3^-) through the hydrogen bonds N(7)–H···O(1A), O(1W)–H···O(6A) and N(7)–H···O(1A), O(1W)–H···O(6A) (Figure 3, Table 3). The molecules of the water of crystallization involved in hydrogen bonds both as the donor and the acceptor, contribute to the formation of a complex system of bonds that connect the components in the crystal. The 3D network from the crystal is also determined by the participation of O atoms from the inorganic NO_3^- anions to the formation of hydrogen bonds as the acceptor.

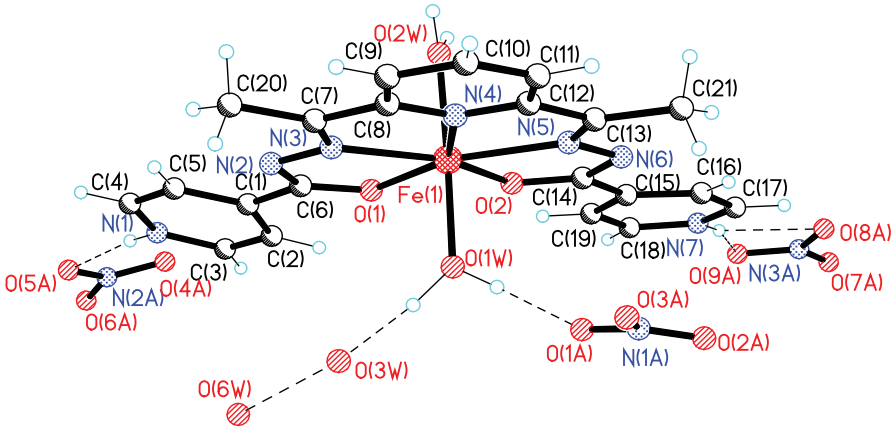

Figure 2. View of formula unit of IV with numbering scheme.

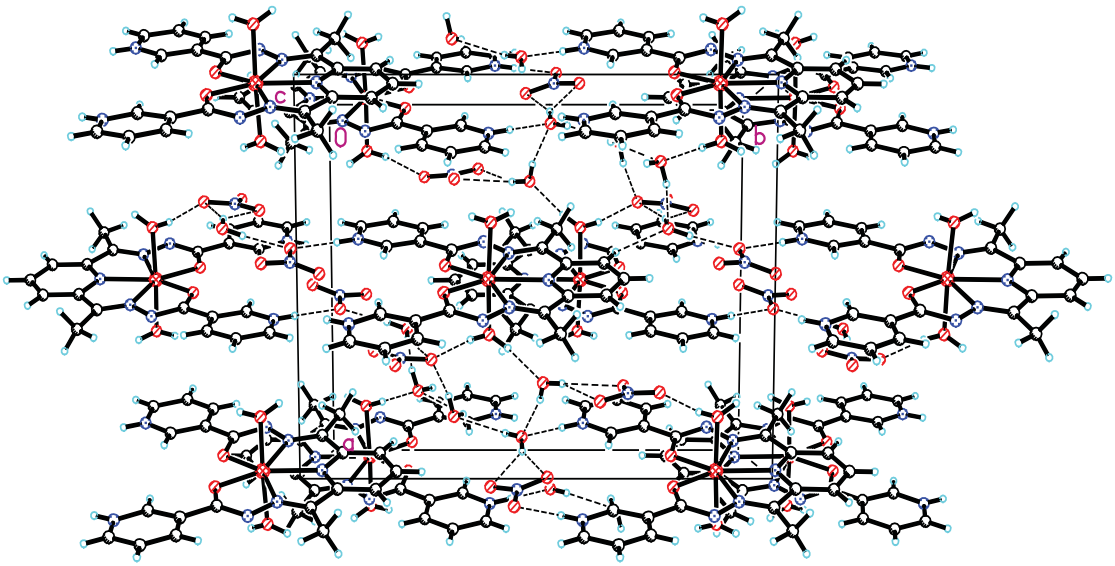

Figure 3. A fragment of crystal packing in III.

In the crystal of **IV** the complex cation $[Fe(H_2L^2)(H_2O)_2]^{3+}$ is connected to the anion (NO_3^-) through the hydrogen bonds N(1)–H···O(5A), N(7)–H···O(8A), N(7)–H···O(9A), O(1W)–H···O(1A), O(2W)–H···O(2A)* and O(2W)–H···O(3A)* (Figure 4, Table 3). In addition, the complex cations are bound to each other through the hydrogen bonds of the type O(2W)–H···O(2)*. The molecules of the water of crystallization involved in hydrogen bonds both as the donor and the acceptor, contribute to the formation of a complex system of bonds that connect the components in the crystal. The 3D network from the crystal is also determined by the participation of O atoms from the inorganic NO_3^- anions to the formation of hydrogen bonds as the acceptor. In the crystal, centrosymmetric clusters of four molecules of water of crystallization and two NO_3^- anions (N(3A), O(3W) and O(6W)) can be seen.

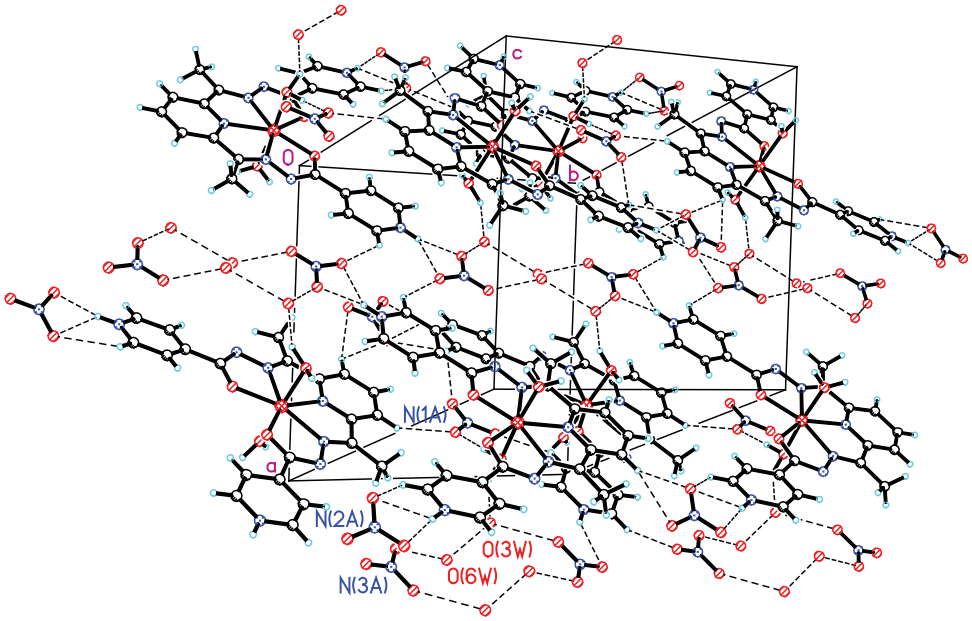

Figure 4. A fragment of crystal packing in IV.

Microbiology

The influence of iron(III) coordination compounds with nitrogen-containing ligands on the enzyme activity of *Aspergillus niger* CNMN FD 10 micromycete is presented in Table 4. Each type of enzyme reacted differently to the addition of the coordination compounds into the nutrient medium.

Cellobiohydrolase is an enzyme acting on the key stages of the hydrolysis of cellulose and releasing cellobiose from the non-reducing ends of the chains. In the control samples, without complexes, on the 6th day of cultivation of the producer, the activity of the enzyme was 0.14 U/mL. The maximal activity of cellobiohydrolase was observed on the 7th day of cultivation, constituting 0.18 U/mL. Coordination complexes have demonstrated an obvious inhibitory effect on the biosynthesis of cellobiohydrolase. Particularly, the inhibition increased with the raise of the concentration of compounds from 5 mg/L to 15 mg/L. Thus, on the day with the maximum biosynthesis of cellobiohydrolase (the 7th day), using compounds **II, III** and **IV** at the concentration of 5 mg/L, the enzyme activity in experimental samples constituted 0.16-0.17 U/mL, which was 5.88-12.5% lower than in the control samples (0.18 U/mL). With the augment of the concentration to 15 mg/L the activity of cellobiohydrolase decreased to 0.11-0.12 U/mL, *i.e.* it was 39-40% lower, as compared to the control. Compound **I** showed the greatest inhibitory effect, reducing the enzyme activity to zero in the concentration of 15 mg/L. On the next days (8th and 9th) the inhibitory effect was maintained.

β-Glucosidase is an enzyme acting at the final stages of cellulose hydrolysis, which cleaves cellobiose (formed after the action of cellobiohydrolase) to glucose. This enzyme reacted less to the addition of coordination compounds in the growth medium, in comparison with cellobiohydrolase.

In the control samples the activity of *β*-glucosidase on the 6th day of cultivation was 2.47 U/mL. The maximal activity of *β*-glucosidase was observed on the 7th day, being 2.80 U/mL. On the 8th day the enzyme activity decreased insignificantly till 2.59 U/mL. On the 9th day a sharp decrease in activity of *β*-glucosidase to 1.69 U/mL was observed.

Table 4

The effect of iron(III) coordination compounds on the enzyme activity (U/mL) of *Aspergillus niger* CNMN FD 10 micromycete.

Compound	*Conc., mg/L*	*Cellobiohydrolase*				*β-Glucosidase*				*Endoglucanase*				*Xylanase*			
		6th day	*7th day*	*8th day*	*9th day*	*6th day*	*7th day*	*8th day*	*9th day*	*6th day*	*7th day*	*8th day*	*9th day*	*6th day*	*7th day*	*8th day*	*9th day*
$[Fe(dig)]Cl_3 \cdot 2H_2O$ **(I)**	5	0.08	0.07	0.0	0.03	2.23	2.36	2.09	1.47	4.08	4.41	4.04	3.91	50.59	52.24	56.16	32.64
	10	0.05	0.0	0.0	0.02	2.08	1.67	2.06	1.36	3.34	4.57	3.51	3.59	47.87	46.78	56.57	32.64
	15	-	0.0	0.0	0.0	1.75	1.82	1.45	1.33	2.81	2.45	3.18	2.20	29.92	29.38	37.53	31.55
$[Fe(HL)SO_4]$ **(II)**	5	0.11	0.16	0.06	0.04	2.28	2.55	2.53	1.63	3.92	4.89	5.06	4.89	52.22	65.28	71.80	39.17
	10	0.07	0.15	0.06	0.03	2.21	2.42	2.55	1.41	4.41	4.73	4.89	3.91	45.69	52.22	52.22	39.17
	15	0.065	0.12	0.01	0.08	2.21	2.39	2.28	1.30	4.08	3.91	4.24	3.67	53.31	41.34	50.05	34.82
$[Fe(H_2L^1)(H_2O)_2](NO_3)_3 \cdot 5H_2O$ **(III)**	5	0.11	0.16	0.07	0.03	2.28	2.66	2.43	1.55	4.73	5.06	5.38	4.49	35.90	69.63	50.05	39.17
	10	0.05	0.11	0.01	0.06	2.23	2.51	2.40	1.41	4.73	5.06	5.14	4.24	31.55	68.54	46.78	27.20
	15	0.03	0.11	0.00	0.01	2.21	2.55	2.28	1.25	4.08	4.89	5.14	3.51	29.38	65.28	38.08	26.12
$[Fe(H_2L^2)(H_2O)_2](NO_3)_3 \cdot 1.5H_2O$ **(IV)**	5	0.07	0.17	0.07	0.07	2.43	2.55	2.47	1.63	3.92	4.57	4.73	4.41	29.38	65.28	65.28	22.85
	10	0.05	0.11	0.07	0.07	2.43	2.51	2.43	1.63	3.75	4.41	4.73	4.08	21.76	60.92	54.40	21.76
	15	0.04	0.12	0.07	0.06	2.36	2.39	2.28	1.36	3.42	3.67	4.08	3.67	28.29	45.69	42.43	21.76
Control	-	0.14	0.18	0.10	0.10	2.47	2.80	2.59	1.69	4.98	5.55	5.66	5.55	53.31	78.33	77.25	43.88

The use of coordination compounds at the lowest concentration (5 mg/L) showed the *β*-glucosidase activity of 2.23-2.43 U/mL (on the 6th day), 2.36-2.66 U/mL (on the 7th day), 2.09-2.53 U/mL (on the 8th day) and 1.47 - 1.63 U/mL (on the 9th day). Comparison with the control samples revealed that the inhibitory effect was not significant. With the elevation of the concentration of compounds to 15 mg/L, the activity of *β*-glucosidase decreased more, however, the enzyme activity of compounds **II**, **III** and **IV** did not exceed 20%. The greatest inhibitory effect both on the biosynthesis of *β*-glucosidase and cellobiohydrolase was shown by the iron complex **I**, containing chloride ions and dig-ligand. At the concentration of 15 mg/L the activity of *β*-glucosidase constituted: 1.75 U/mL (control - 2.47 U/mL) – on the 6th day, 1.82 U/mL (control - 2.80 U/mL) – on the 7th day; 1.45 U/mL (control - 2.59 U/mL) – on the 8th day, which was 41.14%; 53.85% and 78.62% lower than the activity in the control samples, respectively.

Endoglucanases are enzymes that hydrolyze cellodextrins and cellulose derivatives, such as CMC (carboxymethyl cellulose). In the control samples the activity of endoglucanase varied insignificantly– 5.55 - 5.66 U/mL on the 7th-9th days of cultivation with maximal activity on the 8th day. As in the case of cellobiohydrolase and β-glucosidase, all tested complexes demonstrated an inhibitory effect, which enhanced with the increase of the concentration of compounds, regardless of the culture period. Thus, in the day of the maximal activity of the endoglucanase (the 8th day) it decreased depending on the complex and the applied concentration (from 5 mg/L to 15 mg/L) from 5.38 U/mL to 3.18 U/mL. The lowest inhibitory effect was noted in the presence of compound **III**: the enzyme activity decreased from 5.38 U/mL to 5.14 U/mL. The highest inhibitory effect was registered in the presence of compound **I**: the enzyme activity dropped from 4.04 U/mL to 3.18 U/mL.

Similar results were obtained for xylanase, enzyme that decomposes hemicellulose, one of the major components of plant cell walls. In the control samples the maximal activity of the xylanase was on the 7th and 8th days, constituting 78.33 U/mL and 77.25 U/mL, respectively. On the 9th day xylanase activity decreased to 43.88 U/mL. Similarly to the afore-discussed enzymes, the inhibitory effect of all studied coordination compounds raised with the increase of the concentration, regardless of the culture period. For example, on the 7th day of cultivation, xylanase activity decreased, depending on the composition of the complex and the concentration (from 5 mg/L to 15 mg/L) from 69.63 U/mL to 41.34 U/mL, as compared to the activity of xylanase in the control samples of 78.33 U/mL. As in the case of the endoglucanase, the weakest inhibitory effect was shown by complex **III** and the greatest- at the use of complex **I**.

The properties of the investigated iron(III) coordination compounds with different ligands (especially, complex **I**) to inhibit the biosynthesis of cellulases and xylanase at *Aspergillus niger* CNMN FD 10 micromycete suggests the possibility of their use in plant protection, namely in the diseases caused by microscopic fungi of the genus *Aspergillus*.

Conclusions

Iron(III) complexes with Schiff bases with 2,6-diacetylpyridine-bis(nicotinoylhydrazone) and 2,6-diacetylpyridine-bis(isonicotinoylhydrazone) and complexes with semicarbazide diacetic acid dihydrazide and sulfadiazine, have demonstrated biologic activity. The Schiff bases coordinate to iron(III) as pentadentate ligands, forming coordination compounds with pentagonal bipyramidal molecular structure, their base being composed of neutral molecule of the Schiff base that are coordinated *via* the set of the N_3O_2 donor atoms, and the water molecules localized on its peaks.

All tested Fe(III) complexes with nitrogen-containing ligands, caused an inhibitory effect on the biosynthesis of hydrolases at *Aspergillus niger* CNMN FD 10, which increased with the raise of concentration.

Coordination compounds showed different effects on the biosynthesis of the enzymes synthesized by *Aspergillus niger* CNMN FD 10 micromycete, due to the different specificity of action of these hydrolases: complexes largely inhibited cellobiohydrolase and less - *β*-glucosidase. The inhibitory effect on the endoglucanase and xylanase was approximately the same.

The greatest inhibitory effect was demonstrated by $[Fe(dig)]Cl_3 \cdot 2H_2O$ (**I**), containing chloride ion and semicarbazide diacetic acid dihydrazide, the lowest inhibitory effect was shown by $[Fe(H_2L^1)(H_2O)_2](NO_3)_3 \cdot 5H_2O$ (**III**), containing the Schiff base 2,6-diacetylpyridine bis(nicotinoylhydrazone) and NO_3^- anions.

References

1. Ciloci, A.; Bivol, C.; Stratan, M.; Reva, V., Clapco, S.; Tiurin, J.; Rija, A.; Coropceanu, E. The effect of $[Co(DH)_2(An)_2]_2[TiF_6] \cdot 3H_2O$ coordination compound on polypeptide spectrum of amylolytic preparation from *Aspergillus niger* 33-19 CNMN FD 02a strain. The Annals of Oradea University, Biology Fascicle, 2012, 19(2), pp. 128-132.
2. Clapco, S.; Bivol, C.; Ciloci, A.; Stratan, M.; Coropceanu, E.; Tiurin, J.; Rija, A.; Labliuc, S.; Bulhac, I. The effect of some metal complexes of oxime ligands on proteolytic activity of *Fusarium gibbosum* CNMN FD 12 strain. The Annals of Oradea University, Biology Fascicle, 2013, 20(1), pp. 53-58.

3. Deseatnic-Ciloci, A.; Tiurina, J.; Ciapurina, L.; Turta, C.; Bivol, C.; Clapco, S.; Dvornina, E.; Labliuc, S. Coordination compounds of copper with aminoacids as potential stimulators of micromycetes extracellular hydrolases biosynthesis. Priorities of Chemistry for a Sustainable Development, PRIOCHEM, Bucharest, Romania, 2013, pp. 119-121.
4. Bourosh, P.; Coropceanu, E.; Ciloci, A.; Clapco, S.; Bologa, O.; Bivol, C.; Tiurina, J.; Bulhac, I. New Co(III) dioximates with hexafluorophosphate ion as stimulators of the proteolytic activity of the micromycete *Fusarium gibbosum* CNMN FD 12. Russian Journal of Coordination Chemistry, 2013, 39(11), pp. 777-786.
5. Coropceanu, E.; Deseatnic, A.; Stratan, M.; Rija, A.; Bologa, O.; Tiurin, J.; Labliuc, S.; Clapco, S.; Bulhac, I. The study of the biological activity of some cobalt(III) dioximates with fluorine containing anions. Chemistry Journal of Moldova, 2008, 3(2), pp. 70-80.
6. Dulcevscaia, G.; Kravtsov, V.; Macaev, F.; Duca, Gh.; Stingachi, E.; Pogrebnoi, S.; Boldescu, V.; Clapco, S.; Tiurina, J.; Deseatnic-Ciloci, A.; Lipkowski, J.; Liu, S.-X.; Decurtins, S.; Baca, S. New copper(II) complexes with isoconazole: synthesis, structures and biological properties. Polyhedron, 2013, 52, pp. 106-114.
7. Bivol, C.; Lazarescu, A.; Turta, C.; Rudic, V. Action of some coordinative compounds of Fe(III) with α-aminoacids on photosynthetical pigments content in microalgae *Dunaliella salina* CVNMN-AV-01. Journal of Academy of Sciences of Moldova. Life sciences, 2012, 3(317), pp. 149-154. (in Romanian).
8. Rudic, V.; Cepoi, L.; Rudi, L.; Miscu, V.; Chiriac, T.; Cojocari, A.; Lozan, V.; Coropceanu, E.; Bologa, O. Influence of coordinative compounds of cobalt with dioximates on biosynthetical processes in red alga *Porphiridium cruentum*. Journal of Academy of Sciences of Moldova. Life sciences, 2012, 1(316). pp. 144-151. (in Romanian).
9. Rudi, L.; Cepoi, L.; Miscu, V.; Chiriac, T.; Valuta A.; Codreanu, S.; Sadovnic, D.; Rudic, V. Biomass and carotenoid production by green alga Haematococcus pluvialis during the life cycle under the influence of Co(II) Schiff base complexes. Journal of Academy of Sciences of Moldova. Life sciences, 2014, 2(323), pp. 163-171. (in Romanian).
10. Valuta, A.; Cepoi, L.; Rudi, L.; Bulhac, I.; Bourosh, P.; Bologa, O. Phycobiliprotein accumulation in cyanobacterium *Nostoc linckia* and modification of antioxidant activity. The Annals of Oradea University, Biology Fascicle, 2015, 22(1), pp. 13-19.
11. Ciobanica, O.; Bourosh, P.; Bologa, O.; Bulhac, I.; Lozan, V.; Shofransky, V. Synthesis and crystal structure of a new Fe(ii) α-dioximate with triazine. Chemistry Journal of Moldova, 2013, 8(1), pp. 78-82.
12. Usatii, A.; Topala, L.; Chirita, E. Calcatiniuc, A., Borisova, T. Productivity, lipidogenesis and carotinogensis of yeast *Rhodotorula gracilis* CNM-YS-III/20 at the cultivation in presence of coordinative compounds of Mo(IY), Cr(III), Co(III), V(V). Journal of Academy of Sciences of Moldova. Life sciences, 2003, 1, pp. 99-103. (in Romanian).
13. Vomisescu, C.; Bourosh, P.; Kravtsov, V.; Dragancea, D. Nickel(II) complex derived from 2-hydroxy-3-methoxybenzaldehyde semicarbazone and 2,2'-bipyridine. Chemistry Journal of Moldova, 2013, 8(2), pp. 78-82.
14. Ciloci, A.; Tiurina, J.; Bologa, O.; Clapco, S.; Labliuc, S.; Pasha, L.; Coropceanu, E.; Rija, A. Coordinative compounds of Mo and V as possible stimulators of biosynthesis of exocellular cellulases of micromycete *Penicillium expansum* CNMN FD 05 C. Journal of Academy of Sciences of Moldova. Life sciences, 2012, 3(318), pp. 158-165. (in Russian).
15. Lemenovschi, D.A. Metalic composition in nature. Soros Educational Journal, 1997, 9, pp. 48-54. (in Russian).
16. Ershov, Iu.A.; Pletneova, T.V. The chemistry of biogenic elements. Vysshaja shkola: Moscow, 1993, 560 p. (in Russian).
17. Verejan, A.V. Coordination compounds of transition metals with semicarbazide diacetic acid and its derivatives. Ph.D. Thesis, A.V. Bogatskii Physico-Chemical Institute, Ukrainian Academy of Sciences, Odessa, Ukraine, 1991. (in Russian).
18. Gerbeleu, N.V.; Verejan, A.V.; Byrca, M.C.; Turta, C.I.; Lozan, V.I.; Bologa, O.A. Mössbauer spectra of coordination compounds of iron(III) with semicarbazide diacetic acid and its dihydrazide. Proceedings of the VIth Conference on Spectroscopy of Coordination Compounds, Krasnodar, Russia, 1990, p. 170. (in Russian).
19. Sheldrick, G.M. A short history of SHELX. Acta Crystallographica, 2008, A64 (1), pp. 112-122.
20. Ciloci, A.; Tiurina, J.; Clapco, S.; Labliuc, S.; Stratan, M.; Grumeza, M. Fungal strain *Aspergillus niger* – producer of cellulozolytic and xylanolytic enzymes. MD Patent, 2010, No. 4072. (in Romanian).
21. Haritonov, Iu.Y.; Machoshvili, R.I.; Gogorishvili, P.V.; Shamilishvili, O.H. Investigation of metal coordinative complexes with oxalyl dihydrazide by IR spectroscopy. Russian Journal of Inorganic Chemistry, 1972, 17(11), pp. 2992-2995. (in Russian).
22. Haritonov, Iu.Y.; Machoshvili, R.I.; Goeva, L.V.; Scelokov, R.N. Metal coordinative compounds with diformyl hydrazine. Russian Journal of Coordinative Chemistry, 1975, 1(3), pp. 333-341. (in Russian).
23. Nakamoto, K. IR spectra and Raman spectra of inorganic and organic coordinative compounds. Mir: Moscow, 1991, 536 p. (in Russian).
24. Nakanisi, K. Infrared spectra and structure of organic compounds. Mir: Moscow, 1965, 216 p. (in Russian).
25. Bellami, L. Infrared spectra of complex molecules. IL: Moscow, 1963, 590 p. (in Russian).

26. Tarasevici, B.N. Infrared spectra of basic class of organic compounds. Reference materials. Moscow, 2012, 54 p. (in Russian).
27. Andjelkovic, K.; Bacchi, A.; Pelizzi, G.; Jeremic, D.; Ivanovic-Burmazovic, I. Diaqua-(2',2'''-(2,6-pyridinediyldiethylidyne)dioxamohydrazide)-iron(III) perchlorate hydrate WUTPIK. Journal of Coordination Chemistry, 2002, 55, pp. 1385-1392.
28. Palenik, G.J.; Wester, D.W.; Rychlewska, U.; Palenik, R.C. Pentagonal-Bipyramidal Complexes. Synthesis and crystal structures of Diaqua[2,6-diacetylpyridine bis(semicarbazone)]chromium(III) hydroxide dinitrate hydrate and Dichloro[2,6-diacetilpyridine bis(semicarbazone)]iron(III) chloride dehydrate. Inorganic Chemistry, 1976, 15(8), pp. 1814-1819.
29. Allen, F.H. Cambridge structural database. Acta Crystallographica, 2002, 58B(3-1), pp. 380-388.
30. Palenik, G.J.; Wester, D.W. Pentagonal-Bipyramidal complexes. Crystal and molecular structures of chloroaqua(2,6-diacetylpyridine bis(semicarbazone))manganese(II),-iron(II),-cobalt(II), and –zinc(II) chloride dehydrates. Inorganic Chemistry, 1978, 17(4), pp. 864-870.
31. Bonardi, A.; Carini, C.; Merlo, C.; Pelizzi, C.; Pelizzi, G.; Tarasconi, P.; Vitali, F.; Cavatorta F. Synthesis, spectroscopic and structural characterization of mono- and bi-nuclear iron(II) complexes with 2,6-diacetylpyridine bis(acylhydrazones). Journal of the Chemical Society. Dalton Transactions, 1990, pp. 2771-2777.
32. Gao-Feng, Liu; Filipovic, M.; Heinemann, F.W.; Ivanovic-Burmazovic, I. Diaqua-(2,6-diacetylpyridinebis(semiox amazide)-N,N',N'',O,O')-iron(II) dinitrate monohydrate TIRFAC. Inorganic Chemistry, 2007, 46, pp. 8825-8835.
33. Bar, A.K.; Pichon, C.; Gogoi, N.; Duhayon, C.; Ramasesha, S.; Sutter J. Single-ion magnet behavior of heptacoordinated Fe(II) complexes: on the importance of supramolecular organization. Chemical Communications, 2015, 51(17), pp. 3616-3619.

SYNTHESIS OF NEW DRIMANE AND HOMODRIMANE LACTAMS BY BECKMANN REARRANGEMENT OF SOME KETOXIMES

Elena Secara

Institute of Chemistry of the Academy of Sciences of Moldova, 3 Academiei str., Chisinau MD-2028, Republic of Moldova
e-mail: esecara8@gmail.com

Abstract. The synthesis of new drimane and homodrimane lactams, derivatives of octahydro-1H-benzo[d]azepine and octahydro-1H-benzo[c]azepine, from norambreinolide is reported. Those compounds were prepared by the Beckmann rearrangement of the corresponding ketoximes.

Keywords: drimane, homodrimane, lactam, ketoxime, synthesis, Beckmann rearrangement.

Received: March 2016/ Revised final: April 2016/ Accepted: May 2016

Introduction

Many drimane and homodrimane sesquiterpenoids, including those with nitrogen, exhibit various types of a biological activity: antifungal, antibacterial, antiviral, cytotoxic, antifeedant, etc. [1]. Therefore, the development of synthetic methods for these compounds is of a scientific and practical importance.

In a search for new biologically active compounds and in continuation of our group's investigations of obtaining nitrogen-containing sesquiterpenoids [2-5], in the present paper the synthesis of new drimane and homodrimane lactams by the Beckmann rearrangement of some ketoximes is described.

Earlier Grant *et al.* reported the preparation of amides **1-4** by the Beckmann rearrangement of *Z*- and *E*- isomers of oxime **5** obtained from 14,15-dinorlabd-8(17)-en-13-one **6** [6]. Then, Barrero *et al.* described a multi-step synthesis of amide **7** from (-)-sclareol [7]. Later, amides **8** and **9** were synthesized by the Beckmann rearrangement of oxime **10** of 11-dihomodriman-8α-ol-12-one **11** [8] (Figure 1).

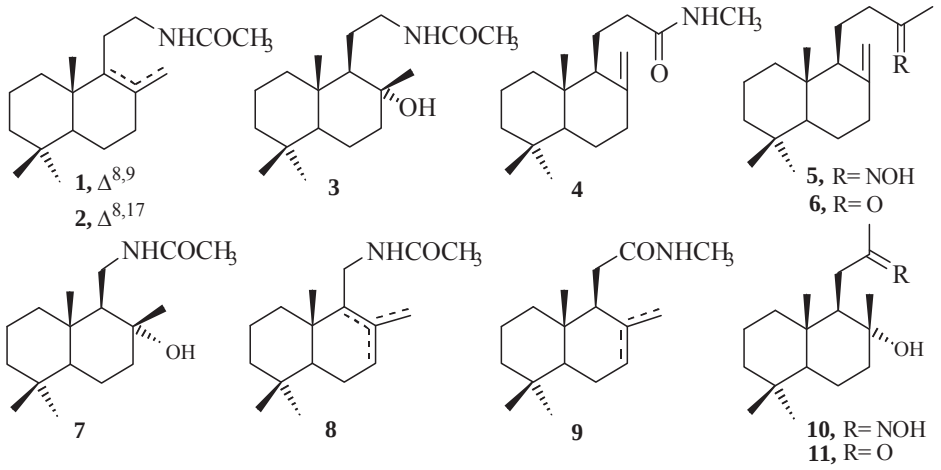

Figure 1. Tri-, tetra- and pentanorlabdane amides obtained by the Beckmann rearrangement and their precursors.

The Beckmann rearrangement is known to occur stereospecifically as a result of anti-migration of the bulkier radical. Therefore, it has been expected that the major product of the Beckmann rearrangement of oxime **10** would be amide **7**. However, in the case of oxime **10**, amide **9** is obtained as a result of the migration of CH_3- group and concomitant dehydration.

Recently, Kharitonov *et al.* have obtained a mixture of isomeric furanolactams, derivatives of octahydro-1H-benzo[d]azepine **12** and octahydro-1H-benzo[c]azepines **13** and **14** by the Beckmann rearrangement of the respective 7-oxo-phlomisoic acid ketoxime **15** and its methyl ester **16** (Figure 2) [9].

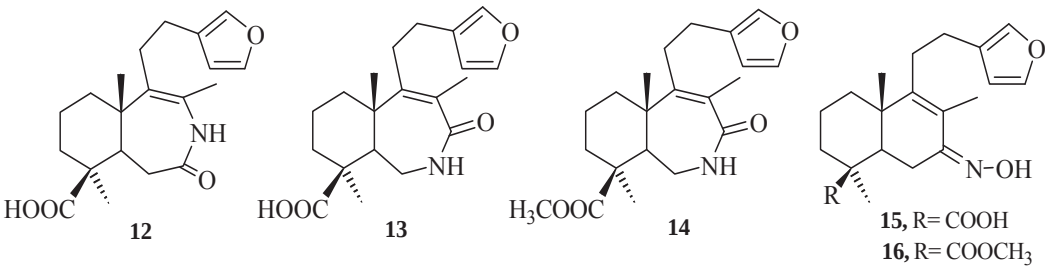

Figure 2. Furanolactams obtained by the Beckmann rearrangement of 7-oxo-phlomisoic acid ketoximes and their precursors.

Results and discussion

Herein, the synthesis of new drimane and homodrimane lactams **17-21** by the Beckmann rearrangement of the corresponding oximes **22** and **23** is described. Oximes **22** and **23** have been obtained earlier [10] from the commercially available norambreinolide **24** according to the procedure [11].

The treatment of ketoxime **22** with thionyl chloride in anhydrous dioxane according to the literature procedure [9,12] resulted in a mixture of isomeric lactams **17** and **19**. The Beckmann rearrangement of oxime **23** under these conditions gave a mixture of lactams **20** and **21** (Scheme 1).

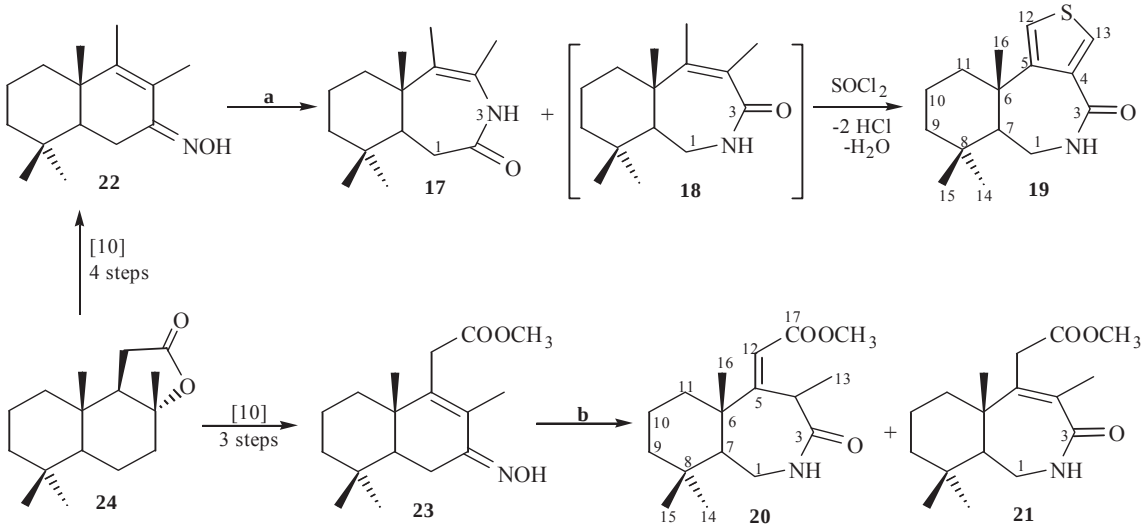

Scheme 1. Synthesis of new drimane and homodrimane lactams.
Reagents and conditions: a) $SOCl_2$, dioxane, 50-60 °C, 9h; b) $SOCl_2$, dioxane, 60-65 °C, 17 h.

It is very likely that thiophenolactam **19** is formed as a result of the interaction of the intermediate lactam **18** with thionyl chloride. The presence of the *α,β*–unsaturated carbonyl group in the molecule of lactam **18** activated the methyl groups and promoted the reaction of lactam **18** with thionyl chloride.

It is known that the analogous reactions of *o*-toluidine and ring-substituted *o*-toluidines **25** with thionyl chloride in xylene at reflux temperature yield 2,1-benzisothiazoles **26** (Scheme 2) [13].

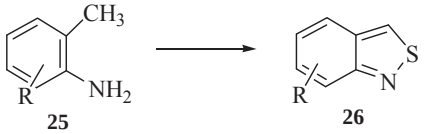

Scheme 2. Synthesis of 2,1-benzisothiazoles from *o*-toluidines.
Reagents and conditions: $SOCl_2$/xylene, reflux.

The structures of all new compounds were confirmed by the IR, ^{1}H, ^{13}C, ^{15}N- NMR spectral data and by elemental analysis.

The NMR data of compound **20** have been assigned (Figures 3, 4) on the base of their 1D (^{1}H, ^{13}C, DEPT-135°) and 2D homo- ($^{1}H/^{1}H$ COSY-45°, $^{1}H/^{1}H$ NOESY) and heteronuclear ($^{1}H/^{13}C$ HSQC, $^{1}H/^{15}N$ HMQC and $^{1}H/^{13}C$ HMBC, $^{1}H/^{15}N$ HMBC) correlation spectra. According to the NMR spectral data, compound **20** is a homodrimane lactam. An analysis of ^{1}H, ^{13}C, $^{1}H/^{1}H$ COSY and $^{1}H/^{13}C$ HSQC NMR spectra suggested the presence of three isolated spin systems: $CH_2CH_2CH_2$ (C-11 to C-9), $CHCH_2NH$ (C-7 to NH), and $CHCH_3$ (C-4 to C-13) (Figure 3). Key $^{1}H/^{13}C$ HMBC and $^{1}H/^{15}N$ HMBC correlations for lactam **20** are also depicted in Figure 3. The rearranged carbon framework of compound **20** becomes obvious at a detailed analysis of its $^{1}H/^{13}C$ HMBC spectrum. Thus, the observed correlations from H-12 to sp^2 hybridized carbon (C-5, δ_C 169.9) are indicative for the $\Delta^{5(12)}$ localization, which was supported also by the correlations H-12/C-4 and H-12/C-6. A signal of a lactam nitrogen atom has been found at δ_N 110 ppm in the $^{1}H/^{15}N$ HMQC spectrum, while its proton resonates at δ_H 5.93 ppm as a broad triplet with $J = 5.8$ Hz. The position of lactam has been corroborated by both $^{1}H/^{15}N$ HMBC and $^{1}H/^{13}C$ HMBC spectra. Thus, the H-7/N-2 cross-peak in the $^{1}H/^{15}N$ HMBC spectrum, as well as H_3-13/C_3, H_3-13/C_4 and H_3-13/C_5 in the $^{1}H/^{13}C$ HMBC spectrum, prove the localization of a lactam function as depicted in Figure 3.

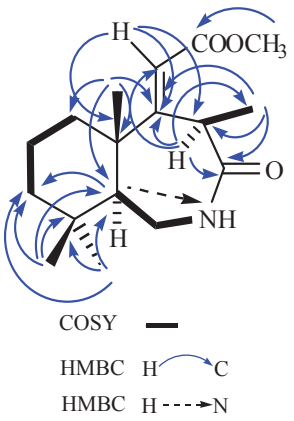

Figure 3. Key COSY and HMBC correlations in lactam 20.

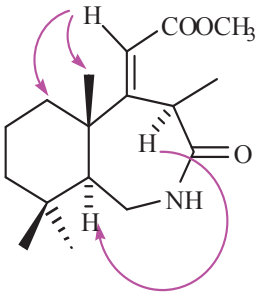

Figure 4. Key NOESY correlations in lactam 20.

The migration of a double bond $\Delta^{4(5)}$ in precursor **23** to $\Delta^{5(12)}$, as a result of the reaction, has additionally generated two centres of isomerism: a geometrical centre at C-5/C-12 and an optical one at C-4. The NOESY correlations between H-12 and H_3-16, as well as H-12 and H-11, demonstrate the *trans* nature of the isomer at $\Delta^{5(12)}$. The NOESY correlation between H-4 and H-7 indicates that they are in the α-plane and determines the *(R)* relative configuration at C-4 (Figure 4).

Conclusion

New drimane and homodrimane lactams, derivatives of octahydro-1H-benzo[d]azepine and octahydro-1H-benzo[c]azepine, which are of a scientific and practical importance as compounds with a potential biological activity, were synthesized.

Experimental

General experimental procedure

Melting points (m.p.) have been determined on a Boetius heating stage and were not corrected. The IR spectra have been recorded on a Perkin-Elmer Spectrum 100 FT-IR spectrometer. The NMR spectra have been recorded on a Bruker 400 Avance III spectrometer at 400.13 MHz for ^{1}H, 100.62 MHz for ^{13}C and 40.55 MHz for ^{15}N in $CDCl_3$, with tetramethylsilane (TMS) as an internal standard. Proton chemical shifts (δ) are reported in parts per million (ppm) and are compared against the residual non-deuterated solvent peak (7.26 ppm for $CHCl_3$ of $CDCl_3$). Chemical shifts of carbon atoms (δ) are reported in ppm and are compared against the deuterated solvent peak (77.00 ppm for ^{13}C of $CDCl_3$) and relative to $MeNO_2$ in the ^{15}N NMR spectra. Coupling constants (J) are recorded in Hertz. Signals in the ^{1}H and ^{13}C NMR spectra have been assigned using the DEPT-135, $^{1}H/^{1}H$ COSY-45, $^{1}H/^{13}C$ HSQC, $^{1}H/^{13}C$ HMBC, and $^{1}H/^{1}H$ NOESY experiments whereas the $^{1}H/^{15}N$ HMBC experiments have been used for the assignment of the ^{15}N nuclei chemical shift. The course of reactions has been monitored by the TLC on Silufol plates with the detection by I_2 vapours. The column chromatography has been performed on Silica Gel (L 70-230 mesh Fluka). Chemicals have been

of commercially available reagent grades being used without further purification. All solvents have been purified and dried by standard techniques before use.

Beckmann rearrangement of oxime 22

A solution of oxime **22** (200 mg, 0.849 mmol) in anhydrous dioxane (10 mL) has been cooled in an ice bath and treated dropwise with freshly distilled $SOCl_2$ (0.185 mL). Then the reaction mixture has been heated at 50-60°C for 9 h, cooled, diluted with H_2O (100 mL), and extracted with Et_2O (3x50 mL). The extract has been washed with water (3x20 mL) and dried over anhydrous $MgSO_4$. The evaporation of the solvent under a reduced pressure gives the crude product (220 mg) which has been chromatographed on a column of silica gel (7 g). The elution with a mixture of EtOAc/light petroleum ether (1:1) gives pure lactam **19** (105 mg, 53 %) as white solid. The elution with EtOAc gives lactam **17** (7.3 mg, 4 %) as oil.

4,5,14,15,16-Pentamethyl-2-oxo-2,3,6,7,8,9,10,11-octahydro-1H-benzo[d]azepine (17). Calculated, % for $C_{15}H_{25}NO$: C 76.54, H 10.70, N 5.95. Found, %: C 76.51, H 10.67, N 5.93. IR (ν, cm^{-1}): 3329, 2924, 2863, 1647, 1605, 1497, 1460, 1392, 1377, 1354, 1304, 1129, 1036, 893, 819, 774, 716. ^{1}H NMR (δ, ppm): 0.88 (3H, s, CH_3-14), 0.94 (3H, s, CH_3-15), 1.19 (3H, s, CH_3-16), 1.47 (1H, t, J=3.8, J=3.66, H-7), 1.74 (3H, d, J=1, CH_3-12), 1.90 (3H, d, J=0.96, CH_3-13), 3.08-3.11 (2H, m, H-1a, H-1b). ^{13}C NMR (δ, ppm): 17.91 (q, C-12), 18.58 (q, C-13), 18.76 (t, C-10), 20.88 (q, C-16), 22.39 (q, C-15), 33.27 (q, C-14), 34.40 (s, C-8), 38.09 (t, C-11), 39.27 (t, C-1), 40.83 (t, C-9), 45.59 (s, C-6), 58.22 (d, C-7), 124.7 (s, C-4), 151.64 (s, C-5), 174.49 (s, C-2). ^{15}N NMR (δ, ppm): 121.0 (NH).

14,15,16-Trimethyl-4,5-(3,4-thiopheno)-3-oxo-2,3,6,7,8,9,10,11-octahydro-1H-benzo[c]azepine (**19).** M.p. 188-190°C (from $CHCl_3$ – MeOH (1:1)). Calculated, % for $C_{15}H_{23}NOS$: C 67.88, H 8.73, N 5.27, S 12.08. Found, %: C 67.85, H 8.75, N 5.25, S 12.03. IR (ν, cm^{-1}): 3323, 3133, 2924, 2862, 1645, 1606, 1496, 1461, 1392, 1377, 1354, 1304, 1129, 1036, 893, 819, 774, 724. ^{1}H NMR (δ, ppm): 0.91 (3H, s, CH_3-15), 1.03 (3H, s, CH_3-14), 1.40 (3H, s, CH_3-16), 1.69 (1H, dd, J=5.64, 2.52, H-7), 2.28 (2H, m, H-1a, H-1b), 7.05 (1H, d, J=3.72, H-12), 8.17 (1H, d, J=3.68, H-13). ^{13}C NMR (δ, ppm): 19.18 (t, C-10), 22.08 (q, C-15), 25.93 (q, C-16), 33.12 (q, C-14), 34.33 (s, C-8), 39.84 (t, C-1), 41.14 (t, C-9), 41.86 (s, C-6), 42.64 (t, C-11), 55.35 (d, C-7), 121.45 (d, C-12), 133.87 (d, C-13), 135.01 (s, C-4), 152.31 (s, C-5), 167.34 (s, C-3). ^{15}N NMR (δ, ppm): 118.0 (NH).

Beckmann rearrangement of oxime 23

A solution of oxime **23** (150 mg, 0.511 mmol) in anhydrous dioxane (7.5 mL) has been cooled in an ice bath and treated dropwise with freshly distilled $SOCl_2$ (0.180 mL). Then the reaction mixture has been heated at 60-65°C for 17 h, cooled, diluted with H_2O (75 mL), and extracted with Et_2O (3x35 mL). The extract has been washed with water (3x15mL) and dried over anhydrous $MgSO_4$. The evaporation of the solvent under a reduced pressure gives the crude product (141 mg) which has been chromatographed on a column of silica gel (7 g). The elution with a mixture of EtOAc/light petroleum ether (3:2) gives pure lactam **20** (55 mg, 37%) as white solid. The elution with EtOAc/light petroleum ether mixture (4:1) gives lactam **21** (28 mg, 19%) as oil.

5-Carbomethoxymethinyl-13,14,15,16-tetramethyl-3-oxo-2,3,6,7,8,9,10,11-octahydro-1H-benzo[c]azepine (20). M.p. 127-129°C (from MeOH). Calculated, % for $C_{17}H_{27}NO_3$: C 69.59, H 9.27, N 4.77. Found, %: C 69.57, H 9.30, N 4.74. IR (ν, cm^{-1}): 3290, 3239, 3099, 2929, 1722, 1664, 1620, 1468, 1458, 1379, 1170, 1029, 867, 769. ^{1}H NMR (δ, ppm): 0.91 (3H, s, CH_3-14), 1.01 (3H, s, CH_3-15), 1.22 (1H, td, J=13.2, 4.7, H-9a), 1.23 (1H, dd, J=6.3, 1.5, H-7α), 1.38 (3H, s, CH_3-16), 1.44 (3H, d, J=7.1, CH_3-13), 3.29 (1H, ddd, J=15.9, 6.6, 1.5, H-1a), 3.41 (1H, dd, J=15.9, 6.4, H-1b), 3.73 (3H, s, OCH_3), 4.69 (1H, q, J=7.1, H-4α), 5.84 (1H, s, H-12), 5.93 (1H, brt, J=5.8, NH). ^{13}C NMR (δ, ppm): 19.19 (q, C-16), 19.59 (t, C-10), 19.71 (q, C-13), 22.67 (q, C-15), 33.41 (q, C-14), 35.18 (s, C-8), 38.88 (t, C-11), 39.40 (t, C-1), 41.24 (d, C-4), 41.53 (t, C-9), 45.05 (s, C-6), 51.27 (q, OCH_3), 56.89 (d, C-7), 112.56 (d, C-12), 167.14 (s, C-17), 169.56 (s, C-5), 176.66 (s, C-3). ^{15}N NMR (δ, ppm): 110.0 (NH).

5-Carbomethoxymethyl-13,14,15,16-tetramethyl-3-oxo-2,3,6,7,8,9,10,11-octahydro-1H-benzo[c]azepine (21). Calculated, % for $C_{17}H_{27}NO_3$: C 69.59, H 9.27, N 4.77. Found, %: C 69.56, H 9.30, N 4.75. IR (ν, cm^{-1}): 3293, 3223, 3083, 2945, 1716, 1661, 1616, 1464, 1434, 1391, 1359, 1169, 1032, 916, 731. ^{1}H NMR (δ, ppm): 0.95 (3H, s, CH_3-14), 0.97 (3H, s, CH_3-15), 1.33 (3H, s, CH_3-16), 1.65 (1H, m, H-7), 1.89 (3H, s, CH_3-13), 3.30 (2H, s, H-12a, H-12b), 3.71 (3H, s, OCH_3), 6.07 (1H, brt, J=5.6, NH). ^{13}C NMR (δ, ppm): 17.89 (q, C-13), 18.90 (t, C-10), 22.18 (q, C-16), 22.49 (q, C-15), 33.57 (q, C-14), 34.83 (s, C-8), 35.67 (t, C-12), 38.75 (t, C-11), 39.57 (t, C-1), 40.71 (t, C-9), 44.09 (s, C-6), 52.05 (q, OCH_3), 57.13 (d, C-7), 121.90 (s, C-4), 146.43 (s, C-5), 171.73 (s, C-17), 174.69 (s, C-3). ^{15}N NMR (δ, ppm): 108.0 (NH).

Acknowledgments

I would like to thank my scientific adviser Doctor habilitate Aculina Aricu for her help and encouragement during research.

References

1. Jansen, B.J.M.; De Groot, A. Occurrence, biological activity and synthesis of drimane sesquiterpenoids. Natural Product Reports, 2004, 21, pp. 449-477.
2. Kuchkova, K.; Aricu, A.; Barba, A.; Vlad, P.; Shova, S.; Secara, E.; Ungur, N.; Zbancioc, G.; Mangalagiu, I.I. An efficient and straightforward method to new organic compounds: homodrimane sesquiterpenoids with diazine units. Synlett, 2013, 24, pp. 697 – 700.
3. Kuchkova, K.; Aricu, A.; Barba, A.; Secara, E.; Vlad, P.; Ungur, N. Synthesis of 12-amino-11-dihomodrimane sesquiterpenoids from norambreinolide. Chemistry of Natural Compounds, 2014, 50(3), pp. 458-461.
4. Kuchkova, K.; Aricu, A.; Secara, E.; Barba, A.; Dragalin, I.; Vlad, P.; Ungur, N. Synthesis of 13-amino-14,15-dinorlabd-8(9)-ene from sclareol. Russian Chemical Bulletin, International Edition, 2014, 63(9), pp. 1-3.
5. Kuchkova, K.; Aricu, A.; Secara, E.; Barba, A.; Vlad, P.; Ungur, N.; Tuchilus, C.; Shova, S.; Zbancioc, G.; Mangalagiu, I.I. Design, synthesis, and antimicrobial activity of some novel homodrimane sesquiterpenoids with a diazine skeleton. Medicinal Chemistry Research, 2014, 23, pp. 1559 – 1568.
6. Grant, P.K.; Prasad, J.S.; Rowan, D.D. Structure odour studies with nitrogen derivatives of diterpene-derived acetals. Australian Journal of Chemisty, 1983, 36(6), pp.1197-1202.
7. Barrero, A.F.; Alvarez-Manzaneda, E.J.; Chahboun, R.; Gonzalez Diaz, C. New routes to ward drimanes and nor-drimanes from (-)-sclareol. Synlett, 2000, 11, pp. 1561-1564.
8. Kuchkova, K.I.; Aricu, A.N.; Vlad, P.F.; Deleanu, C.; Nicolescu, A. Sythesis of N-containing drimane sesquiterpenoids from 11-dihomodriman-8α-ol-12-one. Chemistry of Natural Compounds, 2010, 46(4), pp. 539-544.
9. Kharitonov, Yu.V.; Shults, E. E.; Gatilov, Yu.V.; Bagryanskaya, I.Yu.; Shakirov, M.M. and Tolstikov, G. A. Synthetic transformations of higher terpenoids. Synthesis of 7-hydroxylabdanoids and their transformations. Chemistry of Natural Compounds, 2012, 48(2), pp. 250-257.
10. Lungu, L. Synthesis of new nitrogen-containing drimane and homodrimane sesquiterpenoids from sclareolide. Chemistry Journal of Moldova, 2015, 10(2), pp. 58-61.
11. Kuchkova, K.I.; Aricu, A.N.; Barba, A.N.; Vlad, P.F.; Lipkovskii, J.; Simonov, Yu.A.; Kravtov, V.Kh. Synthesis of nitrogen-containing drimane sesquiterpenoids from 11-dihomodrim-8(9)-en-12-one. Chemistry of Natural Compounds, 2011, 47(2), pp. 223-228.
12. Krstic, N.M.; Bjelakovic, M.S.; Dabovic, M.M.; Lorenc, L.B.; Pavlovic, V.D. Photochemical and Beckmann rearrangement of (Z)-cholest-4-en-6-oneoxime. Journal of the Serbian Chemical Society 2004, 69(6), pp. 413-420.
13. Davis, M.; White, A.W. Synthesis of substituted 2,1-benzisothiazoles. Journal of Organic Chemistry, 1969, 34(10), pp. 2985-2988.

SYNTHESIS AND ANTIMICROBIAL EVALUATION OF SYMMETRICAL DIQUATERNARY AMMONIUM SALTS BEARING BIS-1,3,4-OXADIAZOLE RINGS MOIETIES

Sofiane Daoudi[a*], Tahar Benaissa[a], Djallal Eddine Adli[b], Nisserine Hamini-Kadar[c]

[a]*Physical Chemistry Studies Laboratory, University of Dr. Moulay Tahar, Saïda 20000, Algeria*
[b]*Department of Biology, Faculty of Sciences and Technology, University of Dr. Moulay Tahar, Saïda 20000, Algeria*
[c]*Laboratory of Applied Microbiology, Department of Biology, Faculty of Nature Sciences and Life, University of Ahmed Ben Bella 1.BP 16. Es-Senia 31100, Oran, Algeria*
[*]*e-mail: daoudi_20@yahoo.fr*

Abstract. This study describes the synthesis of some novel compounds containing bis-1,3,4-oxadiazole bearing quaternary ammonium salt moieties. The target compounds were prepared from 2-(dimethylamino)ethyl methacrylate (DMAEMA) or 2-(diethylamino) ethyl methacrylate (DEAEMA), using adipic acid as starting material. All the newly synthesized compounds showed satisfactory analytic data for the proposed structures, which were confirmed by IR and NMR (^{1}H and ^{13}C) spectroscopy. The newly synthesized compounds were evaluated for their antibacterial activity against various gram-positive and gram-negative strains of bacteria, and the antifungal activities were tested against three phytopathogenic fungi namely, *Fusarium oxysporum, Fusarium commune* and *Fusarium rodelens.* Some of the tested compounds displayed promising antibacterial and antifungal activities.

Keywords: 1,3,4-oxadiazole, quaternary ammonium compounds, DMAEMA, DEAEMA, antimicrobial activities.

Received: February 2016/ Revised final: March 2016/ Accepted: March 2016

Introduction

The treatment of bacterial and fungal infectious diseases remains a challenging problem because of the increasing number of microbial pathogens [1-3]. The current interest in the development of new antimicrobial agents can be partially ascribed both to the increasing emergence of bacterial resistance to antibiotic therapy and to newly emerging pathogens [4]. It reinforces the need for the development of new and potent chemical entities or an improvement in the activity of the well-known chemical compounds. Considering this statement, the synthesis of analogues can be seen as an efficient approach to optimize an active chemical structure and design new drugs [5-8], since simple structural changes can lead to better biological activities through modifications of physicochemical properties [9].

Literature survey reveals that compounds containing 1,3,4 oxadiazole nucleus have demonstrated a wide range of pharmacological activities [10,11], including: anti-inflammatory [12], antimicrobial [13], analgesic [14], antiviral [15], antiproliferative [16], antitumor [17], antihypertensive [18,19], antioxidant [20], antitubercular [21], sedative-hypnotic [22] and antibacterial and antifungal activities [23].

Quaternary ammonium salts (QAS) constitute an important class of organic compounds that are present in a large number of biologically active molecules [24]. It was reported that the quaternary ammonium compounds have antimicrobial properties [25], show adsorption on negatively charged solids, act on the cell wall and have a direct or indirect lethal effect on the cell [26]. QAS were introduced as antimicrobial agents by Domagk over eighty years ago [27].

In recent years the number of applications of QAS has been continuously increasing. They are widely used as biocides [28,29], antibiotic [30], disinfectants [31], antimalarial [32] and antimicrobial properties [33,34]. In the design of new drugs, the combination of different pharmacophores frame may lead to compounds with interesting biological profiles [35]. Also, QAS incorporating heterocycles, *e.g.* 1,3,4-oxadiazole, displayed various pharmacological properties [36]. Prompted by these investigations, we have synthesized compounds **5a** and **5b** containing bis-1,3,4oxadiazole fragment with the attached quaternary ammonium group and their antimicrobial activity has been evaluated.

Materials and methods

All solvents and reagents were obtained from Sigma Aldrich and BIOCHEM. The purity of compounds was routinely checked by thin layer chromatography (TLC) using silica gel F254 supplied by MERCK, and spots were observed using iodine as visualizing agent.

All melting points were determined in open capillary tubes on a BÜCHI 540 melting point apparatus and are uncorrected.

The IR spectra in the range of 4000-400 cm^{-1} were recorded as potassium bromide discs on a Shimadzu FTIR-8300 spectrophotometer.

The ^{1}H and ^{13}C NMR Spectra were measured in DMSO-d_6 on a Bruker AM 300 MHz spectrometer (University of Oran, Es-Senia), operating at 300 MHz for ^{1}H and 75 MHz for ^{13}C nuclei, relative to the internal standard of tetramethylsilane (TMS). Chemical shift values are expressed in parts per million (δ, ppm).

Preparation of diethyl adipate 2

Diethyl adipate **2** was prepared according to the reported in the literature procedure [37]. The adipic acid (5 g, 0.034 mol) was dissolved in 200 mL of absolute ethanol and a few drops of conc. sulphuric acid was added. The mixture was heated at 80°C in an oil bath for 8 hours, the progress of the reaction being monitored by TLC. After completion of the reaction, the excess of ethanol was removed under reduced pressure and the residue was extracted with chloroform. The organic layer extract was washed with a 5% solution of sodium bicarbonate, then the solvent was evaporated and the product was collected. Yield of compound **2**-76%. Liquid, R*f* = 0.45 ($CHCl_3/CH_3OH$= 8/2); IR (KBr, υ cm^{-1}): 1706.9 (C=O), 1070.4 (C-O-C).

Adipic acid dihydrazide 3

A mixture of diethyl adipate **2** (5 g, 0.028 mol) and an excess of hydrazine hydrate (0.05 mol) in absolute ethanol (150 mL) were refluxed for 6 hours on a water bath. The purity of the products was checked by single spot TLC, the reaction mixture was cooled. Then the solvent was evaporated under reduced pressure to give adipic acid dihydrazide **3**. Yield- 67%. Powder, m.p. 180–181°C, R*f* = 0.40 ($CHCl_3/CH_3OH$ =9/1); IR (KBr, υ cm^{-1}): 3222.8 (NH-NH_2), 1606.6 (C=O). ^{1}H-NMR: 8.34 (3H, O=C-N**H**N**H**$_2$), 1.99 (2H, O=C-C**H**$_2$$CH_2$), 1.42 (2H, O=C-$CH_2$C**H**$_2$). ^{13}C-NMR: 178.2 (O=**C**-$NHNH_2$), 39.8 (O=C-**C**$H_2$$CH_2$), 26.3 (O=C-$CH_2$**C**$H_2$).

2,2'-butane-1,4-diylbis[5-(bromomethyl)-1,3,4-oxadiazole] (4). A mixture of adipic acid dihydrazide **3** (3g, 0.017 mol), bromoacetic acid (4.78 g, 0.034 mol) and phosphours oxychloride (5 mL) was refluxed at 80-90°C for 6 hours. After completion of reaction, as indicated by TLC, the mixture was cooled and poured into ice water and then sodium bicarbonate solution was added. The resulting solid was collected by filtration, washed with cold water, and dried. Then the solvent was evaporated under reduced pressure to give 2,2'-butane-1,4-diylbis[5-(bromomethyl)-1,3,4-oxadiazole] **4**. Yield- 85%. Crystalline solid, m.p. 114-115°C, R*f* = 0.42 ($CHCl_3/CH_3OH$= 4/1); IR (KBr, υ cm^{-1}): 1643.2 (C=N), 1105.1(C-O-C), 497(C-Br). ^{1}H-NMR: 8.30 (2H, O=C-C**H**$_2$-Br), 2.17 (2H, N=C-C**H**$_2$$CH_2$), 1.45 (2H, N=C-$CH_2$C**H**$_2$). ^{13}C-NMR: 174.8 (N=**C**-$CH_2$$CH_2$), 172.1 (O=**C**-$CH_2$-Br), 39.7 (N=C-**C**$H_2$$CH_2$), 33.8 (N=C-$CH_2$**C**$H_2$), 24.4 (O=C-**C**$H_2$ Br).

N,N'-[butane-1,4-diylbis(1,3,4-oxadiazole-5,2-diylmethylene)]bis[N,N-diethyl-2-(methacryloyloxy)ethan ammonium] bromide (5a). According to the procedure adopted by Guiqian Lu *et al.* [38], a mixture of compound **4** (1 g, 0.003 mol) and tertiary amine DEAEMA (0.97 g, 0.005 mol) was dissolved in dry acetone (50 mL), in the presence of hydroquinone. The mixture was gently refluxed for 40 hours on water bath. After cooling, diethyl ether was added, the target diquaternary ammonium salt **5a** was collected by filtration under reduced pressure and washed several times with diethyl ether. Yield- 82%. Pasty mass, R*f*= 0.50 ($CHCl_3/CH_3OH$= 4/1); IR (KBr, υ cm^{-1}): 1737.7(C=O), 1625.9 (C=N), 1460 (C=C), 1026.1 (C-O-C). ^{1}H-NMR: 6.12-5.76 (2H, =C**H**$_2$), 4.44 (2H, N^+CH_2C**H**$_2$), 3.73 (2H,N=C-C**H**$_2$ N^+), 3.44 (2H, N^+C**H**$_2$$CH_2$), 2.55 (3H, N^+C**H**$_3$), 1.93 (2H, N=C-C**H**$_2$$CH_2$), 1.49 (3H,C(C**H**$_3$)=$CH_2$), 1.23 (2H, N=C-$CH_2$C**H**$_2$). ^{13}C-NMR: 174.0 (N=**C**-$CH_2$$CH_2$), 166.5 (**C**=O), 157.0 (N=**C**-CH_2N^+), 136.0 (**C**(CH_3)=CH_2), 125.6 (=**C**H_2), 63.3 (N^+**C**$H_2$$CH_2$) 55.7 (N=C-**C**$H_2$ N^+), 50.6 (N^+CH_2**C**H_2), 47.2 (N^+**C**H_3), 26.7 (N=C-**C**$H_2$$CH_2$), 24.4 (N=C-$CH_2$**C**$H_2$), 17.8 (C(**C**$H_3$)=$CH_2$).

N,N'-[butane-1,4-diylbis(1,3,4-oxadiazole-5,2-diylmethylene)]bis[2-(methacryloyloxy)-N,N-dimethylethan ammoinium] bromide (5b). Compound **4** (1 g, 0.003 mol) was dissolved in dry acetone (40 mL) and the resulting solution was mixed with DMAEMA (0.81g, 0.005 mol), in the presence of hydroquinone. The mixture was gently refluxed for 40 hours on water bath. After completion of the reaction, the solvent was evaporated and the formed precipitate was filtered, washed with diethyl ether and dried. Yield of compound **5b-** 79%. Pasty mass, R*f* = 0.58 ($CHCl_3/CH_3OH$= 4/1); IR (KBr, υ cm^{-1}): 1737.7 (C=O), 1647.1 (C=N), 1460 (C=C), 1022.2 (C-O-C). ^{1}H-NMR: 6.17-5.75 (2H, =C**H**$_2$), 4.40 (2H, N^+CH_2C**H**$_2$), 3.71 (2H, N=C-C**H**$_2N^+$), 3.39 (2H, N^+C**H**$_2$$CH_2$), 2.78 (3H, N^+C**H**$_3$), 2.50 (2H, N=C-C**H**$_2$$CH_2$), 1.90 (3H,C(C**H**$_3$)=$CH_2$), 1.14 (2H, N=C-$CH_2$C**H**$_2$). ^{13}C-NMR: 174.9 (N=**C**-$CH_2$$CH_2$), 167.0 (**C**=O), 155.67 (N=**C**-CH_2 N^+), 136.0 (**C**(CH_3)=CH_2), 128.0 (=**C**H_2), 62.3 (N^+**C**$H_2$$CH_2$), 59.0 (N=C-**C**$H_2$ N^+), 50.1 (N^+CH_2**C**H_2), 43.1 (N^+**C**H_3), 27.1 (N=C-**C**$H_2$$CH_2$), 24.3 (N=C-$CH_2$**C**$H_2$), 17.8 (C(**C**$H_3$)=$CH_2$).

Testing the biological activity

Determination of minimum inhibitory concentration (MIC)

MIC of the synthesized compounds **3**, **4**, **5a** and **5b** was determined by using the broth microdilution method [39]. The solutions of each tested compounds were prepared in DMSO to get a concentration of 100 mg/mL. From this stock solution, serial dilutions of the compounds (100, 50, 25, 12.5, 6.25, 3.12, 1.56, 0.78, 0.39, 0.19, and 0.097 mg/mL) were prepared. The MIC was recorded in each case as the minimum concentration of the compound, which inhibited the visible growth of the tested microorganism, and DMSO was used as a negative control.

Antibacterial activity

In order to evaluate the antibacterial activity eleven bacteria have been used: *Enterobacter aerogenes* (ATCC 51697), *Citrobacter freundii* (ATCC 8090), *Acetobacter aceti* (ATCC 15973), *Escherichia coli* (ATCC 25933), *Klebsiella*

pneumoniae (ATCC 70603), *Enterobacter cloacae* (ATCC 13047), *Pseudomonas aeruginosa* (ATCC 27853) and *Salmonella enterica* (ATCC 13312) as gram negative bacteria and *Methicillin-resistant Staphylococcus aureus (MRSA)* (ATCC 43300), *Curtobacterium flaccumfaciens* (ATCC 53934) and *Staphylococcus wavy* as gram positive bacteria.

All microorganisms were obtained from Microbiology Laboratory, Institute of Biology, University of Dr. Moulay Tahar, Saïda. The bacterial strains were maintained on Muller-Hinton agar and the tested compounds were dissolved in DMSO to make a stock solution of 100 mg/mL and the other concentrations were prepared by dilution. A suspension of the organisms was introduced onto the surface of sterile agar plates, and then incubated at 37 °C for 18 – 24 hrs. After incubation, MIC was determined. All the tests were performed in triplicate.

Antifungal activity

Antifungal activity has been tested on three pathogenic fungi of tomato, such as *Fusarium oxysporum* MIAE 00123, *Fusarium commune* MIAE 00112 and *Fusarium rodelens* MIAE 00129 by the diffusion plate method [40].

All the fungal strains were obtained from collection of pure cultures of the laboratory of Applied Microbiology Faculty of Nature Sciences and Life, Oran University, Algeria. The test compounds were dissolved in DMSO (1 mL), mixed with potato dextrose agar PDA at concentrations of 50, 100, 150 and 200 µg/mL and poured onto sterile Petri dishes (with diameter of 9 cm). A 6 mm disc containing mycelia was transferred to the center of PDA plate. Tree replications were maintained for each concentration and DMSO was used as a control solvent. Then the inoculated plates were incubated at 37°C for 4 days and the zone of inhibition was observed and measured. The relative inhibition rate of the circle mycelium compared to blank assay was calculated *via* the following equation:

$$\textit{Relative inhibition rate (\%)} = [(T - C)/T] \times 100\% \quad (1)$$

where: T is the extended diameter of the circle mycelium during the blank assay,

C is the extended diameter of the circle mycelium during testing.

Results and discussion

Chemistry

The target compounds **5a** and **5b** were synthesized by a multiple-step procedure as shown in Figure 1. The synthetic route started from esterfication of adipic acid **1** using ethanol in the presence of sulphuric acid. This ester reacted with hydrazine hydrate in ethanol to give adipic acid dihydrazide **3.** Bis-1,3,4-oxadiazole **4** was obtained by ring closure reaction upon treating acid hydrazide **3** with bromoacetic acid in phosphorus oxychloride. Finally, the products **5a** and **5b** were obtained by refluxing compound **4** with the appropriate tertiary amine (DEAEMA or DMAEMA) in acetone to give the corresponding quaternary ammonium salts.

The physiochemical data of the synthesized compounds (**2-4, 5a** and **5b**) are presented in Table 1. The percentage yield of all the synthesized compounds was found to be in the range of 67-85%.

The purity of the synthesized compounds was checked by thin layer chromatography and melting points values. The structures of all the synthesized compounds were confirmed by IR, ^{1}H and ^{13}C NMR spectral data.

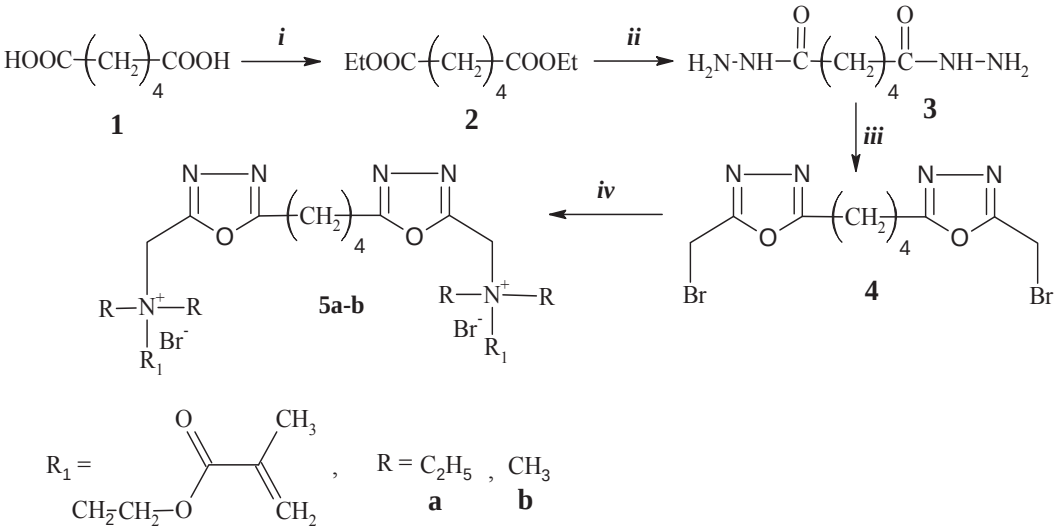

Figure 1. Synthetic route of the final compounds 5a-b.

Reagents and conditions: (*i*) C_2H_5OH and conc. H_2SO_4, reflux for 8 h; (*ii*) NH_2NH_2-H_2O, C_2H_5OH, reflux for 5 h; (*iii*) $POCl_3$, $BrCH_2COOH$, reflux for 6 h; (*iv*) DMAEMA/DEAEMA, acetone, reflux for 40 h.

Table 1

Physical properties and analytical data of the synthesized compounds.

Compound	*Colour*	*Yield, %*	*Melting point, °C*	*Rf value*	*Solvent system* $CHCl_3/CH_3OH$
2	Colorless	76	liquid	0.45	8/2
3	White	67	180-181	0.40	9/1
4	White	85	114-115	0.42	4/1
5a	Brown	82	semi-solide	0.50	4/1
5b	Brown	79	semi-solide	0.58	4/1

Biological activity

Antibacterial activity

The synthesized compounds have been tested *in vitro* for their antibacterial activity against eleven bacteria, such as *Enterobacter aerogenes* ATCC 51697, *Citrobacter freundii* ATCC 8090, *Acetobacter aceti, Escherichia coli, Klebsiella pneumoniae, Enterobacter cloacae, Pseudomonas aeruginosa* and *Salmonella enterica* ATCC 13312 as gram negative bacteria and *Methicillin-resistant Staphylococcus aureus (MRSA)* ATCC 43300*, Curtobacterium flaccumfaciens* and *Staphylococcus wavy* as gram positive bacteria. The obtained results are summarized in Table 2.

Table 2

Minimal inhibitory concentration in mg/mL of synthesized compounds against tested bacterial strains by microdilution method.

Strains	*Compound and values of MIC in mg/mL*			
	3	**4**	**5a**	**5b**
Enterobacter aerogenes (ATCC 51697)	0.097	12.5	25	12.5
Citrobacter freundii (ATCC 8090)	12.5	0.39	0.19	0.097
Acetobacter aceti (ATCC 15973)	1.56	6.25	6.25	6.25
Escherichia coli (ATCC 25933)	6.25	1.56	100	50
Klebsiella pneumoniae (ATCC 70603)	6.25	0.78	25	25
Enterobacter cloacae (ATCC 13047)	3.12	12.5	12.5	12.5
Pseudomonas aeruginosa (ATCC 27853)	3.12	12.5	12.5	12.5
Salmonella enterica (ATCC 13312)	0.78	12.5	12.5	12.5
Methicillin-resistant Staphylococcus aureus (MRSA) (ATCC 43300)	25	0.78	0.78	0.78
Curtobacterium flaccumfaciens (ATCC 53934)	3.12	12.5	25	25
Staphylococcus wavy	1.56	12.5	12.5	25

As it is shown in Table 2, the results of evaluating the antibacterial properties suggest that all compounds have very good potential to act as antibacterial agents. The values of MIC ranged between: 0.097-100 mg/mL. Compounds **3** and **4** have shown the highest antibacterial activity against all tested microorganisms. The best activity was observed against *Citrobacter freundii* ATCC 8090 and MRSA by compound **5a** and **5b**, but relatively low antibacterial activity (MIC 50-100 μg/mL) was observed against *Escherichia coli.*

Antifungal activity

Similarly, the newly prepared compounds were screened *in vitro* for their antifungal activity against three pathogenic fungi of tomato, such as *Fusarium oxysporum* MIAE 00123*, Fusarium commune* MIAE 00112 and *Fusarium rodelens* MIAE 00129. The results of *in vitro* antifungal activities are presented in Table 3. The antifungal screening showed that the maximum inhibitory activity was found for compound **3** against all of tested fungi at concentration of 200 μg/mL, and compound **4** showed good activity against the tested fungi, compound **5a** and **5b**, showed moderate activity against *Fusarium oxysporum* and *Fusarium rodelens*. However, lower activity was observed for compound **5b** against *Fusarium commune.*

Table 3

Relative inhibition rate (%) of synthesized compounds against tested fungal strains.

Compound	*Relative inhibition rate (%)*											
	Fusarium oxysporum				*Fusarium commune*				*Fusarium rodelens*			
	Concentration in μg/mL											
	50	*100*	*150*	*200*	*50*	*100*	*150*	*200*	*50*	*100*	*150*	*200*
3	14.5	15.5	16.6	18.8	3.3	12.2	21.1	22.2	6.6	8.8	30	30
4	12.2	12.9	13.3	15.5	10	11.1	11.1	11.1	7.7	8.8	11.1	11.1
5a	5.5	6.6	6.6	7.7	3.3	5.5	6.6	6.6	6.6	6.6	7.7	8.8
5b	5.5	5.5	7.4	14.4	1.1	1.1	3.3	4.4	5.5	6.6	7.7	7.7

Conclusions

The present study reports on the successful synthesis and antimicrobial activity of some novel bis-1,3,4-oxadiazole compounds containing quaternary ammoniums salt moiety. The 1,3,4-oxadiazole heterocycle was synthesized by ring-closing reaction, and quaternary ammonium salt was obtained by *N*-alkylation. All the synthesized compounds were structurally characterized using IR and NMR spectroscopic techniques. The newly synthesized compounds were evaluated for their antibacterial and antifungal activity. The results of biological tests indicated that most of the synthesized compounds exhibited promising results. Thus, the mixed compounds containing both 1,3,4-oxadiazole and quaternary ammonium salts moieties can serve as interesting lead molecules for further synthetic and biological evaluation.

Acknowledgments

The authors are grateful to Mrs HIDOUR Hanaa (University of Oran, Es-Senia) for recording the NMR spectra.

References

1. Rodrigo, S.; Lisa, R.; Michael, B.; Teresa, Z.; Wanseon, L.; Duccio, C.; Luigina, R.; Brian, M.; Ivo, G.; Manuel, S.; Philippe, P.; Paul, B.; Misha, K. Systems biology of infectious diseases: a focus on fungal infections. Immunobiology, 2011, 216, pp. 1212–1227.
2. Gharamah, A.A.; Moharram, A.M.; Ismail, M.A.; Al-Hussaini, A.K. Bacterial and fungal endophthalmitis in upper Egypt: related species and risk factors. Asian Pacific Journal of Tropical Biomedicine, 2012, 2(8), pp. 655-659.
3. Kawecki, D.; Kwiatkowski, A.; Sawicka, G.A.; Durlik, M.; Mlynarczyk G.; Chmura, A. Bacterial and fungal infections in the early post-transplantation period after simultaneous pancreas-kidney transplantation: etiological agents and their susceptibility.Transplant Proceedings, 2014, 46(8) , pp. 2802-2805.
4. Garba, I.; Farouq, M.D.; Tiamiyu, A.B.; Zaiyad, G.H.; Isa, M.T.; Abdulrazaq, G.H. Pattern of antibiotic prescription and resistance profile of common bacterial isolates in the internal medicine wards of a tertiary referral centre in Nigeria. Journal of Global Antimicrobial Resistance, 2015, 3, pp. 91–94.
5. Kevin, K.C.L.; Subas, M.S.; Christopher, J.O.; Andrew, C.F.; Hong, X.D. Synthetic approaches to the 2010 new drugs. Bioorganic & Medicinal Chemistry, 2012, 20, pp. 1155–1174.
6. Kevin, B.P.; Emma, D.B.; Charlotte, H.; Dominic, P.W. Selection of new chemical entities with decreased potential for adverse drug reactions. European Journal of Pharmacology, 2006, 549(1-3), 7, pp. 1–8.
7. Hong, X.D.; Carolyn, A.L.; Robert, E.K.J.; Kevin, K.C.L.; Sarah, J.F.; Andrew C.F.; Christopher J.O. Synthetic approaches to the 2013 new drugs. Bioorganic & Medicinal Chemistry, 2015, 23, pp. 1895–1922.
8. Mouhssen L. The Success of Natural Products in Drug Discovery. Pharmacology & Pharmacy, 2013, 4, pp. 17−31.
9. Vanessa, L.C.; Daniel, F.K.; Dílson, B.S.J.; Ivone, C. Carrageenans: biological properties, chemical modifications and structural analysis–A review. Carbohydrate Polymers, 2009, 77, pp. 167–180.
10. Kavitha, S.; Gnanavel, S.; Kannan, K. Biological aspects of 1,3,4-oxadiazole derivatives. Asian Journal of Pharmaceutical and Clinical Research, 2014, 7(4), pp.11-20.
11. Musmade, D.S.; Pattan, S.R.; Manjunath, S.Y. Oxadiazole a nucleus with versatile biological behaviour. International Journal of Pharmaceutical Chemistry, 2015, 5(1), pp. 11-20.
12. Sumit, B.; Manju, B.; Sharad, K.S.; Shivani, C.; Shoumyo, B.; Varun, B.; Sumit, S.; Alex, J. Design and synthesis of novel 2-phenyl-5-(1,3-diphenyl-1H-pyrazol-4-yl)-1,3,4-oxadiazoles as selective COX-2 inhibitors with potent anti-inflammatory activity. European Journal of Medicinal Chemistry, 2014, 80, pp. 167-174.
13. Shivi, B.; Monika, G. 1,3,4-Oxadiazole as antimicrobial agents: An overview. Journal of Chemical and Pharmaceutical Research, 2011, 3(3), pp. 137-147.
14. Abbas, S.; Mohammad, A.; Amir, N.; Nasir, S.; Nasim, V.; Sayyed, A.T.; Reza, K. Synthesis and analgesic activity of new 1,3,4-oxadiazoles and 1,2,4-triazoles. Medicinal Chemistry Research, 2011, 20(4), pp. 435-442.
15. Li, Z.; Zhan P.; Liu X. 1,3,4-Oxadiazole: A privileged structure in antiviral agents. Mini-Reviews in Medicinal Chemistry, 2011, 11, pp. 1130-1142.
16. Gamal El-Din, M.M.; El-Gamal, M.I.; Abdel-Maskoud, M.S.; Yoo, K.H.; Oh, C.H. Synthesis and broad-spectrum antiproliferative activity of diarylamides and diarylureas possessing 1,3,4-oxadiazole derivatives. Bioorganic & Medicinal Chemistry Letters, 2015, 25(8), pp. 1692-1699.
17. Kai, Z.; Peng, W.; Li-Na, X.; Xiao Y.F.; Fen, J.; Sha, L.; Yu-Ming, L.; Bao-Quan, C. Synthesis and antitumor activities of novel hybrid molecules containing 1,3,4-oxadiazole and 1,3,4-thiadiazole bearing Schiff base Moiety. Bioorganic & Medicinal Chemistry Letters, 2014, 24(22), pp. 5154–5156.
18. Bankar, G.R.; Nandakumar, K.; Nayak, P.G.; Thakur, A.; Chamallamudi, M.R.; Nampurath, G.K. Vasorelaxant effect in rat aortic rings through calcium channel blockage: A preliminary *in vitro* assessment of a 1,3,4-oxadiazole derivative. Chemico-Biological Interactions, 2009, 181, pp. 377–382.
19. Vardan, S.; Mookherjee, S.; Eich, R. Effects of tiodazosin, a new antihypertensive, hemodynamics and clinical variables. Clinical Pharmacology & Therapeutics, 1983, 34(3), pp. 290–296.

20. Liang, M.; Yu, X.; Cong, L.; Zheng-Lu, X.; Dong-Dong, L.; Yan-Ting, W.; Hai-Tian, M.; Hai-Liang, Z.; Ming-Hua, W.; Yong-Hao, Y. Synthesis and antioxidant activity of novel Mannich base of 1,3,4-oxadiazole derivatives possessing 1,4-benzodioxan. Bioorganic & Medicinal Chemistry, 2013, 21, pp. 6763–6770.
21. Somani, R.R.; Balkund, V.D.; Nikam, S.R.; Shirodkar, P.Y.; Zope, D.B. Synthesis, antibacterial and anti-tubercular evaluation of some 1,3,4-oxadiazole based Mannich bases. International Journal of ChemTech Research, 2013, 5(5), pp. 2588-2592.
22. Sayyed, A.T.; Elham, R.Z.; Hamed, R.; Bagher, A.; Bijan, S.; Majid, S.; Abbas, S.; Mehrdad, F. Evaluation of anxiolytic, sedative-hypnotic and amnesic effects of novel 2-phenoxy phenyl-1,3,4-oxadizole derivatives using experimental models. Iran Journal of Pharmaceutical Research, 2015, 14, pp. 51–57.
23. Deepak, S.; Rakshit, A.; Ritu, V. Microwave-assisted synthesis of some 1,3,4-oxadiazole derivatives and evaluation of their antibacterial and antifungal activity. Organic Chemistry International. Volume 2014, Article ID 694060. http://dx.doi.org/10.1155/2014/694060.
24. Dörwald, F.Z. Lead Optimization for Medicinal Chemists: Pharmacokinetic Properties of Functional Groups and Organic Compounds. John Wiley & Sons: New York, 2013, pp. 118-119.
25. Xiaoshuai, Q.; Yancai, L.; Fang, Z.; Lixia, R.; Yunhui, Z.; Xiaoyan, Y. Polydimethylsiloxane-polymethacrylate block copolymers tethering quaternary ammonium salt groups for antimicrobial coating. Applied Surface Science, 2015, 328, pp. 183–192.
26. Sauvet, G.; Dupond, S.; Kazmierski, K.; Chojnowski, J. Biocidal polymers active by contact. V. Synthesis of polysiloxanes with biocidal activity. Journal of Applied Polymer Science, 2000, 75, pp. 1005–1012.
27. Domagk, G. A new class of disinfectant. Deutsche Medizinische Wochenscherift, 1935, 61(21), pp. 829–832, (in German).
28. Jeffrey, G.L.; Peter, N.C.; Preston, A.F.; James, H.W. Relationship between surface concentration of amphiphilic quaternary ammonium biocides in electrospun polymer fibers and biocidal activity. Reactive & Functional Polymers, 2014, 77, pp. 39–46.
29. Anqiang, Z.; Qiongqiong, L.; Yufeng, L.; Shuanghao, H.; Yaling, L. Synthesis and antimicrobial activities of acrylamide polymers containing quaternary ammonium salts on bacteria and phytopathogenic fungi. Reactive & Functional Polymers, 2015, 88, pp. 39–46.
30. Chamari, W.; Marianna, B.; Lívia, B.; Magdolna, E.S.; Ilona, P. Optimization of liposomal encapsulation for ceftazidime for developing a potential eye drop formulation. Journal of Basic and Clinical Pharmacy, 2013, 4(3), pp. 73–75.
31. Ulas, T.; Spyros, G.P. Quaternary ammonium disinfectants: Microbial adaptation, degradation and ecology. Current Opinion in Biotechnology, 2015, 33, pp. 296–304.
32. Nicoletta, B.; Mara, M.; Denise, P.; Donatella, T.; Riccardo, S.; Elena, P. Modified quaternary ammonium salts as potential antimalarial agents. Bioorganic & Medicinal Chemistry, 2015, 23, pp. 4681–4687.
33. Yaling, L.; Qiongqiong, L.; Liujun, C.; Yufeng, L.; Anqiang, Z. Synthesis and antimicrobial activities of polysiloxane-containing quaternary ammonium salts on bacteria and phytopathogenic fungi. Reactive & Functional Polymers, 2014, 85, pp. 36–44.
34. Xu, Z.S.; Ning, W.; Di, C.; Zi, Y.H.; Pu, M.; Hai, B.Z.; Xiao, H.Z. The antimicrobial activities of a series of bis-quaternary ammonium compounds. Chinese Chemical Letters, 2011, 22, pp. 887–890.
35. Yashumati, R.B.; Ashutosh, P.; Vivek, J.; Dharma, K.; Chemical delivery systems and soft drugs: Retrometabolic approaches of drug design. Saudi Pharmaceutical Journal, 2014, 22, pp. 290–302.
36. Guo-Qiang, H.; Li-Li, H.; Guo-Qiang, W.; Nan-Nan, D.; Xiao-Yi, W.; Tie-Yao, C.; Jun, Y.; Wei, W.; Song-Qiang, X.; Wen-Long, H. Part IV: design, synthesis and antitumor activity of fluoroquinolone C-3 heterocycles: bis-oxadiazole methylsulfide derivatives derived from ciprofloxacin. Acta Pharmaceutica Sinica, 2012, 47(8), pp. 1017−1022.
37. Furniss, B.S.; Hannford, A.J.; Smith, P.W.G.; Tatchell, A.R. Vogel's Text Book of Practical Organic Chemistry. John Wiley & Sons: New York, 5th edition, 1989, pp. 1076.
38. Guiqian, L.; Dingcai, W.; Ruowen, F. Studies on the synthesis and antibacterial activities of polymeric quaternary ammonium salts from dimethylaminoethyl methacrylate. Reactive & Functional Polymers, 2007, 67, pp. 355–366.
39. Reference method for broth dilution antifungal susceptibility testing of yeasts, Approved Standard, 2nd Edition, Clinical and Laboratory Standards Institute (USA), NCCLS document M27-A2, 2002, 22(15), 51p.
40. Hamini, K.N.; Hamdane, F.; Boutoutaou, R.; Kihal, M.; Henni, J.E. Antifungal activity of clove (*Syzygium aromaticum* L.) Essential oil against phytopathogenic fungi of tomato (*Solanum lycopersicum* L.) in Algeria. Journal of Experimental Biology and Agricultural Sciences, 2014, 2(5), pp. 448-454.

STUDIES OF THE SUBSTITUTION EFFECTS ON THE ELECTRONIC PROPERTIES FOR BIPHENYL AND DERIVATIVE MOLECULES BY USING DFT METHOD

Rajaa Khedir Al-Yasari

University of Karbala, College of Science, Physics Department, Karbala, Iraq
e-mail: ralyasarair@gmail.com

Abstract. DFT method has been carried out to study the substitution effects of NO_2 group on the electronic properties (ionization potential, electron affinity, electronegativity, hardness, softness and electrophilicity index) and IR spectral properties of biphenyl and derivative molecules by using the B3LYP functional and the 3-21G basis set, as well as the optimization structure. The calculated values of HOMO and LUMO energies, as well as predicted by ChemBioDraw program ^{1}H and ^{13}C NMR spectra for the studied compounds are in a good agreement with experimental data. All properties were calculated by using Gaussian 09 program and GaussianView 5.08 program, except NMR characteristics.

Keywords: DFT calculation, electronic properties, IR and NMR spectra, biphenyl molecule.

Received: September 2015/ Revised final: January 2016/ Accepted: January 2016

Introduction

Biphenyl is an aromatic hydrocarbon with a molecular formula ($C_{12}H_{10}$), which is an organic compound that forms colorless crystals. It consists of two connected phenyl rings and has D_2 symmetry [1]. Biphenyl has density 1.04 g/cm^3, melting point 69.71°C and boiling point 255°C [2], being used in organic syntheses, food preservatives, heat transfer fluids and as an intermediate for polychlorinated biphenyls [3]. The biphenyl derivatives, such as polychlorinated biphenyls (PCB), were widely used as dielectric and coolant fluids in electrical apparatus, cutting fluids for machining operations and carbonless copy paper. 4-Aminobiphenyl has been used formerly as a rubber antioxidant and it is still used in the detection of sulfates and as a model carcinogen in mutagenicity studies and cancer research [4,5]. Many studies have been carried out on the theoretical calculations of electronic structure, ionization energy and IR spectra for azide group in 3′-azido-3′-deoxythymidine (AZT), compared to small azide compounds by the using DFT method and B3LYP/6-311G** basis set [6].

Geometry optimization has been performed and the electronic structure, total energy, electronic potential surface, UV and IR spectra were computed using TD-DFT//B3LYP method with 6-311G (d, p) basis sets for isoniazid and its derivative N-cyclopentylidenepyridine-4-carbohydrazide molecules [7]. The correlation between the crystalline structure and vibrational modes of the latter has been discussed [7]. Theoretical study of calculating the molecular structure and electronic properties of diphenylanthrazolines molecule was performed using density functional theory with B3LYP/6-31G* level [8]. Finally, a study has been carried out to highlight the substitution effects of H, NH_2, NMe_2, OCH_3, CH_3, Cl, Br, CN, NO_2 on the electronic structure and properties, such as HOMO, LUMO, energy gap and dipole moment of 2,4-domino-5-p-substituted-phenyl-6-ethyl-pyrimidines by using the DFT method and B3LYP with 6-311G (d) basis set [9].

In the light of the above-mentioned, the aim of this work was to study the influence of hydrogen atom substitution by NO_2 groups in different positions on the electronic and spectral properties for biphenyl and derivative molecules using the B3LYP functional and the 3-21G basis set.

Calculations

The DFT methods have been carried out using the Gaussian 09 program [10]. The geometric optimization of biphenyl **1** and derivative molecules **2-6** with the substitution of hydrogen atom by NO_2 groups in the different positions have been performed with a B3LYP/3-21G level in the gas phase. The hybrid functional B3LYP basis set has been shown highly successful for calculating the electronic properties, such as electronic states, ionization potentials and energy gaps, since calculation of the exchange-correlation energy and interaction effects between electrons also show the most accurate results. Figure 1 shows the geometry optimization of biphenyl **1** and derivative molecules **2-6** in the gas phase using DFT methods with B3LYP/3-21G level. The E*HOMO* represents the energy of highest occupied molecular orbital, while E*LUMO* represents the lowest unoccupied molecular orbital.

The ionization potential (*IP*) and electron affinity (*EA*) in the framework of Koopmans' theorem could be calculated from the energies of *HOMO* and *LUMO* as follows by Eqs.(1) and (2) [11]:

$$IP = -EHOMO \quad (1)$$

$$EA = -ELUMO \tag{2}$$

The electronegativity (χ) has been calculated by Eq.(3) [12]:

$$\chi = -\frac{IP + EA}{2} = -(EHOMO+ELUMO)/2 \tag{3}$$

Where the hardness (η) is defined by Eq.(4) [11]:

$$\eta = \frac{IP - EA}{2} \tag{4}$$

The softness (S) and electrophilicity index (W) have been calculated by using the Eqs.(5) and (6) [13, 14]:

$$S = \frac{1}{2\eta} \tag{5}$$

$$W = \frac{\chi^2}{2\eta} \tag{6}$$

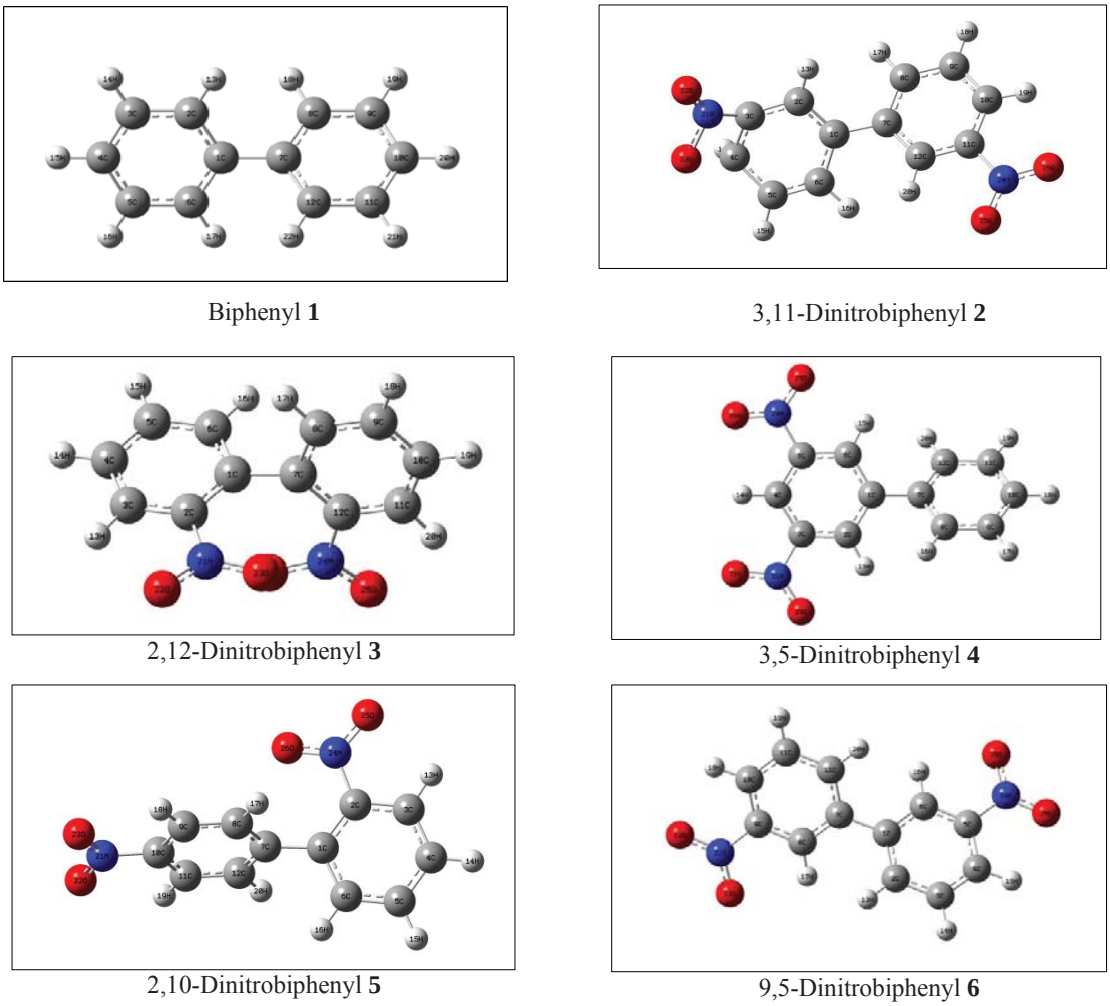

Biphenyl **1**

3,11-Dinitrobiphenyl **2**

2,12-Dinitrobiphenyl **3**

3,5-Dinitrobiphenyl **4**

2,10-Dinitrobiphenyl **5**

9,5-Dinitrobiphenyl **6**

Figure 1. The optimized structures of biphenyl 1 and derivative molecules 2-6 using DFT-B3LYP/3-21G method.

Results and discussion

Molecular geometry

The optimized structural parameters of molecules calculated by using DFT –B3LYP levels with the 3-21G basis set are listed in Table 1, in accordance with the atom numbering scheme shown in Figure 1. As results from Table 1, there is no convergence between the bond lengths for $R_{C–C}$, R_{C-H}, R_{C-N} and R_{N-O} bonds. The C-H bond lengths are in the

range of 1.079 - 1.085 Å and C-C bond length is at 1.373 Å and 1.498 Å, whereas C–N bond length varies from 1.338 Å to 1.476 Å. The N-O bond length of dinitrobiphenyl molecules varies in the range of 1.282 - 1.285 Å. All angles of the dinitrobiphenyl ring (C-C-C angles) vary from 117.602 to 120.220 A(°).

Electronic properties

All properties are computed by the DFT/B3LYP 3-21G method for biphenyl **1** and derivative molecules **2-6**. Table 2 shows the calculated energy values of *HOMO* and *LUMO* and electronic properties (values of *IP* and *EA* calculated by Eqs.(1) and (2), χ values (Eq.(3)), η values (Eq.(4)), *S* values (Eq.(5)), and *W* values calculated by Eq.(6)). It is clear from Table 2 and Figures 2-7 that the substitution of hydrogen atom by NO_2 group leads to decreasing the energy values of *HOMO* and increasing the energy values of *LUMO*. Figures 2-7 show the electronic density distribution along the rings C-C. In the different parts of dinitrobiphenyl molecules the electronic density distribution is homogeneous. It was noticed for all molecules that *HOMO* shows a bonding character and *LUMO* shows an antibonding character. While the values of *IP* are increasing, the values of *EA* are decreasing with the substitutions. The values of χ, η, *S* and *W* are increasing. The approximate values of *HOMO* and *LUMO* energies are in a good agreement with experimental values [15].

Table 1

Optimized geometrical parameters of biphenyl 1 and derivative molecules 2-6, *R* (Å) bond length, bond angles *A* (°).

Molecules	*Bond length*	*Our data (Å)*	*Bond angles*	*Our data (°)*
1	R(C1 - C2)	1.4051	A(C2-C3-C4)	120.2203
	R(C1-C7)	1.4886	A(C2-C1-C6)	118.6205
	R(C2 – C3)	1.3949	A(C8-C7-C12)	118.6205
	R(C3 – C4)	1.3970	A(C1-C6-H17)	119.2746
	R(C2 – H13)	1.0840	A(C9-C10-C11)	120.2203
2	R(C1- C2)	1.3738	A(C2-C1-C6)	119.5174
	R(C1 – C7)	1.4793	A(C4-C3-N21)	94.8932
	R(C3– N21)	1.3386	A(C1-C6-H16)	116.6752
	R(C2 – H13)	1.0825	A(O25-N24-O26)	125.7101
	R(N24-O26)	1.2824	A(O22-N21-O23)	125.8611
3	R(C1- C2)	1.4012	A(C2-C1-C6)	117.6027
	R(C1 – C7)	1.4984	A(C2-C3-N21)	116.8991
	R(C2– N21)	1.4613	A(C1-C6-H16)	118.5167
	R(C3 – H13)	1.0794	A(O25-N24-O26)	125.0666
	R(N24-O26)	1.2850	A(C12-N24-O25)	117.3061
4	R(C1 - C2)	1.4027	A(C2-C1-C6)	118.3123
	R(C11 – C10)	1.3970	A(C2-C3-N21)	118.9294
	R(C9– H17)	1.0835	A(C1-C6-H15)	121.7931
	R(C3-N21)	1.4675	A(O25-N24-O26)	126.1181
	R(N24-O26)	1.2809	A(C3-N21-O23)	116.9433
5	R(C1-C2)	1.4030	A(C2-C1-C6)	117.4296
	R(C11–C10)	1.3886	A(C3-C2-N21)	116.3391
	R(C9–H18)	1.0797	A(C7-C12-H20)	119.5894
	R(C10 -N21)	1.4625	A(N22-O21-N23)	125.6262
	R(N21-O22)	1.2841	A(C10-N21-O23)	117.1702
6	R(C1- C2)	1.4069	A(C2-C1-C6)	118.6886
	R(C10 – C11)	1.3928	A(C10-C9-N21)	119.0676
	R(C10 - N21)	1.4667	A(C1-C2-H13)	119.3218
	R(C2 – H13)	1.0834	A(O22-N21-O23)	125.7443
	R(N21-O22)	1.2824	A(C5-N24-O26)	117.1239

Table 2

***HOMO*, *LUMO* energies and electronic properties (*IP*, *EA*, χ, η, *S* and *W*) in (eV) units for biphenyl 1 and derivative molecules 2-6 using DFT with B3LYP/3-21G basis set.**

Molecules	*HOMO*	*LUMO*	*IP*	*EA*	χ	η	*S*	*W*
1	-6.21309	-0.59891	6.213088	0.598914	-3.40600	2.807087	1.403543	16.28228
2	-6.02588	-2.88681	6.025876	2.886815	-4.45635	1.569530	0.784765	15.58466
3	-7.14887	-2.78532	7.148874	2.785318	-4.96710	2.181778	1.090889	26.91446
4	-7.19377	-3.23566	7.193772	3.235660	-5.21472	1.979056	0.989528	26.90850
5	-7.27432	-2.97416	7.274317	2.974162	-5.12424	2.150077	1.075039	28.22818
6	-7.34262	-2.90450	7.342616	2.904502	-5.12356	2.219057	1.109529	29.12608

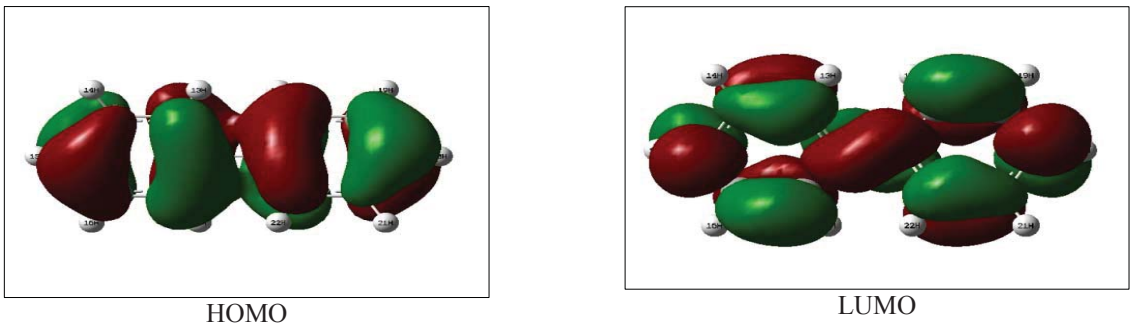

HOMO LUMO

Figure 2. *HOMO* and *LUMO* shapes of the biphenyl 1 molecule using the B3LYP/3-21G method.

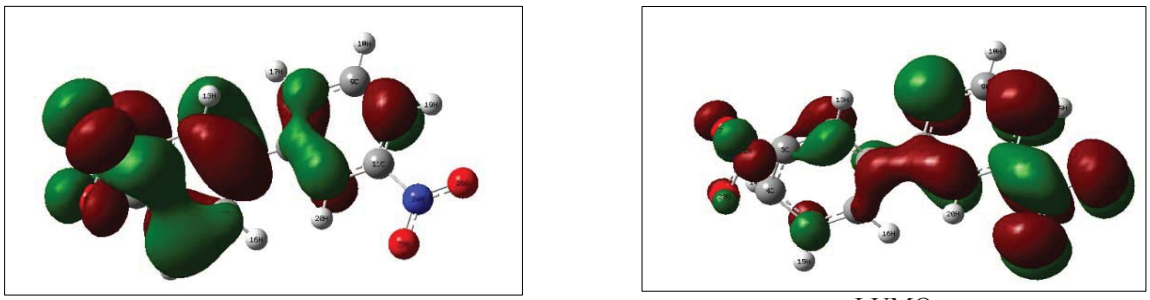

HOMO LUMO

Figure 3. *HOMO* and *LUMO* shapes of the 3,11-dinitrobiphenyl 2 molecule using the B3LYP/3-21G method.

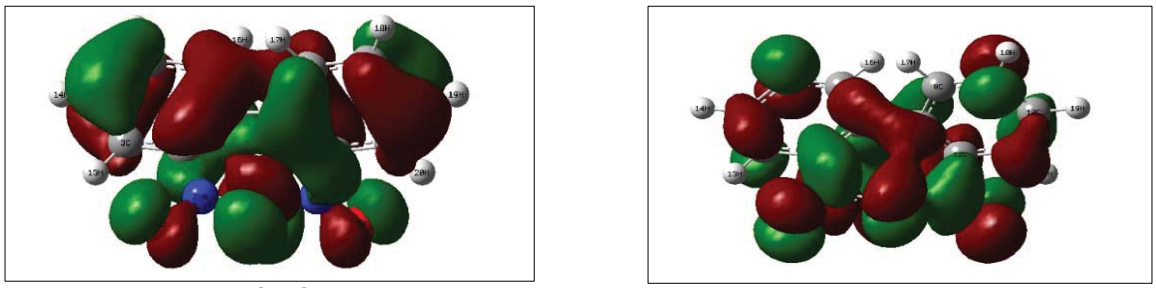

HOMO LUMO

Figure 4. *HOMO* and *LUMO* shapes of 2,12-dinitrobiphenyl 3 molecule using the B3LYP/3-21G method.

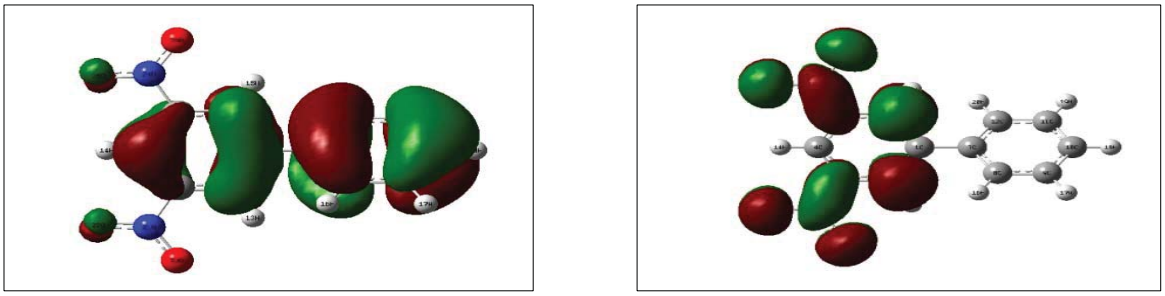

HOMO LUMO

Figure 5. *HOMO* and *LUMO* shapes of 3,5-dinitrobiphenyl 4 molecule using the B3LYP/3-21G method.

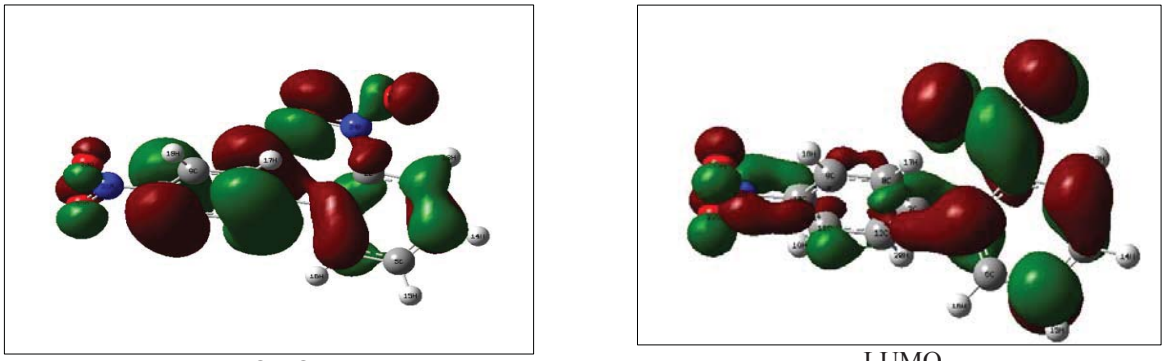

HOMO LUMO

Figure 6. *HOMO* and *LUMO* shapes of 2,10-dinitrobiphenyl 5 using the B3LYP/3-21G method.

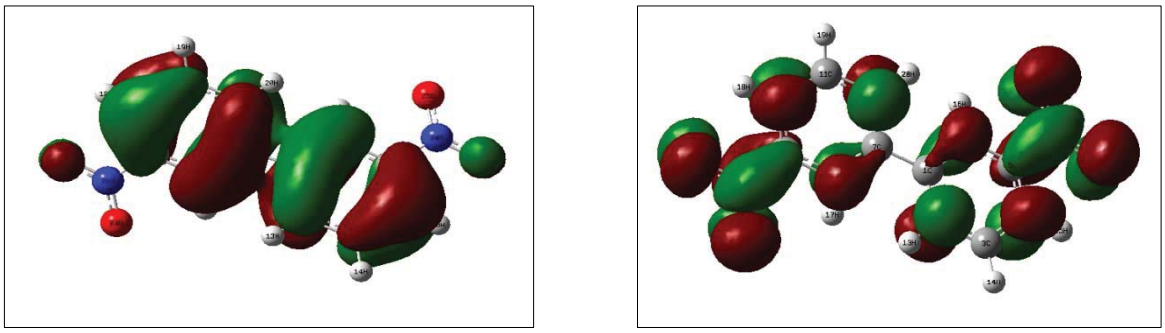

HOMO LUMO

Figure 7. *HOMO* and *LUMO* shapes of 9,5-dinitrobiphenyl 6 molecule using the B3LYP/3-21G method.

IR spectra

Figures 8-10 show the computed IR spectra of biphenyl molecules **1-6**. The harmonic vibrational frequencies were calculated for the studied molecules by using B3LYP level with a 3-21G basis set. The substitution of hydrogen atoms by NO_2 leads to increasing in the number of vibrational modes. According to the rule of (3N-6), the biphenyl molecule has 60 degrees of freedom, while the dinitrobiphenyl molecules have 72 degrees of freedom. All degrees of freedom for biphenyl **1** and its derivatives **2-6** are represented by stretching, bending, rocking and scissoring mode. For a biphenyl molecule, the (C–H) symmetric stretching has been studied around 3221.33 cm^{-1} and asymmetric- at 3205.55 cm^{-1}. The in-plane vibrations have been calculated at 957.55 cm^{-1}. The out-of-plane (C-H) vibrations found at 557.30 cm^{-1} are in a good agreement with experimental values at 552.90 cm^{-1} [1]. The (C-C) stretching vibrations have been studied in the region 1634.33 cm^{-1} and (C–C-C)- at 516.16 cm^{-1}. According to Figures 8-10, in the IR spectra of dinitrobiphenyl molecules **2-6** the new peaks in the vibration modes are registered, in comparison with biphenyl molecule **1,** due to existing of stretched bond, such as (C-N), (C-H) and (N-O) for 2-6 molecules. The symmetric stretching of (C-H) has been observed in the range of 3265.99-3225.80 cm^{-1} and asymmetric stretching- in the region 3194.29 – 3208.81 cm^{-1}. The (C-N) stretching has been observed in the region 1600.77 - 1190.03 cm^{-1}, whilst the stretching of (C-C) bond is shown in the range of 1648.56 - 1632.25 cm^{-1} and the stretching of (N-O) bond is shown in the region 1362.28 -1458.81 cm^{-1}. The NO_2 groups have the rocking mode appeared in the region 74.03 - 270.29 cm^{-1}, while the wagging modes appeared in the region 262.77 - 411.34 cm^{-1} and the scissoring mode appeared in the region 701.63 – 874.59 cm^{-1}.

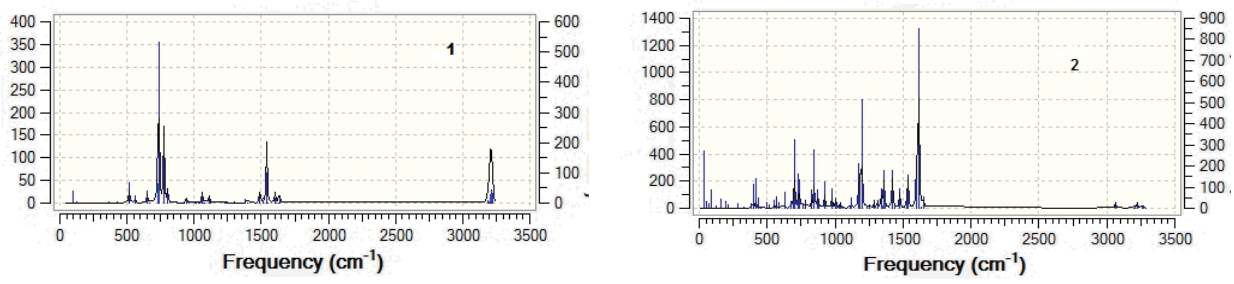

Figure 8. Calculated IR spectra of biphenyl 1 and its derivative 2.

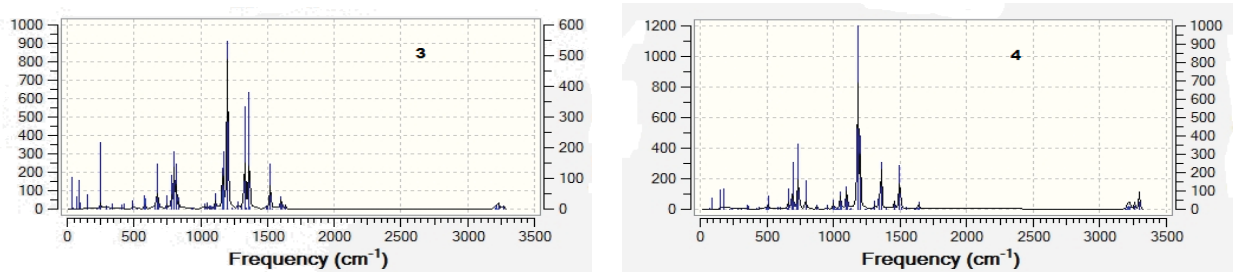

Figure 9. Calculated IR spectra of biphenyl derivatives 3 and 4.

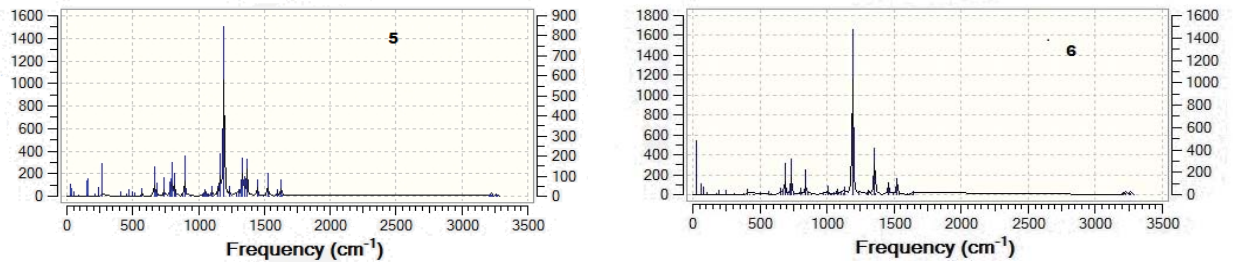

Figure 10. Calculated IR spectra of biphenyl derivatives 5 and 6.

NMR spectra

NMR spectra of ^{1}H and ^{13}C of biphenyl **1** and derivative molecules **2-6** (Figures 11-16) were computed by using the ChemBioDraw Program. Shielding has been considered to be one of the most effective factors that influence the chemical shift. In sites around the nucleus, where the electronic density is higher, the diamagnetic shielding becomes higher. It is clear from Figures 11-16 that the substitution of hydrogen atoms by NO_2 groups in dinitrobiphenyl molecules **2-6** leads to increasing of the value of chemical shift in ^{1}H NMR spectra and weak increase in chemical shift of ^{13}C nuclei. The molecules **3** and **5** have a complex ^{1}H NMR spectrum, because of the mutual influences between the nuclei inside the molecules. The molecule **4** has high values of chemical shift for ^{1}H nuclei that are found in the interval 7.4 - 9.4 ppm and ^{13}C nuclei in the interval 117.0 - 149.3 ppm. This is due to the effect of electronic density cyclic currents and electrons delocalization causing the strong shielding. The values of chemical shifts for ^{1}H and ^{13}C nuclei in NMR spectra for biphenyl **1** are in a good agreement with experimental values [16].

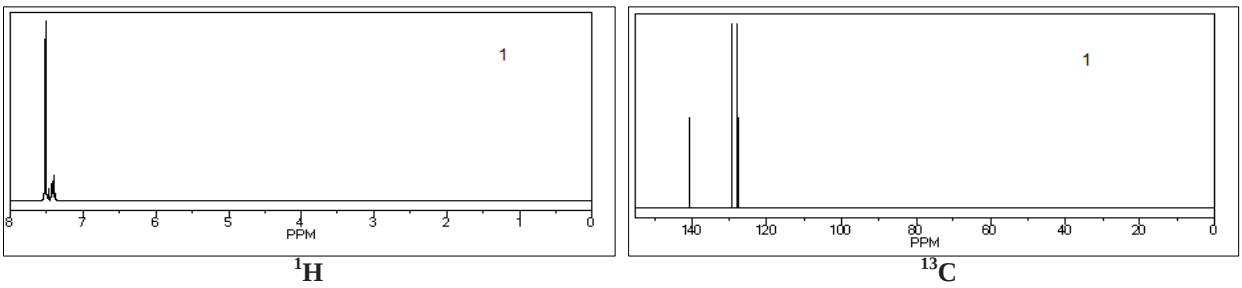

Figure 11. Predicted ^{1}H and ^{13}C NMR spectra for biphenyl 1.

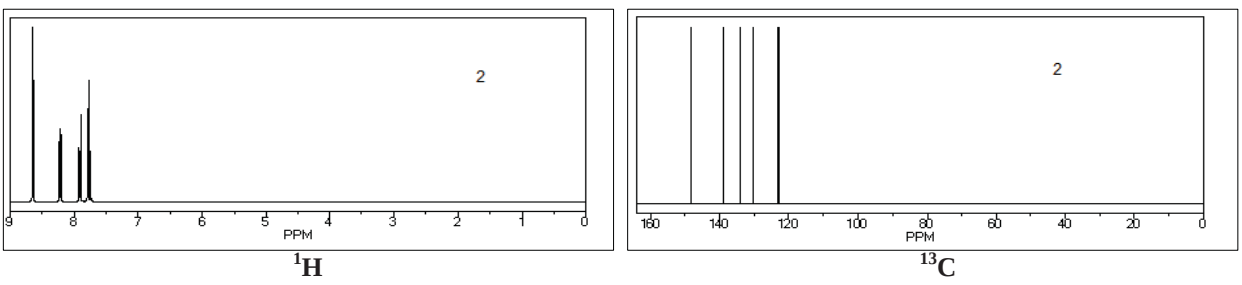

Figure 12. Predicted ^{1}H and ^{13}C NMR spectra for biphenyl derivative 2.

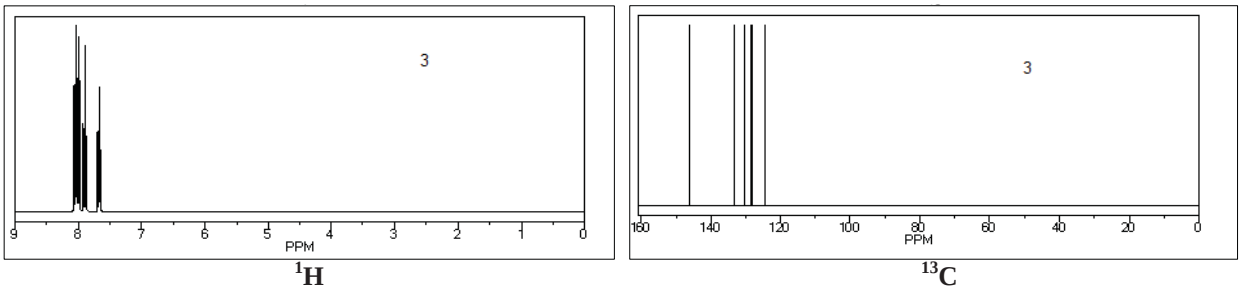

Figure 13. Predicted ^{1}H and ^{13}C NMR spectra for biphenyl derivative 3.

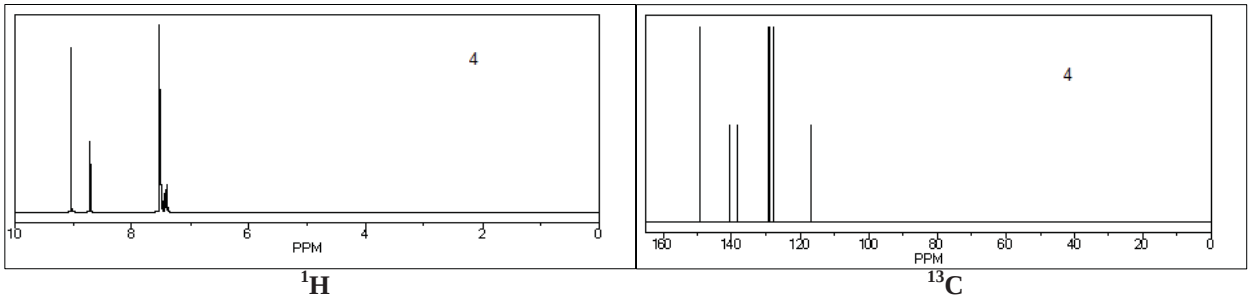

Figure 14. Predicted ^{1}H and ^{13}C NMR spectra for biphenyl derivative 4.

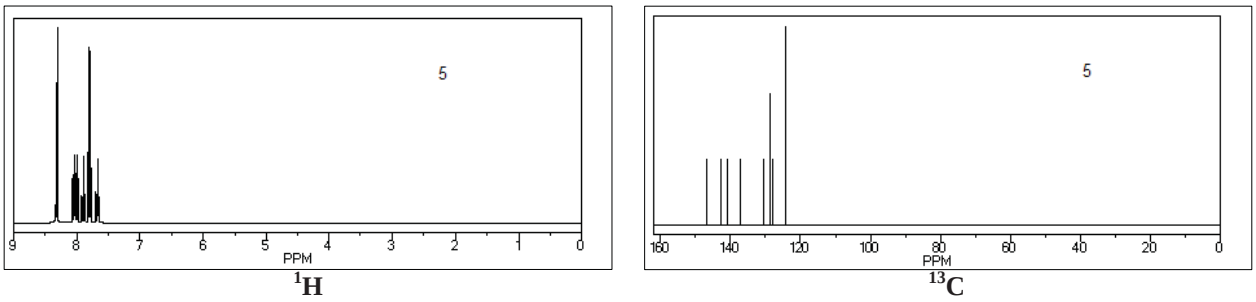

Figure 15. Predicted ^{1}H and ^{13}C NMR spectra for biphenyl derivative 5.

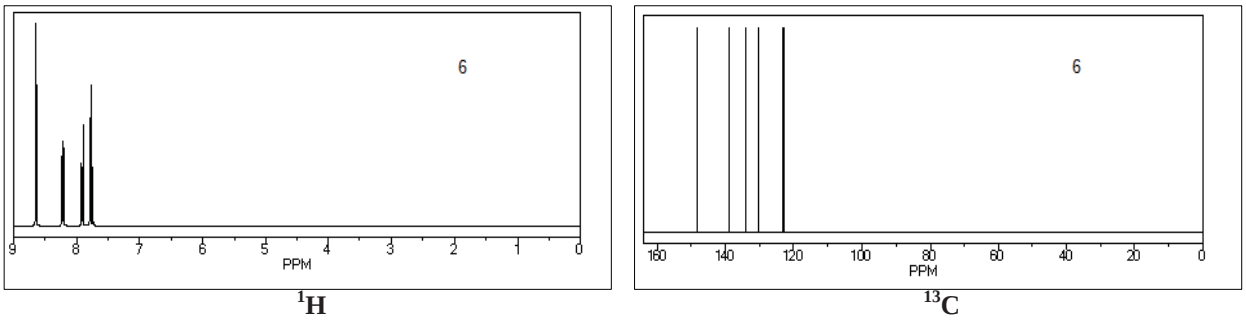

Figure 16. Predicted ^{1}H and ^{13}C NMR spectra for biphenyl derivative 6.

Conclusions

The values of geometric optimization (bond length and its angles) for dinitrobiphenyl molecules **2-6** are slightly different in the case of substitution of hydrogen by NO_2 groups, also depending on the substituted atom's position.

The *HOMO* energy values are decreasing, while the *LUMO* energy values are increasing at the substitution of hydrogen atoms by NO_2 groups, the *HOMO* and *LUMO* energy values for biphenyl molecule **1** being in a good agreement

with experimental values. The electronic density is distributed to the different parts of dinitrobiphenyl molecules **2-6** and along the C-C rings.

The values of *IP* are increasing, while the values of the *EA* are decreasing in case of the substitution of the hydrogen atoms by NO_2 groups, while the calculated values of χ, *S*, η and *W* are increasing.

According to the IR spectra, the substitution of hydrogen atoms by NO_2 groups leads to increasing the number of vibrational modes, also the stretching vibrations of dinitrobiphenyl molecules **2-6** are increasing compeer with biphenyl molecule **1.**

According to the data of ^{1}H and ^{13}C NMR spectra, it was found that the substitution of hydrogen atoms by NO_2 groups causes appearance of new peaks for dinitrobiphenyl molecules **2-6**. The molecules **3** and **5** have a complex ^{1}H NMR spectrum, because of the mutual influences between the nuclei inside the molecules, which lead to increase in intensity of some lines with respect to the other spectrum lines. The molecule **4** has high values in chemical shift of ^{1}H nuclei and ^{13}C nuclei in comparison with the other dinitrobiphenyl molecules.

Acknowledgments

I gratefully thank to my supervisor Prof. Dr. Dhia Hamdi Al-Amiedy, College of Science for Women, University of Baghdad-Iraq, for his invaluable assistance during preparation of this paper.

References

1. Zhuravlev, K.K.; McCluskey, M.D. Infrared spectroscopy of biphenyl under hydrostatic pressure. Journal of Chemical Physics, 2002, 117(8), pp. 3748-3752.
2. Budavari, S.; O'Neil, M.J.; Smith, A.; Heckelman P.E. Eds. The Merck Index. 11th Edition, Merck&Co Inc.: New York, 1989, 1258 p.
3. Sittig, M. Ed. Handbook of Toxic and Hazardous Chemicals and Carcinogens. 2nd Edition, Noyes Publications: New York, 1985, 3040 p.
4. Robertson, W.; Hansen, G. PCBs: recent advances in environmental toxicology and health effects. University Press of Kentucky, Lexington, KY: Kentucky, 2001, p. 11
5. O'Neil, M. The Merck Index, 14th Edition, Merck&Co Inc.: New York, 2006, p. 204.
6. Chen, F.-F.; Wang, F. Electronic structure of the azide group in 3′-azido-3′-deoxythymidine (AZT) compared to small azide compounds. Molecules, 2009, 14(7), pp. 2656-2668.
7. Kumar Pandey, A.; Bajpai, A.; Baboo, V.; Dwivedi, A. Structural, electronic, and vibrational properties of isoniazid and its derivative N-cyclopentylidenepyridine-4-carbohydrazide: A quantum chemical study. Journal of Theoretical Chemistry, 2014, Article ID 894175, 15 p., doi:10.1155/2014/894175.
8. Glossman-Mitnik, D.; Barraza-Jiménez, D.; Flores-Hidalgo, M.A.; Rodriguez-Valdez, L.M. Molecular structure and substitution effects on diphenylanthrazolines for organic semiconductors: A theoretical study. Journal of Molecular Structure, 2008, 863, pp. 99–104.
9. Saleha, B.A.; Abood, H.A.; Miyamoto, R.; Bortoluzzi, M. Theoretical study of substituent effects on electronic and structural properties of 2,4-diamino-5-para-substituted-phenyl-6-ethyl-pyrimidines. Journal the Iranian Chemical Society, 2011, 8(3), pp. 653-661.
10. Frisch, M.J.; Trucks, G.W.; Schlegel, H.B. et al. Gaussian 09, Revision A.02; Gaussian, Inc.: Wallingford, CT, 2009.
11. Vektariene, A.; Vektaris, G.; Svoboda, J. A theoretical approach to the nucleophilic behavior of benzofused thieno[3,2-b]furans using DFT and HF based reactivity descriptors. ARKIVOC, 2009, (vii), pp. 311-329.
12. Dwivedi, A.; Baboo, V.; Bajpai, A. Fukui function analysis and optical, electronic, and vibrational properties of tetrahydrofuran and its derivatives: a complete quantum chemical study. Journal of Theoretical Chemistry, 2015, Article ID 345234, 11 p., doi:10.1155/2015/345234.
13. Zeroual, A.; Hammal, R.; Ryachi, K.; Barhoumi, A.; Benharref, A.; Hajbi, A.El. Understanding the regioselectivity and reactivity of β-himachalene using zeroual function as a new regioselectivity. International Journal of Innovation and Applied Studies, 2014, 8(2), pp. 750-755.
14. Parr, R.; von Szentpa´ly, L.; Liu, S. Electrophilicity index. Journal of the American Chemical Society, 1999, 121, pp. 1922-1924.
15. von Marius, B. Phase coherent electronic transport through single molecules and graphene nanostructures. Universität Karlsruhe (TH), 2008. http://www.tfp.uni-karlsruhe.de/Publications/Pub2008/diplom_buerkle.pdf.
16. Jin, Y.; Lei, W. Synthesis and Characterization of Dinuclear NHC–Palladium Complexes and Their Applications in the Hiyama Reactions of Aryltrialkyoxysilanes with ArylChlorides. Electronic Supplementary Material (ESI) for Dalton Transactions, 2012. http://www.rsc.org/suppdata/dt/c2/c2dt31174g/c2dt31174g.pdf.

ELECTRON MICROSCOPY OF ANIONIC SURFACTANT-DIRECTED SYNTHESIS OF MAGNETITE NANOPARTICLES

Sharali Malik[a*], Ian James Hewitt[b], Annie Katherine Powell[a,b]

[a]*Institute of Nanotechnology, Karlsruhe Institute of Technology, North Campus, Karlsruhe D-76021, Germany*
[b]*Institute of Inorganic Chemistry, Karlsruhe Institute of Technology, South Campus, Karlsruhe D-76131, Germany*
[*]*e-mail: sharali.malik@kit.edu*

Abstract. Here we report new work on the synthesis and an electron microscopy study of the earliest known magnetic material, magnetite (Fe_3O_4). We have synthesized a variety of magnetite nanoparticles which appear to have biogenic signatures and could give insights into how the nanomagnetite in biological systems forms, and how they may be associated with Alzheimer's disease. We have also synthesized mesoporous magnetite nanoparticles which have potential use in the targeted drug delivery.

Keywords: magnetite, magnetic nanoparticles, hydrothermal synthesis, drug delivery.

Received: October 2015/ Revised final: December 2015/ Accepted: December 2015

Introduction

Magnetite (Fe_3O_4) in the form of lodestone is the original magnetic material used by mankind to navigate the Earth by following geomagnetic field lines. It is also used for navigation in Nature by honey bees, homing pigeons and bacteria. Currently, magnetic nanoparticles are used for data storage, magnetic resonance imaging (MRI) and are the potential colloidal mediators for cancer magnetic hyperthermia. This area of nanotechnology spans the boundaries of chemistry, biology, medicine and materials science.

The earliest reported medical use of magnetite powder for internal applications was in the 11th century A.D. by the Persian physician and philosopher Avicenna of Bokhara [1,2]. Today magnetic nanoparticles are used for magnetic resonance imaging (MRI) and as colloidal mediators for magnetic hyperthermia cancer treatment [3].

In 1992, it was reported that magnetite (Fe_3O_4) is present in the human brain [4] and more recently that nanoscale biogenic magnetite is associated with neurodegenerative diseases such as Alzheimer's [5]. Although this association was first discovered over fifty years ago by Goodman [6], to date the magnetite's origin and formation are not certain. Here we show that the synthesis of magnetite in the presence of the surfactant sodium dodecyl sulphate (SDS) gives rise to a variety of nanoscale morphologies, some of which look remarkably similar to magnetite found in organisms, suggesting that similar processes may be involved. Furthermore, these 0D materials with nanoscale dimensions and with the potential to show quantum confinement effects are of interest in the areas of biosensors [7], biomedical imaging [8] and as tunneling magnetoresistance (TRM) sensor elements in magnetic random access memory (MRAM) configurations, which can be used to form magnetic, programmable biochips [9].

In the more extensively studied magnetotactic bacteria [10], biogenically controlled morphologies of magnetite, which normally crystallises in a cubic space group, occur in the form of nanocrystals.These have been found to have elongated {111} axes often with rhombic or truncated dodecahedral morphology. They are part of intracellular structures called magnetosomes [11], which consist of a nanocrystal surrounded by a lipid bilayer membrane. They arrange in a 1D array to form a "compass needle", which is utilised by the bacteria to sense the Earth's magnetic field [12,13]. Figure 1 shows two typical examples of these magnetotactic bacteria [14].

Taking this lead from biology, where the biogenic templates produce magnetite of defined shapes and sizes, we have been interested in investigating how surfactant molecules could similarly influence magnetite formation.

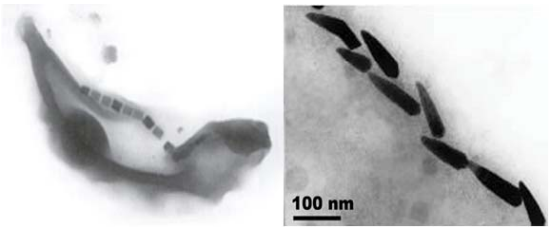

Figure 1. Two examples of magnetite in magnetotactic bacteria. Left: *Magnetospirillum magnetotacticum* (whole organism) showing the location of magnetoite crystals and Right: an example of a string of bullet-shaped crystals within a magnetotactic bacterium [14],
Copyright (2008) Federation of European Microbiological Societies.

Presented at the XVIII-th International Conference "Physical Methods in Coordination and Supramolecular Chemistry"
(Dedicated to the memory of the professor Constantin Turta and professor Mihail Revenco), 8-9 October 2015, Chisinau, Republic of Moldova

Experimental

Materials

All chemicals were reagent grade and used without further purification. Ferrous chloride tetrahydrate ($FeCl_2 \cdot 4H_2O$ > 99%), sodium hydroxide (NaOH > 97%) and sodium dodecyl sulphate (SDS > 99%) were purcheased from Sigma-Aldrich. Double distilled water, sodium hydroxide solutions and SDS solutions were deoxygenated by bubbling through N_2 gas for 1 h prior to use. The synthesis of magnetite was performed under nitrogen in an autoclave using a 20 mL Teflon insert.

Compounds 1-5 preparation

To an aqueous solution containing $FeCl_2 \cdot 4H_2O$ and SDS, a deoxygenated aqueous NaOH solution was added (Table 1). The autoclave was heated to 200 °C for 24 h and after cooling the magnetite was isolated as detailed below.

Table 1

Reagent quantities and concentrations used to prepare compounds 1-5.

Compound	*$FeCl_2 \cdot 4H_2O$ (0.2 M)*	*NaOH (1 M)*	*SDS*
1	5.0 mL	2.0 mL	0.5 mL (15 mM)
2	5.0 mL	1.0 mL	2.0 mL (15 mM)
3	5.0 mL	1.0 mL	0.5 mL (35 mM)
4	5.0 mL	1.0 mL	0.5 mL (35 mM)
5	5.0 mL	1.0 mL	0.5 mL (35 mM)

The suspended magnetite/surfactant product was put in a sonication bath (Qualilab USR-30 H) for 1 h. The suspension was then diluted with a 20 fold excess of distilled water before being sonicated again for 10 min and centrifuged (Heraeus Instruments, Labofuge 400) at 3500 rcf for 30 min. The samples containing particles less than 100 nm in size were filtered (NC10; Schleicher & Schuell) prior to sonication and centrifugation. The magnetite sediment was suspended in ethanol and sonicated for a few seconds and then "spotted" onto carbon coated copper grids of 400 mesh size for TEM examination and onto 1 cm squares of polished silicon wafers for SEM examination and then dried before analysis.

Equipment

Scanning electron microscopy (SEM) was performed using a LEO 1530 scanning electron microscope operating at 3 KeV. Transmission electron microscopy (TEM) measurements were performed using a Tecnai T20 ST transmission electron microscope operating at 200 KeV.

Results and discussion

In the course of our experiments, we found that hydrothermal conditions can be used to produce octahedral magnetite (Figure 2) as typically observed under geological conditions (Figure 3).

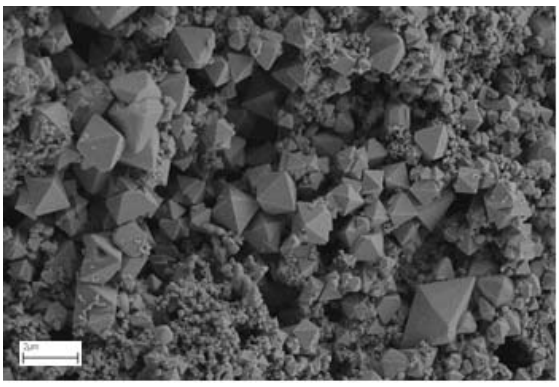

Figure 2. Octahedrally shaped magnetite. SEM of magnetite formed hydrothermally without SDS present.

Figure 3. Geological octahedrally shaped magnetite crystallised on feldspar and quartz found in Bolivia (photo by S. Malik).

However, when SDS (Figure 4) is present, we found instead a variety of magnetite morphologies, which appear to have biogenic trademarks. SDS (Figure 4) is commonly used to mimic hydrophobic binding environments such as cell membranes [15] and has been used to study the folding and thermal stability of cytochrome c (cyt c), which is a biologically important electron transfer system [16].

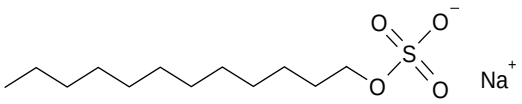

Figure 4. The anionic surfactant SDS.

The synthesis of magnetite in the presence of SDS under hydrothermal conditions yielded a variety of magnetite morphologies, as revealed by SEM and TEM. We discuss five of these morphologies here.

Firstly, bullet shaped needles with an aspect ratio of 1:6-8 and 1-2 μm in length with square-pyramidal endings (system 1, Figure 5) can be observed as aligned bundles and rather unusually these crystals frequently grow with a 90° bend. Acicular magnetite and maghemite with similar aspect ratios and sizes are commonly used for magnetic media devices. However, the route of synthesis of these crystallites is not straightforward and typically involves the synthesis of goethite (α-FeOOH) or lepidocrocite (γ-FeOOH), followed by dehydration to form hematite (α-Fe_2O_3) and then reduction to magnetite. Then, this can be re-oxidised to give maghemite [17,18].

Arrays of magnetite octahedra (system 2, Figure 6) were observed having 80-100 nm dimensions and forming 1D stacks of up to 4 μm in length. In 2008, Schumann *et al*. reported magnetofossils derived from magnetotactic bacteria which, as seen from their SEM images and drawings depicted in Figure 7, show similar morphological features with spearhead-like magnetite particles.

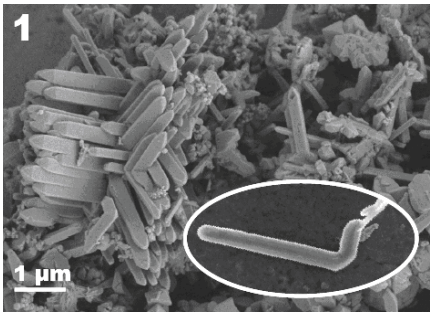

Figure 5. Bullet shaped needles which are frequently observed with a 90° bend.

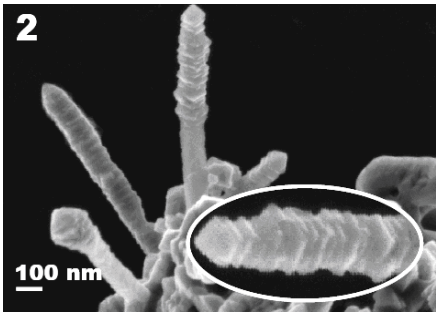

Figure 6. SEM of ordered 1D array of nanocrystallites.

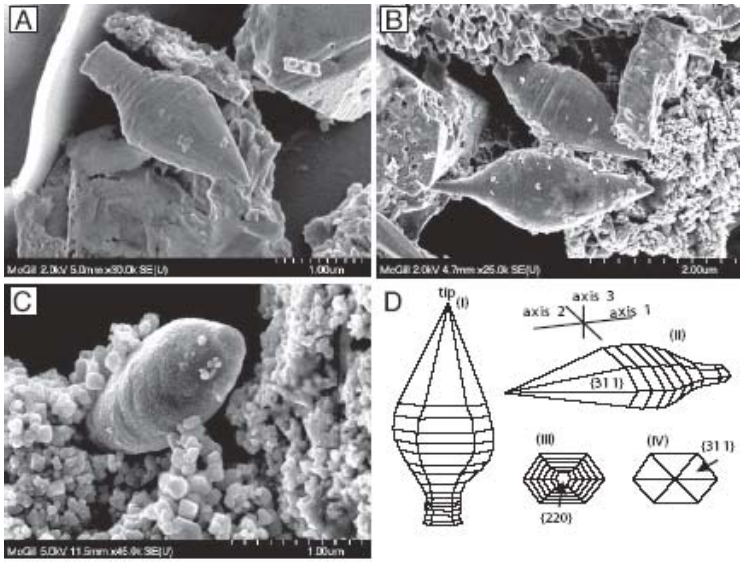

Figure 7. Magnetofossils derived from magnetotactic bacteria [19].
Copyright (2008) National Academy of Sciences, USA.

Whiskers with an aspect ratio of 1:10 (system 3, Figures 8 *(a)* to *(d)*), typically around 100-200 nm in length, are also formed and they self-assemble into 2D hexagonal plates and 3D ”flower” motifs.

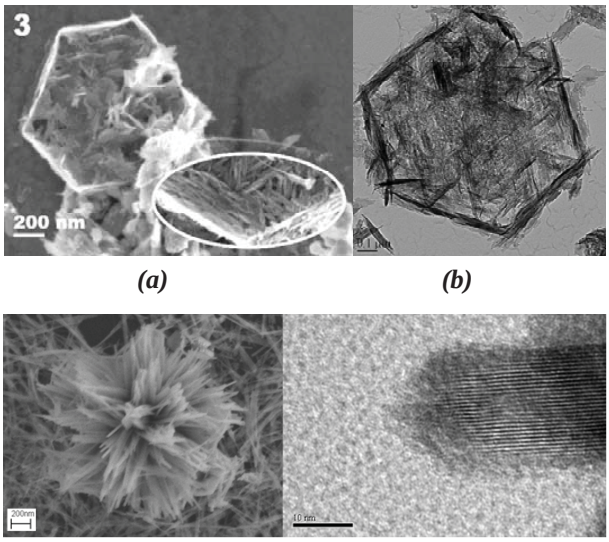

(a) *(b)*

(c) *(d)*

Figure 8. ***(a)*** **SEM overview and detail (inset);**
(b) **TEM overview of whiskers forming 2D hexagonal plate motifs;**
(c) **SEM overview of magnetite whiskers in 3D flower motifs;**
(d) **TEM detail of whisker tip.**

String-like crystallite assemblies are observed (system 4, Figure 9) with the strings composed of nanocrystals less than 10 nm in diameter arranged in helical bundles of 70-200 nm in diameter and up to 5 **μm** in length. These are reminiscent of the magnetite spheres reported by Hou *et al*. [20], which were prepared hydrothermally by reducing [$Fe(acac)_3$] in the presence of various surfactants, and is the only other report of such an unusual form of magnetite produced hydrothermally. Finally, mesoporous nanocrystallites form (system 5, Figure 10 *(a)* and *(b)*) with diameters of 40-100 nm and morphology similar to the widely reported truncated dodecahedral shape seen in certain magnetotactic bacteria [12]. These nanocrystallites, as observed for system 3, also seem to self-align. The "question-mark" motif seen in Figure 10 *(a)* is typical.

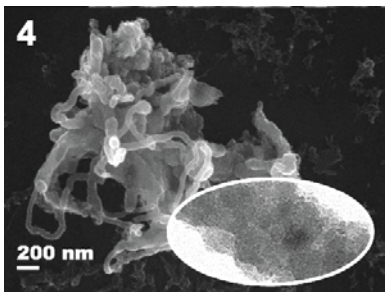

Figure 9. SEM of string-like assemblies composed of nanocrystallites (the insert shows a TEM image).

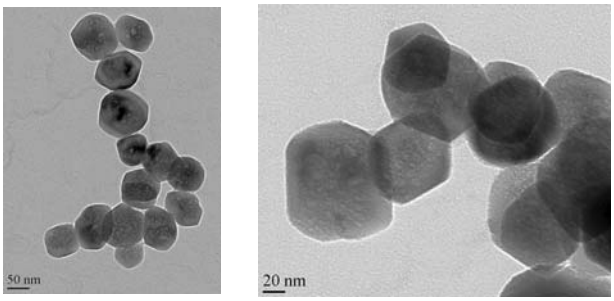

(a) *(b)*

Figure 10. ***(a)*** **TEM overview and** ***(b)*** **TEM detail of mesoporous magnetite nanocrystallites.**

It has been reported that magnetosome vesicles are present before magnetite formation in magnetotactic bacteria [21] and we can draw a parallel to this situation given the presence of SDS micelles providing a reaction space for formation of nanocrystalline magnetite arrays. In addition to its "biogenic signature", this mesoporous nanomagnetite may prove useful for targeted drug delivery [22].

Conclusions

In Nature, the synthesis of the bacterial magnetosome seems to be a complex process that involves several discrete steps, including magnetosome vesicle formation, iron uptake by the cell, iron transport into the magnetosome vesicle and controlled Fe_3O_4 biomineralization within the magnetosome vesicle. In general, there has been little research regarding the methods by which bacteria synthesize these mineral crystals in specific morphologies.

In our experiments, we have shown that the synthesis of magnetite in the presence of the surfactant sodium

dodecyl sulphate gives rise to a variety of nanoscale morphologies, some of which look remarkably similar to magnetite found in organisms, suggesting that similar morphological control processes may be involved.

Furthermore, these 0D materials with nanoscale dimensions are of interest in the areas of biosensors and biomedical imaging. The magnetite whiskers, in particular, are ideally suited for use in "lab-on-a-bead" devices, which have whisker morphology and are set to be the next-generation lab-on-a-chip devices. They are both cheaper and better suited to use in field diagnostics and theranostics. In addition, the whiskers are the ideal shape for use as tunneling magnetoresistance (TRM) sensor elements in magnetic random access memory (MRAM) configurations, which can be used to form magnetic, programmable biochips.

Acknowledgements

The authors would like to thank the D.F.G. Center for Functional Nanostructures for financial support. They would also like to thank Harald Rösner (now at University of Münster) for assistance with the TEM. This work is part of COST Action TD1402 "Multifunctional Nanoparticles for Magnetic Hyperthermia and Indirect Radiation Therapy (RADIOMAG)".

References

1. Avicenna (Abu Ali Sina). The Canon of Medicine, 1025, 510 p. https://archive.org/stream/AvicennasCanonOfMedicine/9670940-Canon-of-Medicine#page/n0/mode/2up
2. Andrä, W.; Nowak, H. Eds. Front Mater, in Magnetism in Medicine: A Handbook. Second Edition. Wiley-VCH Verlang GmbH & Co. KGaA: Weinheim, Germany. 2007, doi: 10.1002/9783527610174.fmatter.
3. Mornet, S.; Vasseur, S.; Grasset, F.; Veverka, P.; Goglio, G.; Demourgues, A.; Portier, J.; Pollert, E.; Duguet. E. Magnetic nanoparticle design for medical applications. Progress in Solid State Chemistry, 2006, 34, pp. 237-247.
4. Kirschvink, J.L.; Kobayashi-Kirschvink, A.; Woodford, B.J. Magnetite biomineralisation in the human brain. Proceedings of the National Academy of Sciences, 1992, 89, pp. 7683-7687.
5. Hautot, D.; Pankhurst, Q.A.; Khan, N.; Dobson, J. Preliminary evaluation of nanoscale biogenic magnetite in Alzheimer's disease brain tissue. Proceedings of the Royal Society B (Supplementary), 2003, 270, pp. S62-S64.
6. Goodman L. Alzheimer's disease: A clincopathologic analysis of twenty-three cases with a theory on pathogenesis. Journal of Nervous and Mental Diseases, 1953, 118, pp. 97-130.
7. Murphy, C. J. Biosensors: Plasmons spring into action. Nature Materials, 2007, 6, pp. 259-260.
8. Bratschitsch, R.; Leitenstorfer A. Quantum dots: Artificial atoms for quantum optics. Nature Materials, 2006, 5, pp. 855-856.
9. Reiss, G., Brueckl, H.; Huetten, A.; Schotter, J.; Brzeska, M.; Becker, A.; Kamp, P.B.; Puehler, A.; Wojczykowski, K.; Jutzi, P. Magnetoresistive sensors and magnetic nanoparticles for biotechnology. Journal of Materials Research, 2005, 20(12), pp. 3294-3302.
10. Frankel, R.B.; Blakemore, R.P. Iron Biominerals, Plenum, New York, 1990, 435 p.
11. Balkwil, D.L.; Maratea, D.; Blakemore, R.P. Ultrastructure of a magnetic spirillum. Journal of Bacteriology, 1980, 141, pp. 1399-1408.
12. Cornell, R.M.; Schwertmann, U. The Iron Oxides. Wiley-VCH: Weinheim, 1996, 664 p.
13. Schüler, D. Molecular analysis of a subcellular compartment: the magnetosome membrane in *Magnetospirillum gryphiswaldense*. Archives of Microbiology, 2004, 181, pp. 1-7.
14. Schüler D. Genetics and cell biology of magnetosome formation in magnetotactic bacteria. Federation of European Microbiological Sciences, Microbiological Reviews, 2008, 32, pp. 654-672.
15. Jones, M.N. Biological interfaces: An Introduction to the Surface and Colloid Science of Biochemical and Biological System. Elsevier: Amsterdam, 1975, 240 p.
16. Xu, Q.; Keiderling, T.A. Effect of sodium dodecyl sulfate on folding and thermal stability of acid-denatured cytochrome c: A spectroscopic approach. Protein Science, 2004, 13, pp. 2949-2959.
17. Büchel, K.H.; Moretto, H.-H.; Woditsch, P. Industrial Inorganic Chemistry. Wiley-VCH: Weinheim, 2000, 655 p.
18. Sharrock, M.P.; Bodnar, R.E. Magnetic materials for recording: An overview with special emphasis on particles, Journal of Applied Physics, 1985, 57, pp. 3919-3924.
19. Schumann, D.; Raub, T.D.; Kopp, R.E.; Guerquin-Kern, J-L.; Wu, T-D.; Rouiller, I.; Smirnov, A.V.; Sears, S.K.; Lücken, U.; Tikoo, S.M.; Hesse, R.; Kirschvink, J.L.; Vall, H. Gigantism in unique biogenic magnetite at the Paleocene-Eocene Thermal Maximum. Proceedings of the National Academy of Sciences, 2008, 105(46), pp. 17648-17653.
20. Hou, Y.; Gao, S.; Ohta, T.; Kondoh, H. Towards 3-D Spherical Self-Assembly by Ternary Surfactant Combinations: The Case of Magnetic Nanoparticles. European Journal of Inorganic Chemistry, 2004, 6, pp. 1169-1173.
21. Komelli, A.; Vali, H.; Beveridge, T.J.; Newman, D.K. Magnetosome vesicles are present before magnetite formation and MamA is required for their activation. Proceedings of the National Academy of Sciences, 2004, 101(11), pp. 3839-3844.
22. Andrä, W.; Nowark H. Magnetism in Medicine. Wiley-VCH: Berlin, 1998, 629 p.

DFT (B3LYP) COMPUTATIONAL STUDY ON THE MECHANISMS OF FORMATION OF SOME SEMICARBAZONES

Abdulfatai Siaka[a*], Adamu Uzairu[b], Sulaiman Idris[b], Hamza Abba[a]

[a]*Department of Applied Chemistry, Federal University, P.M.B 5001, Dutsin-ma 823103, Katsina, Nigeria*
[b]*Department of Chemistry, Ahmadu Bello University, P.M.B 51, Zaria 810001, Kaduna, Nigeria*
[*]*e-mail: fatsaadaby@gmail.com*

Abstract. Thermodynamic and kinetic mechanisms of forming six semicarbazones have been investigated computationally by DFT B3LYP method. All the reactions proceed *via* two transitions and include two consecutive steps: bimolecular and unimolecular. The computed transition steps have varying equilibrium constants values, enthalpy of activation and Gibbs energy of activation, depending on the semicarbazone involved. Also depending on the semicarbazones involved some of the consecutive steps are found to have varying enthalpy of reactions and spontaneity.

Keywords: semicarbazone, kinetics, bi- and unimolecular step, transition step, spontaneity.

Received: October 2015/ Revised final: February 2016/ Accepted: February 2016

Introduction

Semicarbazones are derivatives of imines formed by a condensation reaction between ketones or aldehydes and semicarbazide. They are classified as imine derivatives since they are formed from the reaction of an aldehyde or ketone with the terminal amino group of semicarbazide, which behaves similarly to primary amines. Some semicarbazones, such as nitrofurazone and thiosemicarbazones are known to have anti-viral and anti-cancer activity, usually mediated by binding to copper or iron in cells. Many semicarbazones are crystalline solids, useful for the identification of the parent aldehydes or ketones by melting point analysis [1]. Semicarbazones show a wide range of bioactivities, and their chemistry and pharmacological applications have been extensively studied. The biological properties of semicarbazones are often related to metal ion coordination. A variety of 5-nitrofuryl semicarbazone derivatives have been developed for the therapy of Chagas disease, a major problem in the Central and the South America [2]. Antiepileptic drug search has come a long way, particularly of the last two decades. With increased understanding of the pathophysiology of epilepsy, the conventional approaches have, to a great extent, been replaced by mechanism based approaches. The last decade has witnessed the emergence of semicarbazones as potential anticonvulsant agents [3,4]. Due to their biological activity there is a huge interest in the chemistry of semicarbazones [5-7]. Dimmock *et al.* have reported semicarbazones as potential anticonvulsant agents. A number of aryloxy aryl semicarbazones have shown significant anticonvulsant activity [8]. Also Padeya and his co-workers have reported on the synthesis of several analogs of semicarbazones and thiosemicarbazones with anticonvulsant properties [9-11]. To the best of our knowledge, literature on theoretical or semi-empirical kinetic and thermodynamic data on the reaction mechanisms of preparation of these very important molecules is very scanty. Current study attempts to provide information in this area by using theoretical and computational methods.

Computational Methods

The computation was carried out using SPARTAN14 program suite on intel(R) CORE(TM) i5-4200U CPU @ 1.60GHz 2.30 GHz hp computer. The geometries of the reactants, transition states, intermediates and products were optimized using Molecular mechanics to remove strain energies. This was followed by semi empirical optimizations at RM1 theory level. Finally, DFT Becke's three parameter nonlocal exchange functional with the nonlocal correlation functional of Lee, Yang, Parr (B3LYP) with 6-311+G** basis set calculations was employed. Intrinsic reaction coordinate calculation was carried out at B3LYP theory level. Furthermore, heat of formation was calculated for all the stationary points using thermochemical recipe at T_1 theory level after the optimization. For equilibrium geometries and transition states, the nature of the critical points was confirmed by an analytic frequency computation, and all the transition states have imaginary frequencies. All the energy parameters of the reaction mechanisms are calculated using the reported in literature expressions. Gibbs energy change, reaction rates (*k*) and equilibrium constants (*K)* were calculated using the expressions (1)-(5) given below [12]:

$$\Delta G^{\ddagger}_{(298.15K)} = \Delta H^{\ddagger} - T\Delta S^{\ddagger} \quad (1)$$

$$k_{(298.15K)} = \frac{k_B T}{hc^o} e^{\Delta S^{\ddagger}/R} e^{-\Delta H^{\ddagger}/RT} \quad (2)$$

$$K_{(298.15K)} = e^{-\Delta G^o/RT} \quad (3)$$

$$K_{(298.15K)} = e^{-\Delta G^o/RT} \quad (3)$$

$$A = \frac{e^2 k_B T}{hc^o} e^{\frac{\Delta S^{\#}}{R}}, \text{ for bimolecular step} \quad (4)$$

$$A = \frac{e k_B T}{h} e^{\frac{\Delta S^{\#}}{R}}, \text{ for unimolecular step} \quad (5)$$

where $\Delta G^{\#}$, $\Delta H^{\#}$ and $\Delta S^{\#}$ stand for Gibbs energy change, enthalpy change and entropy change, respectively, for reaction between reactant(s) and a transition state, k_B is Boltzmann's constant, R is gas constant, h is Planck's constant, c^o is concentration (taken as unity), T is temperature and stands for Gibbs energy change for reaction between reactant(s) and intermediate or product.

Results and discussion

Reaction between m-nitrobenzaldehyde and semicarbazide

The computed general reaction mechanism of forming the (*E*)-2-(3-nitrobenzylidene)hydrazinecarboxamide and water from *m*-nitrobenzaldehyde and semicarbazide is presented and discussed herein. Figures 1 and 2 show the general reaction mechanism and schematic diagram of relative electronic energy of reaction, respectively, while Tables 1 and 2, respectively, present thermodynamic and kinetic parameters of the computed reaction mechanism.

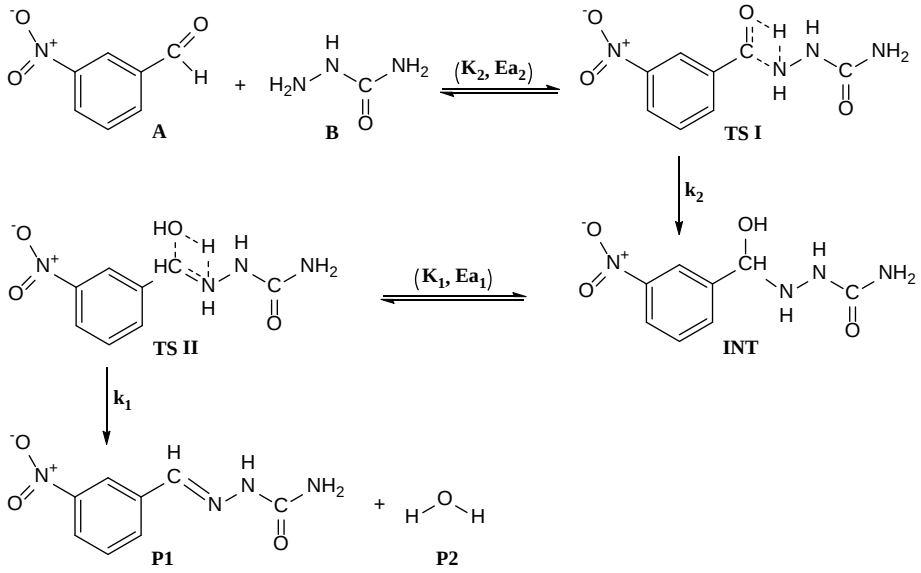

Figure 1. General scheme for the mechanism of reaction between *m*-nitrobenzaldehyde and semicarbazide.

Table 1

DFT B3LYP (6-311+G) calculated thermodynamic parameters for reaction between *m*-nitrobenzaldehyde and semicarbazide.**

Steps	$\Delta S^{\#}_{reaction}$ *(Jmol^{-1}K^{-1})*	$\Delta H^{\#}_{reaction}$ *(kJmol^{-1})*	$\Delta G^{\#}_{reaction}$ *(kJmol^{-1})*	$\Delta S^{o}_{reaction}$ *(Jmol^{-1}K^{-1})*	$\Delta H^{o}_{reaction}$ *(kJmol^{-1})*	$\Delta G^{o}_{reaction}$ *(kJmol^{-1})*
A + B⇌TSI	-238.89	-24.16	+47.06			
A+B→INT				-246.60	-40.82	+32.71
INT⇌TSII	+36.78	-0.60	-11.12			
INT→P1+P2				+173.30	+9.99	-41.68

Table 2

DFT B3LYP (6-311+G) calculated activation energy (E_a), frequency factor (A), rate constant (k) and equilibrium constant (K) for reaction between *m*-nitrobenzaldehyde and semicarbazide.**

Steps	E_a *(kJmol^{-1})*	A	k_2 *(dm^{3}mol^{-1}s^{-1})*	K_2	k_1 *(s^{-1})*	K_1
A+B⇌TSI	+55.92	15.26 dm^{3}mol^{-1}s^{-1}		1.86×10^{-6}		
A+B→INT			3.53×10^{4}			
INTI⇌TSII	+31.24	1.41×10^{15}s^{-1}				2.00×10^{7}
INT →P1+P2					5.18×10^{14}	

From Tables 1 and 2, the first transition step has a huge energy barrier to overcome. This step is also associated with positive Gibbs energy of activation, suggesting that the step is non-spontaneous, and so energy input is a necessity to initiate it. Meanwhile the second transition step is less demanding in terms of energy, having less activation energy, but it is also reasonably spontaneous (having negative Gibbs energy of activation). Thus, the first step is exothermic but non-spontaneous. The spontaneity barrier for this step will be overcome by the higher exothermic value of the step, making the step energetically feasible. The second step is slightly endothermic but averagely spontaneous. The first transition step is associated with less pre-exponential factor, as compared to the second step, hence supporting the low equilibrium constant computed for the bimolecular transition step and the rate determining bimolecular step. The energy profile of the reaction is shown in Figure 2.

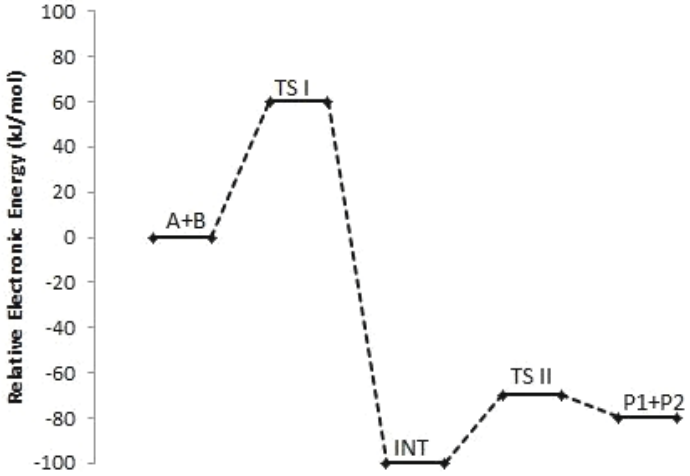

Figure 2. Diagram of relative electronic energies along the channels of the reaction between *m*-nitrobenzaldehyde and semicarbazide.

Reaction between furfural and semicarbazide

Presented as Figure 3 below is the general formation pathways for (*Z*)-2-(furan-2-ylmethylene) hydrazinecarboxamide and water from furfural and semicarbazide. Figure 4 shows the schematic diagram of the relative electronic energies of this reaction. Tables 3 and 4 present thermodynamic and kinetic parameters of the computed reaction mechanism, correspondingly.

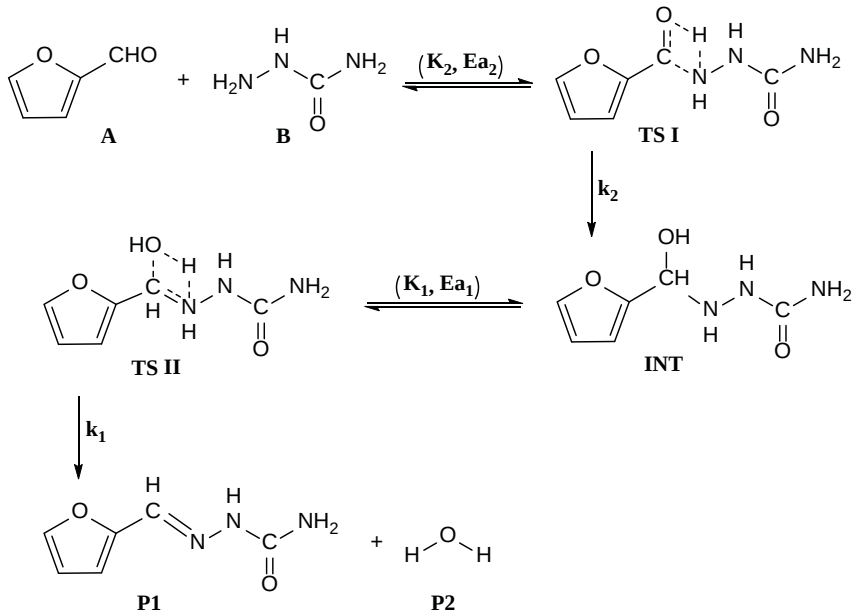

Figure 3. General scheme for the mechanism of reaction between furfural and semicarbazide.

Table 3

DFT B3LYP (6-311+G) calculated thermodynamic parameters for reaction between furfural and semicarbazide.**

Steps	$\Delta S^{\#}_{reaction}$ *(Jmol^{-1}K^{-1})*	$\Delta H^{\#}_{reaction}$ *(kJmol^{-1})*	$\Delta G^{\#}_{reaction}$ *(kJmol^{-1})*	$\Delta S^{o}_{reaction}$ *(Jmol^{-1}K^{-1})*	$\Delta H^{o}_{reaction}$ *(kJmol^{-1})*	$\Delta G^{o}_{reaction}$ *(kJmol^{-1})*
A + B⇌TSI	-225.75	-12.55	+54.76			
A+B→INT				-234.53	-52.74	17.19
INT⇌TS II	+6.66	+4.27	+2.28			
INT→P1+P2				169.80	7.59	-43.04

Table 4

DFT B3LYP (6-311+G) calculated activation energy (E_a), frequency factor (*A*), rate constant (*k*) and equilibrium constant (*K*) for reaction between furfural and semicarbazide.**

Steps	E_a *(kJmol^{-1})*	*A*	k_2 *(dm^{3}mol^{-1}s^{-1})*	K_2	k_1 *(s^{-1})*	K_1
A+B⇌TSI	168.06	74.09 dm^{3}mol^{-1}s^{-1}		9.75×10^{-4}		
A+B→INT			1.58×10^{3}			
INT⇌TS II	+157.01	3.76×10^{13}s^{-1}				3.47×10^{7}
INT→P1+P2					2.47×10^{12}	

From the high energy requirements (Gibbs energy of activation and activation energy) presented in Tables 3 and 4, the first transition step appears almost impossible without energy input into the system. Though exothermic from the enthalpy of activation value, the energy release from this step does not reach the huge energy requirement. This position is complimented by the low equilibrium constant, as presented in Table 4, suggesting some adjustment in reaction conditions for forward reaction. Similar trend is also observed in the second transition step that have high energy barrier, Gibbs energy of activation and enthalpy of activation, being also associated with low equilibrium constant. The frequency factor is indicative that only a small fraction of the reacting species is able to undergo useful collision (with required threshold energy) and finally resulting in product formation. Again the second transition step is highly demanding in energetics for forward reaction. The first step of the consecutive reaction has a very high exothermic enthalpy but slightly positive Gibbs energy of activation. This is favourable in terms of energy requirements, since the exothermic enthalpy value is much more than the Gibbs energy of reaction. Conversely, the second consecutive step is computed to be slightly endothermic but highly spontaneous. So, the energy needed for the forward reaction is compensated for by the Gibbs energy of reaction. The bimolecular step is also found to be the rate determining step. The Figure 4 shows the energy reaction profile of the reaction scheme between furfural and semicarbazide.

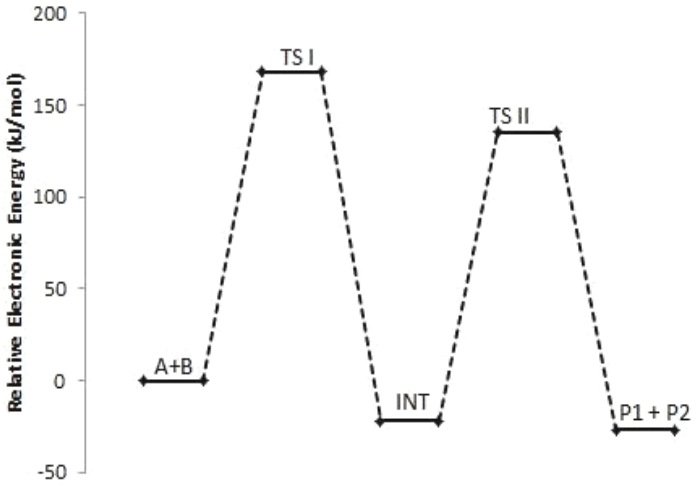

Figure 4. Diagram of relative electronic energies along the reaction channels between furfural and semicarbazide.

Reaction between p-chlorobenzaldehyde and semicarbazide

The mechanism of synthesis of 2-((4-chlorophenyl(hydroxy)methyl) hydrazinecarboxamide and water starting from *p*-chlorobenzaldehyde and semicarbazide is schematically presented in Figure 5. Figure 6 shows the schematic diagram of the electronic energies for this mechanism of reaction. Thermodynamic and kinetic data are presented in Tables 5 and 6, respectively.

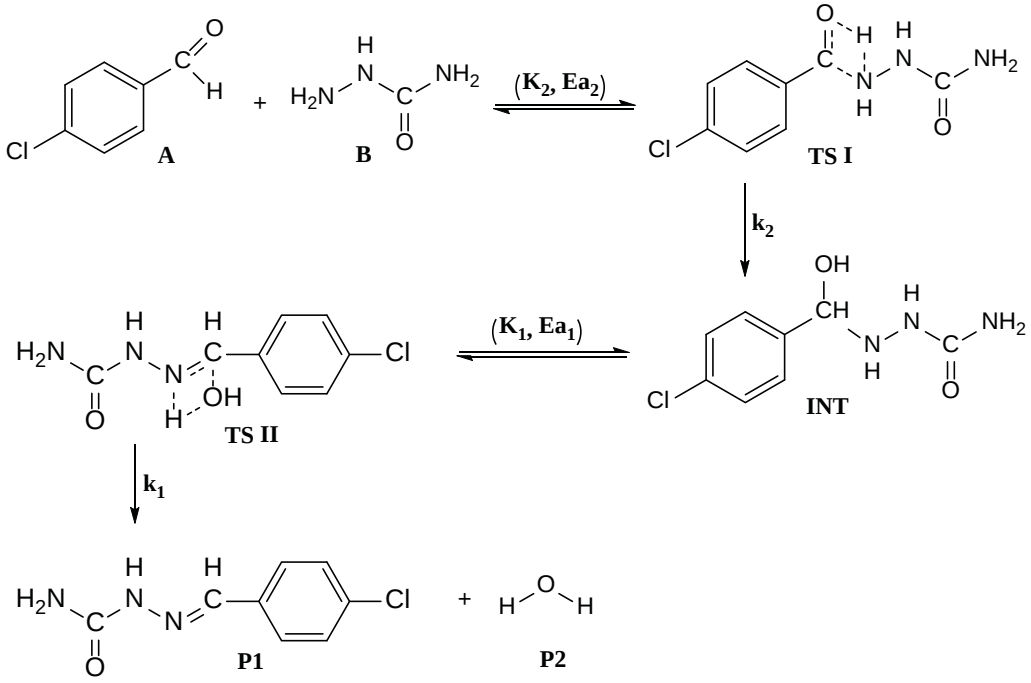

Figure 5. General mechanism scheme for reaction between *p*-chlorobenzaldehyde and semicarbazide.

Table 5

DFT B3LYP (6-311+G) calculated thermodynamic parameters for reaction between *p*-chlorobenzaldehyde and semicarbazide.**

Steps	$\Delta S^{\#}_{reaction}$ *(Jmol^{-1}K^{-1})*	$\Delta H^{\#}_{reaction}$ *(kJmol^{-1})*	$\Delta G^{\#}_{reaction}$ *(kJmol^{-1})*	$\Delta S^{o}_{reaction}$ *(Jmol^{-1}K^{-1})*	$\Delta H^{o}_{reaction}$ *(kJmol^{-1})*	$\Delta G^{o}_{reaction}$ *(kJmol^{-1})*
A + B⇌TSI	-235.91	-14.04	+56.30			
A+B→INT				-243.19	-32.74	+39.77
INT⇌TSII	+26.99	+6.44	-1.61			
INT→P1+P2				+171.20	+3.01	-48.03

Table 6

DFT B3LYP (6-311+G) calculated activation energy (E_a), frequency factor (*A*), rate constant (*k*) and equilibrium constant (*K*) for reaction between *p*-chlorobenzaldehyde and semicarbazide.**

Steps	E_a *(kJmol^{-1})*	*A*	k_2 *(dm^{3}mol^{-1}s^{-1})*	K_2	k_1 *(s^{-1})*	K_1
A+B⇌TSI	+57.76	21.85 dm^{3}mol^{-1}s^{-1}		1.08×10^{-7}		
A+B→INT			8.52×10^{4}			
INT⇌TS II	+32.29	4.34×10^{14}s^{-1}				2.60×10^{8}
INT→P1+P2					1.18×10^{13}	

The bimolecular transition step, though exothermic, is highly non spontaneous, and it has slightly high energy barrier to overcome. Hence energy input is necessary to kick start the reaction. The energy parameters for this step are presented in Table 5. Very small percentage of the reacting molecules possesses the threshold energy to undergo useful collision; this is evident from frequency factor and equilibrium constant values presented in Table 6. The unimolecular transition step is calculated to be sparingly endothermic and spontaneous, as suggested by the values of enthalpy of activation and Gibbs energy of activation (Table 5). This step has relatively less activation energy to overcome, when compared to the bimolecular step, and it is also favoured more by both pre-exponential factor and equilibrium constant

values. The first bimolecular step is found to be exothermic (by enthalpy of reaction) and non-spontaneous (by reaction free energy), indicating on the slight feasibility of this step, since the energy requirements (Table 5) for the reaction to be spontaneous are compensated for by the reaction enthalpy. Thus, bimolecular step is calculated to be the rate determining step and hence the rate determining of the overall reaction mechanism. The data for the reaction kinetics are presented in Table 6. The unimolecular consecutive step is predominantly spontaneous and slightly endothermic by the enthalpy value. In terms of energy, this step is highly feasible, as the energy requirements for endothermicity are by far overwhelmed by the Gibbs energy of reaction. Energy reaction profile for the mechanistic scheme of reaction is shown in Figure 6.

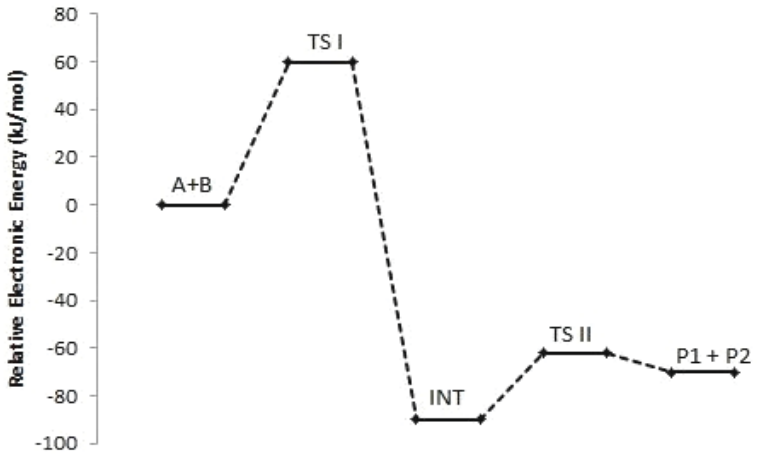

Figure 6. Diagram of relative electronic energies along the channels of the reaction between *p*-chlorobenzaldehyde and semicarbazide.

Reaction between benzaldehyde and semicarbazide

The computed mechanism of combination between benzaldehyde and semicarbazide, resulting in formation of (*E*)-2-benzylidenehydrazinecarboxamide and water, is shown in Figure 7, while Figure 8 presents the schematic diagram of the electronic energies for this reaction mechanism. The calculated thermodynamic and kinetic parameters are shown in Tables 7 and 8, respectively.

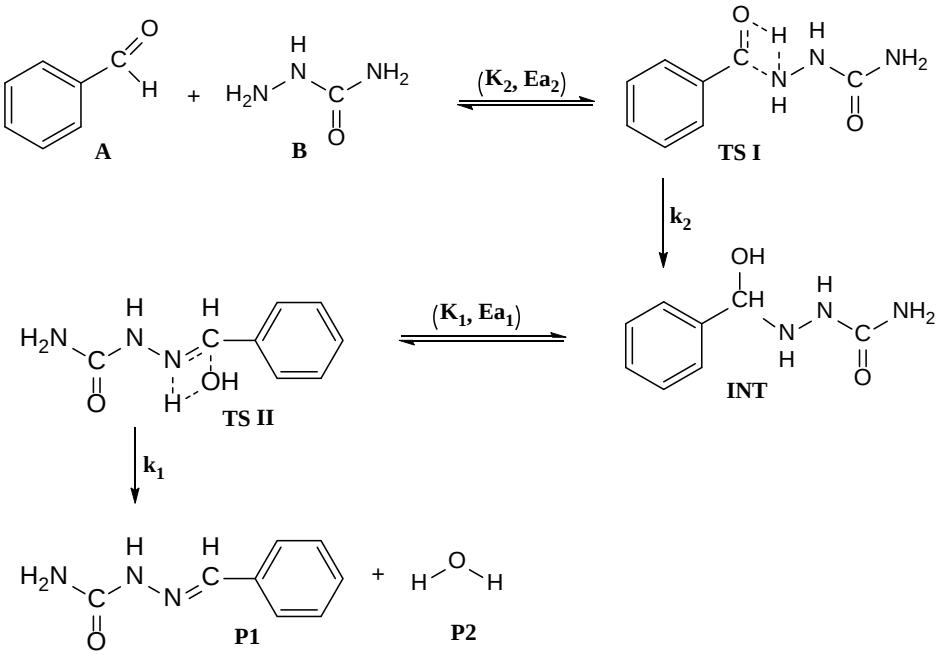

Figure 7. General scheme for the mechanism of reaction between benzaldehyde and semicarbazide.

Table 7

DFT B3LYP (6-311+G) calculated thermodynamic parameters for reaction between benzaldehyde and semicarbazide.**

Steps	$\Delta S^{\#}_{reaction}$ *(Jmol^{-1}K^{-1})*	$\Delta H^{\#}_{reaction}$ *(kJmol^{-1})*	$\Delta G^{\#}_{reaction}$ *(kJmol^{-1})*	$\Delta S^{o}_{reaction}$ *(Jmol^{-1}K^{-1})*	$\Delta H^{o}_{reaction}$ *(kJmol^{-1})*	$\Delta G^{o}_{reaction}$ *(kJmol^{-1})*
A + B⇌TSI	-232.78	-24.89	+44.51			
A+B→INT				-241.47	-26.76	+45.23
INT⇌TS II	+14.84	-15.40	-19.83			
INTI→P1+P2				+173.83	+15.07	-36.76

Table 8

DFT B3LYP (6-311+G) calculated activation energy (E_a), frequency factor (*A*), rate constant (*k*) and equilibrium constant (*K*) for reaction between benzaldehyde and semicarbazide.**

Steps	E_a *(kJmol^{-1})*	*A*	k_2 *(dm^{3}mol^{-1}s^{-1})*	K_2	k_1 *(s^{-1})*	K_1
A+B⇌TSI	+66.69	31.84 dm^{3}mol^{-1}s^{-1}		1.19×10^{-8}		
A+B→INT			9.88×10^{4}			
INT⇌TS II	+213.72	1.01×10^{14}s^{-1}				2.75×10^{6}
INT→P1+P2					1.85×10^{16}	

From Tables 7 and 8, the first (bimolecular) transition step has high activation energy to overcome and it is non-spontaneous too, though the step is computed to have an exothermic enthalpy of activation. The net effect is that some energy has to be supplied in order to initiate the reaction. As in the mechanisms of formation of the other semicarbazones under discussion in the current paper, the first transition step is characterized by low collision frequency factor and equilibrium constant values. These values suggest that the reaction conditions need to be adjusted for forward reaction, leading to product formation. The unimolecular transition step is calculated to be slightly spontaneous and exothermic. The energy from these spontaneity and exothermicity do not match huge activation energy demand of this step, therefore some intervention in form of energy input is necessary for the reaction to proceed. However, this step is found to be associated with high pre-exponential factor and equilibrium constant values. In the consecutive reaction steps, the unimolecular step is exothermic and non-spontaneous with energy deficit of about 20 kJmol^{-1} (Table 7). The energy deficit in the bimolecular step is offset by the excess energy in the unimolecular step, and hence, overall, the consecutive step is feasible. In addition, the second step in the consecutive scheme is computed to be the rate determining step and the reaction rate overall.

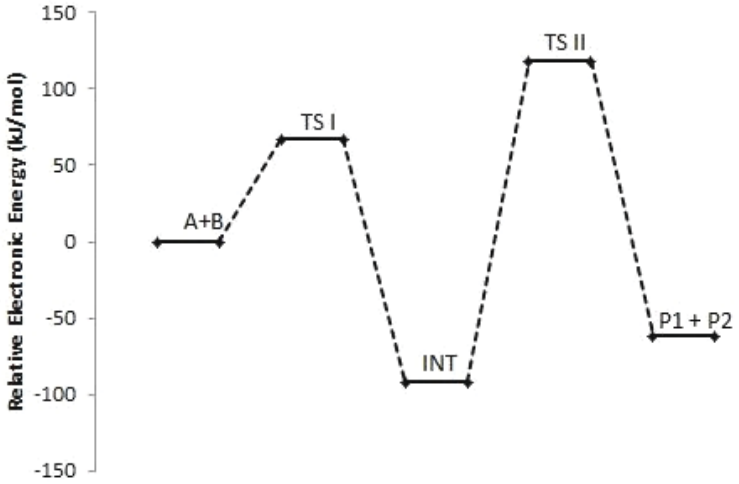

Figure 8. Diagram of relative electronic energies along the channels of the reactions between benzaldehyde and semicarbazide.

Reaction between p-methylbenzaldehyde and semicarbazide

Figure 9 illustrates the general reaction mechanism of formation of (*E*)-2-(4-methylbenzylidene) hydrazinecarboxamide (semicarbazone) and water, starting with *p*-methylbenzaldehyde and semicarbazide, while

Figure10 depicts the schematic diagram of the electronic energy of the discussed reaction mechanism. Tables 9 and 10 present thermodynamic and kinetic parameters, correspondingly, for the computed mechanism.

As shown in Tables 9 and 10, the first transition step was computed to have positive activation energy and positive Gibbs energy of activation, *i.e*. reaction is non-spontaneous, but exothermic (from enthalpy of activation). The step has huge energy deficit of slightly above 90 kJ/mol, which need to be supplied in order to initiate the reaction. The step is calculated to have very low frequency factor and small equilibrium constant values, also suggesting some adjustment in the reaction conditions to favour forward reaction. Furthermore, the second transition step is found to be hugely demanding in terms of energy, as it is calculated to have high energy barrier, and be highly non-spontaneous (from Gibbs energy of activation) and also endothermic (from enthalpy of activation) values. The first bimolecular step is exothermic and non-spontaneous, with an energy deficit as presented in Table 9. The second consecutive step is slightly exothermic but highly spontaneous with energy surplus of above 73 kJ/mol. So, the deficit in the bimolecular step is being compensated for by the surplus in the unimolecular consecutive step. Also, the second step is found to be the rate determining step, as presented in Table 10.

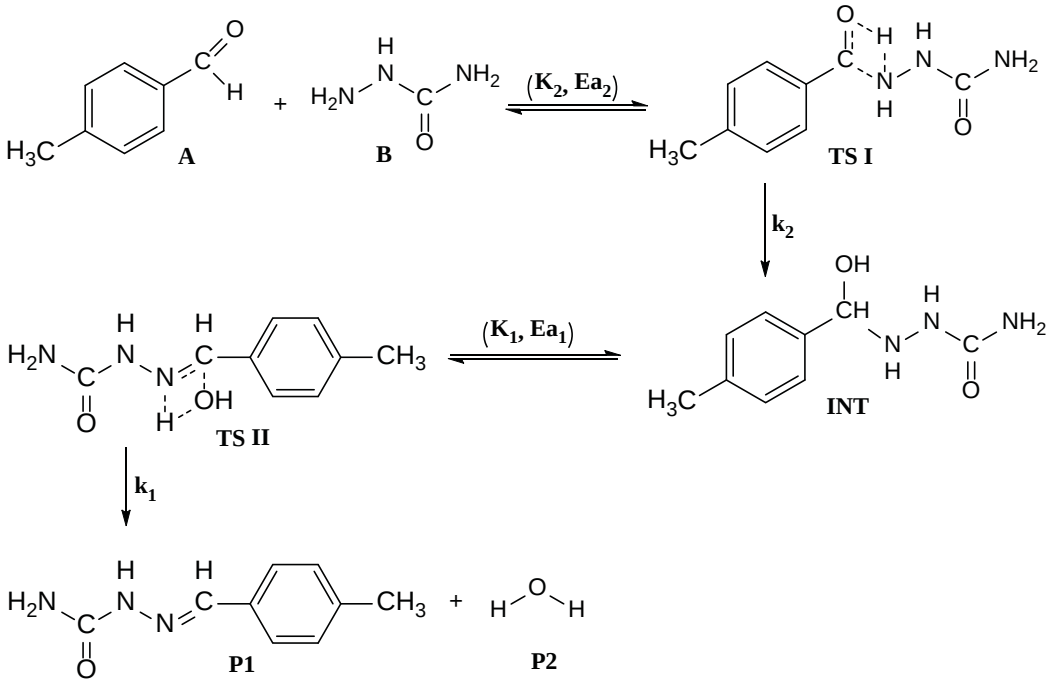

Figure 9. General scheme for the mechanism of reaction between *p*-methylbenzaldehyde and semicarbazide.

Table 9

DFT B3LYP (6-311+G) calculated thermodynamic parameters for reaction between *p*-methylbenzaldehyde and semicarbazide.**

Steps	$\Delta S^{\#}_{reaction}$ *(Jmol^{-1}K^{-1})*	$\Delta H^{\#}_{reaction}$ *(kJmol^{-1})*	$\Delta G^{\#}_{reaction}$ *(kJmol^{-1})*	$\Delta S^{o}_{reaction}$ *(Jmol^{-1}K^{-1})*	$\Delta H^{o}_{reaction}$ *(kJmol^{-1})*	$\Delta G^{o}_{reaction}$ *(kJmol^{-1})*
A + B⇌TSI	-234.54	-23.12	+46.81			
A+B→INT				-242.36	-28.53	+43.73
INT⇌TS II	+8.52	+280.45	+277.91			
INT→P1+P2				+238.25	-1.90	-72.93

Table 10

DFT B3LYP (6-311+G) calculated activation energy (E_a), frequency factor (A), rate constant (k) and equilibrium constant (K) for reaction between *p*-methylbenzaldehyde and semicarbazide.**

Steps	E_a *(kJmol^{-1})*	A	k_2 *(dm^{3}mol^{-1}s^{-1})*	K_2	k_1 *(s^{-1})*	K_1
A + B⇌TSI	+68.79	25.77 dm^{3}mol^{-1}s^{-1}		2.18×10^{-8}		
A+B→INT			3.92×10^{4}			
INT⇌TS II	+183.26	4.70×10^{13}s^{-1}				5.99×10^{12}
INT→P1+P2					1.28×10^{-36}	

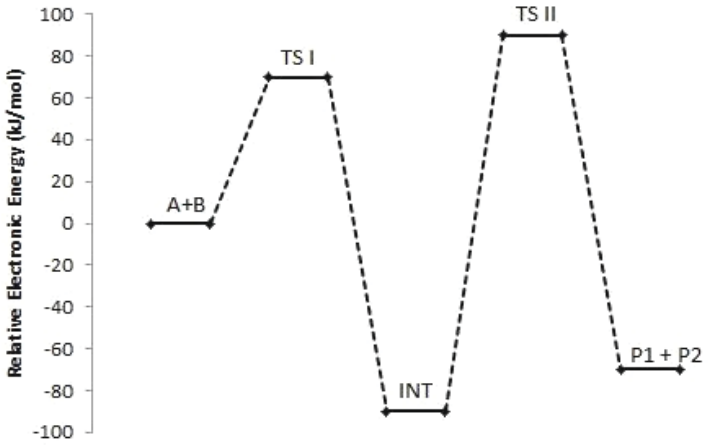

Figure 10. Diagram of relative electronic energies along the channels of the reaction between *p*-methylbenzaldehyde and semicarbazide.

Reaction between o-hydroxybenzaldehyde and semicarbazide

The computed mechanism of formation of (*E*)-2-(2-hydroxybenzylidene)hydrazinecarboxamide and water from *o*-hydroxybenzaldehyde and semicarbazide is presented in Figure 1. Figure 12 presents the schematic diagram of the electronic energy of the reaction mechanism. Tables 11 and 12, respectively, present thermodynamic and kinetic data for this reaction mechanism.

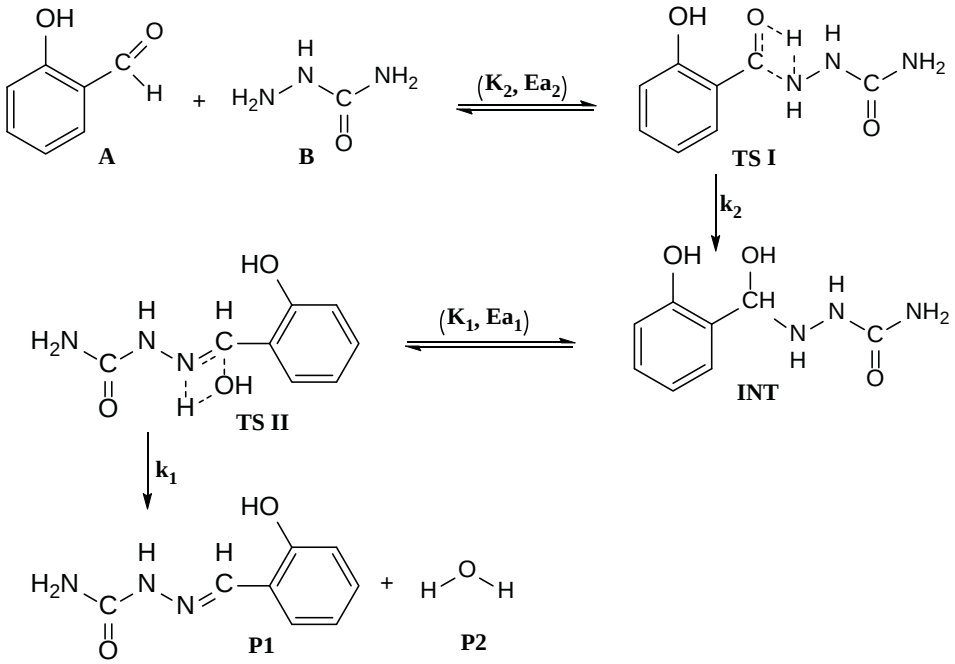

Figure 11. General scheme for the mechanism of reaction between *o*-hydroxybenzaldehyde and semicarbazide.

Table11

DFT B3LYP (6-311+G) calculated thermodynamic parameters for reaction between *o*-hydroxybenzaldehyde and semicarbazide.**

Steps	$\Delta S^{\#}_{reaction}$ *(Jmol^{-1}K^{-1})*	$\Delta H^{\#}_{reaction}$ *(kJmol^{-1})*	$\Delta G^{\#}_{reaction}$ *(kJmol^{-1})*	$\Delta S^{o}_{reaction}$ *(Jmol^{-1}K^{-1})*	$\Delta H^{o}_{reaction}$ *(kJmol^{-1})*	$\Delta G^{o}_{reaction}$ *(kJmol^{-1})*
A+B⇌TSI	-196.39	-22.75	+35.80			
A+B→INT				-204.96	-43.59	+17.52
INT⇌TS II	-6.69	+25.68	+27.67			
INT→P1+P2				+135.74	+109.03	+68.56

Table 12

DFT B3LYP (6-311+G) calculated activation energy (E_a), frequency factor (A), rate constant (k) and equilibrium constant (K) for reaction between *o*-hydroxybenzaldehyde and semicarbazide.**

Steps	E_a *(kJmol^{-1})*	*A*	k_2 *(dm^{3}mol^{-1}s^{-1})*	K_2	k_1 *(s^{-1})*	K_1
A+B⇌TSI	+60.91	2.53×10^{3}dm^{3}mol^{-1}s^{-1}		8.53×10^{-4}		
A+B→INT			3.32×10^{6}			
INT⇌TS II	+257.04	2.08×10^{20}s^{-1}				9.39×10^{-13}
INT→P1+P2					6.05×10^{00}	

After computing the first transition step we found that it is exothermic and non-spontaneous with somewhat high activation energy to overcome. It has an energy deficit of about 74 kJ/mol. The collision factor of this step is less, in comparison with that of the second transition step. The unimolecular transition step is endothermic (from enthalpy of activation) and non-spontaneous (from Gibbs energy of activation), with very high activation barrier. The energy requirements for this step are found to be in the neighbourhood of 300kJ/mol, suggestive of energy supply to sustain the reaction. However, the pre-exponential factor of the step seems to indicate otherwise. The first bimolecular step has an appreciable amount of energy released to the system, as compared to Gibbs energy required for the step to be spontaneous and hence, the reaction is expected to proceed in the presented direction easily. Meanwhile, the unimolecular consecutive step appears to be highly demanding as it is computed to be highly endothermic and non-spontaneous. For this step to be feasible external energy intake is actually a necessity and the step is calculated to be the rate determining step.

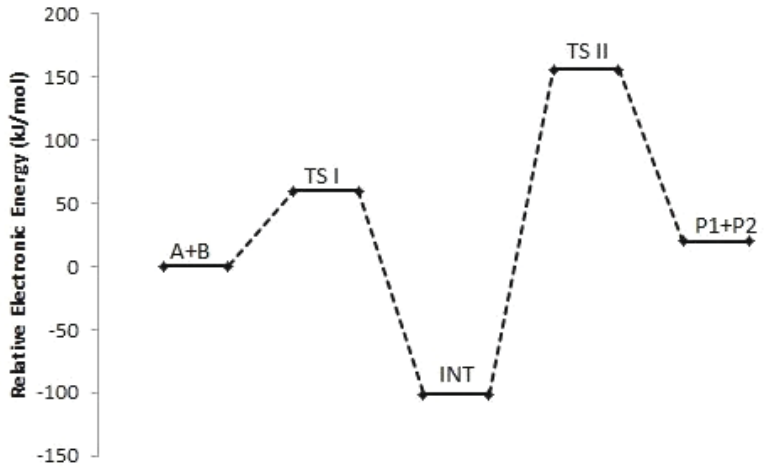

Figure 12. Energy profile for reaction between *o*-hydroxylbenzaldehyde and semicarbazide.

General mechanism and rate law of the reaction of synthesis of semicarbazones

From all the general reaction schemes given above, the reaction mechanism consists of the following steps:

$$A + B \underset{k'_{-2}}{\overset{k'_2}{\rightleftharpoons}} AB^{\#}$$

$$AB^{\#} \xrightarrow{k_2} C$$

$$C \underset{k'_{-1}}{\overset{k'_1}{\rightleftharpoons}} C^{\#}$$

$$C^{\#} \xrightarrow{k_1} P$$

The rate laws for all the products of the reaction can be written as follows:

$$\frac{d\,[P]}{dt} = k_1[C^{\#}] \tag{6}$$

$$\frac{d[C^{\#}]}{dt} = -k_1[C^{\#}] - k'_{-1}[C^{\#}] + k'_1[C] \tag{7}$$

$$\frac{d[C]}{dt} = -k_1'[C] + k_{-1}'[C^{\#}] + k_2[AB^{\#}] \quad (8)$$

$$\frac{d[AB^{\#}]}{dt} = -k_2[AB^{\#}] - k_{-2}'[AB^{\#}] + k_2'[A][B] \quad (9)$$

Using steady state approximation, from Eq.(7)

$$[C^{\#}] = \frac{k_1'}{k_1 + k_{-1}'}[C] \quad (10)$$

Using Eq.(8) and Eq.(10), we have

$$[C] = \frac{k_2(k_1 + k_{-1}')[AB^{\#}]}{k_1' k_1} \quad (11)$$

Similarly, from Eq.(9), we have

$$[AB^{\#}] = \frac{k_2'}{k_2 + k_{-2}'}[A][B] \quad (12)$$

Eq.(11) and Eq.(12) yield:

$$[C] = \frac{k_2 k_2'(k_1 + k_{-1}')}{k_1' k_1(k_2 + k_{-2}')}[A][B] \quad (13)$$

From Eq.(13) and Eq.(10), we have

$$[C^{\#}] = \frac{k_2 k_2'}{(k_2 + k_{-2}')}[A][B] \quad (14)$$

Therefore, the overall rate law can be written as:

$$\frac{d[P]}{dt} = \frac{k_2 k_2'}{(k_2 + k_{-2}')}[A][B] \quad (15)$$

where $\frac{k_2 k_2'}{(k_2 + k_{-2}')} = K'$, experimental rate constant.

Conclusions

According to the obtained results, some steps in the semicarbazones's formation mechanisms were found to require energy input, while in other steps huge amount of energy was released to the system, and the energy barriers were not too high, thus making the reaction thermodynamically feasible on the whole. The mechanisms of the reaction were found to consist of two transition states (bi- and unimolecular), in some of the mechanisms the first bimolecular step was computed to be the rate determining step, while in others it was the unimolecular step that determines the reaction pace. Furthermore, the substituent position (*ortho*-, *para*- and *meta*-) significantly influenced the reaction feasibility: *para*- and *meta*- positions enhanced the reaction, *ortho*- position was noted to have negatively influenced the reaction, leading to endothermic reaction, as observed in the case of interaction between *ortho*-hydroxybenzaldehyde and semicarbazide. Kinetically, the rate constant values of the examined reaction mechanisms were also found to be unambiguous.

References

1. Williamson, K.L. Macroscale and Microscale Organic Experiments, 3rd ed. Boston: Houghton-Mifflin, 1999, 426 p.
2. Cerecetto, H.; González, M. Current Topics in Medicinal chemistry, Chemotherapy of chagas' disease: status and new development. Current Topics in Medicinal Chemistry, 2002, 2, pp. 1185-1190.
3. Micale, N.; Zappala, M.; Zuccala, G.; Menniti, F.S.; Ferreri, G.; De Sarro, G.; Grasso, S. Synthesis of 2-semicarbazonomethyl-4,5- methylenedioxyphenylacetic acids as anticonvulsant agents. Farmaco, 2005, 60, pp. 231-235.

4. Yogeeswari, P.; Sriram, D.; Thirumurugan, R.; Raghavendran, J.V.; Sudhan, K.; Pavana, R.K.; Stables, J.P. Discovery of N-(2,6- Dimethylphenyl)-Substituted Semicarbazones as Anticonvulsants: Hybrid Pharmacophore-Based Design. Journal of Medicinal Chemistry, 2005, 48, pp. 6202-6211.
5. Mishra, V.; Pandeya, S.N. Analgesic activity and hypnotic effect of (±)-3-mentone semicarbazone and thiosemicarbazone derivatives. Acta Pharmaceutica, 2001, 51, pp. 183- 188.
6. Singhal, M.; Paul, A.; Singh, H.P.; Dubey, S.K.; Gaur, K. Evaluation of reducing power assay of chalcone semicarbazones. Journal of Chemical and Pharmaceutical Research, 2011, 3, pp. 639-645.
7. Rajasekaran, S.; GopalKrishna R.; Sanjay Pai, P.N.; Gurpreet, S.S. Synthesis, Antibacterial and in vitro Antioxidant Activity of 2,3-Substituted Quinazolin-4(3H)-ones. Journal of Chemical and Pharmaceutical Research, 2010, 2, pp. 482-488.
8. Dimmock, J.R.; Puthucode, R.N.; Smith, J.M.; Hetherington, M.; Quail, J.W.; Pugazhenthi, U.; Lechler, T.; Stables, J.P. (Aryloxy)aryl semicarbazones and related compounds: A novel class of anticonvulsant agents possessing high activity in the maximal electroshock screen. Journal of Medicinal Chemistry, 1996, 39, pp. 3984-3997.
9. Pandeya, S.N.; Mishra, V.; Singh, P.N.; Rupainwar, D.C. Anticonvulsant activity of thioureido derivatives of acetopheononesemicarbazones. Pharmacological Research, 1998, 37, pp.17-22.
10. Pandeya, S.N.; Mishra, V.; Ponnilavarasan, I.; Stables, J.P. Anticonvulsant activity of p-chlorophenyl substituted arylsemicarbazones – the role of primary terminal amino group. Polish Journal of Pharmacology, 2000, 52, pp. 283-290.
11. Pandeya, S.N.; Sowmayalakshmi, V.; Panda, S.S.; Pandey, A.; Stable, J.P. Anticonvulsant activity of semicarbazone derivatives of Mannich bases. Indian Journal of Chemistry, 2003, 42, pp. 2657- 2661.
12. Engel, T.; Reid, P. Physical Chemistry. Pearson Prentice Hall: New York, 2006, 924 p.

PHOTOELECTRIC PROPERTIES OF HETEROSTRUCTURES BASED ON PEPC AND MEH-PPV FILMS DOPED WITH ZINC OCTABUTYLPHTHALOCYANINE

Nicolay Davidenko[a], Irina Davidenko[a*], Oleg Korotchenkov[a], Victor Kravchenko[b], Elena Mokrinskaya[a], Andrey Podolian[a], Sergey Studzinsky[a], Larisa Tonkopiyeva[a]

[a]*Kiev Taras Shevchenko National University, 64, Volodymyrska str., Kiev 01601, Ukraine*
[b]*Institute of Physical Organic Chemistry and Coal Chemistry, 50, Kharkivske Road, Kiev 02160, Ukraine*
[*]*e-mail: irynadavydenko@gmail.com; phone: (+38) 067 409 55 37*

Abstract. Planar organic heterostructures have been prepared using poly-N-epoxypropylcarbazole films and poly[2-methoxy-5-(2'-ethylhexyloxy)-1,4-phenylenevinylene] by the method of successive deposition adding 2,3,9,10,16,17,23,24-zinc octabutylphthalocyanine. Photoelectric, photodielectric and photovoltaic properties of the heterostructures have been studied. It has been found that the structure photosensitivity in the red part of spectrum is remarkably enhanced by adding the metal complex into the π-conjugate polymer. It has also been established that metal sensitizers are capable of slowing down the photovoltaic rise and decay transients exhibited after the illuminating light is switched on and off, respectively. The likely origin of these effects is suggested, relating to deep traps generated by the metal complex.

Keywords: organic heterostructures, MEH-PPV, metal complexes, photovoltaic effect.

Received: February 2016/ Revised final: March 2016/ Accepted: March 2016

Introduction

Over the last decades, the considerable effort has been devoted to the development of low-cost and flexible organic photonic devices based on molecular composition of aromatic and heteroaromatic compounds absorbing light within the solar range. Quite recently, the superior photovoltaic performance has been demonstrated employing phthalocyanines, and the new class of conjugate polymers containing *para*-phenylenevinylene (PPV), porphyrin and fullerene fragments have been reported [1-4]. One of the most popular material of this type is poly[2-methoxy-5-(2'-ethylhexyloxy)-1,4-phenylenevinylene] (MEH-PPV) with the long-wavelength absorption edge occurred at about 600 nm.

It has been previously reported that MEH-PPV–based film structures reveal the photoelectric effect, and the photovoltage (PV) have been observed in these structures [5]. In order to shift the photosensitivity spectrum of this material to the near infrared, the polymer composite films (PCF) doped by organic dyes or metal complexes have been usually employed [6-11]. The occurrence of the light absorbing centres and the resulting generation of electron-hole (*e–h*) pairs provide the pathways for the inner photoeffect sensitizing observed in PCF. The effectiveness of the light-electricity transformation is mainly determined by the *e–h* pair lifetime. The lifetime can be considerably enhanced by introducing the hetero-interface, consisting of two PCF with different electronic properties. In this case, the transport probability for carriers, moving from one PCF to the other one, depends upon the energy barriers occurring at the interface and can reduce the geminate recombination probability of the carriers.

This type of heterostructures can be designed using, e.g. MEH-PPV and carbazolyl-containing polymers or oligomers (for example, poly-N-epoxypropyl-carbazole, PEPC). The first structure possesses both the electron and whole conductivity, whereas the second one is solely of *p*-type. Despite the large number of papers regarding the photovoltaic devices with carbazolyl groups [12], there is a lack of experimental studies aimed to investigate the photoelectric properties of film heterostructures containing MEH-PPV and PEPC with sensitizing dopants.

Therefore, the purpose of this work was to develop the photosensitive PCF heterostructures based on PEPC and MEH-PPV doped with sensitizing 2,3,9,10,16,17,23,24-zinc octabutylphthalocyanine ($Pc^{Bu}Zn$). The photoconductive, photovoltaic and photo-dielectric properties of these devices have been investigated together with the photoexcited carrier dynamics.

Experimental

The starting materials were PEPC, MEH-PPV and $Pc^{Bu}Zn$ with the structural formulas shown in Figure 1. The glass substrates (3×2cm^2) were initially cleaned with a liquid mixture of acetone and rinsed with distilled water. A thin (≈ 1000nm) conductive Indium Tin Oxide (ITO, SnO_2:In_2O_3) layer was deposited onto the substrate. The PEPC or MEH-PPV polymer films, with (concentration of 3 wt%) or without metal additives, were then spin-coated from polymer solutions onto the ITO covered substrates and dried on air at 80°C during 24 hours. The thickness of polymer layers was L = 2.0μm in all the sample structures, as measured by an interference microscope. The structures were finally Ag-covered by a thermal evaporation technique.

In this work, three types of the PCF samples, sketched in Figure 2 and marked below as CC1, CC2 and CC3, were used.

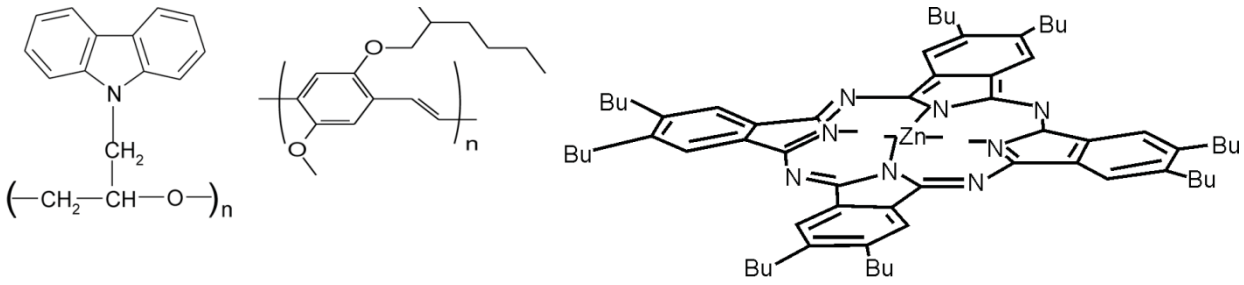

Figure 1. Structural formulas of PEPC (a), MEH-PPV (b), Pc^{Bu}Zn (c).

Application of voltage *U* (1 to 300V) between the ITO and Ag electrodes (Figure 2) allows the current generation with the density of *j* to flow in PCF. It changes when the layers are illuminated through the bottom side of the structures shown in Figure 2. Importantly, PEPC is colourless and it does not absorb in the visible part of the spectrum because its absorption falls within the near ultraviolet part of the spectrum. In turn, MEH-PPV absorbs effectively the light within 300 – 600 nm limits with a peak at about 500 nm (Figure 3, spectrum 1), whereas Pc^{Bu}Zn absorbs within the range from 500 to 800 nm, as it shown in spectrum 2 (Figure 3). To mediate between the photoexcitations of MEH-PPV and Pc^{Bu}Zn, nearly resonant conditions are employed using green and red light-emitting diodes (LEDs) with the peak wavelengths close to the peak absorption of MEH-PPV (Figure 3, spectra 1 and 4) and Pc^{Bu}Zn (Figure 3, spectra 2 and 3).

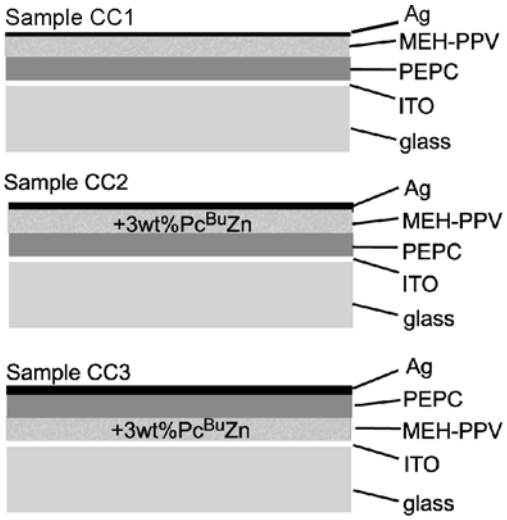

Figure 2. Schematic structure of the samples used in experiments.

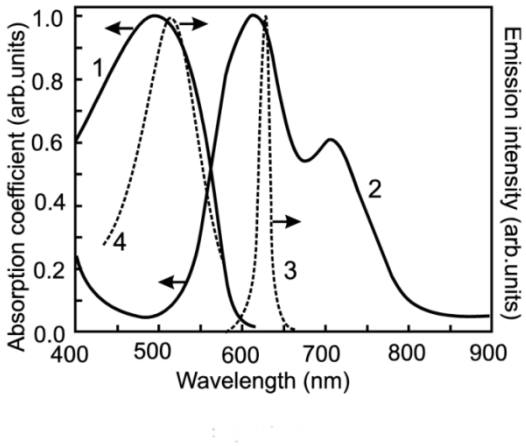

Figure 3. Absorption of MEH-PPV (1) and Pc^{Bu}Zn (2) compared with the red (3) and green (4) LED emission spectra.

The same green and red light is used for generation of photocurrent (PC) and PV signals which ones are directly registered at the ITO and Ag electrodes by an amplifier followed by a digital oscilloscope. With the electrical circuitry used, the positive sign of PV indicates that the Ag contact becomes positive with respect to ITO. The LEDs were controlled by the external bias in the form of square-function pulse. Light pulse lengths of 230 s and 300 ms to 100 s were used for the PC and PV measurements, respectively, with rise and fall times of 1ms. The PC and PV signals were supplied to a voltmeter, followed by a digital oscilloscope and stored on a computer. The electrical circuitry details are given elsewhere [13].

Several decay transients, taken with a single light pulse, were stored on a computer with the time interval of 20 and 40 min between the consecutive pulses for samples CC2 and CC3, respectively, which were greater than the PC and PV decay times. Then the stored transients were averaged as many times as required to achieve a given signal-to-noise ratio.

The electrical loss tangent (*tan*δ), inherent to dispersion in electrical conductivity, and capacitance (*C*) of the sandwich structure were taken employing standard techniques at 1-kHz rf voltage ranged from 1 to 30V, both in dark and under the LED illumination. The values of $\Delta tan\delta = (tan\delta_{PH} - tan\delta_0)/tan\delta_0$ and $\Delta C = (C_{PH} - C_0)/C_0$ were analyzed, where the subscripts 0 and PH correspond to appropriate values measured before and at the illumination, respectively. All measurements were recorded at room temperature.

Results and discussion

The PC transients are shown in Figure 4. Samples CC1 have exhibited the lowest peak of PC signal, whereas samples CC2 have shown the highest one. The PC decays, measured after the light is turned off, are also markedly different, depending on the polarity of the applied voltage *U*. As seen in Figure 4, sample CC3 has exhibited the longest decay.

The peak PC j_{max} depends on the strength of the applied electric field (Figure 5), and the curves appear to be linear in the double-log coordinates, so that $j_{max} \sim U^m$ with $m > 2$.

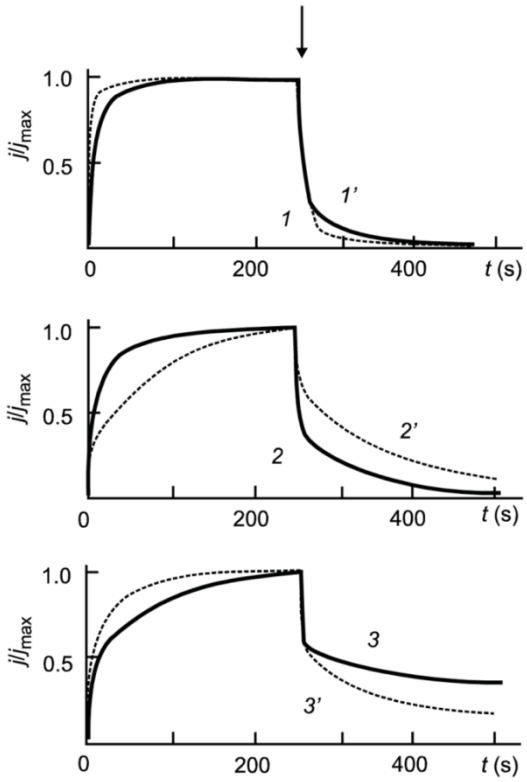

Figure 4. Normalized PC transients taken in samples CC1 (1, 1'), CC2 (2, 2') and CC3 (3, 3') at the positive (1 to 3) and negative (1' to 3') polarity of applied voltage *U* on the ITO electrode. The green LED with a peak intensity of 20 W/m² is used as illumination source. Arrow indicates the moment when the light is turned off.

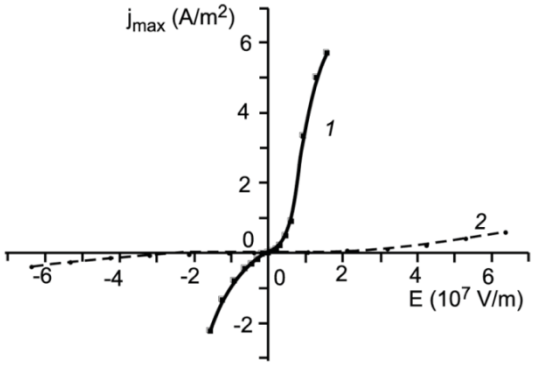

Figure 5. The peak PC value j_{max} *vs* applied electric field strength *E* taken in samples CC2 (1) and CC3 (2) at illumination with the green LED having a peak intensity of 20 W/m².

The PV transients are shown in Figures 6-8. The most important, samples CC1, made-up without the phthalocyanine complex, exhibited a very weak PV with very short rise and decay times (Figure 6).

The PV signal is substantially greater in samples CC2 and CC3, the PV transients depend rather sensitively on the illumination wavelength (Figures 7 and 8). It may thus be concluded that doping of MEH-PPV with the $Pc^{Bu}Zn$ complex enhances PV, even in the spectral range of a maximum absorption of MEH-PPV. Next, the PV transient shapes have changed considerably when the transients are taken repeatedly, although the decay relaxes to zero value in all cases. This may be considered to be a memory effect during consecutive illuminations.

It is also found that, after the LED light is switched on, the *tan*δ and *C* values increase symbatically. These ones are completely relaxed after the light is switched off. Figure 9 illustrates the changes in *tan*δ upon illumination. It is seen that, similar to the PC and PV transients, samples CC1 posses the lowest times of the photo-dielectric response. According the data presented in Figures 4 and 9, it can concluded that, in contrast to samples CC1, samples CC2 and

CC3 contain deep traps capturing photoexcited carriers and slowing down the transients. The traps are obviously due to $Pc^{Bu}Zn$ complexes. This is also supported by the PV data shown in Figures 6-8, illustrating that the PV kinetics is symbate with the kinetics of *tan*δ and *C* taken after light is switched on and switched off. Therefore, $Pc^{Bu}Zn$ in MEH-PPV has sensitizing properties, which are most likely to be due to deep traps arisen in the vicinity of the $Pc^{Bu}Zn$ molecule.

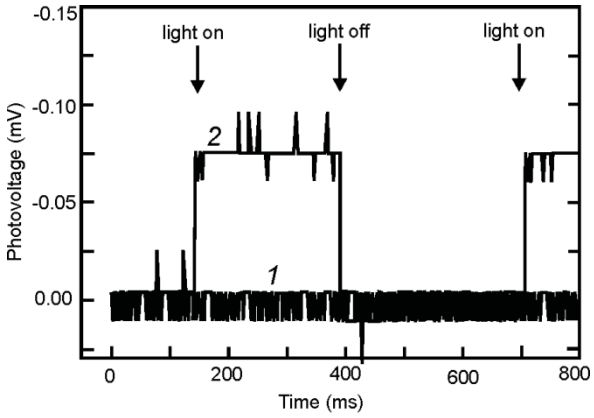

Figure 6. Time-dependent PV of sample CC1 at the red (1) and green (2) LED illumination. Curve 2 is arbitrarily shifted in the vertical direction.

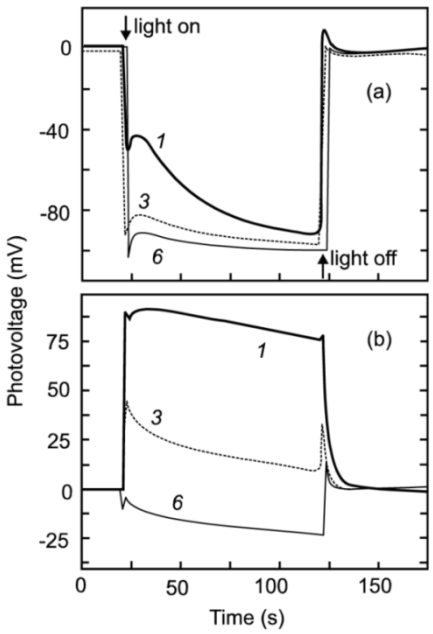

Figure 7. Time-dependent PV of sample CC2 at the red (a) and green (b) LED illumination. Curve numbers indicate the consecutive decay traces captured with the time intervals of 20 min.

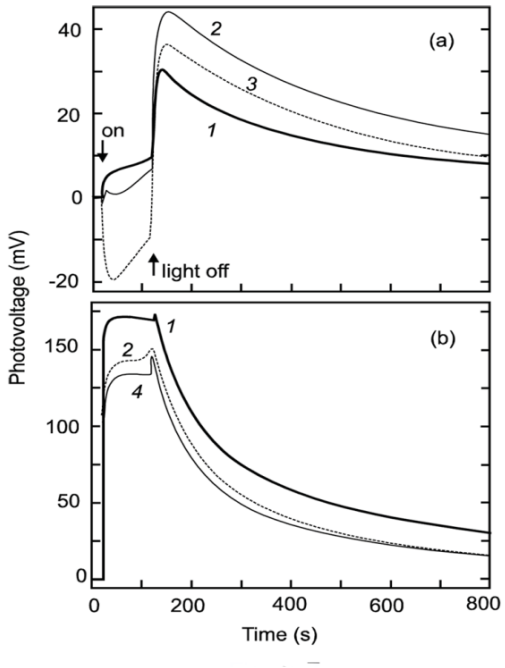

Figure 8. Time-dependent PV of sample CC3 at the red (a) and green (b) LED illumination. Curve numbers indicate the consecutive decay traces captured with the time intervals of 40 minutes.

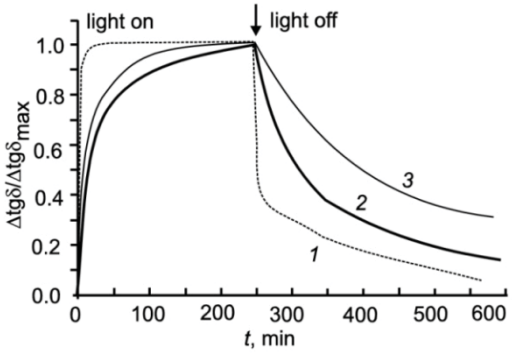

Figure 9. Time-dependent Δtan*δ* of samples CC1 (1), CC2 (2) и CC3 (3) at the green LED illumination.

Conclusions

$Pc^{Bu}Zn$-sensitized MEH-PPV heterostructures have a superior photovoltaic performance in comparison with MEH-PPV structures. It is suggested that zinc octabutylphthalocyanine complexes incorporated into MEH-PPV produce deep traps localized at the $Pc^{Bu}Zn$ molecule. The trap-mediated photo-electric and photo-dielectric transients exhibit prolonged transient times, indicative of trap-induced capture of charges. This charge turns out to screen the electric field developed at the hetero-interface and the barrier field due to metal contacts. The latter fact is capable of reversing the photovoltage sign due to prolonged light illumination.

References

1. Huang, C.; Wang, N.; Li, Y.; Li, C.; Li, J.; Liu, H.; Zhu, D. A New class of conjugated polymers having porphyrin, poly(p-phenylenevinylene), and fullerene units for efficient electron transfer. Macromolecules, 2006, 39, pp. 5319-5325.
2. Braun, D.; Heeger, A.J. Visible light emission from semiconducting polymer diodes. Applied Physics Letters, 1991, 58, pp. 1982-1984.
3. Yu, G.; Zhang, C.; Heeger, A.J. Dual-function semiconducting polymer devices: Light-emitting and photodetecting diodes. Applied Physics Letters, 1994, 64, pp. 1540-1543.
4. Sariciftci, N.S.; Braun, D.; Zhang, C.; Srdanov, V.I.; Heeger, A.J.; Stucky, G.; Wudl, F. Semiconducting polymer-buckminsterfullerene heterojunctions: Diodes, photodiodes, and photovoltaic cells. Applied Physics Letters, 1993, 62, pp. 585-588.
5. Shi, Q.; Hou, Y.; Li, Y.; Feng, Z.; Liu, X. Wavelength dependence of transient photovoltage polarity**.** Physics Letters A**,** 2008, 372, pp. 5853-5856.
6. Iyengar, N.A.; Harrison, B.; Duran, R.S.; Schanze, K.S.; Reynolds, J.R. Morphology evolution in nanoscale light-emitting domains in MEH-PPV/PMMA blends**.** Macromolecules, 2003, 36, pp. 8978-8985.
7. Maltsev, E.I.; Brusentseva, M.A.; Rumiantseva, V.D.; Lysenko, D.A.; Berendiayev, V.I.; Mironov, A.F.; Novikov, S.V.; Vannikov, A.V. Electric phosphorescence if aromatic polyimides doped with Pt-porphyrins. High-molecular compounds, 2006, 48, pp. 254-259 (in Russian).
8. Marletta, A.; Goncalves, V.; D'ebora, T. Photoluminescence of MEH-PPV/PS Blends. Brazilian Journal of Physics, 2004, 34, pp. 697-698.
9. Kumar, A.; Bhatnagar, P.K.; Mathur, P.C.; Tada, K.; Onoda, M. Improved electrical and optical properties of MEH-PPV light emitting diodes using Ba buffer layer and porphyrin**.** Applied Surface Science, 2006, 252, pp. 3953-3958.
10. Kazukauskas, V. Investigation of carrier transport and trapping by oxygen-related defects in MEH-PPV diodes**.** Semiconductor Science and Technology**,** 2004, 19, pp. 1373-1377.
11. Davidenko, N.A.; Spitsina, N.G.; Lobach, A.S.; Breusova, M.O.; Tomilova, L.G.; Yakushchenko I.K. Electrical conductivity and photoconductivity of films of composites based on poly[2-methoxy-5-(2′-ethylhexyloxy)-1,4-phenylenevinylene] with additions of zinc octabutyl phthalocyanine and C_{60}**.** Theoretical and Experimental Chemistry, 2006, 42, pp. 277-281.
12. Grazulevicius, J.V.; Strohriegl, P.; Pielichowski, J.; Pielichowski, K. Carbazole-containing polymers: Synthesis, properties and applications**.** Progress in Polymer Science**,** 2003, 28, pp. 1297-1301.
13. Podolian, A.; Kozachenko, V.; Nadtochiy, A.; Borovoy, N.; Korotchenkov, O. Photovoltage transients at fullerene-metal interfaces. Journal of Applied Physics**,** 2010, 107, pp. 093706-093713.

BENZOYL PEROXIDE DECOMPOSITION BY NITROGEN-CONTAINING CARBON NANOMATERIALS

Daryna Haliarnik[a], Oleg Petuhov[b], Olga Bakalinska[a*], Tudor Lupascu[b], Mykola Kartel[a]

[a]*Chuiko Institute of Surface Chemistry, National Academy of Sciences of Ukraine, 17, General Naumov Str., Kyiv 03164, Ukraine*
[b]*Institute of Chemistry of Academy of Sciences of Moldova, 3, Academiei str., Chisinau MD-2028, Republic of Moldova*
**e-mail: bakalin2008@ukr.net; phone: (+38 044) 422 96 02; fax: (+38 044) 424 94 64*

Abstract. In this paper the determination of catalytic activities of nanoporous KAU and SKN carbon materials, as well as catalytic activities of their modified (oxygen– and nitrogen–containing) forms and of enzyme catalase by calculating the Michaelis constants according to the kinetics of substrate decomposition has been reported. It has been shown that nitrogen–containing materials provide the highest catalytic activity in non–aqueous media, while the activity of catalase in non-aqueous media is small. It has been established that the catalytic activity of the samples does not correlate with structural parameters but depends on the change of their surface chemistry. The catalytic activity is decreased by the addition of oxygen atoms and, vice-versa, is increased by addition of nitrogen atoms. It has been found that the catalytic activity of studied samples correlates with surface basicity as well as the presence of quaternary nitrogen in the chemical structure.

Keywords: carbon nanomaterials, activated carbon, benzoyl peroxide, catalytic activity, Michaelis constant.

Received: March 2016/ Revised final: May 2016/ Accepted: May 2016

Introduction

Recent increase in the number of enterprises of chemical, pharmaceutical, metallurgical and food industry leads to a continuous environmental pollution with harmful organic and inorganic substances. Mankind is in a continuous search to solve this problem. Due to high surface area, nanoporous carbon materials (NCM) are used as absorbers in sorption technologies and catalysts supports for water and air purification from harmful organic substances [1]. Activated carbon (AC) ranks first among these materials because of a number of its advantages: it is a cost-effective, affordable and not specific sorbent, while the possibility of significant variation of parameters increases its applicability. Activated carbon is a widely used adsorbent for air purification from harmful gases, such as SO_2, CO_2 [2] and it is also used as a catalyst for the oxidation of SO_2 to SO_3 [3]. AC is known to be also used for wastewater treatment from heavy metals and their compounds (Cr(VI), Cu(II), Ni(II), Pb(II), Hg [4-6]), from organic compounds (diphenyl, phenol and chlorinated organic compounds [7-9]).

Pollution by pharmaceutical products, such as tetracycline, a residue of veterinary drugs found in wastewater, as well as in drinking water, has been reported [10]. Wastewater may be purified by adsorption of tetracycline by carbon nanotubes [10]. Nowadays, carbon nanotubes become promising materials for replacing AC adsorbents in water purification from organic pollutants.

NCM can also be used as catalysts in heterogeneous catalysis. In particular, AC is used as a catalyst in reactions of halogenation, organic compounds decomposition, oxidation-reduction, dehydrogenation etc. [11]. These properties of AC are suitable for drinking water purification from organic pollutants as well as for wastewater treatment.

In this paper the study regarding the catalytic activity of carbon nanoporous materials with different contents of heteroatoms in a model reaction of benzoyl peroxide decomposition in non-aqueous media is presented. This investigation has been resulted in establishing correlations between the structure of the carbon matrix, modification of their surface chemistry and the catalytic activity.

Experimental

Materials

In this study two series of nanoporous carbon materials have been used: i) nitrogen-containing active carbon SKN (obtained from nitrogen-containing precursor vinylpyridine resin) and its modified forms - SKNo (oxidized with nitric acid) and N-SKN (nitrogen-enriched, obtained by urea impregnation followed by the heat treatment [12]); ii) active carbon KAU (obtained from the shells of apricot stones) and its modified forms – KAUo (oxidized with nitric acid), nitrogen-containing N-KAU (obtained by urea impregnation followed by the heat treatment [12]) and KAUo-NH_2 (oxidized KAUo chemically modified with 1,5-pentanediamine).

Enzyme catalase (from bovine liver, K 1.11.1.6, activity 329300 a.u.) was purchased from Fluka, powdered benzoyl peroxide (contained 25 % water) and ethyl acetate (for liquid chromatography, 99.8 %) were purchased from Merck KGaA.

Methods

The structure and adsorption parameters of AC were determined from nitrogen adsorption-desorption isotherms at 77 K. The isotherms were measured using Autosorb-1-MP (Quantachrome), with prior degassing at 473 K for 12 hours. The specific surface area (S_{BET}) was calculated using the Brunauer–Emmett–Teller (BET) equation. The volume of micropores (V_{mi}) was determined using the *t*-method. The Density Function Theory (DFT) was used to calculate the pore volume distribution as a function of radius and pore radius (R_p). The sorption volume (V_s) of pores was determined by measuring the benzene adsorption in desiccator, elemental composition – by Prehlya and Dumas methods [13,14].

Qualitative and quantitative characterization of functional groups on the surface of AC samples was performed by the Böehm titration method [15].

The chemical state of nitrogen atoms on the surface of NCM samples was examined by X-rays photoelectron spectroscopy (XPS) on the instrument VG ESCA.

The catalytic activity of nanoporous carbon materials and enzyme catalase has been determined on a model reaction of benzoyl peroxide decomposition by Michaelis constants calculation.

Weighed portions of benzoyl peroxide (BP) were used to prepare solutions (ethyl acetate) with desired concentrations (from 1 to 10 %). The BP concentration in the product was determined by iodometric titration.

The kinetics of BP decomposition in non-aqueous media was studied by the volumetric method. The BP decomposition was performed in a thermostated cell with stirring. The temperature of the reaction mixture was measured with an accuracy of ± 0.5 °C, ambient temperature with accuracy of ± 1 °C, the amount of gases released in the reaction, with an accuracy of ± 0.01 mL. The released gas volume measurements were carried out for 120 minutes. Each experiment was performed using 10 mL of BP solution. Michaelis constant (K_m, mM) was used for quantitative assessment of catalytic activity and for the comparison of this value for carbon nanomaterials and their modified forms. Initial reaction velocity (V_o) for different substrate concentrations was used to determine the Michaelis constant [16]. The affinity constant (K_{af}) (an inverse value to the Michaelis constant) was calculated to facilitate the perception of obtained data.

The linear correlation of the catalytic activity (Y) expressed in terms of the K_m on parameters (X_n) of carbon nanomaterials was studied.

Results and discussion

In order to establish the factors that affect the catalytic activity of the carbon material in a chosen reaction, a series of NCM samples have been synthesized with different structural and sorption characteristics, surface chemistry, and the presence of heteroatom in the structure. It has been shown that sorption pore volume and specific surface area vary within the range of 0.50-0.90 cm^3/g and 650-2140 m^2/g, respectively.

Considering the KAU type carbon as an example, it can be observed that it is a material of mixed porosity with a predominance of micropores, which is evident in the sample N-KAU (77.4 % micropores) (Figure 1). The oxidation of KAU type carbon material leads to an insignificant decrease in the number of micropores and a reduced surface area (Table 1). At the same time, impregnation of carbon with urea increases the fraction of micropores, and to a lesser extent the specific surface area, which can be explained by the different influence of urea and nitric acid on the AC modification. Impregnation with urea does not affect the microporous structure, while the interaction with the carbon matrix occurs in mesopores, part of them being converted into micropores. Nitric acid, in its turn, also oxidizes the surface of the micropores, thus reducing their surface.

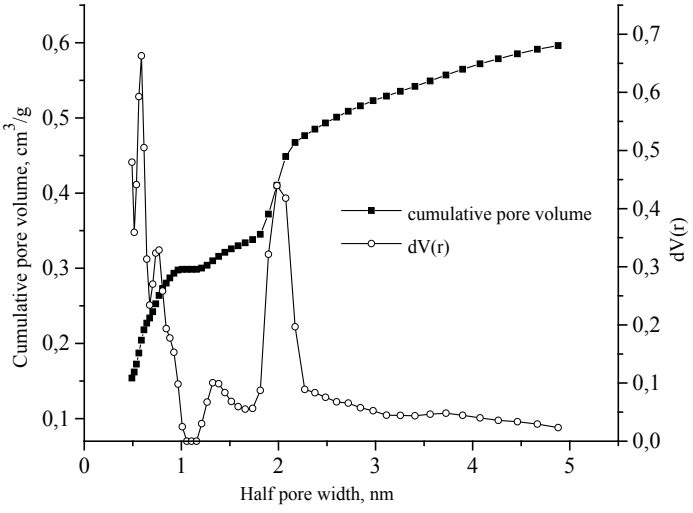

Figure 1. N-KAU pore size distributions by DFT method.

Elemental analysis of carbon samples shows that during oxidation the number of oxygen atoms increases twice and 35-fold for SKN and activated carbon KAU, respectively. The increase in the number of hydrogen atoms suggests the formation of oxygen-containing functional groups on the SKN and KAU samples surfaces (Table 1). Titration results reveal that newly formed surface groups have a predominantly acid character. The total number of acidic groups increases during carbon oxidation by 18 and 20 times for SKN and KAU, respectively. Chemical immobilization of 1,5-pentanediamine on the surface of oxidized KAU leads to an almost 2-fold decrease of the total number of acid groups. Moreover, titration results show only the presence of phenolic groups on the AC surface.

Table 1

Structural and sorption characteristics, and elemental composition of studied samples.

NCM	*Elemental composition, wt%*				V_s, cm^3/g (X_1)	*Fraction micropore volume, %*	R_p, *nm*	S_{BET}, m^2/g (X_2)
	C	H	O (X_6)	N (X_5)				
KAU	99.40	0.20	0.06	0.30	0.50	55.0	0.58	920
KAUo	96.30	1.10	2.10	0.60	0.85	53.8	0.57	790
N-KAU	89.20	2.33	6.24	2.20	0.91	77.4	0.55	940
KAUo-NH_2	78.60	1.98	16.80	3.30	0.56	66.7	0.73	650
SKN	91.20	0.96	6.50	1.30	0.75	n.d.*	n.d.	1970
SKNo	85.80	0.90	11.20	2.00	0.80	n.d.	n.d.	2140
N-SKN	91.25	1.20	3.70	3.85	0.84	n.d.	n.d.	1650
R^2	n.d.	n.d.	0.01	0.13	0.34	n.d.	n.d.	0.01

**n.d.- not determined*
V_s- total pore volume
R_p- pore radius
S_{BET}- surface area determined by BET

Basic groups on samples surfaces were determined for SKN, N-SKN, N-KAU and KAUo-NH_2 (Table 2) in amounts ranging from 0.12 to 1.90 meq/g, probably, due to the presence of nitrogen atoms in the structure of these materials. According to elemental analysis, the lowest nitrogen atoms content of 0.30% was found in the carbon KAU. The number of nitrogen atoms in AC structure increased twice as a result of oxidation by nitric acid, possibly because of carbon surface nitration processes. Functionalization of KAU allowed including nitrogen atoms up to 2.20%. SKN contained nitrogen obtained from the vinylpyridine resin [17]. The total nitrogen content in the synthetic carbon SKN increased with oxidation, too. The highest nitrogen content of 3.85% was achieved for the N-SKN carbon. It should be noted that the number of basic groups in the N-SKN activated carbon increased by 12 times compared to the initial material. The chemical immobilization of 1,5-pentanediamine on the surface of KAUo resulted in the appearance of basic groups associated with the presence of nitrogen in the structure, but their content was 8.6 times lower compared to the N-KAU.

Table 2

Functional groups on the surfaces of investigated samples.

NCM	*Functional groups, meq/g*				
	carboxylic	*lactonic*	*phenolic*	*Σ of acidic groups* (X_3)	*basic groups* (X_4)
KAU	0.04	0.06	0.02	0.12	0.00
KAUo	0.84	0.20	1.39	2.43	0.00
N-KAU	0.00	0.45	0.05	0.50	1.90
KAUo-NH_2	0.00	0.00	1.27	1.27	0.22
SKN	0.08	0.02	0.02	0.12	0.12
SKNo	1.04	0.10	1.01	2.15	0.00
N-SKN	0.00	0.00	0.73	0.73	1.44
R^2	n.d.*	n.d.	n.d.	0.14	0.93

**n.d.- not determined*

Analysis of the temperature-programmed desorption mass spectra of BP decomposition product showed that decomposition of 1 mole BP released 2 moles of gas that allowed performing quantitative determination of changes in BP concentration in time by the measurement of the released gas volume [18].

The catalytic activity of materials during the process of BP decomposition was experimentally determined (Figure 2). The coefficient of determination (R^2) of calculated affinity constants and the Michaelis constant during an experiment was not lower than 0.85.

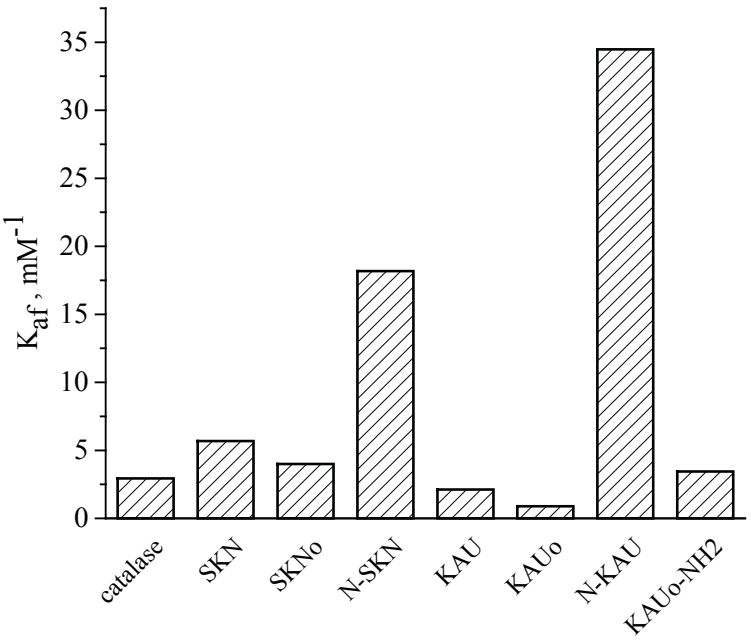

Figure 2. The catalytic activity of the investigated materials.

It was established that the catalytic activity of the investigated materials (K_{af}, mM^{-1}, (Y)) decreased in the following order: N-KAU (34.5) > N-SKN (18.2) > SKN (6.2) > SKNo (4.0) > catalase (3.7) > KAUo-NH_2 (3.4) > KAU (2.1) > KAUo (0.9). The catalytic activity of nitrogen containing NCM was larger than that of enzyme catalase. Among all investigated materials the N-KAU showed the highest value. On the other hand, N-SKN showed a significant activity, 3-folds higher than that of the initial SKN. The SKNo was characterized by less activity than other nitrogen-containing NCM. The KAUo-NH_2 material was more active than KAU and KAUo, which had the lowest activities. Thus, nitrogen-containing materials provided higher catalytic activity than other NCMs, which could be explained by the fact that nitrogen as an electron-donating element provided a higher mobility of electrons in the carbon matrix and reduced the electron work function at the carbon/liquid or carbon/gas interfaces. Oxidation of carbon materials decreased their catalytic activity reducing the electron-donating ability which hindered the electron transport through the BP molecule. The catalytic activity of catalase in the BP decomposition process in non-aqueous media had an intermediate value between the nitrogen-containing NCM material KAUo-NH_2 and SKNo. This indicates that carbon nanomaterials can be used as biocatalysts in non-aqueous environment and under certain conditions to achieve a higher efficiency compared to enzymes.

Next, the factors influencing the catalase-like activity of investigated NCM in BP decomposition in non-aqueous media have been investigated. No correlation (R^2) between catalytic activity (K_{af}, Y) and structural factors (X_1 and X_2) has been detected: $R_1^2 = 0.34$ and $R_2^2 = 0.01$, respectively (Table 1), indicating that those parameters are of secondary importance. The total content of surface acidic groups (X_3) and oxygen content (X_6) (Table 2) affects also the catalytic activity: $R_3^2 = 0.14$ and $R_6^2 = 0.01$, respectively. At the same time, a correlation has been found between the presence of basic groups (X_4) and the catalytic activity: $R_4^2 = 0.93$. It has been suggested that surface basicity is related to the presence of nitrogen-containing groups in the NCM structure. However, the catalytic activity is not correlated with the total nitrogen content (X_5) $R_5^2 = 0.13$. Probably, the catalytic activity of nitrogen-containing NCM depends on the chemical state of the nitrogen atoms, and not on the total nitrogen content in the structure.

The chemical state of nitrogen atoms and their relative content in the studied NCM was determined from the analysis of N 1s spectra XPS (Table 3). It was shown that the catalytic enzyme-like activity of carbon nanomaterials

correlated with the presence of quaternary nitrogen through increasing electron-donating capacity of the carbon matrix. The higher activity of the modified nitrogen-containing NCM N-KAU and N-SKN compared to SKN could be attributed to the different content of quaternary nitrogen.

The obtained data are in agreement with the correlation between the activity and the basic groups on the NCM surface. Similar conclusions have been made in a published paper [19], where the authors showed that the presence of quaternary nitrogen increased the activity of AC in epoxidation of styrene and oxidative dehydrogenation of propane by increasing electron-donating of carbon atoms.

Table 3

The correlation between the chemical state of nitrogen and catalytic activity of NCM.

Sample	*State of nitrogen atoms (relative content, %)*							K_{ap}, mM^{-1}
	pyrroli-donic	*pyrrolic*	*pyridinic*	*pyridine N-oxide*	NO_2-*group*	*C=N*	*quaternary*	
				X				*Y*
KAU	0.00	35.59	57.58	3.98	2.85	0.00	0.00	2.12
KAUo	0.00	6.44	89.27	2.83	1.46	0.00	0.00	0.89
N-KAU	0.00	1.12	67.38	0.00	4.09	14.18	13.23	34.48
KAUo-NH_2	35.93	0.00	60.67	1.30	0.00	0.00	2.10	3.44
SKN	48.69	0.00	25.52	10.03	2.19	13.57	0.00	6.17
SKNo	0.00	29.41	45.12	0.35	3.07	21.37	0.00	4.00
N-SKN	0.00	0.00	64.45	2.39	0.23	32.39	0.54	18.18
R^2	0.07	0.14	0.01	0.11	0.14	0.23	0.77	

Conclusions

In this work the catalytic activity of carbon nanomaterials in a model reaction of benzoyl peroxide decomposition by Michaelis constants calculation, according to the kinetics of substrate decomposition, has been experimentally determined. A series of N-NCM prospective catalysts for organic peroxides decomposition in non-aqueous media have been synthesized. A number of carbon materials like KAU and SKN, their modified forms (oxidized, nitrogen-containing) and enzyme catalase have been tested. It has been shown that carbon materials exhibit an enzyme-like activity in non-aqueous media. It has been established that the catalytic ability of the samples does not correlate with the structural parameters but depends on their surface chemistry. The introduction of oxygen atoms decreases and nitrogen atoms increases the catalytic activity of the modified carbon nanomaterials. It has been shown that the enzyme-like catalytic activity of carbon nanomaterials correlates with the presence of quaternary nitrogen of the NCM.

Acknowledgments

This research was funded by the People Programme (Marie Curie Actions) of the European Union's Seventh Framework Programme FP7/2007-2013/ under REA, grant agreement No. PIRSESGA-2013-612484.

References

1. Xijun, H.; Lecheng, L.; Chu, H.P.; Yue L.P. Copper/activated carbon as catalysts for organic wastewater treatment. Carbon, 1999, 37, pp. 631–637.
2. Guo, B.; Chang, L.; Xie, K. Adsorption of Carbon Dioxide on Activated Carbon. Journal of Natural Gas Chemistry, 2006, 15, pp. 223–229.
3. Bagreev, A.; Bashkova, S.; Bandosz, T.J. Adsorption of SO_2 on Activated Carbons: The Effect of Nitrogen Functionality and Pore Sizes. Langmuir, 2002, 18, pp. 1257–1264.
4. Attia, A.A.; Khedr, S.; Aelkholy, S.A. Adsorption of Chromium ion (VI) by acid Activated Carbon. Brazilian Journal of Chemical Engineering, 2010, 1, pp. 183 – 193.
5. Kadirvelu, K.; Faur-Brasquet, C.P.; Cloirec, L. Removal of Cu(II), Pb(II), and Ni(II) by Adsorption onto Activated Carbon Cloths. Langmuir, 2000, 16, pp. 8404–8409.
6. Hadi, P.; To, M.; Hui, C. Aqueous mercury adsorption by activated carbons. Water Research, 2015, 73, pp. 37-55.
7. Bautista-Toledo, I.; Ferro-Garcia, M.A.; Rivera-Utrilla, J. Bisphenol a Removal from Water by Activated Carbon. Effects of Carbon Characteristics and Solution Chemistry. Environmental Science and Technology, 2005, 39, pp. 6246–6250.

8. Mahajan, O.P.; Moreno-Castilla, C.; Walker, P.L. Surface-Treated Activated Carbon for Removal of Phenol from Water. Separation science and technology, 1980, 15, pp. 1733-1752.
9. Urano, K.; Yamamoto, E.; Tonegawa, M.; Fujie, K. Adsorption of chlorinated organic compounds on activated carbon from water. Water Research, 1991, 25, pp. 1459-1464.
10. Ji, L.; Chen, W.; Duan, L.; Zhu, D. Mechanisms for strong adsorption of tetracycline to carbon nanotubes: A comparative study using activated carbon and graphite as adsorbents. Environmental Science and Technology, 2009, 43, pp. 2322–2327.
11. Fidalgo, B. Carbon materials as catalysts for decomposition and CO_2 reforming of methane: a review. Chinese Journal of Catalysis, 2011, 32, pp. 207–216.
12. Zhuravsky, S.V.; Kartel, M.T.; Tarasenko, Yu.O.; Villar-Rodil, S.; Dobos, G.; Toth, A.; Tuscon, J.; Laszlo, K. N-containing carbons from styrene-divinylbenzene copolymer by urea treatment. Applied Surface Science, 2012, 258, pp. 2410-2415.
13. Klimova, V.A. Basic Micromethods of Organic Compounds Analysis. Moscow: Khimia, 1967, 208 p. (in Russian).
14. Alekseev, V.N. Quantitative Analysis. Moscow: Khimia, 1972, 504 p. (in Russian).
15. Boehm H.P. Surface oxides on carbon and their analysis: a critical assessment. Carbon, 2002, 40, pp. 145–149.
16. Glevatska, K.V.; Bakalinska. O.M.; Kartel, M.T. The study, description and comparison of catalase activity of carbon sorbents of SKN and KAU type. Scientific notes of NaUKMA, Chemical Science and Technology, 2008, 79, pp. 19–23 (in Ukrainian).
17. Strelko, V.V.; Nemoshkalenko, V.V.; Kartel, N.T.; Medvedev, S.L. On the state of the nitrogen atoms in the graphite lattice of activated carbons. Adsorption and Adsorbents, 1983, 11, pp. 76–80 (in Russian).
18. Haliarnik, D.M.; Bakalinska, O.M.; Palyanytsya, B.B.; Kulyk, T.V.; Kartel, M.T. Organic Peroxides Decomposition by Carbon Nanomaterials in Nonaqueous Media. Surface, 2015, 7(22), pp. 253-263 (in Ukrainian).
19. Podyacheva, O.Y.; Ismagilov, Z.R. Nitrogen-doped carbon nanomaterials: To the mechanism of growth, electrical conductivity and application in catalysis. Catalysis Today, 2014, 249, pp. 12–22.

PHASE DIAGRAM OF GELATINE-POLYURONATE COLLOIDS: ITS APPLICATION FOR MICROENCAPSULATION AND NOT ONLY

Alexei Baerle*, Olga Dimova, Irina Urumoglova, Pavel Tatarov, Larisa Zadorojnai

Technical University of Moldova, 168, Stefan cel Mare Blvd., Chisinau MD-2004, Republic of Moldova
**e-mail: abaerle2003@mail.ru; phone: (+373 79) 78 93 01; fax: (+373 22) 50 99 60*

Abstract. Phase state and the charge of colloidal particles in the gelatine-polyuronate system were studied. A method for comparative evaluation of molecular weight of colloids by means of viscosimetric measurements and electrophoresis was developed. It is shown that the Diagram {Phase state = f (composition, pH)} contains six well-defined regions. The diagram explains and predicts the behaviour of protein-polysaccharide colloids, which are included in beverages or forms the shells of oil-containing microcapsules.

Keywords: protein-polysaccharides, colloids, electrokinetic potential, phase diagram, microcapsules.

Received: March 2016/ Revised final: April 2016/ Accepted: April 2016

Introduction

Poorly soluble or electro-statically agglomerated macromolecular compounds derive from interaction of protein zwitterions with polyanions, in particular, with polyuronic acids and their salts [1]. These interactions are of great practical interest, insofar as much of foods contain biopolymers in different combinations [2]. Recently, there were published many papers devoted to the joint use of the proteins and polysaccharides, originate from different natural raw materials, in various pharmaceutical and food systems [3-6]. These compounds have a greater ability to precipitate the colloidal suspensions, compared to pure linear polymers [7]. It is believed that these mixtures are in fact the covalent chemical compounds or supra-molecular three-dimensional structures with high molecular weight, charged as zwitterions due to the presence of proteins [8-10]. Due to this fact, the mixtures are capable to precipitate not only the neutral particles, but also charged particles, both positive and negative. Such three-dimensional structures (3D) appear also during the complex coacervation of oppositely charged macromolecules on the oil droplets surface in the microencapsulation processes [11]. The optimum conditions of precipitation of alginate-gelatine coacervates were obtained *in vitro,* using measurements of turbidity and viscosity [1].

The study led to the elaboration of different phase diagrams, which reflects complex interactions between the negatively charged polysaccharides and zwitterions of proteins [8,12,13]. The interaction of proteins with polysaccharides was described in numerous research papers, but not in the exhaustive form. Among the problematic issues it can be identified the determination of the molecular weight of the resulting supramolecular structures. In our view, the estimation of the molecular weights will be useful for calculating of the microcapsule shells parameters, as well as to determine the conditions of deposition of neutral colloidal particles. Detailed analysis of the phase state of the gelatine-polyuronate system is important to determine the optimal sedimentation conditions, or opposite, to prevent the coagulation of proteins by small amounts of extraneous poly-anions. In constructing of the phase diagram of the gelatine-polyuronate, it is important to consider the sign and magnitude of charge of generated complexes. Unambiguous information about the charge of colloidal particles is given by method of electrophoresis, allowing to measure the zeta potential and to fractionate the charged particles [14,15]. Values of charges are important for explanation and prognosis of the colloids behaviour in food systems containing proteins and polysaccharides. This equally applies to colloids used for the microencapsulation of biologically active substances [4,8,11].

Experimental part

Preparation of gelatine solutions

Macromolecular complexes were prepared using air-dried instant soluble food gelatine of premium grade (Lisichansk Gelatin Factory, ALC). All gelatine samples were incubated in a bath with boiling water for at least 5 minutes with continuous stirring until their complete dissolution. The native pH of gelatine solutions was in the range of 6.3…6.9. To adjust the desirable pH values, which were situated at the range of 2.5…8.0 units, the pH value was decreased by adding of small crystals of citric acid, or was increased by adding of solid potassium hydroxide. Pure gelatine solutions (0.5%) were prepared to determine the isoelectric point (IEP) of gelatine, in order to determine and to consider its type. The gels with the highest turbidity, indicating zero charge of macromolecules, were obtained after 24h in the vials with pH value ranged from 4.7 to 4.9. These values correspond to IEP of the gelatine type “B”, equal to 4.6…5.4, usually obtained by alkaline hydrolysis of skins [12].

Preparation of polyuronates

Pure preparations of alginic acid and hyaluronic acid were isolated from thallus of *Laminaria Japonica* [16]

and from cockscombs of *Gallus Domesticus* [17], respectively. Potassium salts were prepared by dropwise addition of KOH into suspensions of corresponding acids, up to their complete dissolution at pH = 5.5…7.5. Potassium alginate has been used as the main polyuronate, because of the possibility to separate it in pure form *in situ* [16]. Preparations of hyaluronic acid cannot be considered as "pure", because of inevitable presence of protein traces [9, 17]. Due to this fact, the salts of hyaluronic acid have been used to prepare coacervate microcapsules, in order to verify the applicability of results to similar systems, not only to gelatine-alginate system.

Specific viscosity and viscosimetric molecular weights

Viscosimetric measurements of high molecular compounds (HMC) were determined by viscosimeter "VPJ-1-0.34" (Apparatushhik Co., Russia).

Preparation of colloids

The gelatine-polyuronate colloidal systems only by leisurely addition of polyuronate solutions in the gelatine, never vice versa, were prepared. Combination of biopolymers was accompanied by vigorous stirring, and after that, the colloids were subjected to analysis immediately.

Oil-containing microcapsules

The microcapsules, containing walnut oil or sunflower oil, with gelatine-alginate or gelatine-hyaluronate shells, were obtained by complex coacervation method [18]. The ratio of gelatine/polyuranate in the shells of microcapsules was of 3.0...6.0. Mass fraction of encapsulated oil was no less than 75%. Their sizes were ranged from 5.0 to 50.0 microns. Estimated thickness of shells was approx. 0.38 microns.

Electrokinetic potential

Zeta potential (ζ) of colloids was measured by simply device (Figure 1).

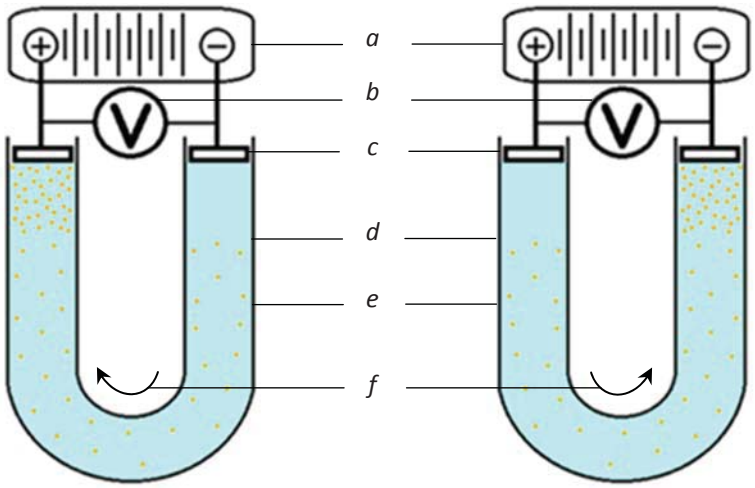

Figure 1. Electrophoretic device: a) source of voltage; b) digital multi-tester; c) stainless steel electrodes; d) sol border; e) U-shaped tube; f) movement of "–"charged particles (on left), "+"charged (right).

Electrophoresis was performed in U-shaped tubes of 1.0 cm width. Process has been occurred on the surface of hand-made integral electrodes, confectioned from stainless steel AISI 304 ("inox" for cookware). The distance between surfaces of the electrodes was from 15.0 to 25.0 cm. The field strength values (E) were adjusted in the range of 100…400 V/m by Stand for Testing of Automatically Equipment (STAE) "SPA-97" (Contragent Co., Ukraine). Operating voltage has been monitored by means of Digital Multi-tester "UT33C" (Shenzhen Sunkoo-Reid Electronic Co., China). The ζ-potential was calculated by the Helmholtz-Smoluchowski equation, Eq.(1) [7,14,15]:

$$\zeta = \frac{\eta \cdot V}{\varepsilon \cdot \varepsilon_0 \cdot H} = \frac{\eta \cdot l \cdot L}{\varepsilon \cdot \varepsilon_0 \cdot U \cdot \tau} \quad (1)$$

where, **constants:** $\eta = 1 \cdot 10^{-3}$ (Pa*)·s* –the viscosity of water; $\varepsilon = 89$, non-dimensional – dielectric constant of water; $\varepsilon_0 = 8.85 \cdot 10^{-12}$ (F/m*)* – electric permittivity of vacuum; **variables:** V (m/s*)* – velocity of colloid particles; H (V/m) – intensity of electric field; l (m*)* – run of colloidal particles in the electric field; τ (s) – time of electrophoresis; L (m) – distance between surfaces of electrodes (effective tube length); U (V) – voltage.

Results and discussion

Molecular weights of high molecular polymeric compounds (HMCs) pure samples

In contrast to the low molecular substances, HMCs do not have constant molecular weight. First, it is characteristic for *in situ* preparations of HMC, obtained from natural sources, having molecular weights that differ in function of characteristics of raw material. Thus, the molecular weights of linear biopolymers ranges from 10^3D to 10^6D (1…1000kD) [2,19]. Secondly, the HMCs molecular weight is almost always seeming, owing to intra- and intermolecular interactions, taking place in the HMCs solutions under the influence of various physical and chemical factors [20]. This is especially characteristic for the macromolecules of proteins and polysaccharides, such as gelatine, alginate, and hyaluronate, because their properties are pH-dependent, due to their polyionic structure, containing acidic or basic functional groups. So-called viscosimetric molecular weight of most types of polymers is usually calculated by Mark-Houwink-Sakurada equation, Eq.(2) [20,21]:

$$M_{HMC} = \left(\frac{[\eta]}{K}\right)^{1/\alpha} \tag{2}$$

where, K and α - constants, properly for the pair polymer-solvent; $[\eta]$ - intrinsic viscosity, which is calculated by extrapolation of function $\eta_{red.} = f\{C(HMC)\}$ to zero concentration of HMC (Figures 2 and 3). For calculations of M_{HMC}, we have considered maximum values of $[\eta]$, because of straightening of HMCs at high pH value [6-7].

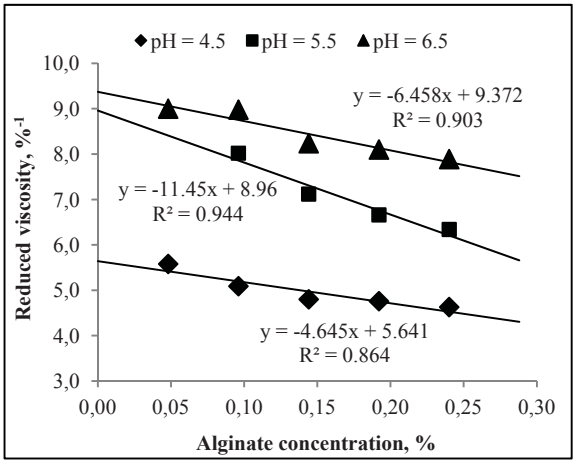

Figure 2. Viscosity of alginate.

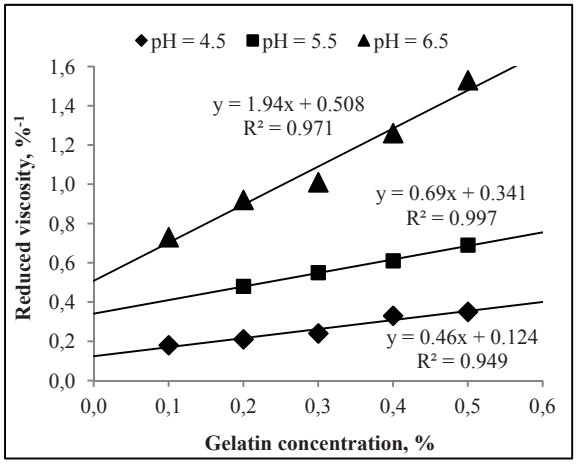

Figure 3. Viscosity of gelatine.

Samples of alginate, separated from thallus of *Laminaria Japonica*, possess intrinsic viscosity $[\eta]$ = 9.37 %$^{-1}$, or 937 mL/g in other units. This value is close to intrinsic viscosity of commercial alginate (Sigma-Aldrich Corporation, USA), equal to 1040 mL/g [21]. For this reason, respective values of K (0.0073) and α (0.92) for commercial alginate were used to calculate molecular weight of "our" native alginate. Resulted value, 357 kD, is in good correlation with many reported results [20-22]. In case of linear proteins, as gelatine, the Mark-Houwink-Sakurada equation usually in form of Eq.(3) is written [19]:

$$\frac{M_{\text{protein}}}{M_0} = \left(\frac{[\eta]}{K}\right)^{1/\alpha} \tag{3}$$

For gelatine type "B", M_0 is equal to 110D, representing average molecular weight of structural unit of protein molecule ("average" amino acid). Experimental intrinsic viscosity of gelatine was 50.8 mL/g. Referenced values [19] of constants K (0.166) and α (0.885) have been used to calculate the molecular weight of gelatine, being equal to 70.8 kD.

Estimation of the molecular weights of colloids

It can be assumed that the formation of gelatine-polyuronate systems is possible in a wide range of pH (2.0...8.0). Extreme values of pH correspond to cationic form of gelatine (Gel^+) and its anionic form (Gel^-), respectively. However, in the pH range from 8.0 to 5.0, any types of condensed (solid) colloidal systems do not form, but their interaction is not excluded. Both polymers at pH > 5.0 contribute to total (specific) viscosity of solution. For transparent mixtures of

gelatine and polyuronic salts this dependence is different. Recall that the charge of polyuronate is an order of magnitude greater than gelatine (zwitter-ion) total charge. Due to this fact, one molecule of alginate or hyaluronate can neutralize several gelatine molecules. The analysis demonstrates that specific viscosity of mixtures depends logarithmically on ratio m_{Gel}/m_{Hur} (Figure 4). This function possesses a good value of approximation accuracy, $R^2 = 0.973$. It allowed us to represent this dependence in the linear form (Figure 5). In our view, this linear relationship is well explained by a large number of charges in polyuronate molecules, being ten times higher than that of gelatine at equal pH values.

The weight ratio of gelatine/polyuronate allowed us to calculate the number of gelatine molecules, accompanied with one molecule of alginate, *i.e.* molar ratio of the biopolymers, n_{Gel} / n_{Alg}, Eq.(4):

$$\frac{n_{\mathrm{Gel}}}{n_{\mathrm{Alg}}} = \frac{m_{\mathrm{Gel}}}{m_{\mathrm{Alg}}} \cdot \frac{M_{\mathrm{Alg}}}{M_{\mathrm{Gel}}} \tag{4}$$

There were also estimated the minimal possible molecular weight of *GelAlg* complexes, M_{GelAlg}, reported to the one molecule of alginate, deducing following equation, Eq.(5):

$$M_{\mathrm{GelAlg}} = M_{\mathrm{Alg}} + \frac{n_{\mathrm{Gel}}}{n_{\mathrm{Alg}}} \cdot M_{\mathrm{Gel}} = M_{\mathrm{Alg}} \left(\frac{m_{\mathrm{Gel}}}{m_{\mathrm{Alg}}} + 1 \right) \tag{5}$$

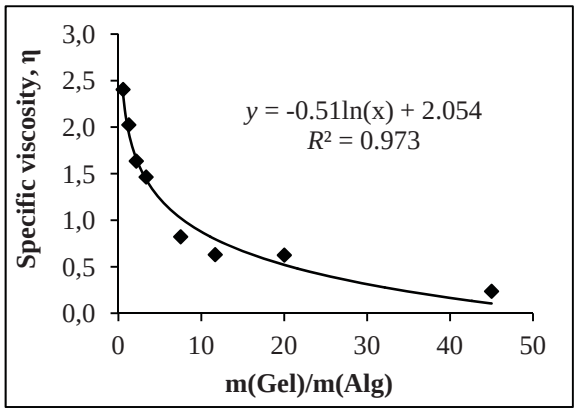

Figure 4. Specific viscosity: logarithmic function.

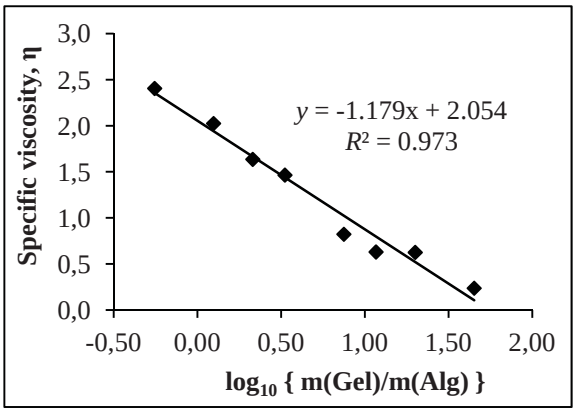

Figure 5. Specific viscosity: linear function.

At pH < IEP the interaction of gelatine with alginate leads to the formation of various colloids, including viscous solutions, large floccules, sols and gels. Naturally, the measuring of zeta-potential for solid colloids was possible only for the stable sols consisting from small particles, which does not precipitate immediately (Table 1).

Table 1

Type of colloidal systems and ζ-potential of stable sols.

m_{Gel}/m_{Alg}	*1.1*	*2.5*	*4.3*	*6.7*	*10*	*15*	*23*	*40*	*90*
$\log_{10}(m_{Gel}/m_{Alg})$	0.041	0.398	0.633	0.826	1.00	1.18	1.37	1.60	1.95
n_{Gel} / n_{Alg}	8	18	30	47	70	105	162	281	632
$M_{GelAlg.} \cdot 10^{-6}$, *D*	0.75	1.25	1.89	2.75	3.93	5.71	8.57	14.6	32.5
pH	*Colloids; sols, if ζ-potential values are showed; Δζ = ± 3.0 mV*								
4.5	high-viscous solutions						-40.7	-32.0	+14.5
4.0	-34.1	-39.8	-22.7	large dense floccules				+17.0	gels
3.5	-37.8	-34.9	-26.2	-20.3	+8.7	+11.6	+17.4	+29.1	gels

As follows from the ζ-potential (Table 1), the *GelAlg* complexes have negative charges, when m_{Gel}/m_{Alg} ratio is low, and they have positive charges, when this ratio is high. By lowering the pH value of biopolymer solutions, the recharging point of resulted particles is gradually shifting in the direction of increasing the alginate concentration. Intersection points of curves $\zeta = f\{\log_{10}(m_{Gel}/m_{Alg})\}$ with values of $\zeta = 0.0$, correspond to the composition of completely neutral colloids (Figure 6). In these conditions, the formation of neutral complexes $GelAlg^0$, able to precipitate quickly,

takes place. The sign inversion occurs at the $\log_{10}(m_{Gel}/m_{Alg}) \approx 1.7$ at the pH = 4.5 (Figure 6, *a*), decreases to ≈ 1.1 at the pH = 4.0 (Figure 6, *b*) and is reduced to ≈ 0.9 at the pH = 3.5 (Figure 6, *c*).

Charge of large floccules, not measurable by electrophoresis

It is problematically to study gelatine-alginate interaction at low pH value, because of precipitation of alginic acid (HAlg) and strong increasing positive charge of gelatine macromolecules. Moreover, the pH values lower than 3.0 are impossible to obtain by means of citric acid, and a small amount of HCl is necessary. In this condition, electrophoresis will be aggravated by electrolyze of HCl solution, resulting $H_{2(Gas)}$ at cathode and $Cl_{2(Gas)}$ at anode. This fact makes impossible to determine correct the zeta potential of colloid particles. The large floccules are formed quickly and are separated spontaneously from the supernatant solutions in many cases. Even in instances when floccules do not precipitate immediately and have been subjected to electrophoresis, they did not form a clearly defined borders so as it was shown in Figure 1. We cannot quantify the charge values in these conditions, but we can estimate the changes of charge sign due to the characteristic behaviour of colloidal suspensions [7]. Thus, after the stirring of obtained colloids about 20…30 minutes in each system was established an equilibrium. The system stability remains unchanged for the next several days (Figure 7).

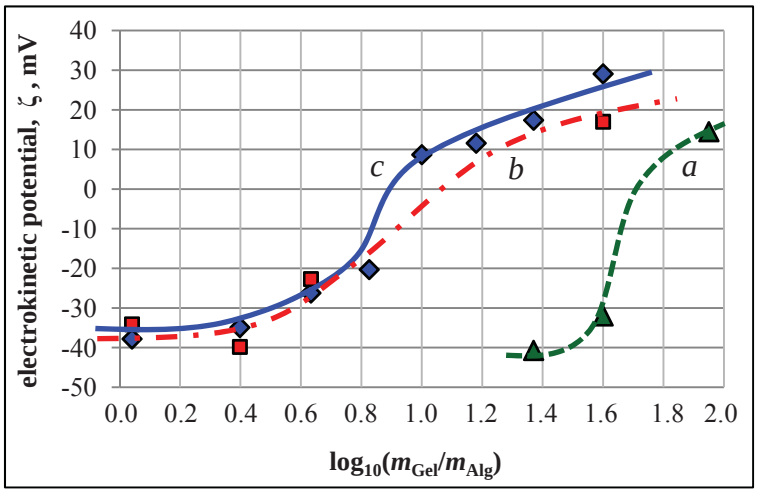

Figure 6. Dependence of electrokinetic potential ζ of the polyelectrolytes concentration ratio: a) at pH = 4.5; b) at pH = 4.0; c) at pH = 3.5.

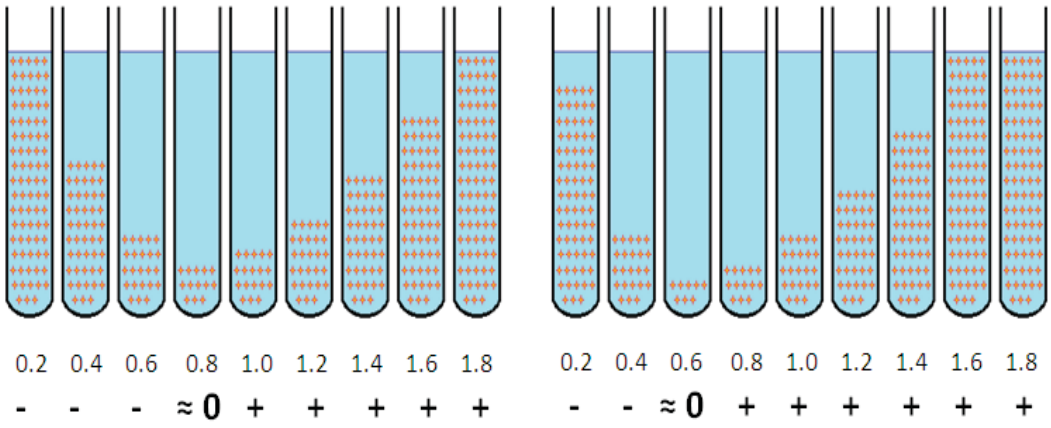

Figure 7. The sedimentation equilibrium aspect; $\log_{10}(m_{Gel}/m_{Alg})$; sign of the floccules charge. Left for pH = 3.0; right for pH = 2.5.

The maximum density of floccules formed at pH = 3.0 corresponds to the range of concentration m_{Gel}/m_{Alg} ratio from 4.0 to 10.0. In a more acidic medium (pH = 2.5) the range of rapid deposition of dense flocks shifted towards lower values of m_{Gel}/m_{Alg} ratio (from 2.0 to 7.0). At the same time, in each case the contents of both external vials remained

in suspension. It is obvious that the formation and rapid deposition of large floccules testifies zero charge of *GelAlg* colloids [7]. Conversely, decreasing the deposition rate in excess of one polyelectrolyte indicates the presence of large quantities of stabilizing charges. Naturally, this charge is negative in the left edge of series, because of excess of alginate anions, and is positive in the right edge of series. At low pH values (3.0 and 2.5), the changes of floccules charge correspond to the ζ-potential changes for particles of sols with high dispersion grade, obtained at pH > 3.0. During the increasing of m_{Gel}/m_{Alg} ratio, the charges of *GelAlg* colloids became positive, similarly with changes shown in Table 1. Neutralization points, obtained using Figures 4 and 5, allow to estimate n_{Gel}/n_{Alg} ratio by Eq.(4) and $M_{GelAlg}{}^{0}$ for neutral 3D-colloids by Eq.(5) (Table 2).

Table 2

Parameters of neutral 3D-colloids GelAlg⁰.

pH	*4.5*	*4.0*	*3.5*	*3.0*	*2.5*
$\log_{10}(m_{Gel}/m_{Alg})$	1.7	1.1	0.9	0.80	0.60
m_{Gel}/m_{Alg}	50.1	12.6	7.9	6.3	4.0
n_{Gel}/n_{Alg}	352	89	56	44	28
$M_{GelAlg}{}^{0} \cdot 10^{-6}$, *D*	18.2	4.86	3.18	2.61	1.79

Results of calculations showed in the Table 2 demonstrate clearly that inversion of charge (neutral) point shifts towards smaller values of the m_{Gel}/m_{Alg} ratio when pH became lower. In other words, at pH values approaching the IEP, even a small amount of polyuronic salts causes the coagulation of the proteins.

Phase diagram construction and its applications for microcapsules

The data obtained and discussed above can be extrapolated in visual interpretation of function pH–composition, resulting phase state diagram of the gelatine-alginate system (Figure 8).

The phase state diagram of gelatine-alginate at various pH values shows the phase phenomena occurring in the pH range of 2.0...6.0 at concentrations from 0.0 % to 3.0 % of gelatine and from 0.0 % to 0.3 % of alginate. These values correspond to the concentrations, used in the producing of beverages by means of protein-carbohydrate interaction [5], and to the conditions of microencapsulation by the method of complex coacervation [4,18]. Recall that at pH values more than IEP, gelatine is in form of negative-zwitterion, and is becoming "pure" anion at pH > 10. At the same time, gelatine is in form of positive charged zwitterion at pH lower than IEP, and is converted in "pure" cation, Gel^{+}, at pH < 2.0 [3,10].

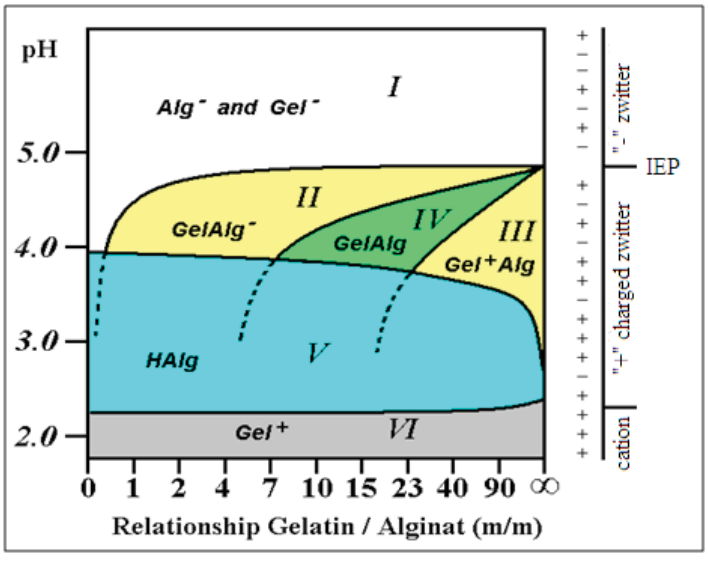

Figure 8. Phase diagram of the gelatine-alginate system.

The **Region I** corresponds to the mutual repulsion of negatively charged zwitterions $Gel^{->+}$ and "pure" anions of Alg^{-}. Although the main part of the Region I is located at pH > 5 (above the isoelectric point of gelatine), it still comes down to a pH of ≈ 4.5 in the left side, wherein the ratio m_{Gel}/m_{Alg} is low. We explain this fact that at high concentrations

of alginate occur full repayments of positive charges of gelatine by the excess of negative charges, as evidenced by the formation of transparent viscous solutions instead of sols and floccules in these conditions.

In the **Region II**, the formation of a high-negatively charged sols or suspensions formed from the large floccules takes place. In such colloidal systems the sedimentation does not occurs for several days. Deposition delay takes place because of powerful repulsion between surfaces of floccules. It is known that alginic or hyaluronic acid occurs in the anionic form at pH greater than 3.5 [9,23]. Due to this fact, there is a sufficient number of negative charges of alginate in this Region, which can neutralize many molecules of gelatine-zwitterion. Excess of negative charges, derived from alginate, is decisive for electrokinetic potential of the colloidal system in this Region, and total charge of resulting colloids ($GelAlg^-$) are negative. Colloids, formed in this Region, can minimize the using of gelatine in production of wines for the consumers, which abstain from the proteins of animal origin [24]. Electrokinetic properties of so charged colloids can be similar to agent properties for the binding of metal ions [25], and in our opinion, can substitute these agents in the production of wines and beverages.

In the **Region III**, there is an interaction similar to that observed in the Region II: colloids are kinetic stable and do not precipitate quickly, i.e., large excess of the gelatine in the form of zwitterions causes the global charge of colloids to be positive. Therefore, we have named as Gel^+Alg the floccules and sols obtained in these conditions.

The **Region IV** characterizes the formation of dense large flocks that undergo rapid sedimentation, which occurs in few minutes. The impossibility to determine their charge by electrophoresis proves that charges of sols and floccules, resulting in the Region IV, are close to zero. Numerically, the change of charge point is shifted to the higher gelatine concentrations, when pH increases (Table 1). Control experiments showed the greatest turbidity of pure gelatine solutions at pH 4.75-5.00. Therefore, the top point of this area corresponds to the isoelectric point of gelatine type "B" [12]. This fact explains nearly neutral charge of complexes *GelAlg* in the conditions, when m_{Gel}/m_{Alg} ratio tends to infinite and pH is near IEP value. Moreover, the neutral flocks form the agglomerates, which quickly lose their ability to peptize. According to the basic knowledge of colloid chemistry, the conditions, corresponding to the Region IV, are of practically importance for the deposition of undesirable colloids in beverages by means of co-sedimentation mechanism [7]. Therefore, it can be argued that the formation of neutral 3D-structures $GelAlg^0$ is not desirable in other cases, when the repulsion between the colloidal particles, but not their mutual coagulation, is necessary. Thus, it should be demonstrated that neutral charge of protein-polyuronate complexes *GelAlg* or *GelHur* is undesirable for stability of oil-containing microcapsules, possessing the shells, which are formed from these biopolymers.

In the **Region V** that is characterized by low pH values, the pattern is a somewhat peculiar. At pH < 4 gelatine solutions acquire high transparency, inherent for the true solutions of HMC and for non-colloids. This transparency appears because of straightening of the molecules due to the intra-molecular repulsion (excess of positive charges in the zwitterions $Gel^{+>}$) [6,7]. At the same time, the solutions of alginate in this pH range, behave quite differently. At pH values below 3.8, the alginate solutions lose their transparency and the alginate precipitates in form of alginic acid at pH ≈ 3.5, taking place a reaction: $Alg^- + H^+ \rightarrow HAlg$. Solutions of the hyaluronates behaved similarly: hyaluronic acid precipitates in the form of gelled sticks by lowering the pH below 3.5. Thus, in the **Region V** the formation of *GelAlg* or *GelHur* floccules is accompanied and is aggravated by the protonation of polyanions.

The above-described phase diagram "gelatine-alginate" explains well the behaviour and stability of lipid-containing microcapsules with gelatine-polyuronate shells under various conditions. In the model solutions with pH corresponding to the Regions II...VI, microcapsules behave differently. In the conditions of Region II the microcapsules are high stable and do not stick (Figure 9, *a*). For neutral $GelAlg^0$ or $GelHur^0$ complexes, microcapsules suffer agglomeration (Figure 9, *b*) and total destruction (Figure 9, *c*).

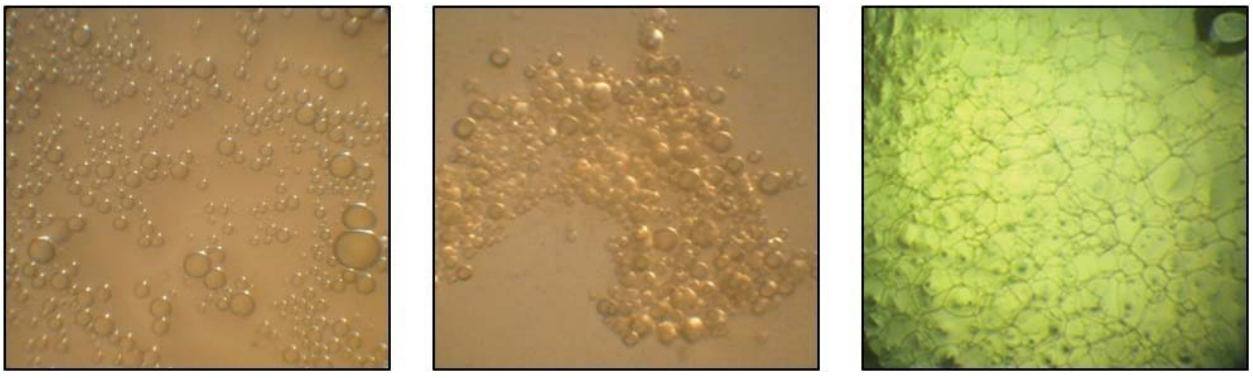

a ***b*** ***c***

Figure 9. Microcapsules with gelatine-hyaluronic shells: a) stable, in the conditions of Region II; b) coagulated in the conditions of Regions V or VI; c) destroyed after 3 days in the conditions of Region VI.

It can be noted that gelatine-alginate or gelatine-hyaluronate shells of microcapsules, being under the conditions of **Region VI**, undergo following reactions:

$$GelAlg^{-} + H^{+} \rightarrow GelAlg^{0} \text{ (or: } GelHur^{-} + H^{+} \rightarrow GelHur^{0}) \quad (6)$$

$$GelAlg^{0} + H^{+} \rightarrow HAlg + Gel^{+} \text{ (or: } GelHur^{0} + H^{+} \rightarrow HHur^{0} + Gel^{+}) \quad (7)$$

In our opinion, the complete destruction of high-molecular structures does not occur immediately. Only structural recombination of shells, described by Eq.(6) and Eq.(7), accompanied by a change of their charge and, obviously, with latent changes in the conformation of macromolecules, take place. Due to this fact, the destruction of microcapsules with removal of lipid phase completed after 3…4 days. Conglutination of microcapsules and recombination of their shells, occurring in Regions V and VI, are accompanied by the release of encapsulated content and with the formation of foam-like dodecahedron structures, consisting of protein-poliuronate colloids (Figure 9, *c*).

The regularities of formation of charged colloids, probably, also refer to protein-based colloids, which are formed with different polyuronic acids, pectins and other polysaccharides possessing acidic functional groups.

Conclusions

There were found the conditions for the formation of negatively charged, the positively charged and the neutral colloids. It was observed that the properties of protein/polyuronate system depend on their mass ratio logarithmically. The molecular weight of neutral charged colloids decreases with diminishing the pH value. A phase state diagram, which reflects the influence of pH and ratio of the components (gelatine and alginate) on electric charge and stability of the resulting polymer complexes, was developed. The Diagram is of great practical interest for predicting the properties of different food systems. In particular, the Diagram shows the most suitable conditions for obtaining of microcapsules with stable gelatine-alginate or gelatine-hyaluronate shells with a negative electric charge {Region II, pH = 3.0...4.5, m_{Gel}/m_{Alg} ratio 2...8, $GelAlg^{-}$, $M_{GelAlg} = (1...3) \cdot 10^{6} D$}. Due to their negative charge, the colloids, obtained in the Region II, can be used for sedimentation of different positively charged particles in different food systems, inclusive wines and beverages. The Region III, with strong positive charge of colloids {pH = 3.0...4.0, m_{Gel}/m_{Alg} = 40...90, $Gel^{+}Alg$, $M_{GelAlg} = (15...35) \cdot 10^{6} D$}, is suitable for microencapsulation, but is characterized by great consumption of gelatine for shell's constructing. Phase diagram shows that gelatine-alginate colloids with $\zeta \approx 0$ {Region IV, pH = 3.0…4.5, m_{Gel}/m_{Alg} ratio 10...30, $GelAlg^{0}$, $M_{GelAlg} = (4...10) \cdot 10^{6} D$} are not suitable for microencapsulation. At the same time, the complexes with zero charge, obtained under the conditions of Region IV, are of greatest interest for quickly clarification of beverages.

Acknowledgements

This work is done within the framework of Research Project 15.817.02.30A ("Development of Methods and Techniques for Modernisation of Nuts (*Juglans Regia L.*) Processing Technology Using the Biologically Active Constituents in the Functional Foods), co-financed by the Academy of Sciences of Moldova and by the Technical University of Moldova.

References

1. Shinde, U.A.; Nagarsenker, M.S. Characterization of Gelatine-Sodium Alginate Complex Coacervation System. Indian Journal of Pharmaceutical Science, 2009, 71(3), pp. 313-317.
2. Belitz, H.-D.; Grosch, W.; Schieberle, P. Food Chemistry. Springer Verlag: Berlin, 2009, 1070 p.
3. Gómez-Guillén, M.C.; Giménez, B.; López-Caballero, M.E.; Montero, M.P. Functional and bioactive properties of collagen and gelatine from alternative sources. Food Hydrocolloids, 2011, 25, pp. 1813-1827.
4. Roy, A.; Bajpai, J.; Bajpai, A.K. Development of Calcium Alginate – Gelatine Based Microspheres for Controlled Release of Endosulfan as a Model Pesticide. Indian Journal of Chemical Technology, 2009, 16, pp. 388-395.
5. Aharnsilawat, T.; Pongsawatmanit, R.; McClements, D.J. Stabilization of Model Beverage Cloud Emulsions Using Protein−Polysaccharide Electrostatic Complexes Formed at the Oil−Water Interface. Journal of Agricultural Food Chemistry, 2006, 54(15), pp. 5540-5547.
6. Heinzmann G.; Tartsch, B. Alginates, chitosanes and xanthans. Characterization of food ingredients by GPC/SEC with triple detection. Agrofood Industry Hightech, 2009, 20(4), pp. 56-59.
7. Birdi, K.S. (editor). Handbook of Surface and Colloid Chemistry. Taylor & Francis Group, 2016, 694 p.
8. Doublier, J.-L.; Garnier, C.; Renard, D.; Sanchez, C. Protein-polysaccharide interactions. Current Opinion in Colloid & Interface Science, 2000, 5, pp. 202-214.
9. Lenormand, H.; Tranchepain, F.; Deschrevel, B.; Vincent, J.-C. The hyaluronan-protein complexes at low ionic

strength: How the hyaluronidase activity is controlled by the bovine serum albumin. Matrix Biology, 2009, 28, pp. 365-372.
10. Steinbuchel, A.; Rhee, S.K. Polysaccharides and Polyamides in the Food Industry. Wiley-VCH: Weinheim. 2005, 783 p.
11. Hammad Umer; Hemlata Nigam; Asif M. Tamboli; M. Sundara Moorthi Nainar. Microencapsulation: Process, Techniques and Applications. International Journal of Researches in Pharmaceutical and Biomedical Sciences, 2011, 2 (2), pp. 474-481.
12. Pignatello, R. Biomaterials Applications for Nanomedicine. Intech: Rijeka, Croatia, 2011, 458 p.
13. Jusova, A.A.; Gusev, I.V.; Lipatova, I.M. Properties of hydro gels based on mixtures of sodium alginate with other polysaccharides of natural origin. Chemistry of vegetable raw materials, 2014, 4, pp. 59-66 (in Russian).
14. Jackson, C.R.; Raja, P.M.V.; Prakash, S. A Novel Electrophoretic Deposition Device: Effects of Alginate Viscosity Grade on Deposition Kinetics. Journal of Biotechnology & Biomaterials, 2012, doi:10.4172/2155-952X.S6-002.
15. Khair, A.S.; Squires, T.M. The Influence of Hydrodynamic Slip on the Mobility of a Spherical Colloidal Particle. Physics of Fluids, 2009, 21(4), 042001. http://dx.doi.org/10.1063/1.3116664.
16. Dimova, O.; Baerle, A.; Tatarov, P.; Verejan, A. Process for producing alginates from brown algae. Republic of Moldova Patent, 2013, No. MD 669 (in Romanian).
17. Zadorojnâi; L. Process for obtaining the sodium hyaluronate, the hyaluronic acid and the protein-hyaluronic acid complex. Republic of Moldova Patent, 2006, No. MD 3099 (in Romanian).
18. Baerle, A.; Tatarov, P.; Dimova, O.; Cojohari, C. Process for microencapsulation of food and cosmetic oil compositions. Republic of Moldova Patent, 2012, No. MD 557 (in Romanian).
19. Masuelli, M.A. Mark-Houwink Parameters for Aqueous-Soluble Polymers and Biopolymers at Various Temperatures. Journal of Polymer and Biopolymer Physical Chemistry, 2014, 2(2), pp. 37-43.
20. Lima, A.M.F.; Soldi, V.; Borsali, R. Dynamic Light Scattering and Viscosimetry of Aqueous Solutions of Pectin, Sodium Alginate and their Mixtures. Effects of Added Salt, Concentration, Counterions, Temperature and Chelating Agent. Journal of Brazilian Chemical Society, 2009, 20(9), pp. 1705-1714.
21. Masuelli, M.A.; Illanes, C.O. Review of the characterization of sodium alginate by intrinsic viscosity measurements. Comparative analysis between conventional and single point methods. International Journal of Biomaterials Science and Engineering, 2014, 1(1), pp. 1-11.
22. Vold, I.M.N.; Kristiansen, K.A.; Christensen, B.E. The Mark-Houwink equation of alginates and chitosans. Biomacromolecules; Addition/Correction. 2007, 8(8), pp. 2627-2627.
23. Fukushima, M.; Tatsumi, K.; Wada, S. Evaluation of the Intrinsic Acid-Dissociation Constant of Alginic Acid by Considering the Electrostatic Effect. Analytical Sciences, 1999, 15, pp. 1153-1155.
24. Pyevich, C. Why is Wine so Fined? Vegetarian Journal, 1997, XVI(1), https://www.vrg.org/journal/vj97jan/971wine.htm.
25. Rinn, J.-C.; Robillard, B. Alginate or pectate gel deficient in gelling ions for use in binding metal ions. United States Patent, 1996, No. US 5567451.